



HAL
open science

Membrane processes for water and wastewater treatment: study and modeling of interactions between membrane and organic matter

Zhaohuan Mai

► **To cite this version:**

Zhaohuan Mai. Membrane processes for water and wastewater treatment: study and modeling of interactions between membrane and organic matter. Other. Ecole Centrale Paris, 2013. English. NNT: 2013ECAP0053 . tel-00969165

HAL Id: tel-00969165

<https://theses.hal.science/tel-00969165v1>

Submitted on 2 Apr 2014

HAL is a multi-disciplinary open access archive for the deposit and dissemination of scientific research documents, whether they are published or not. The documents may come from teaching and research institutions in France or abroad, or from public or private research centers.

L'archive ouverte pluridisciplinaire **HAL**, est destinée au dépôt et à la diffusion de documents scientifiques de niveau recherche, publiés ou non, émanant des établissements d'enseignement et de recherche français ou étrangers, des laboratoires publics ou privés.



**ÉCOLE CENTRALE DES ARTS
ET MANUFACTURES
« ÉCOLE CENTRALE PARIS »**

THÈSE
présentée par

Zhaohuan MAI

pour l'obtention du

GRADE DE DOCTEUR

Spécialité : Génie des Procédés

Laboratoire d'accueil : Laboratoire de Génie des Procédés et Matériaux

SUJET :

**Les procédés membranaires pour le traitement de l'eau: étude et
modélisation des interactions entre membranes et composés
organiques**

**Membrane processes for water and wastewater treatment: study
and modeling of interactions between membrane and organic
matter**

soutenue le : 2 Octobre 2013 devant un jury composé de :

MALFREYT Patrice
GESAN GUIZIOU Geneviève
RAKIB Mohammed
COUALLIER Estelle
BOURSEAU Patrick
FARGUES Claire
ROUSSEAU Bernard

Professeur , ICCF
Directrice de Recherche, INRA
Professeur, ECP
Maître de conférences, ECP
Professeur, Université de Bretagne Sud
Maître de conférences, IUT d'Orsay
Directeur de Recherche CNRS

Rapporteur
Rapporteur
Directeur de thèse
Co-encadrante
Examinateur
Examinatrice
Invité

Acknowledgements

Research requires a high level of planning, executing and discussing. To maximise the quality of the results obtained, we need plentiful opinions, contributions and support. In my opinion, a thesis is not a personal achievement but the result of an enriching experience involving more than one person. During these last three years, I have been supported by many people to whom I am very grateful.

Firstly, I would like to thank gratefully my supervisor Pr. Mohammed RAKIB, for providing me such a good opportunity to work with him and letting me enter and enjoy the research world. Thanks for his guidance during the three years in Ecole Centrale Paris, for his constant support and invaluable advices throughout this study.

I would like to express my sincere gratitude to my supervisor, Dr. Estelle COUALLIER, for her kindly help and guidance on membrane technologies as well as the experiments during my study in ECP. Thanks for her help on learning the simulation, especially for her continuous encouragement and helpful discussions at the last but hardest time of my thesis. From research planning to results discussion, I learned a lot from her. During the three years in France, she not only helped me with my work, but also cared for my living. It is my pleasure and I'm very lucky to work with her.

Special thanks for my co-supervisor, Dr. Bernard ROUSSEAU, for his guidance and constant advices on the simulation part of this work. Thanks for sharing with me his thoughts and reflections on the simulation results. Without his help, I could not resolve so many problems.

I would like to thank my supervisor in Wuhan University, Pr. Feng WU, for his kindly help when I was in China, and thanks for his discussion on my progress during my PhD studies.

I also gratefully acknowledge Pr. Patrice MALFREYT and Dr. Geneviève GESAN-GUIZIO for being external reviewers of this thesis, and Pr. Patrick BOURSEAU and Dr. Claire FARGUES for their

acceptance to participate in the evaluation committee for their questions, suggestions and comments on my thesis.

Many thanks go for Barbara, Hélène, Cyril and Vincent for their help in the lab and for the experimental equipments. Thanks for Jamila and Madame Muriel in Renne for teaching me the sessile drop method.

My best wishes to my friends Jing HE, Yufang ZHANG, Xin WEI, Yaqin YANG, Yu CAO, Yuxiang NI, to whom I shared unforgettable moments in residence during the years in France. Thanks very much to my colleagues Amaury, Sofien, Emene, Mariata, Pin, Sepideh, Liliana, and all other members in LGPM. It was really an unforgettable memory to stay with them.

I would like to thank the financial support from China Scholarship Council (CSC) affiliated with the Ministry of Education of the P.R.China. Thanks for giving me this chance to work in France.

Finally, I would especially like to thank my family, my parents always being there with encouragement; I would like to thank my boyfriend for his love, understanding and support, Without them, I can't overcome any difficulties.

Publications and communications

Z. Mai, E. Couallier, and M. Rakib, Experimental study of surfactants adsorption on reverse osmosis membrane, *Journal of Membrane Science* (in preparation)

Z. Mai, E. Couallier, H. Zhu, E. Deguillard, B. Rousseau and M. Rakib, Mesoscopic simulations of surfactant micellization by dissipative particle dynamics, *Journal of Chemical Physics*(in preparation)

C. Baudequin, E. Couallier, Z. Mai, M. Rakib, I. Deguerry, R. Severac, M. Pabon, reverse osmosis for the retention of fluorinated surfactants in complex media, ***Journal of Membrane Science***, (submitted)

Euromembrane 2012, Londres, C. Baudequin, E. Couallier, Z. Mai, M. Rakib, I. Deguerry, R., Severac, M. Pabon, multiscale experiments for the screening of RO membrane and the design of firefighting water treatment (poster)

Euromembrane 2012, Londres, Z. Mai, E. Couallier, H. Zhu, M. Rakib, B. Rousseau, DPD simulation of surfactants behavior nearby RO membrane : validation of interaction parameters by CMC calculation (poster)

Table of contents

Nomenclature.....	vii
General introduction.....	1
Chapter 1.....	7
Literature review.....	7
1.1 Pressure-driven membrane processes.....	9
1.1.1 Definition.....	9
1.1.2 Membrane flow configurations.....	10
1.1.3 Types of membranes: MF, UF, NF, RO.....	11
1.2 Reverse Osmosis.....	14
1.2.1 Introduction.....	14
1.2.2 RO Process description and terminology.....	16
1.2.3 Material, structure and geometry.....	18
1.2.3.1 Materials.....	18
1.2.3.2 Structure.....	20
1.2.3.3 Geometry.....	20
1.2.4 Concentration polarization and fouling.....	23
1.2.4.1 Concentration polarization.....	23
1.2.4.2 Membrane fouling.....	24
1.2.5 Characterization of membranes.....	27
1.2.5.1 Characterization of membrane chemical structure.....	29
1.2.5.2 Characterization of membrane charge.....	30
1.2.5.3 Characterization of membrane hydrophilicity.....	32
1.2.5.4 Characterization of membrane morphology.....	36
1.3 Surfactants.....	38
1.3.1 Development and applications.....	38

1.3.2	Definition of surfactants.....	39
1.3.3	Chemical structure and classification.....	40
1.3.4	Properties of surfactants.....	43
1.3.4.1	Surfactant micellization.....	43
1.3.4.2	Surfactant adsorption at solid-liquid interface.....	44
1.3.5	Environmental effects of surfactant.....	51
1.3.6	Membrane filtration of surfactants.....	52
1.4	Membrane filtration.....	62
1.5	Simulation of surfactant systems.....	63
1.6	Thesis outline.....	64
Chapter 2.....		65
Experimental part:.....		65
Fouling of RO membranes by surfactants.....		65
2.1	Introduction.....	67
2.2	Materials and methods.....	69
2.2.1	Surfactant solutions.....	69
2.2.2	RO membranes.....	69
2.2.3	Analytical methods.....	71
2.2.4	Filtration set-up and reverse osmosis of surfactant solutions.....	71
2.2.5	Adsorption in reverse osmosis set-up without pressure.....	74
2.2.6	Static adsorption of surfactants onto SG membranes.....	74
2.2.7	Contact angle measurements.....	75
2.3	Results.....	77
2.3.1	Membrane performance.....	77
2.3.1.1	SDS rejection.....	77
2.3.1.2	Permeate flux.....	79
2.3.2	Surfactant adsorption.....	83

2.3.2.1	Adsorption during filtration process	83
2.3.2.2	Adsorption in the filtration system	89
2.3.2.3	Static adsorption.....	91
2.3.2.4	Circulation of surfactant solution in the system without pressure	95
2.3.3	Contact angle measurements.....	97
2.3.4	Mechanism of surfactant adsorption onto membrane surface.....	101
2.4	Conclusions	105
Chapter 3	107
Simulation part:	107
Mesoscopic simulations.....	107
of surfactant micellization and adsorption.....	107
by Dissipative Particle Dynamics.....	107
3.1	Introduction.....	109
3.2	Theory	113
	Dissipative Particle Dynamics	113
3.3	Methodology	117
3.3.1	DPD Models for surfactants and water	117
3.3.2	Detailed DPD simulation procedure	118
3.3.3	Analysis details	121
3.3.3.1	Micelle formation.....	121
3.3.3.2	Cluster definition	124
3.3.3.3	Equilibrium	126
3.3.3.4	Cluster size distribution.....	130
3.3.3.5	Critical micelle concentration.....	134
3.4	Results and discussion.....	135
3.4.1	Parameter set I.....	135
3.4.2	Effect of DPD parameters on micellar properties	138

3.4.3	Effect of intramolecular interactions	142
3.4.4	CMC of surfactants	147
3.4.5	Adsorption of surfactants on the membrane	151
3.4.5.1	The effect of a_{TM}	152
3.4.5.2	The effect of surfactant concentration	154
3.4.5.3	Kinetic competition between micellization and adsorption	157
3.5	Conclusion	159
	General conclusions and perspectives	161
	Appendix	169
	References	173

Nomenclature

1. Symbols

a_0	Cross-sectional area	\AA^2
a_{ij}, a_{ii}	Conservative repulsion parameters in DPD	
A, A_m	Membrane surface area	m^{-2}
A_{SDS}	Cross-sectional area of SDS molecules	\AA^2
C_0	Initial concentration	mol L^{-1}
$C_{A,m}$	Maximum concentration of solute A at the membrane surface	mol L^{-1}
$C_{A,f}$	Bulk/feed concentration of solute A	mol L^{-1}
C_C	Concentrate solute concentration	mol L^{-1}
C_{eq}	Equilibrium concentration of the surfactant in solution	mol L^{-1}
C_F	Feed solute concentration	mol L^{-1}
C_P	Permeate solute concentration	mol L^{-1}
C_t	Retentate concentration when samples are taken at each time interval during RO filtration experiments	mol L^{-1}
dp	Diameter of membrane pores	μm
e	Membrane thickness	μm
E_b	Bonding energy	
E_p	Chemical potentials in DPD system	
F_C	Concentrate flow rate	L h^{-1}
F_F	Feed flow rate	L h^{-1}
\mathbf{F}_i	Total force on bead i in DPD simulation	
\mathbf{F}_B	Bending force in DPD	
$\mathbf{F}_{ij}^C, \mathbf{F}_{ij}^D, \mathbf{F}_{ij}^R$	Conservative force, dissipative force and random force in DPD	
F_P	Permeate flow rate	L h^{-1}
\mathbf{F}_s	Harmonic spring force between bonded beads in DPD simulation	
$g(r)$	Radial distribution function	
J	Flux	$\text{L} \cdot \text{h}^{-1} \cdot \text{m}^{-2}$
J_S	Solute flux	$\text{L} \cdot \text{h}^{-1} \cdot \text{m}^{-2}$

J_w	Water flux	$L \cdot h^{-1} \cdot m^{-2}$
J_{w0}	Initial or pure water flux	$L \cdot h^{-1} \cdot m^{-2}$
k_B	Boltzmann's constant	
K_f, n_f	Constants for a given adsorbate and adsorbent pair at a particular temperature	
K_H	Henry adsorption constant	$L m^{-2}$
K_L	Langmuir constant	$L mol^{-1}$
k_r	Bond spring constant in DPD simulation	
k_θ	Bending constant in DPD simulation	
K_S	Equilibrium constant of the surface aggregation process	
l_c	Length of surfactant hydrophobic group in the core of a micelle	\AA
m_{out}	Total mass of SDS taken out as samples during RO filtration experiments	g
M_{SDS}	Molar mass of SDS molecules	$g mol^{-1}$
N_{agg}	Aggregation number	
n_i	Number of aggregates in the simulated system	
N	Cluster size	
N_i	Number of surfactants that belong to cluster i	
N_m	Number of water molecules contained in one bead	
N_w	Weight-average aggregation number	
n_s	Average aggregation number of the surface aggregate as a general adsorption isotherm	
pH _F	Feed pH	
Q_{ads}	Amount of surfactant adsorption onto the adsorbent	$mol m^{-2}$ or $g m^{-2}$
$Q_{ad,max}$	Maximum adsorption of the surfactant per unit mass of the UF membranes	$mol m^{-2}$
q_f	Mass loss of surfactant during filtration per membrane surface	$mmol m^{-2}$
Q_∞	The limiting surfactant adsorption at high concentration	$mmol m^{-2}$
q_s	Amount of surfactant adsorbed onto the membrane in static adsorption experiments	$mmol m^{-2}$
r	Water recovery of the membrane	
r_0	Equilibrium distance between two consecutive beads in DPD simulation	

r_c	Cutoff radius in DPD simulation	
R	Solute rejection	%
R_{cm}	Distance between surfactant centers of mass	
\mathbf{r}_i	Position of a bead in DPD	
R_{ADS}	Resistance for adsorption	
R_{agg}	Cutoff threshold to distinguish micelles and free surfactants	
R_{CL}	Resistance for cake layer	
R_F	Membrane resistance caused by fouling	
R_G	Resistance for gel layer	
R_m	Membrane resistance	
R_t	Total resistance of all the individual resistance that may happen for a given solution-membrane system	
T	Temperature	
v	Velocity of the flow	m s^{-1}
\mathbf{v}_{ij}	equal to $\mathbf{v}_i - \mathbf{v}_j$, the velocity difference between beads i and j in DPD simulation	
V	Volume	L
$V_0, V_{\text{Hold}}, V_{\text{out}}$	Initial, hold-up and taken out volume of the filtration system	L
V_H	Volume occupied by surfactant hydrophobic groups in the micellar core	\AA^3
W	Adhesion between solid and liquid	
X_1, X_{aggi}	Molar fraction of of the surfactant monomers and the surfactant aggregate with aggregation number i	

2. Greek letters

Δa	Interface/surface area	m^{-2}
ΔG^0	Free energy of adsorption at infinite dilution	J
ΔG_I	Interfacial free energy	J
ΔG_{ii}	Free energy of cohesion i <i>in vacuo</i>	J
ΔG_{sl}	Free energy of interaction required to separate the surface S and a liquid L	J
σ_{ij}	Fluctuation amplitude in DPD simulation	
ε	Membrane porosity	
$\Delta \Pi$	Osmotic pressure	bar
ΔP	Transmembrane pressure	bar
Δt	Time step in DPD simulation	
ζ	Zeta potential	mV
γ	Interfacial/surface tension	J m^{-2}
$\gamma_1, \gamma_2, \gamma_i$	Surface tension of materials 1, 2 or i	J m^{-2}
γ^{AB}	Lewis acid/base (polar)	
$\gamma^{\text{A}}, \gamma^{\text{B}}$	Electron acceptor and electron donor parameters of the surface tension	
γ_{lv}	Liquid-vapor surface tension	
γ_{sl}	Solid and liquid interfacial tension	
γ_{sv}	Solid-vapor surface tension	
γ^{LW}	Lifshitz-Van der Waals component of the surface tension	
γ_{ij}	Friction coefficient in DPD simulation	
ρ	Density of the simulation system	
θ	Contact angle	°
θ_0	Equilibrium angle in DPD simulation	
μ_1, μ_{agg}	Chemical potential of free surfactant monomers and aggregates	
$\omega^{\text{D}}(r_{ij}), \omega^{\text{R}}(r_{ij})$	Weight function for dissipative force and random force in DPD simulation	
χ	Flory–Huggins parameter	
ζ_{ij}	Noise coefficient in DPD simulation	

3. Acronym

AFM	Atomic force microscopy	
ATR-FTIR	Attenuated total Reflectance Fourier transform Infrared Spectroscopy	
BOD	Biological oxygen demand	$\text{g O}_2 \text{ L}^{-1}$
CA	Cellulose acetate	
CAC	Critical aggregation concentration	
CESIO	Comité Européen des Agents de Surface et leurs intermédiaires Organiques	
CG-MD	Coarse-grained molecular dynamics	
CIP	Clean-In-Place	
CM	Center of mass	
CMC	Critical micelle concentration	
COD	Chemical oxygen demand	$\text{g O}_2 \text{ L}^{-1}$
CP	Concentration polarization	
CSLM	Confocal scanning laser microscopy	
CTAB	Hexadecyltrimethylammonium bromide	
DPD	Dissipative Particle Dynamics	
EDS	Energy-Dispersive X-ray Spectroscopy	
EIS	Electrochemical impedance spectroscopy	
ELSD	Evaporative light scattering detector	
ESCA	Spectroscopy for chemical analysis	
FH	Flory-Huggins	
HPLC	High performance liquid chromatography	
IR	Infrared Spectroscopy	
MD	Molecular dynamics simulation	
MEUF	Micellar-enhanced ultrafiltration	
MF	Microfiltration	
MP	Membrane potential	
MSD	Mean square displacement	
MWCO	Molecular weight cut-off	Da
NF	Nanofiltration	

NP	Polyoxyethylene nonylphenyl ether	
NVT	Constant particle number, volume, and temperature	
PA	Polyamide	
PES	Polyethersulfone	
PFOS	Perfluorooctane sulfonate	
PVC	Polyvinyl chloride	
PVDF	Poly(vinylidene fluoride)	
RDF	Radial distribution function	
RO	Reverse osmosis	
SBE	Backscattered electrons	
SDBS	Sodium dodecyl benzene sulfonate	
SDS	Sodium dodecyl sulfate	
SE	Secondary electrons	
SEM	Scanning electron microscope	
SHS	Sodium hexyl sulfate, $C_6H_{13}OSO_3Na$	
SIMS	Secondary Ion Mass Spectroscopy	
SNS	Sodium nonyl sulfate, $C_9H_{19}OSO_3Na$	
SP	Streaming potential	
TDBNC	Tetradecylbenzylammonium chloride	
TEM	Transmission electron microscope	
TFC	Thin film composite	
TMP	Transmembrane pressure	bar
TOC	Total organic carbon	$g\ O_2\ L^{-1}$
TOF-SIMS	Secondary Ion Mass Spectroscopy combined with a mass analyzer called time-of-flight	
UF	Ultrafiltration	
XPS	X-ray Photoelectron Spectroscopy	

General introduction

Because of vastly expanding populations, increasing water demand, and the deterioration of water resource quality and quantity, water is going to be one of the most precious resources in the world. The problem of water shortage is not only a problem of proper techniques, but also a social and educational problem, depending on national and international efforts as well as on technical solutions [1].

In water and wastewater treatment, membrane technology, a term that refers to a number of different processes using synthetic membranes to separate chemical substances, has been recognized as the key technology for the separation of contaminants from polluted sources thus purifying original waters [1]. Membranes are selective barriers that separate two different phases, allowing the passage of certain components and the retention of others. The driving force for transport in membrane processes can be a gradient of pressure, chemical potential, electrical potential or temperature across the membrane. Membrane processes rely on a physical separation, usually with no addition of chemicals in the feed stream and no phase change, thus stand out as alternatives to conventional processes (i.e. distillation, precipitation, coagulation/flocculation, adsorption by active carbon, ion exchange, biological treatment...) for the chemical, pharmaceutical, biotechnological and food industries [1], [2]. In many cases the low energy consumption, reduction in number of processing steps, greater separation efficiency and improved final product quality are the main attractions of these processes [1], [2], [3]. During the past years, membranes have been greatly improved with significantly enhanced performance and commercial markets have been spreading very rapidly throughout the world. In the future, further improvements and innovations are needed, especially in the chemical and morphological design of membrane materials, element and module design of membrane systems, antifouling membranes for wastewater treatment, and so on [1].

Among all technologies available today, reverse osmosis (RO) is gaining worldwide acceptance in both water treatment and desalination applications [4]. RO membranes can be used to remove salinity and dissolved organic matter, while reducing total organic carbon (TOC), chemical oxygen demand (COD) and biological oxygen demand (BOD) [1]. The mass transfer in RO is due to solution-diffusion mechanism, size exclusion, charge exclusion and physical-chemical interactions between solute, solvent and the membrane [4]. The process efficiency is determined by several factors, including operational parameters, membrane and feed water properties. The most common commercially available RO membrane modules include flat sheet and spiral-wound. RO membranes with integrally asymmetric structure from the first generation material cellulose acetate (CA) to thin film composite (TFC) membranes

are most available in the market. Most of commercial RO composite membranes are polyamide-based while other composite membranes (i.e. sulfonated polysulfone) could also be found [2]. The functional groups introduced into the polymer structure control the valence and strength of the membrane charge while the degree of adsorption of dissolved species is determined by membrane hydrophobicity, charge and roughness affect [4], [5].

Though the improvement of RO membranes has been tremendous in the past few years, their performance and economics are still far from perfect. Membrane life time and permeate fluxes are primarily affected by the phenomena of concentration polarization and fouling [6]. During the pressure-driven membrane processes of aqueous effluent containing dissolved organic matters, membrane fouling leads to a decrease in performance with a loss in solvent permeability and changes to solute transmission. The reasons for fouling are reported as consisting of chemical fouling, biological fouling and scale formation [1]. Organic fouling is caused by the adsorption of organic materials from the feed water such as humic substances, proteins, polysaccharides, surfactants etc. onto or into the membrane [2]. The chemical fouling depends on hydrophobic interaction and electrostatic interaction between organic materials in the feed water and membrane surface [7].

In this study we focus on membrane fouling by surfactants. Surfactants are organic compounds used in everyday life and are essential components in many industrial processes and formulations, such as household detergents, personal care formulations, industrial and institutional washing and cleaning, as well as numerous technical applications such as textile auxiliaries, leather chemicals, agrochemicals (pesticide formulations), metal and mining industry, plastic industry, lubricants, paints, polymers, pharmaceutical, oil recovery, pulp and paper industry, etc [8]. They are also occasionally used for environmental protection, e.g., in oil slick dispersions [9]. Moreover, surfactants are molecules with a relatively simple structure compared to proteins for example, and constitute a good example of amphiphilic organic matter.

Surfactants have both hydrophobic (the “tail”) and hydrophilic (the “head”) groups; they can easily self-assemble into the ordered structures at mesoscopic scale (such as micelles, layers, and liquid crystals, etc). They can also interact in different ways with the membranes. The adsorption of surfactants on membrane surfaces in the form of monomers or surface aggregates, affect mass transfer and surface characteristics of the membranes, thus, the performance and efficiency of the membrane filtration.

Although RO membranes have received much attention from both academy and industry and many methods have been proposed to characterize RO membranes in order to obtain structural parameters, the fouling mechanisms of solutes (especially organic components) on the membranes are still not fully understood. Relevant experimental methods permit to identify the mass and sometimes the nature of organic fouling, as well as the change in the surface tension. Though they can localize large structure of accumulated matter, the organization of the compounds at the surface and the nature of interaction with the polymer is still not accessible at the moment. The physical and chemical phenomena involved in the fouling process on dense membranes like those used in RO require building relevant modeling tools to show how molecular interactions are manifested in the microscopic domain as well as how microscopic phenomena are manifested in the macroscopic world that we perceive from experiments [10].

The reproduction or prediction of properties for a preselected system usually requires an accurate model. The most accurate method to simulate the hydrodynamic comportment of an atomistic system is to integrate the equations of motion for all atoms in the system. This is the basis of the molecular dynamics (MD) simulation methods. The MD reproduces every aspect of the atomic motion, which is often too detailed to allow an understanding of physical processes and is limited to a few thousand molecules over a few nanoseconds because of computer processor speeds and memory capacities. If the hydrodynamic collective behavior occurred for time much longer than the collision time and for distance much larger than inter particle distance this approach is inadequate. In the same way, macroscopic simulation starts at a length scale where the materials are sufficiently homogeneous to justify a continuum description. In the membrane processes studies, macroscopic simulation is able to describe flux through membrane versus global resistances, diffusion coefficient and mean concentrations at the interfaces but it does not allow understanding the specific organization of organic molecules in the bulk, in the concentration polarization layer nor in the membrane. Many phenomena occur at mesoscopic scales such as surfactant-polymer interaction. Dissipative particle dynamics (DPD) is an intermediate simulation method allowing the investigation of mesoscopic systems containing millions of atoms with length scale between 10^{-6} and 10^{-3} m and time scale between 10^{-6} and 10^{-3} s, respectively [11], [12]. However, the DPD models for adsorption onto RO membranes are not found in literature.

The objective of this thesis is to deepen the understanding of fouling by modeling the behavior of organic molecules at the membrane interface and by comparing these simulation

results to experimental data. A previous thesis work on RO process of mixed surfactant solutions showed a high rejection of surfactants with a thin-film composite membrane, but the membrane fouling caused by anionic surfactant adsorption during RO processes is significant [13].

The manuscript is outlined as follows. In the first chapter, we briefly recall the necessary definitions on pressure-driven membrane processes paying special attention to RO processes, and then provide an overview of surfactants. The second chapter is devoted to the experimental study of surfactant adsorption on reverse osmosis membrane. The evolution of RO process performances (flux, retention rate) and the surface properties of the membrane surface are investigated. The third chapter deals with DPD simulations of anionic surfactants in aqueous solutions and at the membrane interface. The micellization properties in equilibrium (e.g. the critical micelle concentration, and aggregation number) of surfactants are inferred from the mesoscopic simulations and compared with bulk solution properties from experiments. Investigation on surfactants organization at the membrane interface during reverse osmosis filtration was undertaken by adding a simplified membrane surface to the surfactant system. The interactions between membrane and surfactants are investigated.

Chapter 1

Literature review

The aim of this work is to get a better understanding of the microscopic behavior of organic matters during the membrane processes for the treatment of complex mixtures. This chapter provides a research-based overview of the background information on the membrane processes, the target composition we are going to treat with, and the available technologies in literature to investigate the phenomena that might occur during the membrane processes.

This bibliographic chapter is divided into five parts:

- The first part presents different membrane processes and their applications.
- The second part presents different methods to investigate the physical-chemical characteristics of the membranes.
- The third part presents the surfactants.
- The fourth part presents the state-of-art on the simulation methods.
- The last part presents the problematic and objective of this thesis.

1.1 Pressure-driven membrane processes

1.1.1 Definition

Membrane technology covers a number of different processes for the transport of substances between two fractions with the help of permeable membranes [14]. Membranes used in membrane technology may be regarded as selective barriers separating two fluids and allowing the passage of certain components and the retention of others from a given mixture, implying the concentration of one or more components. The driving force for the transport is generally a gradient of some potential such as pressure, temperature, concentration or electric potential [14].

One of the particular advantages of membrane separation process is that it relies on a physical separation, usually with no addition of chemicals in the feed stream and without phase change [15]. Moreover it can be operated without heating. Therefore, this separation process is energetically usually lower than conventional separation technologies (i.e., distillation, crystallization, adsorption...). What's more, it responds more efficiently to the requirements of process intensification strategy because it permits drastic improvements in industrial production, substantially decreasing the equipment-size/production-capacity ratio,

energy consumption, and/or waste production so resulting in sustainable technical solutions [16]. Although typically thought to be expensive and relatively experimental, membrane technology is advancing quickly becoming less expensive, improving performance, and extending life expectancy. It has led to significant innovations in both processes and products in various industrial sectors (e.g. chemical, pharmaceutical, biotechnological, food sectors, etc) over the past few decades.

1.1.2 Membrane flow configurations

Membrane systems can be operated in various process configurations. There are two main flow configurations of membrane processes: dead-end and crossflow filtrations, as presented in Figure 1 - 1. In a conventional filtration system, the fluid flow, be it liquid or gaseous, is perpendicular to the membrane surface. In this dead-end filtration, there is no recirculation of the concentrate, thus solutes are more probable to deposit on the membrane surface, and the system operation is based on 100% recovery of the feed water. In crossflow filtration, the feed flow is tangential to the membrane surface and then divided into two streams. The retentate or concentrate (solution that does not permeate through the surface of the membrane) is recirculated and blended with the feed water, whereas the permeate flow is tracked on the other side [1], [17].

Both flow configurations offer some advantages and disadvantages. The dead-end membranes are relatively less costly to fabricate and the process is easy to implement. The main disadvantage of a dead-end filtration is the extensive membrane fouling and concentration polarization, which requires periodic interruption of the process to clean or substitute the filter [3]. The tangential flow devices are less susceptible to fouling due to the sweeping effects and high shear rates of the passing flow.

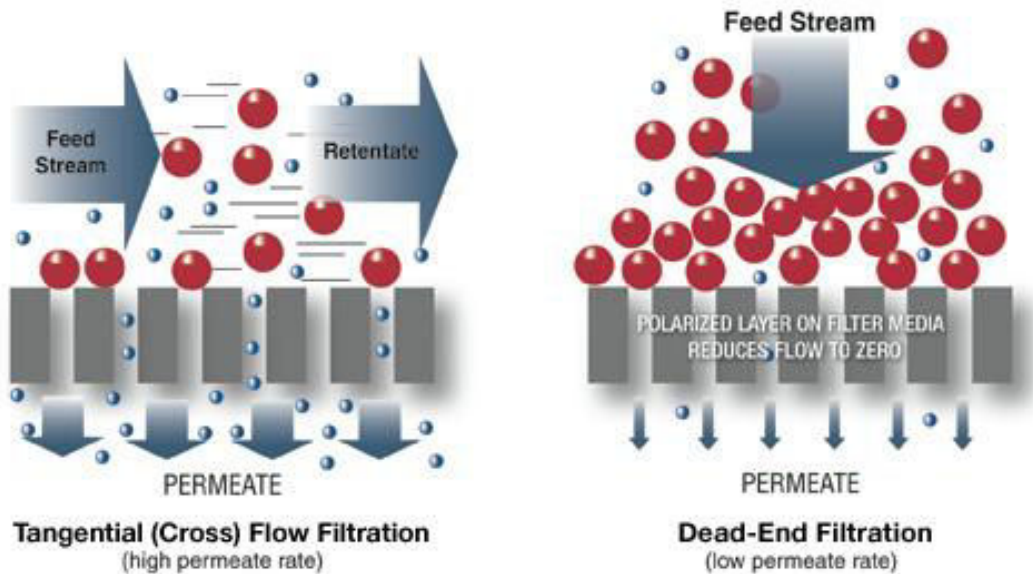


Figure 1 - 1: Membrane flow configurations. Left: Crossflow filtration; Right: Dead-end filtration.

(Source: www.spectrumlabs.com/filtration/Edge.html)

1.1.3 Types of membranes: MF, UF, NF, RO

Membrane separation processes have very important role in separation industry. The first industrial applications of pressure driven membrane processes were water desalination by reverse osmosis in 1960's [1]. There are basically four pressure driven membrane processes allowing separation in the liquid phase: microfiltration (MF), ultrafiltration (UF), nanofiltration (NF) and reverse osmosis (RO). These processes are distinguished by the application of hydraulic pressure as the driving force for mass transport. Nevertheless the nature of the membrane controls which components will permeate and which will be retained, since they are selectively separated according to their molar masses, particle size, chemical affinity, interaction with the membrane [3].

The pore size of a membrane is generally indicated indirectly by membrane manufacturers, through its molecular weight cut-off (MWCO) which is usually expressed in Dalton ($1 \text{ Da} = 1 \text{ g mol}^{-1}$) [3]. MWCO is typically defined as the molecular weight of the smallest component that will be retained with an efficiency of at least 90%.

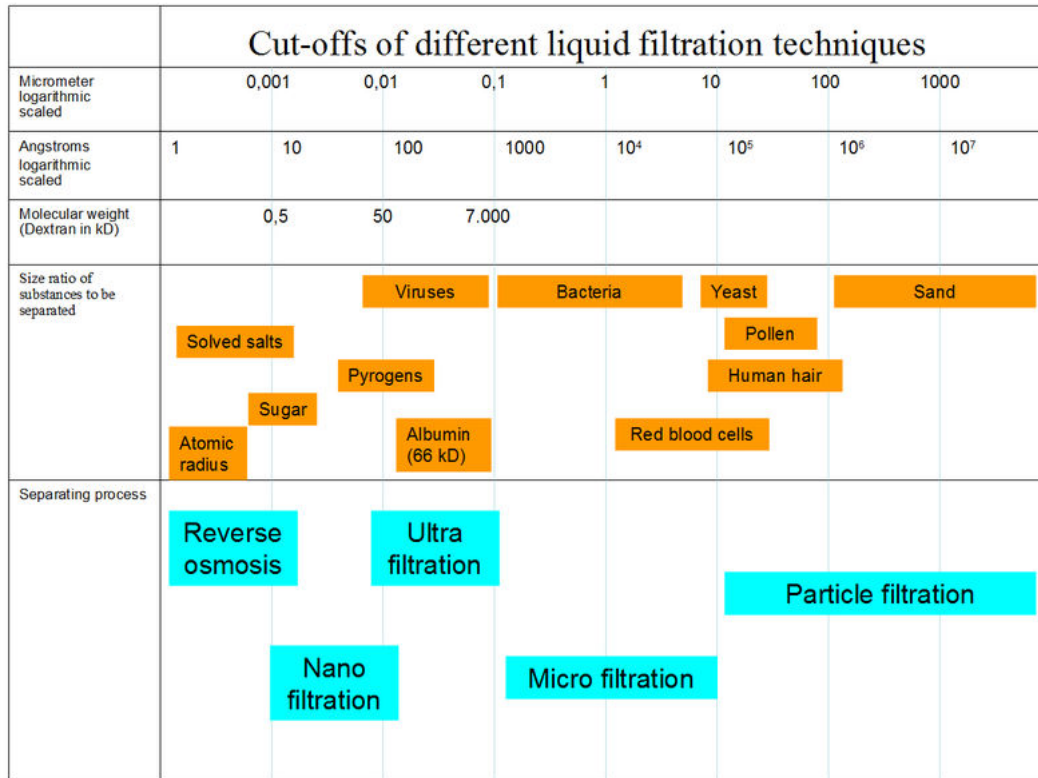


Figure 1 - 2: Cut-offs of different liquid filtration techniques [18]

Figure 1 - 2 relates the size of some typical particles both to the pore size and the molecular weight cut off of the membranes required to remove them. The separation spectrum for membranes, as illustrated in Figure 1 - 2 [19], ranges from reverse osmosis (RO), and nanofiltration (NF) for the removal of solutes, to ultrafiltration (UF) and microfiltration (MF) for the removal of fine particles. Table 1 - 1 shows size of materials retained, driving force, and type of membrane for various membrane separation processes.

Table 1 - 1: Size of Materials Retained, Driving Force, and Type of Membrane [1]

Process	Minimum particle size removed	Applied pressure	Type of membrane
Microfiltration	0.025 - 10 μm microparticles	(0.1 - 5 bar)	Porous
Ultrafiltration	5 - 100 nm macromolecules	(0.5 - 9 bar)	Porous
Nanofiltration	0.5 - 5 nm molecules	(4 - 20 bar)	Porous
Reverse Osmosis	< 1 nm salts	(20 - 80 bar)	Nonporous

Microfiltration (MF)

Microfiltration is a filtration process which uses pressures lower than 0.2 MPa and removes molecules between 0.025 and 10 μm from a fluid by passage through a micro porous membrane. A typical microfiltration membrane pore size range is 0.1 to 10 μm [3]. MF processes have found wide spread use in the food and dairy industry, biotechnology (e.g. cell separation from fermentation broth), the treatment of oil and latex emulsions, pharmaceutical industry [20], [21], [22], [23], [24], [25], [26]. Filtration of protein solutions (e.g. for virus or DNA removal) in the pharmaceutical industry and blood treatment for plasma separation are also examples of the wide applicability of MF [27], [28], [29]. It can be applied in municipal wastewater reclamation [30], anoxic pond effluent treatment [31] and toxic component removal from drinking water [32].

Ultrafiltration (UF)

Historically, it has been customary to refer to MF membranes in terms of their pore size in μm , whilst UF has been defined in terms of the molecular weight of molecules that the membrane pores could reject. The pressures applied are greater than 1 MPa to separate particles with molar masses between 1 and 300 kDa [3]. Suspended solids and solutes of molecular weight higher than 300 kDa are retained, while water and low molecular weight solutes can pass through the membrane. Typical applications of UF include purification of food materials and separation of proteins in the food and dairy industries [33], [34], [35], removal of toxic heavy metals [36], concentration and harvesting of cells or lysozyme or liposome in biotechnology [37], [38], [39], recovery of valuable contaminants in process waste streams and production of potable water [40], [41], [42].

Nanofiltration (NF)

Nanofiltration is a pressure-driven (uses pressures between 4 and 20 MPa) membrane-based separation process in which particles and dissolved molecules with molar masses between 350 and 1000 Da are retained [3], [43]. Nanofiltration is a relatively recent membrane filtration process developed in the mid-1980s [44] and is used most often in surface water and fresh groundwater treatment, with the purpose of softening (polyvalent cation removal) and removal of disinfection by-product precursors such as natural organic matter and synthetic organic matter (herbicides, pharmaceuticals, etc.) [45], [46], [47], [48], [49], [50], [51], [52],

[53]. Nanofiltration is also becoming more widely used in food processing and other applications such as fractionation of oligosaccharides, green biorefinery, coffee extract concentration, etc [54], [55], [56].

Reverse osmosis (RO)

Unlike MF and UF membranes, RO membranes are dense membranes that do not have distinct pores. It is a pressure-driven process (between 20 and 80 MPa) that rejects smallest contaminants and monovalent ions (<350 Da) from solutions [3]. The mass transfer in RO is due to solution-diffusion mechanism, size exclusion, charge exclusion and physical-chemical interactions between solute, solvent and the membrane [4]. RO is most commonly known for its use in drinking water purification from seawater, removing the salt and other substances from water. This technology has been demonstrated to be useful and could provide high removal efficiencies in the treatment of a wide variety of effluents from chemical, textile, pulp and paper, petroleum and petrochemical, food, tanning and metal finishing industries, although it has very strict feedwater requirements as regards the concentration of suspended solids, fibres and oily constituents [5], [57]. RO process can also be combined with UF, pervaporation, distillation, and other separation techniques to produce hybrid processes that result in highly efficient and selective separations [1]. The expansion of RO membrane applications promoted the design of suitable membrane material to take into consideration chemical structure, membrane configuration, chemical stability and ease of fabrication [1]. Detailed information on RO membranes are discussed in the following section.

1.2 Reverse Osmosis

1.2.1 Introduction

The concepts of "osmosis" and "reverse osmosis" have been known for many years. Osmosis is the flow of solvent through a semi-permeable membrane, from a dilute solution to a concentrated solution. This flow results from the driving force created by the difference in chemical potential between the two solutions. The movement of a pure solvent to equalize solute concentrations on each side of a membrane generates a pressure named "osmotic pressure". Reverse osmosis is the reverse of the normal osmosis process (see Figure 1 - 3), in which the solvent is pushed from an area of high solute concentration, through a membrane,

to an area of low solute concentration. Figure 1 - 3 illustrates the processes of osmosis and reverse osmosis [58], [59].

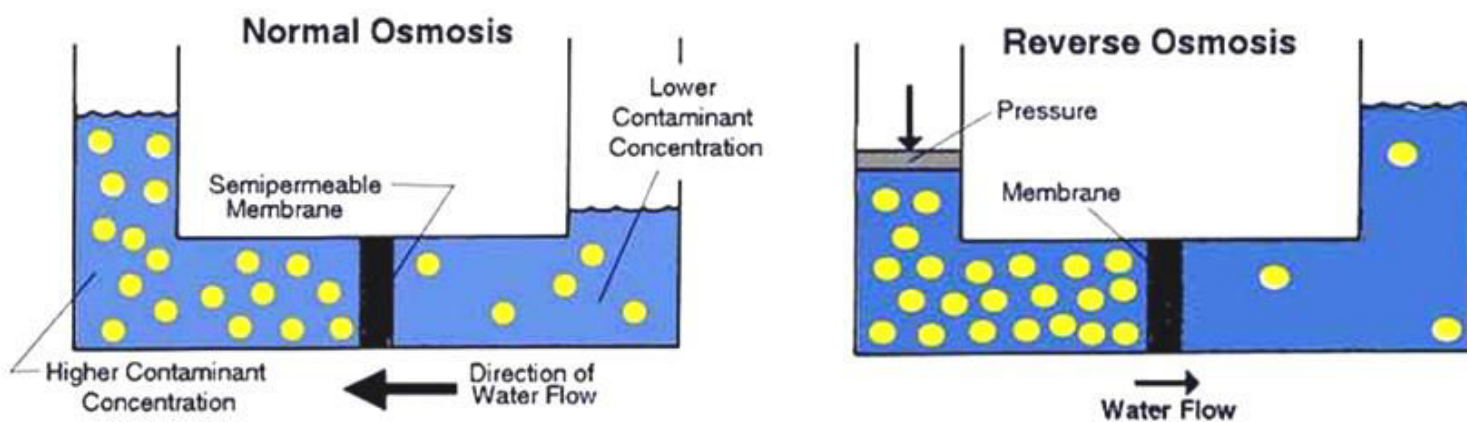


Figure 1 - 3: Osmosis and reverse osmosis system

(Source: <http://www.wqa.org/>)

Although the concept of RO has been known for many years, only since the early 1960's when an asymmetric cellulose acetate membrane with relatively high water flux and separation was produced [60], RO process has become both possible and practical on an industrial scale [44], [60]. Since then, the development of new-generation membranes such as the thin-film, composite membrane that can tolerate wide pH ranges, higher temperatures, and harsh chemical environments and that have highly improved water flux and solute separation characteristics has resulted in many RO applications. It has developed over the past 50 years to a 44% share in world desalination capacity in 2009, and an 80% share in the total number of desalination plants installed worldwide [44]. In addition to the traditional seawater and brackish water desalination processes, RO membranes have found uses in wastewater treatment, production of ultrapure water, water softening, and food processing as well as many others.

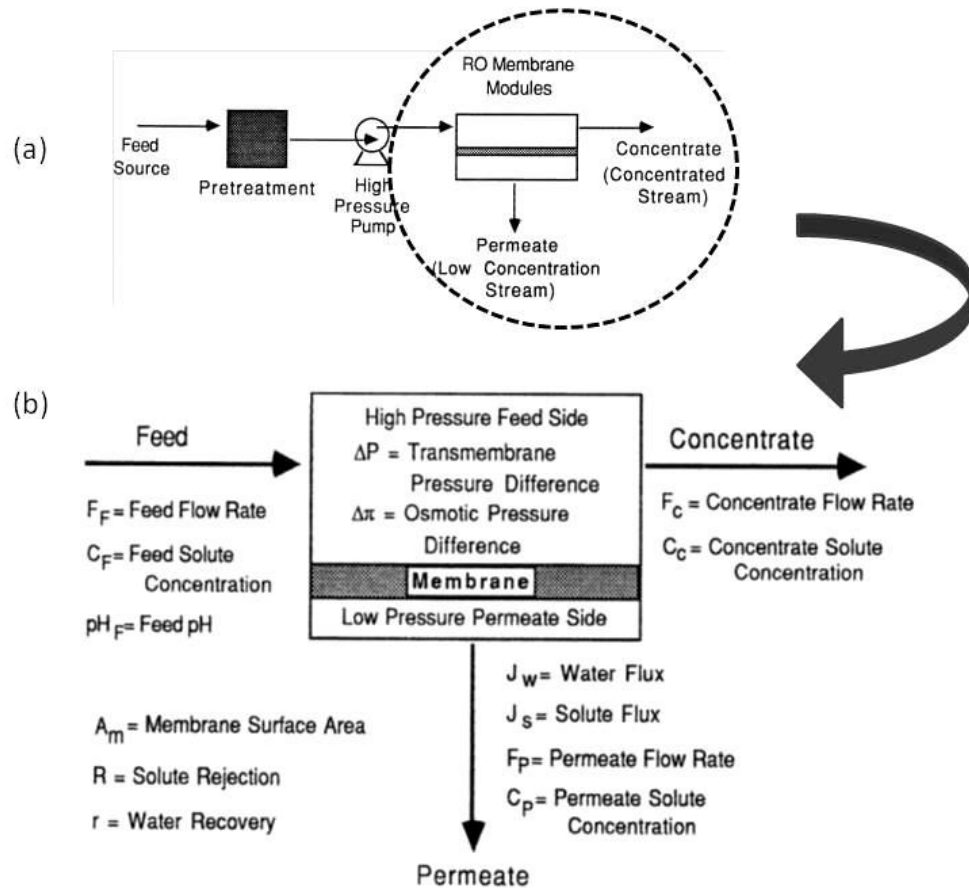


Figure 1 - 4: Schematic of (a) RO Membrane Process and (b) RO Process Streams

1.2.2 RO Process description and terminology

A schematic of the RO process is shown in Figure 1 - 4 (a). The RO process consists of a feed water source, a feed pretreatment, a high pressure pump, RO membrane modules, and, in some cases, post-treatment steps.

The three streams (and associated variables, e.g. F_F, F_C, F_P, C_F, C_C, C_P...) of the RO membrane process are shown in Figure 1 - 4 (b): the feed; the permeate; and the concentrate (or retentate). The water flow through the membrane is reported in terms of water flux, J_w , where

$$J_w = \frac{F_P}{A_m} \quad \text{(Equation 1 - 1)}$$

Solute passage is defined in terms of solute flux, J_s :

$$J_s = \frac{F_P}{A_m} \times C_p \quad (\text{Equation 1 - 2})$$

Solute separation is measured in terms of rejection, R , defined as

$$R = 1 - \frac{C_P}{C_F} \quad (\text{Equation 1 - 3})$$

The quantity of feed water that passes through the membrane (the permeate) is measured in terms of water recovery, r , defined for a batch RO system as

$$r = \frac{\int J_w A_m dt}{V_F} = \frac{V_P}{V_F} \quad (\text{Equation 1 - 4})$$

For a continuous system, where the flow of each stream is supposed to keep constant, the recovery is defined as

$$r = \frac{J_w A_m}{F_F} = \frac{F_P}{F_F} \quad (\text{Equation 1 - 5})$$

In a batch membrane system, water is recovered from the system as the concentrate is recycled to the feed tank; as a result, if the solute is rejected the feed concentration (C_F) continuously increases over time. For a continuous membrane system, fresh feed is continuously supplied to the membrane.

Water flux is sometimes normalized relative to the initial or pure water flux (J_{wo}) as $\frac{J_w}{J_{wo}}$ and flux decline is defined by

$$\text{flux decline} = 1 - \frac{J_w}{J_{wo}} \quad (\text{Equation 1 - 6})$$

1.2.3 Material, structure and geometry

1.2.3.1 Materials

Membranes are the critical component of RO systems. Factors to consider in selecting a membrane material include performance, cost, ease of fabrication, and resistance to environmental factors such as pH, temperature, and pressure.

Table 1 - 2: Summary for main RO membrane materials [1]

Membrane material	Advantages	Other limitations
Asymmetric cellulose acetate	Good tolerance to chlorine Low proneness to adsorption by natural organic matters (e.g. proteins)	Severe flux decline Biologically degradable
Thin film composite polyamides	High water flux High salt rejection High resistance to pressure compaction Wide operating temperature and pH range High stability to biological attack	Bad tolerance to chlorine High proneness to fouling

The most popular RO membrane materials are cellulose acetate and thin film composite polyamides. For a complete study of RO membrane materials for desalination, a recent review on RO membrane materials is reported by Lee and his coworkers [5]. The advantages and limitations of these materials are presented in Table 1 - 2. In general, PA-based RO membranes formed by interfacial polymerization exhibit better performance than CA-based membranes due to higher water flux, enhanced physical and chemical resistance and wider range of processing pH and temperature conditions.

Asymmetric Membrane --- Cellulose Acetate (CA) Membrane

Historically, the asymmetric membrane is formed by casting a thin film acetone-based solution of CA polymer. The first commercially viable RO membrane was developed by Loeb and Sourirajan in 1962 of this kind [60]. The CA membrane has an asymmetric structure with a very thin and dense solute-rejecting active layer on a coarse supporting layer. The membrane is made from only one polymeric material.

Thin Film Composite Membrane --- Polyamide (PA) Membrane

The current RO membrane market is dominated by thin film composite (TFC) polyamide membranes consisting of three layers (see Figure 1 - 5): an ultra-thin selective layer on the upper surface ($0.2\ \mu\text{m}$), a microporous interlayer (about $40\ \mu\text{m}$), and a polyester web acting as structural support ($120\text{--}150\ \mu\text{m}$ thick) [5], [61].

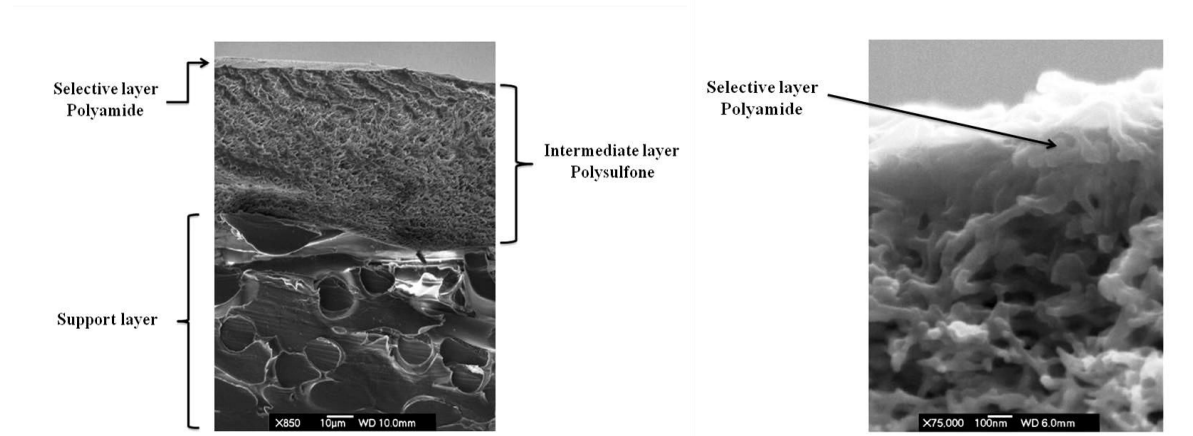


Figure 1 - 5: Cross-section images of a RO membrane: the left image for the whole cross-section ($\times 850$ magnification), the right image for top cross-section ($\times 75,000$ magnification) [61].

The selective barrier layer is most often made of aromatic polyamide by interfacial polymerization based on a polycondensation reaction between two monomers: a polyfunctional amine and a polyfunctional acid chloride. Some commonly used reactants of the polyamide thin films are described by Akin and Temelli (see Figure 1 - 6) [61]. The thickness and membrane pore size (normally less than $0.6\ \text{nm}$) of the barrier layer is reduced to minimize resistance to the permeate transport and to achieve salt rejection consistently higher than 99%. Therefore, between the barrier layer and the support layer, a micro-porous interlayer of polysulfonic polymer is added to enable the ultra-thin barrier layer to withstand high pressure compression. With improved chemical resistance and structural robustness, it offers reasonable tolerance to impurities, enhanced durability and easy cleaning characteristics.

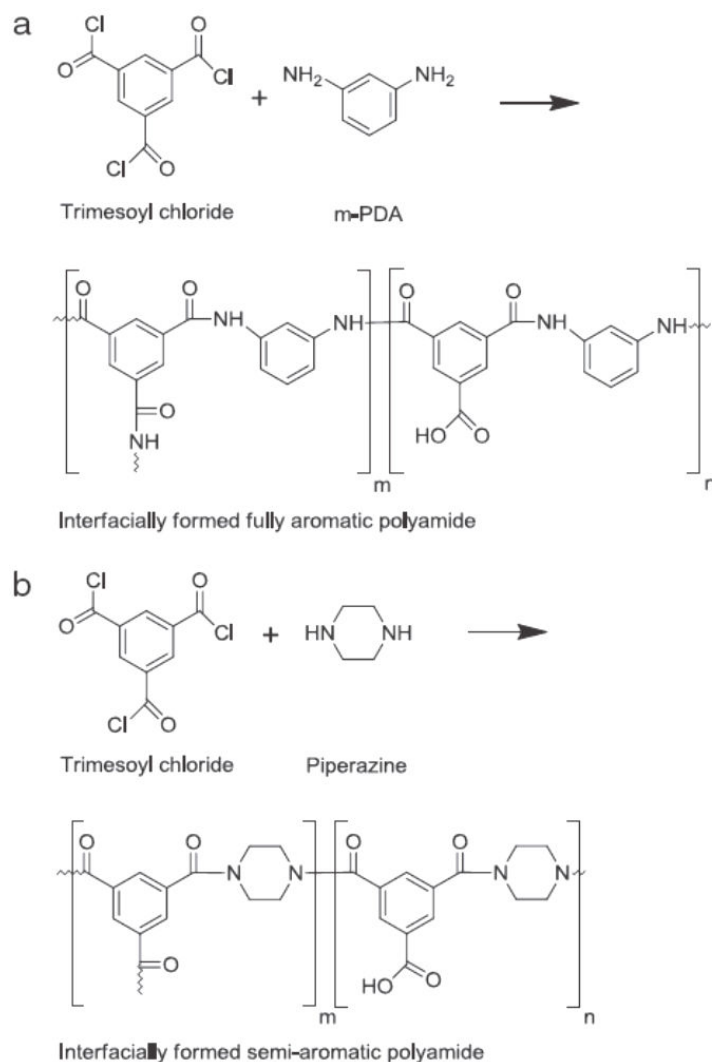


Figure 1 - 6: The polymerization reactions of most commonly used aromatic PA membranes [61]

1.2.3.2 Structure

There are mainly two structures for RO membranes: asymmetric membranes and composite membranes. Asymmetric membranes are made of a single material (e.g. CA) with different structures at different layers: only the thin active layer has fine pores that determine the cut-off, while the support layer has larger pores. The composite membranes are formed of an assembly of several layers of material, the fine filter layer based on layers of greater porosity.

1.2.3.3 Geometry

The most common commercially available membrane modules include flat sheet, tubular, spiral-wound, and hollow fiber elements (see Figure 1 - 7).

Flat sheet membranes are used for the plane modules or in the spiral-wound modules. The tubular modules consist of tube bundles with an inside diameter of 4 to 25 mm. This type of membrane geometry is predominantly used for mineral membranes. The hollow fiber membranes are assembled into the module parallel. This kind of membrane is very thin with a diameter less than 1 mm.

The most extensively used design in RO desalination is the spiral wound membrane module. This configuration stands out for high specific membrane surface area, easy scale up operation, inter-changeability and low replacement costs and least expensive to produce from flat sheet TFC membranes [5]. Polyamide spiral wound membranes dominate RO / NF market sales with a 91% share. Asymmetric cellulose acetate hollow fibre membranes hold a distant second spot [5].

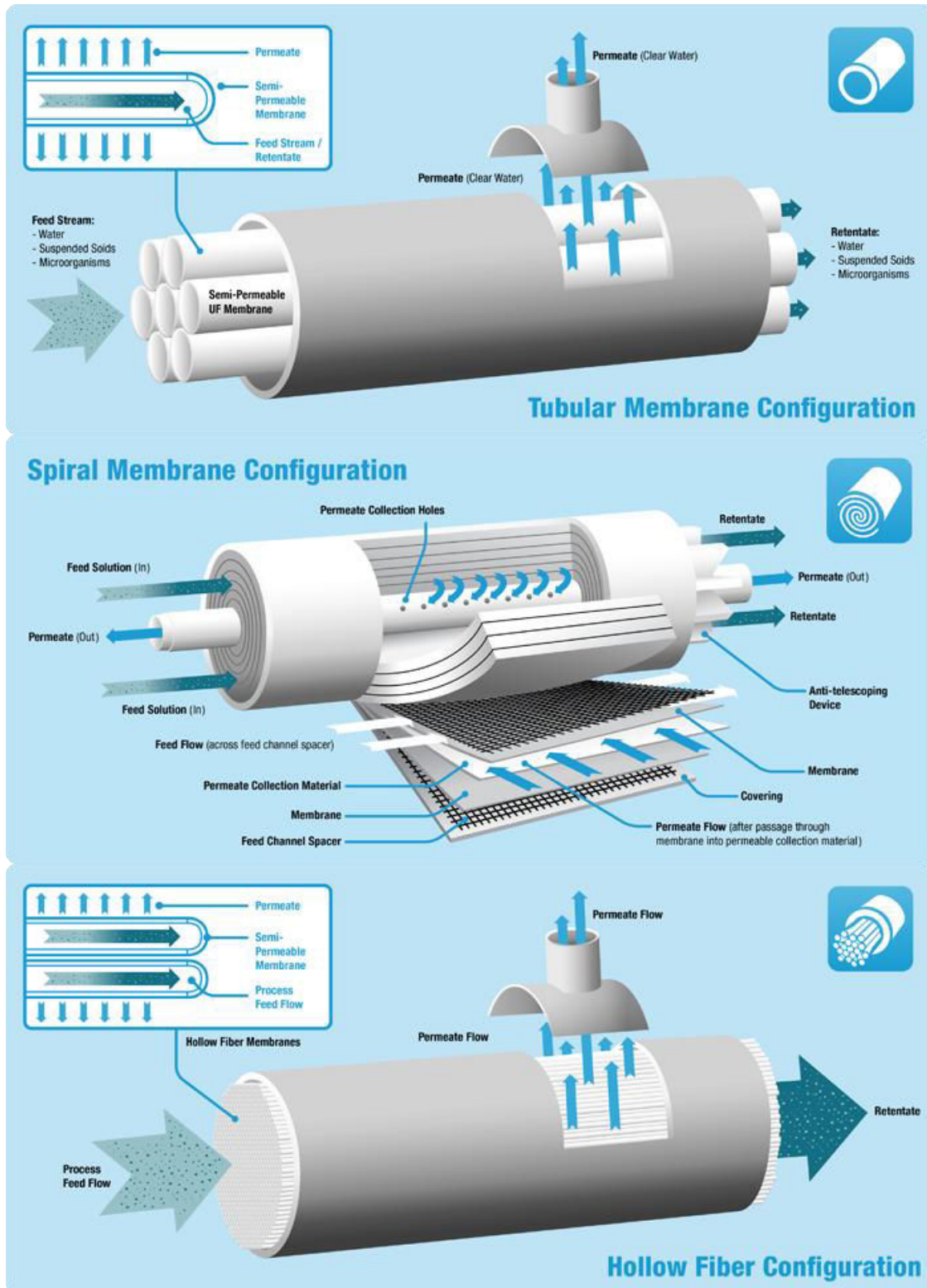


Figure 1 - 7: Membrane configurations: tubular, spiral-wound, and hollow fiber

(Source: <http://www.kochmembrane.com>)

1.2.4 Concentration polarization and fouling

1.2.4.1 Concentration polarization

The pressure driven fluid flow through a selective membrane convectively transports solute towards the membrane surface. The partially or totally retained solutes will accumulate in a thin layer adjacent to the membrane surface generating a concentration gradient, that is to say, the solute concentration near the membrane surface is much higher than that of the bulk feed solution. As a consequence, a diffusive flux of solute back to the feed bulk appears. The solute builds up at the membrane surface until the equilibrium between diffusive and convective solute fluxes is attained [15], [62]. As a result, the solute concentration changes from a maximum at the membrane surface ($C_{A,m}$) to the bulk ($C_{A,f}$), as illustrated in Figure 1 - 8. This phenomenon, known as concentration polarization (CP), increases resistance to solvent flow and thus is responsible for the water flux decline observed in many membrane filtration processes [63], [64], [65], [66]. It is strongly related with the osmotic pressure raise, increase of resistance to permeation (e.g. gel formation) and fouling susceptibility [62]. It might also change the membrane separation properties, for instance due to surface charge variations. The extent of concentration polarization can be reduced by promoting good mixing of the bulk feed solution with the solution near the membrane surface. Mixing can be enhanced through membrane module optimization of turbulence promoters, spacer placement, or by simply increasing tangential shear velocity to promote turbulent flow.

The prediction of the concentration polarization is required for the design and operation of pressure-driven membrane systems. However, the experimental determination of the solute concentration profiles in the polarization layer still presents many limitations [15], [64].

There are several theoretical approaches investigating the concentration polarization by models: osmotic pressure model, film theory, gel-layer model, inertial lift model and shear-induced diffusion model [15].

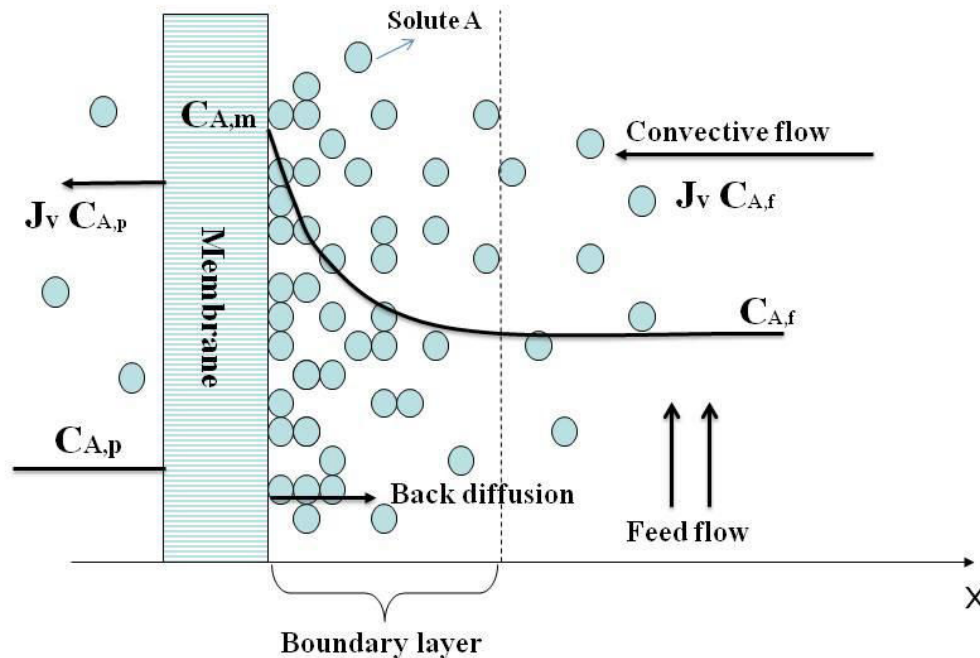


Figure 1 - 8: Concentration polarization phenomenon

1.2.4.2 Membrane fouling

Membrane fouling is a phenomenon where suspended or dissolved substances from the liquid phase deposit onto a membrane surface and/or into membrane pores in a way that degrades the membrane's performance.

Membrane fouling is influenced by three major factors: the membrane material properties (e.g. hydrophilicity, roughness, and electrical charge), the feed solution characteristics (e.g. the nature and concentration of the foulant) and the operating conditions. Fouling and CP are interlinked: the operation in severe conditions of CP creates the conditions for the formation of fouling. The interactions between the membrane and the foulants determine the degree of fouling.

There are various types of fouling:

- organic (oils, polyelectrolytes, humics), such as adsorption of organic matters through specific interactions between the membrane and the solutes (e.g. humic substances, surfactants, etc) and gel layer formation of macromolecular substances on nonporous membranes;
- colloidal, such as precipitation of colloidal silt (clays, flocs), cake formation of colloid or solutes, etc;
- biological, such as the accumulation or growth of microbiological organisms (bacteria, fungi) on the membrane surface;
- scaling, such as precipitation of inorganic salts, particulates of metal oxides.

Membrane fouling is a major obstacle to the widespread use of membrane technology. It can cause severe flux decline, affect the quality of the water produced and increase the trans-membrane pressure drop. The resistance in series model describes the flux of a fouled membrane through the increase in the total hydraulic resistance of the membrane R_t . The basic relationship between flux and driving force is given in (Equation 1 - 7). When fouling occurs, an additional resistance, R_F , is imposed and in some cases (with NF and RO) it may increase the osmotic pressure $\Delta\Pi$ in (Equation 1 - 7). Increasing R_F and/or $\Delta\Pi$ causes a flux decline at constant ΔP (transmembrane pressure, TMP) or causes TMP to rise at constant flux. Severe fouling may lead to serious damage and necessitate intense chemical cleaning or frequent membrane replacement. This increases the operating costs of a treatment plant. Processes that rely on membranes must be protected from fouling [67].

$$J_w = \frac{\Delta P - \Delta \Pi}{\mu (R_m + R_F)} \quad \text{(Equation 1 - 7)}$$

$$R_F = R_{CL} + R_G + R_{ADS} + \dots \quad \text{(Equation 1 - 8)}$$

Where J is the flux, R_m is the membrane resistance, R_F is a total resistance of all the individual resistance that may happen for a given solution-membrane system, with R_{CL} , R_G , R_{ADS} the resistance for cake layer, gel layer and adsorption.

Fouling can be divided into reversible and irreversible fouling based on the attachment strength of particles to the membrane surface. Reversible fouling can be removed by a strong

shear force of backwashing or by lowering driving pressure on the surface. Formation of a strong matrix of fouling layer with the solute during a continuous filtration process will result in reversible fouling being transformed into an irreversible fouling layer which cannot be removed by physical cleaning.

Because RO membranes are nonporous, the dominant fouling mechanism can be due to the formation of a fouling layer on the membrane surface [44]. The development of antifouling membrane by modification of the membrane properties is focused on generally four aspects / surface modification by chemical and physical methods: enhancing hydrophilicity, reducing the surface roughness, improving surface charge, and introducing polymer brushes.

Even though membrane fouling is an inevitable phenomenon during membrane filtration, it can be minimized by strategies such as appropriate membrane selection, choice of operating conditions and cleaning. The first strategy to minimize membrane fouling is the use of the appropriate membrane for a specific operation. The nature of the feed water must first be known; then a membrane that is less prone to fouling when that solution is chosen. For aqueous filtration, a hydrophilic membrane is preferred. Operating conditions during membrane filtration are also vital, as they may affect fouling conditions during filtration. For instance, cross flow filtration is preferred to dead end filtration, because turbulence generated during the filtration entails a thinner deposit layer and therefore minimizes fouling. Membranes can be cleaned physically or chemically. Physical cleaning includes sponges, water jets or back flushing. Chemical cleaning uses acids and bases to remove foulants and impurities. After cleaning, a recovery of the membrane flux can be obtained (see Figure 1 - 9).

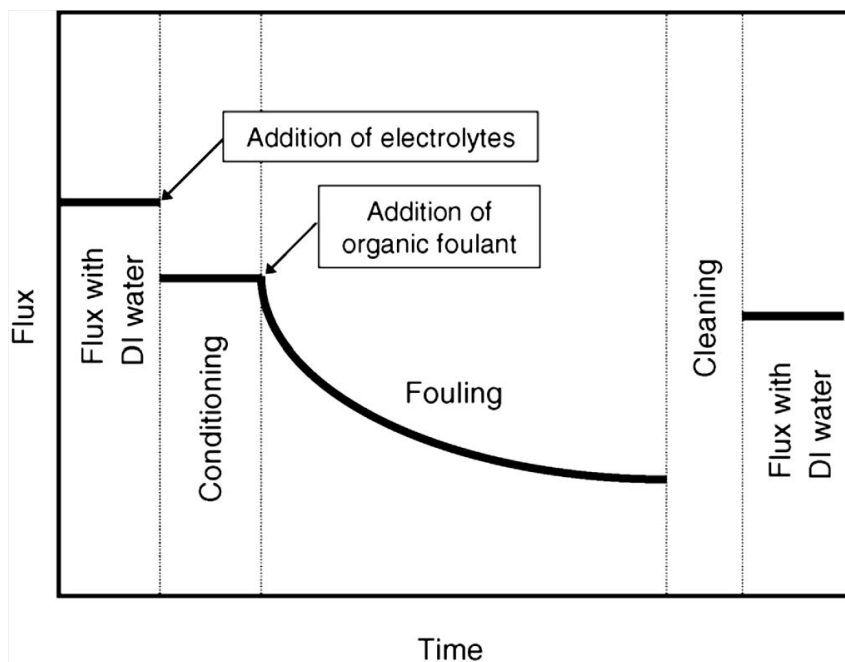


Figure 1 - 9: Fouling and cleaning of RO membrane

1.2.5 Characterization of membranes

The performance of membranes is usually evaluated by water flux or permeability in the filtration process, as well as rejection or selectivity of solutes. These separation properties are influenced by the characteristics of membrane surface (especially the active layer), thus, knowledge of surface characteristics is needed to provide better understanding and explication to the observed membrane performance. In the studies where the behaviors of solutes on the membrane surface and the transport through the membrane must be modeled, the knowledge of the functional, structural and electrical parameters of the membranes is essential to carry out simulations. However, the information given in the data sheets of the membrane manufacturers on membrane material, cut-off value, and sometimes even on membrane charge is often insufficient. Different membrane surface characterization methods are needed to obtain enough information on the membrane properties. The most important characteristics of membranes affecting their performance and stability in a specific application are their chemical composition, hydrophilicity/hydrophobicity, charge and morphology [1]. Several characterization techniques available are briefly summarized in Table 1 - 3. A short description of them is presented together with their applications. The streaming potential, AFM, and contact angle measurements are mainly used for membrane surface characterization [17], [68].

Chapter 1 Literature review

Table 1 - 3: Characterization methods for clean membranes [69]

	Characterization Technique		Parameter	References
Chemical structure characterization	permporometry		Pore size and pore size distribution	[4]
	Spectroscopy	IR(ATR-FTIR), Raman spectroscopy, XPS (or ESCA), SIMS	Chemical composition, Polymer morphology	[61], [70], [71], [72], [73], [74], [75], [76], [77], [78], [79], [80]
Functional characterization	Membrane resistance		Permeability	
	Selectivity			
	Rejection coefficient		Pore size distribution	
Hydrophilicity/hydrophobicity	Contact angle measurement		Contact angle	[61], [70], [74], [76], [77], [78], [81], [82], [83], [84], [85], [86]
Electrical characterization	Electrokinetic measurements (MP, TSP, SP, Titration)		Charge density, zeta potential	[76], [77], [78], [80], [86], [87], [88], [89]
	Electrochemical impedance spectroscopy (EIS)		Ion conductivity in the pore	[90], [91]
Morphological characterization	Microscopy	Optical microscopy	macrostructure	
		CSLM		[92], [93], [94], [95], [96]
		SEM	Top-layer thickness and pore size distribution	[61], [70], [73], [76], [86], [97]
		TEM	Top-layer thickness, roughness and pore size distribution	[87], [88], [98]
		AFM	Surface roughness and pore size distribution	[61], [70], [71], [76], [80], [86], [97], [99], [100]

1.2.5.1 Characterization of membrane chemical structure

Information on the chemical structure of a membrane surface and on its hydrophilicity and charge is needed for a better understanding of membrane stability under different conditions. The knowledge about the surface chemistry also helps in the determination of fouling mechanisms and optimization of cleaning procedures.

The chemical composition and structure of the membrane can be analyzed with spectroscopic methods, of which the attenuated total reflectance Fourier transform infrared (ATR-FTIR) method is the most utilized. Using both Raman spectroscopy and infrared spectroscopy (IR) could provide sufficient and comprehensive information on the membrane chemical structure. If only information from the top layer is needed, X-ray Photoelectron Spectroscopy (XPS) and Secondary Ion Mass Spectroscopy combined with a mass analyzer called time-of-flight (TOF-SIMS) are the most surface-sensitive methods.

Infrared spectroscopy (IR) is often utilized in the determination of the chemical composition of membranes and in the localization of different compounds on the membrane samples, enabling both qualitative and quantitative analysis for inorganic and organic membrane samples. It is able to obtain spectra from a very wide range of solids from the positions and intensity of the absorption bands after IR radiation. The membrane materials absorb the energy at different wavelengths which produce a signal at the IR detector and the generated spectrum is unique for each compound. Attenuated total reflectance Fourier transform infrared spectroscopy (ATR-FTIR) is able to probe *in situ* single or multiple layers of adsorbed/deposited species at a solid/liquid interface. It is used mainly to study for surface modifications and to study the membrane fouling [61], [77], [78], [84], [101].

Raman spectroscopy can be applied to study the chemical structure, morphology of the membrane, polymer orientation, intermolecular interactions and crystallinity [80]. It is a process where a photon interacts with a sample to produce scattered radiation in all directions with different wavelengths. A laser that provides monochromatic light is used [102].

Energy-Dispersive X-ray Spectroscopy (EDS) can be utilized to qualitative and quantitative analysis of all elements above atomic number 4 (Be), and usually is applicable to the chemical identification of surface foulants on membrane surfaces [6], [103]. In an electron microscope a focused electron beam interacts with the atoms in a sample and element-specific

X-rays are generated which can be detected with an energy-dispersive spectrometer coupled to a scanning electron microscope (SEM) or to a transmission electron microscope (TEM). The problem of this method is that wet and nonconducting (e.g. polymeric) membrane samples could not be analyzed except that the samples are pretreated, which might affect the accuracy of the analysis results [86].

X-ray Photoelectron Spectroscopy or elemental spectroscopy for chemical analysis (XPS, or ESCA) is a surface sensitive technique that measures elemental composition (all the elements except hydrogen) in the dry membrane sample and provides information on chemical binding for the top 1-10 nm [4]. In XPS, interactions between X-rays and the dry samples under ultrahigh vacuum cause different photoemissions, especially photoemissions of core electrons. The detection of the emitted electrons and their kinetic energies enable an identification of the elements of the samples. This method has been applied to the analysis of thin membrane skin layers, NF membrane structures, and modifications of membrane surfaces [61], [71], [73], [74].

Secondary Ion Mass Spectroscopy (SIMS) is very suitable for the characterization of both clean and fouled membrane surfaces as well as in the examination of adsorbate-membrane interactions [104]. In SIMS, a beam of primary ions (e.g., He^+ , Ne^+ , Ar^+ , Xe^+ , Ga^+ and Cs^+) is focused to the sample surface and cause the sputtering of some materials from the surface. Positive and negative secondary ions, which take up a small fraction of the sputtering materials, are detected with a mass spectrometer. When it combines with time-of-flight (TOF), the determination of the chemical structure and the composition of a surface, including all the elements from hydrogen to uranium, is possible. Compared to XPS, this method provides more precise molecular information of polymers. The major problem of this technique is the matrix effects [105].

1.2.5.2 Characterization of membrane charge

Membrane charge strongly affects the filtration properties of the membrane, so information on the electrical characteristics is required. Though membrane charge can be predicted based on known membrane chemical structure, more accurate information is needed. Several methods can be applied in the characterization of the electrical properties of the membrane. The most utilized technique is the determination of the zeta potential from streaming potential measurements. The zeta potential values give information about the overall membrane surface

charge, while the charge inside the membrane can be determined with membrane potential measurements. Thus, the zeta potential is more useful when knowledge on the membrane surface charge affecting the interaction with the molecules of the feed in the filtration process is needed, whereas membrane potential measurement results increase knowledge on the mobility of ions in the membrane material and on its Donnan properties [1]. If information about the electrical properties of different sublayers of the membrane is needed, electrochemical impedance spectroscopy can be used. Information on the negative and positive groups in the membrane can also be determined with titration.

The origin of a membrane charge is clear. When brought into contact with an aqueous electrolyte solution, membranes do acquire an electric charge through several possible mechanisms, *i.e.*, dissociation of functional groups, adsorption of ions from solution, and adsorption of polyelectrolytes, ionic surfactants, and charged macromolecules. These charging mechanisms can take place on the exterior membrane surface as well as on the interior pores of the membrane. Then a charge separation occurs producing the “electrical double layer” that is formed in the membrane-solution interface [106].

Streaming potential (SP) measurements can be used to determine the zeta potential of a membrane. SP measurement also gives information about the charge related modifications on the surface/inside the pores of a membrane [76], [77], [78], [80], [86], [87], [88], [89]. Membrane surface charge has an influence on the distribution of the ions in the solution due to requirement of the electroneutrality of the system. This leads to the formation of an electrical double layer, so that we have a charged surface and a neutralizing excess of counterions in the adjacent solution. The zeta potential is the potential at the plane of shear between a charged surface and a liquid that move in relation to each other. In SP measurements, when an electrolyte solution is forced to flow through a membrane, an electrical potential is generated which is known as streaming potential (SP). The SP results are strongly affected by the chemical structure, the asymmetric nature, the porosity and pore geometry of the membranes, as well as the nature of the ions in the electrolyte solution.

Electrochemical impedance spectroscopy (EIS) is usually used to study the electrical properties of complex materials [107], [108]. The operation mode consists in applying an electrical signal and performing a frequency scanning, and the impedance of the system can be measured. With EIS, the thickness and porosity for each sublayer of the membrane can be evaluated from the resistance and capacitance values [109].

Membrane potential (MP) measurements evaluate the amount of charge inside the membrane. The MP technique is based on the diffusive transport of the ions through the membrane induced by an electrolyte concentration gradient. In MP measurements, the membrane is positioned between two half-cells filled with the same electrolyte solutions but at different concentrations. The electrical potential difference, or the membrane potential, is generated and measured by inserting electrodes directly into the bulk solutions.

Titration can be utilized to determine the positively and negatively charged groups on the membrane surface separately [1]. By immersing the membrane into solutions with higher or lower ion concentrations, the original counterions of the membrane surface are exchanged. Then negatively or positively charged groups on the membrane surface could be determined from the immersion solution.

1.2.5.3 Characterization of membrane hydrophilicity

1.2.5.3.1 Interfacial tension

Usually, it is hard to define the hydrophobicity or hydrophilicity of a solid surface. This notion can be described by the degree of wettability of the solid surface. Firstly, theories on interfacial tension are needed to be presented. The interfacial tension γ is defined as the interfacial free energy of the interface ΔG_I per unit area Δa , expressed by the following equation:

$$\gamma = \Delta G_I / \Delta a \quad (\text{Equation 1 - 9})$$

where ΔG_I , γ and Δa are in units of J, J m⁻² and m², respectively.

Interfacial tensions are responsible for the contact angle (θ) of a drop of liquid L deposited on a flat solid surface S (Figure 1 - 10). The link between the contact angle θ and interfacial tensions is expressed in the Young equation in thermodynamic equilibrium:

$$\gamma_{sv} = \gamma_{sl} + \gamma_{lv} \cos \theta \quad (\text{Equation 1 - 10})$$

where θ is the equilibrium contact angle. γ_{sl} is the interfacial tension between solid and liquid. γ_{sv} and γ_{lv} are the surface tensions of the solid and liquid against the vapor. It is used to describe interactions between the forces of cohesion and adhesion, and measure

surface/interfacial tension. From Young's equation we see that by measuring the equilibrium contact angle θ , the difference $\gamma_{sv} - \gamma_{sl}$ can be obtained.

Contact angles are the most experimentally accessible data accounting for affinities between interfaces: the higher the affinity, the lower the interfacial tension. Contact angles with water can be used to assess hydrophobicity or hydrophilicity of different surfaces, or more generally to study the wetting of a solid or liquid interface by another liquid.

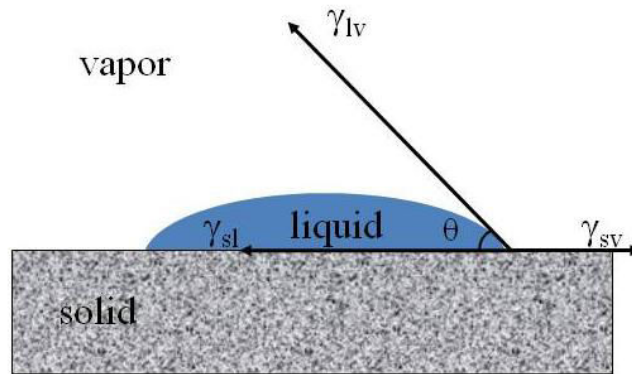


Figure 1 - 10: Schematic of a liquid drop showing the quantities in Young's equation

When a liquid L is brought to the contact of a surface S , the free energy of interaction ΔG_{sl} required to separate the surface S and a liquid L or reversible work of adhesion W_{sl} , is expressed by the Dupré equation:

$$W_{sl} = \Delta G_{sl} = \gamma_{sl} - \gamma_{lv} - \gamma_{sv} \quad (\text{Equation 1 - 11})$$

This equation dictates that neither γ_{sv} nor γ_{sl} can be larger than the sum of the other two surface tensions. It can be predicted that complete wetting occurs when $\gamma_{sv} > \gamma_{sl} + \gamma_{lv}$ and zero wetting when $\gamma_{sl} > \gamma_{sv} + \gamma_{lv}$.

Inserted into the Young's equation (Equation 1 – 10) this yields the Young-Dupré equation:

$$-\Delta G_{sl} = \gamma_{lv}(1 + \cos \theta) \quad (\text{Equation 1 - 12})$$

As the apolar and polar components of the free energies of interfacial interaction are additive, Van Oss proposed to take both γ^{LW} and γ^{AB} into account to the total surface tension γ , expressed as:

$$\gamma = \gamma^{LW} + \gamma^{AB} \quad (\text{Equation 1 - 13})$$

where γ^{LW} and γ^{AB} are calculated from the Lifshitz-Van der Waals (apolar) and Lewis acid/base (polar) interactions.

Especially, the LW interfacial tensions γ^{LW} between two apolar compounds 1 and 2 is defined as:

$$\gamma_{12}^{LW} = \left[(\gamma_1^{LW})^{\frac{1}{2}} - (\gamma_2^{LW})^{\frac{1}{2}} \right]^2 \quad (\text{Equation 1 - 14})$$

The electron-accepter-electron donor interaction γ^{AB} is composed of two different interfacial tensions: γ^A the electron acceptor and γ^B the electron donor components. It can be calculated as follows:

$$\gamma^{AB} = 2 (\gamma^A + \gamma^B)^{\frac{1}{2}} \quad (\text{Equation 1 - 15})$$

Noticing that surface tension of a liquid or solid is defined as minus one-half of the free energy change due to cohesion (see Equation 1 – 16) of the material *in vacuo* where ΔG_{ii} is the free energy of cohesion *i in vacuo*:

$$\gamma_i = \frac{1}{2} (\Delta G_{ii}) \quad (\text{Equation 1 - 16})$$

Upon combination with Equation 1 – 12, 1 – 13, 1 – 14, 1 – 15, and 1 – 16, the complete Young-Dupré equation linking contact angle and interfacial tension components then becomes:

$$(1 + \cos \theta) \gamma_{lv} = 2 \left[(\gamma_{sv}^{LW} \times \gamma_{lv}^{LW})^{\frac{1}{2}} + (\gamma_{sv}^A \times \gamma_{lv}^B)^{\frac{1}{2}} + (\gamma_{sv}^B \times \gamma_{lv}^A)^{\frac{1}{2}} \right] \quad (\text{Equation 1 - 17})$$

Given the previous equations and contact angle measurements, it is possible to determine γ_{sv} . For this, contact angle measurements with the surface *S* and three liquids with known surface-thermodynamic properties are required. With the three resulting contact angles, one can solve the system of three equations (one Equation 1 – 17 per liquid) to get the three unknown

γ_{sv}^{LW} , γ_{sv}^A and γ_{sv}^B constituting γ_{sv} (Equations 1 – 14 and 1 - 15). Then γ_{sl} can be determined either by using the previously obtained γ_{sv} in Young's equation (Equation 1 - 10). In the case of an interface between water and an immiscible apolar liquid, interfacial tension can be directly measured by appropriate tensiometers.

1.2.5.3.2 Contact angle measurements for membrane

Membrane hydrophilicity is a crucial factor affecting membrane performance when organic molecules are separated from aqueous solutions [97], [110], [111], [112]. Therefore, it is important to determine the membrane hydrophilicity to investigate the relationship between membrane performance and its surface characteristics.

In water treatment, a hydrophilic membrane has some obvious advantages. Firstly, the membrane is easily wetted, and this results in easy operating procedures and high permeabilities. Secondly, hydrophilic surface tends to resist attachment due to absorption by organics, and such a surface is referred to as a low fouling surface [113]. However, hydrophilicity is essential for maintaining the membrane's mechanical and chemical stability as well as high salt rejection [114]. Membrane grafting or chemical surface modification can be used to increase the hydrophilicity of the membrane surface while preserving other essential properties within the sub-layer [115]. Ahmed et al, reported that the modification of a TFC co-polyamide membrane by adding carboxylic group improved the permeability of the modified membrane by about 20% [116].

The most common method for the determination of membrane hydrophilicity is the contact angle measurement, which could also be utilized in the characterization of the interfacial tension of a membrane, because the contact angle depends on the interfacial tensions of the interfaces involved [82], [83], [84], [85]. When a drop of liquid is put on a solid surface under air, the shape of the drop is modified under the gravity and the different surface-interfacial tensions until an equilibrium state is achieved (see Figure 1 - 10) [106], [117].

This contact angle measurement provides a useful method for surface characterization. The easiest way to measure the contact angle between liquid and a membrane surface is the sessile drop method. It is performed by observing the shape of liquid drop on a surface through microscope. By connecting the drop to a pipette, the drop can be made smaller or larger.

A hydrophilic surface is one which is completely wetted by water, whilst on hydrophobic surface, where the solid surface tension is low, water forms droplets. If completely wetted, the contact angle is small. For a strongly hydrophobic surface, the contact angle is higher than 90°. While contact angle is commonly used to measure the hydrophilicity of the membrane surface owing to the simplicity of the method, the data should be used with some caution. Membrane surface roughness can influence contact angle measurement due to capillary effects and results from different measurement methods may vary considerably. If roughness is higher than 100 nm, the measured contact angles are meaningless. On very rough surfaces, contact angles are larger than on chemically identical smooth surfaces [17].

1.2.5.4 Characterization of membrane morphology

Direct information on membrane porous structure and sublayer structure is obtained with microscopic methods. The most commonly applied methods are SEM and AFM because the resolution of the microscopes is good enough for characterization of UF, NF and even RO membranes. In rough surface characterization conventional optical microscopy can also be used. Optical microscopy can be only used to characterize the surface macrostructure in the order of 1 μm , the resolution of which is poor compared to the other microscopic characterization methods. Confocal scanning laser microscopy (CSLM), Scanning electron microscopy (SEM) and Transmission electron microscopy (TEM) can be utilized to characterize the chemical composition of the membranes, but the resolution of CSLM is sufficient only for characterization of MF membranes [118], [119], [120], [121], [122]. Therefore, we focus on the SEM, TEM and AFM techniques.

Scanning electron microscopy (SEM) allows the direct observation of membrane morphology and the fouling layer from surface images or cross section images of the membrane [61], [70], [73], [76], [86], [97]. In SEM measurements, a fine beam of electrons scans the membrane surface, causing several kinds of interactions which generate signals like secondary electrons (SE) and backscattered electrons (SBE). The images of SE can be used to visualize membrane morphology three-dimensionally, such as pore geometry, pore size, pore size distribution and surface porosity. BSE images could also provide information on sample topography and chemical composition of the sample. However, the resolution of SEM is no larger than 5 nm, only macrostructure of MF and UF membranes are possible.

Transmission electron microscopy (TEM) visualizes the pore size of the membrane with a maximum resolution of 0.3-0.5 nm, and could provide information on pore size distribution and multiphase morphologies of the inner structure of the membrane sample. It can be used in the characterization of NF and RO membranes. In TEM, an electron beam is focused on the membrane sample and the electrons passing through the sample are detected for image forming. The inconvenience of this technique is that sample preparation is difficult because the sample has to be dry and thin enough (less than 50 nm) for electrons to penetrate.

Atomic force microscopy (AFM) can be used in the examination of the forces (London-van der Waals and the electrical double-layer forces) affecting the interaction between the membrane surface and the colloids in the process feed. An AFM measurement consists of an extremely sharp tip mounted to the end of a tiny cantilever spring, which is moved by a mechanical scanner over the membrane surface sample. Every variation of the surface height varies the force acting on the tip and therefore varies the bending of the cantilever. This bending is measured and recorded line by line [115]. The image is then reconstructed by computer software associated with the AFM. Figure 1 - 11 shows AFM images describing the surface roughness of the RO membranes AK and SG from GE Osmonics (Minnetonkam MN), respectively [61]. The resolutions of AFM measurements can reach to the subnanometer range. Thus it is widely used in the characterization of membrane surface morphology from MF to RO membranes, for the determination of pore size, surface porosity, pore density, pore size distribution and surface roughness[61], [70], [71], [76], [80], [86], [97], [99], [100].

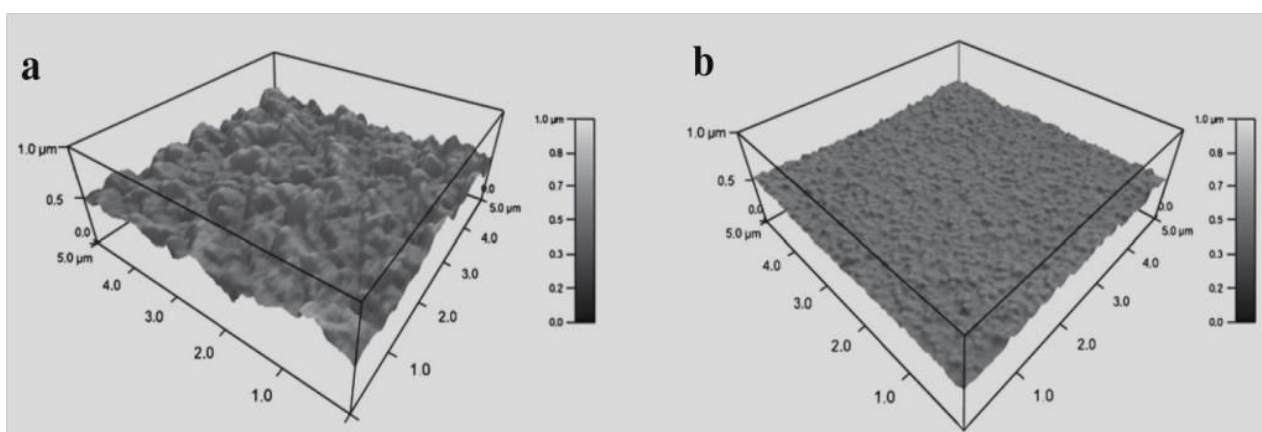


Figure 1 - 11: Atomic force microscopy images of RO membranes (a) AK (roughness 54.2 nm) and (b) SG (roughness 15.3 nm) [61]

It has been reported that surface roughness has an important effect in membrane fouling behaviour [80] [123]. Because of the ridge-and valley structure of rough membrane surfaces, colloids are thought to be preferentially transported into the valleys (path of least resistance), which results in “valley clogging” and hence in a more severe flux decline in comparison with smooth membranes.

The choice of characterization method is generally made based on the problem to which an answer is required and on the time, cost and resources available. However, the best knowledge is always obtained by combining results from different characterization methods.

1.3 Surfactants

1.3.1 Development and applications

Surfactants may be from natural or synthetic sources. The first category includes naturally occurring amphiphiles such as the lipids, which are surfactants based on glycerol and are vital components of the cell membrane [124], [125]. Soaps remained the only source of natural detergents from the seventh century till the early twentieth century, with gradually more varieties becoming available for shaving and shampooing, as well as bathing and laundering. In 1916, in response to a World War I-related shortage of fats for making soap, the first synthetic detergent was developed in Germany. Known today simply as detergents, synthetic detergents are washing and cleaning products obtained from a variety of raw materials [126] [127]. Nowadays, synthetic surfactants are essential components in many industrial processes and formulations, such as household detergents, personal care formulations, industrial and institutional washing and cleaning, as well as numerous technical applications such as textile auxiliaries, leather chemicals, agrochemicals (pesticide formulations), metal and mining industry, plastic industry, lubricants, paints, polymers, pharmaceutical, oil recovery, pulp and paper industry, etc [8]. They are also occasionally used for environmental protection, e.g., in oil slick dispersions [9].

The production of surfactants has increased over the last decades. In 2000, 2.5 Mt/year of surfactants were produced in Western Europe countries. In 2011, total annual tonnage of surfactants produced in Western Europe had already increased to 2.95 Mt/year, according to the CESIO (Comité Européen des Agents de Surface et leurs intermediaries Organiques)

statistics for surfactants' production in 2011 (CESIO Statistics 2011, 2012). The statistics surveyed Western European companies, representing more than 50 surfactants manufacturers, 70% of the European surfactants' market (CESIO News – Dec 2012). As it can be seen in Figure 1 - 12, non-ionic surfactants are the most produced type of surfactant followed by anionic ones. The production of cationic and amphoteric surfactants is quite lower.

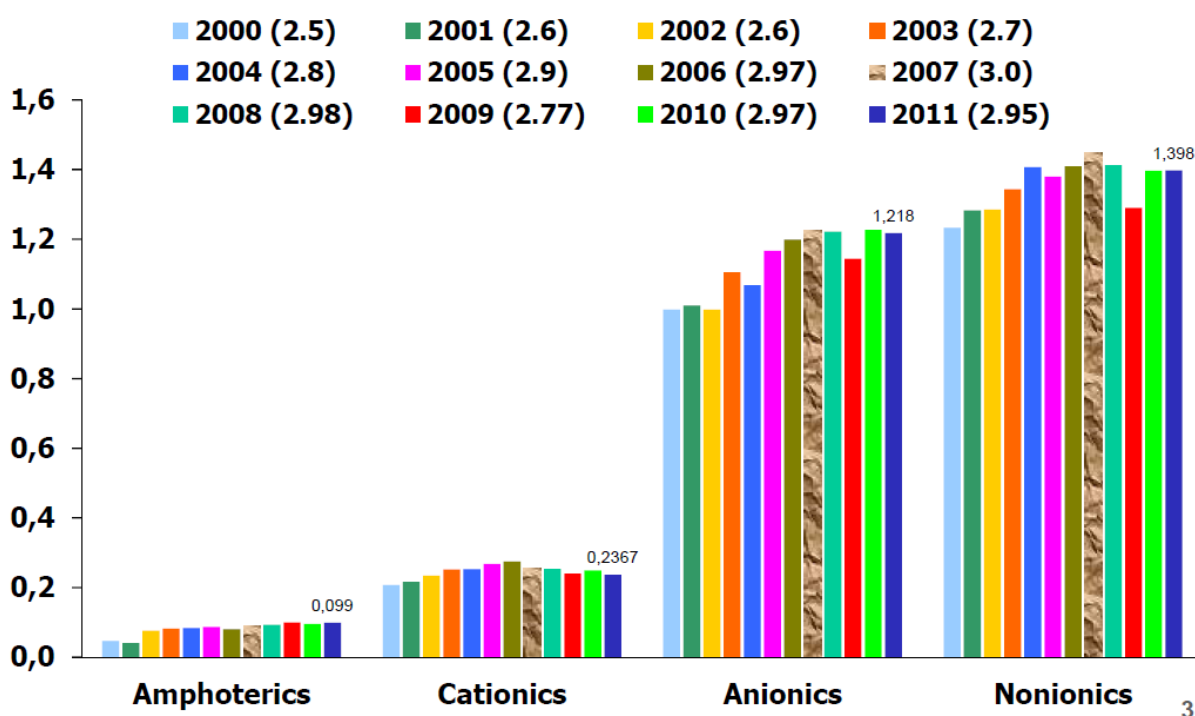


Figure 1 - 12: Annual production of surfactants in Western Europe from 2000 to 2011 (CESIO Statistics 2011, Dec 2012)

1.3.2 Definition of surfactants

Surfactant is an abbreviation for surface active agent, which literally means active at a surface. The molecular structure of surfactants is amphiphilic, consisting of both non polar (hydrophobic, or tail) and polar (hydrophilic, or head) parts, as shown in Figure 1 - 13. When dissolved in a solvent, surfactants tend to adsorb (or locate) at interfaces, with hydrophilic head retaining in the polar phase (usually water) while the hydrophobic tail facing the apolar phase, thereby altering significantly the physical properties of those interfaces. The driving force for a surfactant to adsorb at an interface is to lower the free energy of that phase boundary [128].

Critical micelle concentration (CMC) is the concentration below which virtually no micelles are detected and above which virtually all additional surfactant molecules form micelles. And aggregation number is the number of surfactant molecules present in a micelle once the CMC has been reached.

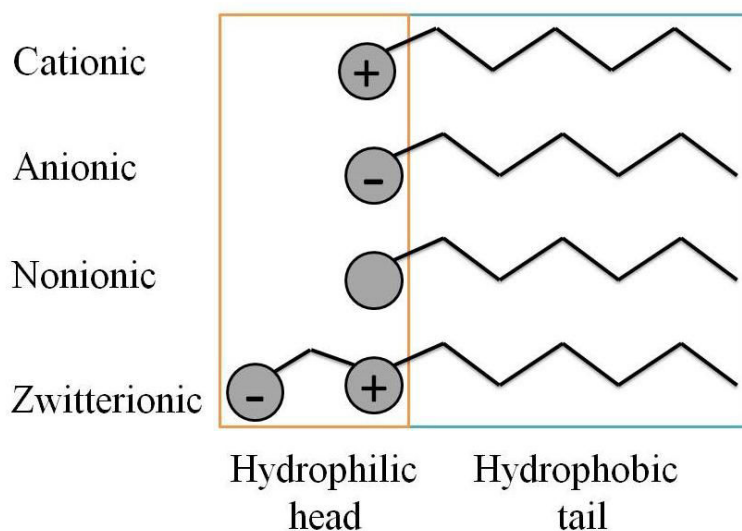


Figure 1 - 13: Amphiphilic structure of surfactants. The head corresponds to the hydrophilic part of the surfactant molecule, which is polar; while the tail represents the hydrophobic group of the surfactant molecule, which is apolar.

1.3.3 Chemical structure and classification

Chemical structure of surfactants

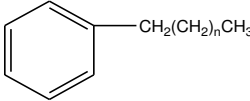
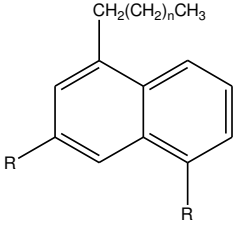
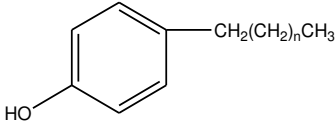
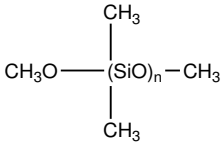
Numerous variations are possible within the structure of both the head and tail group of surfactants. The hydrophobic group of the surfactant structure is usually a single or double straight or branched hydrocarbon chain, but may also be a fluorocarbon, or a halogenated or oxygenated hydrocarbon or siloxane chain. Typical hydrophobic groups are listed in Table 1 - 4. The hydrophilic part of the structure may be represented by non-ionic polar groups or ionic groups as listed in Table 1 - 5.

Surfactants are classified by the polar head group

Chapter 1 Literature review

Depending on the nature of the hydrophilic head group, surfactants are therefore classified into four basic types: anionic, cationic, non-ionic and zwitterionic surfactants (see Figure 1 - 13).

Table 1 - 4: Common hydrophobic groups used in commercially available surfactants [7]

Group	General structure	
Natural fatty acids	$\text{CH}_3(\text{CH}_2)_n$	$n = 12-18$
Olefins	$\text{CH}_3(\text{CH}_2)_n\text{CH}=\text{CH}_2$	$n = 7-17$
Alkyl benzenes		$n = 6-10$, linear or branched
Alkyl aromatics		$n = 1-2$ for water soluble, $n = 8$ or 9 for oil soluble surfactants
Alkyl phenols		$n = 6-10$, linear or branched
Polyoxypropylene	$\text{CH}_3\underset{\text{X}}{\text{C}}\text{HCH}_2\text{O}(\underset{\text{CH}_3}{\text{C}}\text{HCH}_2)_n$	$n =$ degree of oligomerisation, $\text{X} =$ oligomerisation initiator
Fluorocarbons	$\text{CF}_3(\text{CF}_2)_n\text{COOH}$	$n = 4-8$, linear or branched, or H terminated
Silicones		

Anionic surfactants are those molecules of which the surface-active portion bears a negative charge. Common anionic surfactants are sulfonic acid salts, sulfuric acid ester salts, carboxylic acid salts, phosphoric and polyphosphoric acid esters, and perfluorocarboxylic acids.

Cationics contain a hydrophilic group positively charged, for example, long-chain amines and their salts, acylated diamines and polyamines and their salts, quaternary ammonium salts.

Nonionics bear no apparent ionic charge in their hydrophilic part, which include a highly polar (non charged) moiety, such as monoglyceride of long-chain fatty acid, polyoxyethylenated alkylphenol, polyoxyethylenated alcohol.

Table 1 - 5: Common hydrophilic groups found in commercially available surfactants [7]

Class	General structure
Sulfonate	$R-SO_3^-M^+$
Sulfate	$R-OSO_3^-M^+$
Carboxylate	$R-COO^-M^+$
Phosphate	$R-OPO_3^-M^+$
Ammonium	$R_xH_yN^+X^-(x = 1 - 3, y = 4 - x)$
Quaternary ammonium	$R_4N^+X^-$
Betaines	$RN^+(CH_3)_2CH_2COO^-$
Sulfobetaines	$RN^+(CH_3)_2CH_2CH_2SO_3^-$
Polyoxyethylene(POE)	$R-OCH_2CH_2(OCH_2CH_2)_nOH$
Polyols	Sucrose, sorbitan, glycerol, ethylene glycol, etc
Polypeptide	$R-NH-CHR-CO-NH-CHR'-CO-\dots-COOH$
Polyglycidyl	$R-(OCH_2CH[CH_2O]CH_2)_n-\dots-OCH_2CH[CH_2OH]CH_2OH$

Zwitterionics (or amphoteric) carry both positive and negative charges in the head group. Long-chain amino acid and sulfobetaine are the most encountered examples of this type of surfactants.

With the continuous search for improving surfactant properties and for enhanced biodegradability, new structures have recently emerged that exhibit interesting synergistic interactions or enhanced surface and aggregation properties. These novel surfactants have attracted much interest, and include the catanionics, bolaforms, gemini (or dimeric) surfactants, polymeric and polymerisable surfactants [7].

1.3.4 Properties of surfactants

1.3.4.1 Surfactant micellization

When dissolved in water, amphiphilic surfactants that contain hydrophobic groups distort the structure of water and therefore increase the free energy of the system. To minimize the free energy of the solution, they concentrate at the surface by orienting their hydrophobic groups away from the solvent (water), or they self-assemble into clusters with their hydrophobic groups directed toward the interior of the cluster and their hydrophilic groups directed toward the water when total surfactant concentration rises to the CMC.

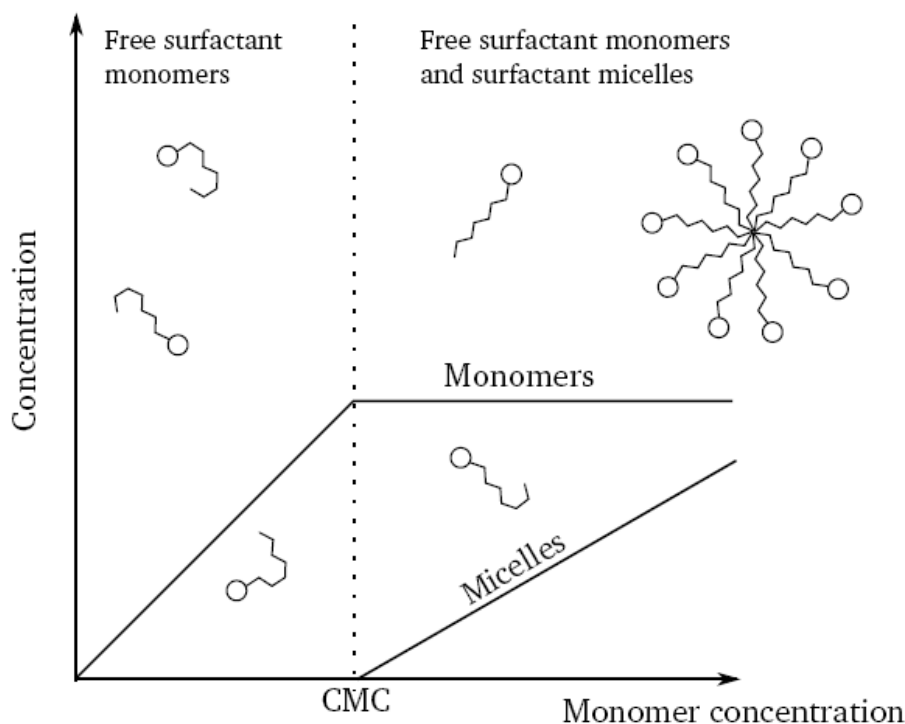


Figure 1 - 14: Surfactant monomers and micelle formation in water

Above their critical micelle concentration, there is equilibrium between monomers, small aggregates and micelles. Any further increase of total surfactant concentration results in the formation of more micelles, and the concentration of free surfactants keeps constant around the CMC (see Figure 1 - 14). Surfactants aggregate spontaneously form a wide variety of assemblies ranging from micelles, rodlike structures, and bilayers to more complex phases such as cubic phases. The micellar aggregation number and shape of the surfactant aggregates

depend on the type of surfactant (the volume V_H occupied by the hydrophobic groups in the micellar core, the length of the hydrophobic group in the core l_c , and the cross-sectional area a_0 occupied by the hydrophilic group at the micelle-solution interface) and the solution conditions.

The thermodynamics of micellization is described in details in several reports [7], [129], [130]. The surfactant solution can be considered as a multi-component system consisting of water, singly dispersed surfactant molecules, and aggregates of all possible shapes and aggregation numbers N_{agg} . At equilibrium, the chemical potential of free monomers must equal the chemical potential of surfactants involved in each aggregate μ_{agg} :

$$\mu_{aggi}^0 + kT \ln X_{aggi} = n_{agg} [\mu_i^0 + kT \ln X_1] \quad (\text{Equation 1 - 18})$$

where μ_{aggi}^0 , μ_i^0 are the standard state chemical potentials and X_{aggi} , X_1 the molar fraction of the surfactant aggregate with aggregation number i and of the surfactant monomers, respectively [7]. Every addition of a surfactant molecule to the solution leads an increase of free energy by the interplay of molecular interactions with water. The CMC is the threshold concentration at which the chemical potential of the free monomer becomes equal to that of monomers involved in micelles.

The surfactant self-assembly process depends primarily on surfactant architecture, the solvent, the presence of added components (i.e., co-surfactants or salts) and temperature. The micellization of surfactant cause sharp breaks at the CMC in the physical properties that depends on size or number of particles in solution, including electrical conductivity, surface or interfacial tension, etc [7]. This self-aggregation process of surfactants is of fundamental importance to many biological and industrial processes.

1.3.4.2 Surfactant adsorption at solid-liquid interface

The surfactants have strong tendency to adsorb at interfaces in an oriented way. The adsorption of surfactants at the solid-liquid interface is strongly influenced by several factors [131]:

- the nature of the structural groups on the solid surface: the charged sites or essentially nonpolar groupings and the constitution (e.g. the atoms and functional groups) of these sites or groupings;

- the molecular structure of the surfactant being adsorbed: the charge of the hydrophilic part, and the structure of the hydrophobic tail group (i.e. length of the straight or branched chain, aliphatic or aromatic hydrocarbons) of the surfactant molecule;
- the chemical and physical conditions of the aqueous solution: the pH, temperature, the presence of any electrolytes or other additives (alcohol, urea, etc)

1.3.4.2.1 Mechanisms of surfactant adsorption at solid-liquid interface

The mechanisms by which surfactants may adsorb onto solid surfaces from aqueous solutions are determined together by the factors as listed above. Several mechanisms are briefly described as follows:

- Ion exchange between surfactant ions and similarly charged counterions adsorbed onto the solid surface from the solution.
- Ion pairing of surfactant ions from solution onto oppositely charged sites of the solid surface, which has been occupied by counterions.
- Acid-base interaction via either Lewis acid-base reaction, or hydrogen bonding between surfactant molecules and the solid surface.
- Attraction by polarization of π electrons. This may occur if the solid surface contains strongly positive sites and there are electron-rich aromatic nuclei in the surfactant molecule.
- π - π interaction between aromatic nuclei of the surfactant molecule and of the solid surface if both contain such function group.
- Adsorption by London-van der Waals dispersion forces between surfactant and solid surface molecules.
- Hydrophobic bonding between tail groups of the surfactant molecules drives them to escape from water and onto the solid surface, while hydrophobic bonding between the tail groups of the surfactant molecules and hydrophobic sites on the solid surface.

In aqueous systems, the structures formed are determined by the interaction of the surfactant molecules with the solid surface in order to minimize exposure of the hydrophobic groups to water. The organization and structure of surfactant molecules or aggregates onto solid surfaces could be observed from scanning probe microscopic techniques like AFM,

fluorescence quenching and neutron reflectivity [132] [133]. The most observed structures of surface aggregates on a variety of solid surfaces have been reported to be hemimicelles, admicelles, monolayers, hemispherical bilayers, and cylinders [7], [134], [135], [136]. The orientation of the adsorbed surfactants onto a smooth, nonporous planar solid surface could be determined from the contact angle measurements (Section 1.2.5.3). The comparison of the obtained contact angles before and after surfactant adsorption could also provide information of the modification of membrane hydrophilicity due to surfactant adsorption. Orientation of the surfactants with their hydrophilic groups predominantly away from the solid surface will make it more hydrophilic than before the adsorption of surfactants [7].

In this thesis, since we focus on the active layer of RO membrane surface, the majority of which available in the market is made of polyamide (see Figure 1 - 6), the probable interactions between the membrane surface and the surfactant molecules could be [128]:

- Electrostatic interactions: the carboxylic acid ($-\text{COOH}$) and free amine ($-\text{NH}_2$) groups that are not engaged in the cross-linking of the amide bond may be ionized when in contact with a surfactant solution, carrying a negative or positive charge, thus they are possible to interact with the ionic surfactants through electrostatic forces.
- Hydrogen bonding: this may occur in the carboxylic acid ($-\text{COOH}$) and free amine ($-\text{NH}_2$) groups with the surfactants.
- π - π interaction between aromatic nuclei of the membrane surface and aromatic surfactants.
- Hydrophobic interactions between surfactants and the hydrophobic sites on the membrane surface.
- Mutual attraction (via hydrophobic bonding) of surfactant molecules with those adsorbed onto the membrane.
- London-van der Waal forces by the amide bond.
- Lewis acid-base interactions: this may occur in the carboxylic acid ($-\text{COOH}$) and free amine ($-\text{NH}_2$) groups.

1.3.4.2.2 Adsorption isotherms at solid-liquid interface

The adsorption isotherm is a mathematical expression that relates the concentration or amount of adsorbate on the solid surface to its equilibrium concentration in the liquid phase. It is usually used to describe the surfactant adsorption at the liquid-solid interface. The information on the solid surface, such as the area covered by surfactant and the maximum surfactant adsorption can be measured. After complementary analysis, the change of solid surface properties by the surfactant adsorption, the equilibrium adsorbed surfactant morphology, as well as the mechanism by which the surfactant is adsorbed at the interface could be predicted.

The most frequently used models for the adsorption isotherm are: linear adsorption isotherm, Langmuir and Freundlich adsorption isotherm.

Linear adsorption isotherm

The linear adsorption isotherm formally resembles Henry's law, so it is also called Henry's adsorption isotherm. In this model, the amount of the adsorbate onto solid surface is directly proportional to its concentration in solution.

$$Q_{ads} = K_H C_{eq} \quad (\text{Equation 1 - 19})$$

where Q_{ads} is the amount of surfactant adsorption onto the adsorbent, mol m⁻² or g m⁻²,

K_H is the Henry adsorption constant, L m⁻²;

C_{eq} is the equilibrium concentration of the surfactant in solution, mol L⁻¹.

The linear isotherm can be used to describe the initial part of many practical isotherms for low concentrations/surface coverage or very low interaction energy between the adsorbate and the adsorbent.

Langmuir adsorption isotherm (L type)

This model is commonly used to the surfactant adsorption from aqueous solutions, expressed by [100][131]:

$$Q_{ads} = \frac{Q_m C}{C + 1/K_L} \quad (\text{Equation 1 - 20})$$

where Q_{ads} = the surface concentration of the surfactant per unit area (or per unit mass) of the solid adsorbent, in mol m⁻² (or mol g⁻¹), at monolayer adsorption,

C = the concentration of the surfactant in the liquid phase at adsorption equilibrium in mol L⁻¹,

K_L = the Langmuir constant, in L mol⁻¹, containing information related to the adsorbate-adsorbent interaction free energy in the system. $1/K_L = 55.3 \exp(\Delta G^0/RT)$, at absolute temperature T , in the vicinity of room temperature and where ΔG^0 is free energy of adsorption at infinite dilution.

The application of Langmuir-type model is valid in theory only when the following restrictions are met: (1) the solid surface is homogeneous consisting of adsorption sites; (2) all adsorbed surfactants interact only with one site and not with each other; (3) the adsorption film is monomolecular. This model also has been very useful for studying adsorption systems between surfactants and polymeric materials.

Xiarchos et al. has successfully fitted their experimental data from the adsorption of nonionic surfactants onto UF membranes during filtration to the following Langmuir model [100]:

$$Q_{ads} = \frac{Q_{ad,max}K_L C_{eq}}{K_L C_{eq} + 1} \quad (\text{Equation 1 - 21})$$

where C_{eq} = the concentration of the surfactant in the liquid phase at adsorption equilibrium in mol L⁻¹,

$Q_{ad,max}$ = maximum adsorption of the surfactant per unit mass of the UF membranes, in mol m⁻², at monolayer adsorption,

K_L = the Langmuir constant, in L mol⁻¹, containing information related to the adsorbate-adsorbent interaction free energy in the system.

S type adsorption isotherm

Due to attractive lateral interactions between surfactant molecules, the Langmuir isotherm may become S-shaped or stepped [137]. A two-step adsorption mechanism has been proposed: in the first step, the surfactant molecules are adsorbed as individual molecules or ions; then in the second step, there is a sharp increase in the adsorption as surface aggregates form through interaction of the hydrophobic chains among the surfactant molecules.

$$Q_{ads} = \frac{Q_{\infty} K_S C^{n_s}}{K_S C^{n_s} + 1} \quad (\text{Equation 1 - 22})$$

where Q_{∞} = the limiting surfactant adsorption at high concentration C ,

K_S = the equilibrium constant of the surface aggregation process,

n_s = the average aggregation number of the surface aggregate as a general adsorption isotherm.

(Equation 1 - 22 can be transformed to the linearized expression as follows:

$$\log [Q_{ads}/(Q_{\infty} - Q_{ads})] = \log K_S + n_s \log C \quad (\text{Equation 1 - 23})$$

The values of K_S and n_s could be obtained from a plot of $\log [Q_{ads} / (Q_{\infty} - Q_{ads})]$ versus $\log C$ if there is a linear relationship between them. If $n_s > 1$, this means surfactant aggregation at the solid surface occurs.

The adsorption isotherm of an ionic surfactant on an oppositely charged solid surface usually follows a more complicated mechanism. This typical adsorption isotherm can be subdivided into four regions when plotted on a log-log scale (see Figure 1 - 15) [138]. In the first region, the surfactants adsorb as individual molecules on single surface sites at low concentrations. The amount of adsorbed surfactants is very low and the interaction between adsorbed surfactants is negligible, thus this first region is governed by Henry's law. The second region shows a sudden increase of adsorption due to the formation of primary aggregates, known as hemimicelles, when the critical aggregation concentration (CAC) is reached. In the third region, the solid surface is neutralized by the adsorbed surfactant ions, the electrostatic attraction is no longer operative and adsorption takes place due to lateral attraction alone with a weaker increasing up to a plateau region with constant adsorbed amount. The plateau indicates that the surfactant monomer activity becomes constant and any further increase in concentration contributes only to the micellization in solution and it does not change the adsorption quantity. In some cases, the fourth region can contain a weak maximum before arriving at the plateau. The isotherm of surfactants on hydrophobic surfaces as well as the form of adsorbed surfactant molecules is proposed in Figure 1 – 15 [13].

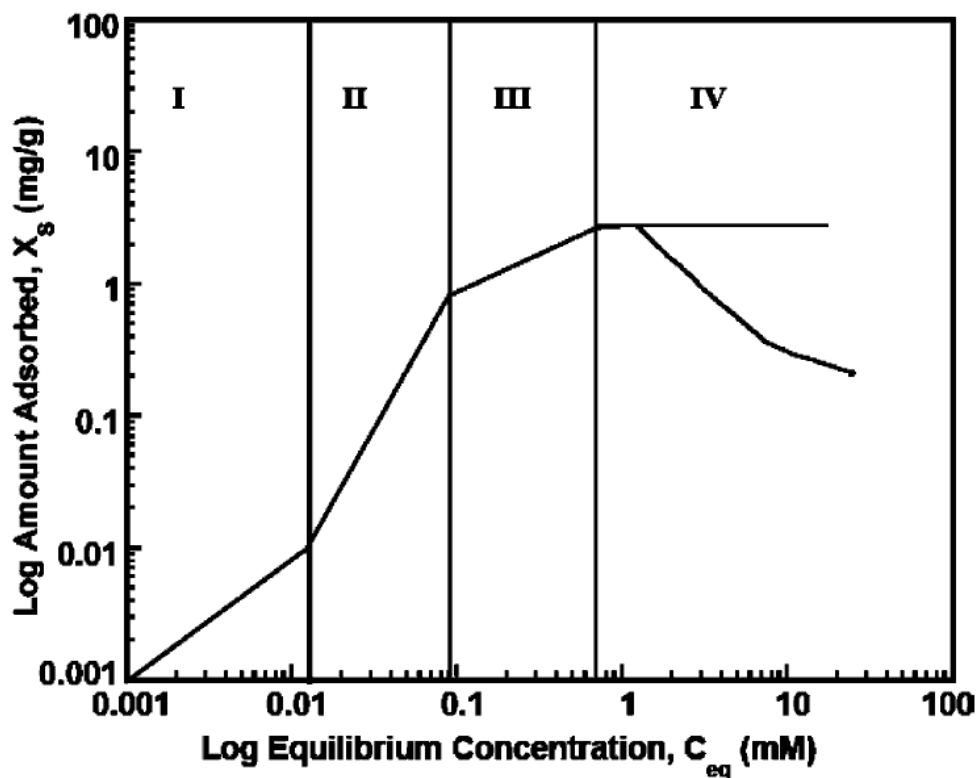


Figure 1 - 15: Schematic presentation of typical four-region adsorption isotherm [139]

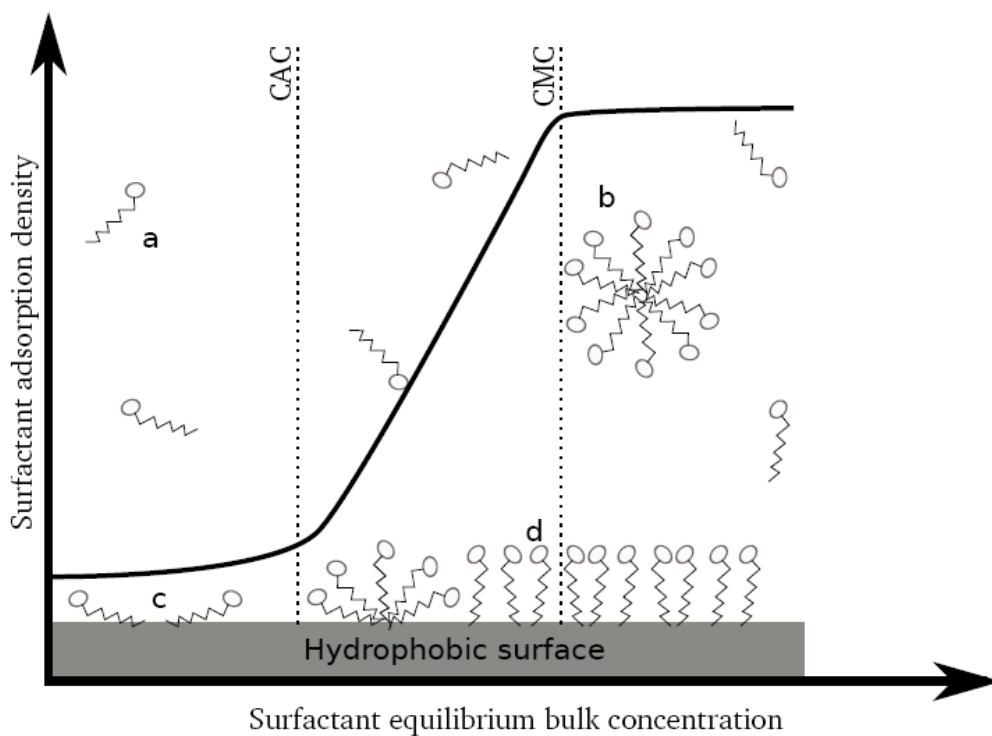


Figure 1 - 16: Adsorption of surfactants on hydrophobic surface. a: surfactant monomers; b: surfactant micelles; c: isolated adsorbed surfactant monomers; d: surface aggregates[13] .

Freundlich Adsorption Isotherm

The Freundlich equation is an empirical expression with the assumption that the adsorbent has a heterogeneous surface composed of adsorption sites with varying energy [140]. It represents the amount of a solute on the adsorbent, to the concentration of the solute in the liquid phase at different solution concentrations. This equation is expressed as follows:

$$Q_{ads} = K_f C_{eq}^{\frac{1}{n_f}} \quad (\text{Equation 1 - 24})$$

where Q_{ads} is the amount of particle adsorption onto the adsorbent, mol m^{-2} or g m^{-2} ,

K_f and n_f are empirical constants for a given adsorbate and adsorbent pair at a particular temperature, with n_f generally greater than unity;

C_{eq} is the equilibrium concentration of the adsorbate in solution, mol L^{-1} .

Even though this model does not describe clearly the physical phenomenon, it can be applied to the case with a heterogeneous surface where there are different adsorption sites for attachment of the solute. Since the adsorbent would not be saturated by the adsorbate in this model, the infinite surface coverage indicates multilayer sorption of the surface.

Freundlich isotherm could be rewritten to the logarithmic form and a linear relationship could be obtained as follows:

$$\log Q_{ads} = \log K_f + \frac{1}{n_f} \log C_{eq} \quad (\text{Equation 1 - 25})$$

1.3.5 Environmental effects of surfactant

Due to the significant production and the widespread use of surfactant-based formulations, wastewaters containing surfactants are generally encountered. Direct discharge of wastewaters containing surfactant into rivers may cause foam formation and may origin anomalies to algae growth and toxicity to aquatic organisms [127]. If sent to a wastewater treatment plant, they can cause disruption of the plant, preventing sewage from being treated, and forcing the plant to discharge raw sewage.

1.3.6 Membrane filtration of surfactants

Various organic materials, such as phenols, surfactants, pesticides, herbicides, aromatic hydrocarbons, among many others are typically found in industrial effluents. Specially, surfactants are usually present in domestic wastewater, food engineering discharged effluents and cleaning solutions for membrane stacks used in water treatment. Those substances are examples of highly stable organic pollutants. Their persistence to the environment has been demonstrated and, many times, the symptoms of contamination may not manifest themselves until several generations after initial contact with the chemical of concern. Thus, wastewaters containing such non-biodegradable pollutants need to be treated and pollutants removed to avoid associated environmental pollution.

Surfactants have been extensively used in membrane processes, such as pretreatment of membranes with surfactant solutions, removal of low molecular weight organic toxic compounds and metal ions from solutions by micellar-enhanced ultrafiltration (MEUF). Removal of surfactants and estimation of interactions at surfactant membrane interface have also been studied. In this work, we focus on the removal of surfactants from wastewaters by membrane filtration processes.

Most of the membrane filtration studies published to date concerning about the treatment of surfactant solution have been carried out with crossflow UF, which have been widely used to remove surfactants from wastewaters. The surfactant micelles are retained by the membrane while monomers are too small and pass through the membrane. The permeate concentration of surfactants is close to their CMC. If the surfactant concentration is lower than the CMC, where the surfactant exist mainly as monomers, nanofiltration has been suggested as an effective removal process [141]. Studies on the RO processes applied in removing surfactants from wastewaters are rather limited in the literature. The removal of surfactants could be higher than 90% and even 99% for NF and RO, respectively [142], [143], [144].

Membrane fouling during filtration of surfactant solutions has been studied mainly in the case of UF. In general, surfactants may cause severe fouling problems and thus decrease the membrane flux. The reason for the flux decline in some cases has been due to concentration polarization caused by retained micelles. Another reason for the decrease of permeate flux has

been attributed to adsorption of surfactant molecules in the membrane pores or on the membrane surfaces through hydrophobic and/or electrostatic interactions. The flux decline is thought to be related to the adsorbed amount [112]. But in some cases, the adsorption of surfactants on the membrane surface increased membrane hydrophilicity due to the orientation of adsorbed surfactant molecules, leading to a higher permeate flux [145], [146]. Therefore, they are also used in the cleaning solution for surface modification to improve membrane performance [147], [148], [149], [150].

The orientation of adsorbed surfactant molecules or layers is determined by the interactions between surfactant molecules and membrane surface, and/or between surfactant molecules, which may influence the membrane surface properties, leading to deterioration or improvement of membrane performance. The adsorption structure of the surfactants on the membrane surface has been reported as a close compact structure (e.g. monolayer) at high concentrations, with the hydrophilic head groups or hydrophobic tail groups facing towards the aqueous solution, thus modifying the surface properties of the membrane, and consequently influencing the membrane performances (i.e. transport and separation properties); while at low concentrations or at the early stage of adsorption, the surfactant molecules lay parallel to the membrane surface.

There are examples of surfactant solution in connection with different membrane processes: MF of nonionic, anionic and cationic surfactant [145], [151]; UF of nonionic and ionic surfactants [9], [100], [129], [141], [145], [146], [152], [153], [154], [155], [156], [157], [158], [159], [160]; micellar-enhanced ultrafiltration [161], [162], [163]; NF of nonionic, anionic and cationic surfactants [112], [156], [164], [165]; surfactant enhanced NF and RO membranes [147]; RO of different surfactants [144], [166], [167], [168], [169], [170], [171]; anionic surfactant (SDS) effects on the RO membrane (thin-film composite polyamide) [148], [149]; cleaning of RO membrane using anionic surfactant (SDS) [150]; shear induced surfactant filtration [172]. Since the properties of solutions of surfactants change markedly when micelle formation occurs, surfactant was used at concentrations below its CMC in several filtration experiments [9], [100], [129], [145], [152], [153], [154], [155], [156], [157], [158], [159], [160]. Some membrane processes for the removal of a variety of surfactants from solution in the literature are summarized in Table 1 - 6.

Table 1 - 6 a: Membrane filtration of surfactants in literature: microfiltration

Membrane			Surfactant				Operating condition	Interesting results	Reference
	MWCO	Composition	Composition	Charge	CMC (25 °C)	Concentration			
MF	0.2 µm	cellulose acetate	Linear alkyl benzene sulfonate (C ₁₃ H ₂₇ C ₆ H ₄ SO ₃ H)	Anionic	2.0 mM	0 -10 mM	ΔP = 150 kPa, T = 30 °C, V = 1.18m s ⁻¹	(1) The removal of surfactants is attributed to the formation of a secondary membrane on the surface and within the pores of the MF membrane. (2) Increase in transmembrane pressure and pore size of the membrane decreased the surfactant rejection rates. (3) Increase in cross-flow velocity increased the rejection rate.	[151]
			Cetyl trimethyl ammonium bromide (C ₁₉ H ₄₂ NBr)	Cationic	0.92 mM	0 -10 mM			

Table 1 - 6: b: Membrane filtration of surfactants in literature: ultrafiltration

PES : Polyethersulfone, PS : Polysulfone, C: Regenerated cellulose, CA: Cellulose acetate, PA: Aromatic polyamide, PVDF: Poly(vinylidene fluoride)

Membrane			Surfactant					Operating condition	Interesting results	Ref.
	MWCO (KDa)	Composition	Composition		Charge	CMC (25 °C)	Conc.			
UF	5,10,30	PES	SDS	Sodium dodecyl sulfate $C_{12}H_{25}SO_4Na$	Anionic	7.83 mM	0.017 – 2.08 mM (< CMC)	P = 0.05 – 0.20 MPa, T = 25 °C, pH = 7	(1) Hydrophobic membranes are more susceptible to fouling than hydrophilic membranes. (2) Fouling would be increased with the increase in membrane cut-off. (3) Increasing the pressure will cause an increase in permeability, but a slight decrease in surfactant rejection. (4) Membrane permeability and SDS rejection decreased with the increase in the surfactant concentration.	[141]
	5,10,30	PS								
	5,10,30	C								
	5,10,30	CA								
	5,10,30	PA								
UF	10	hydrophilic PES	SDBS	Sodium dodecyl benzene sulfonate $C_{12}H_{25}(C_6H_4)SO_4Na$	anionic	1.88 mM	C/CMC = 0.5 – 5		(1) The effect of the concentration polarization was greatly reduced due to the high shear rates on the membrane. (2) The permeate flux rises with increasing the surfactant concentration. (3) Compared to new membranes, a higher surfactant concentration gives a bigger increase in the hydrophilicity of PES membrane after treated with the surfactant solution. (4) The surfactant retention decreased as feed concentration rose, due to the existence of sub-micellar aggregates, and higher permeate flux.	[146]

UF	20	PS (GR 61 PP)	Tritons	Alkylphenol ethoxylates $C_8H_{17}(C_6H_4)O(CH_2CH_2O)_n$ H $n = 5,8,10,12$	Non-ionic	0.15 – 0.37 mM	$C \leq CMC$ ($C/CMC =$ 0.1, 0.33, 0.5, 0.75, 1.0)	$\Delta P = 0.05 -$ 0.20 MPa, $T = 20\text{ }^\circ\text{C}$, $pH = 7$ $v = 4\text{ m s}^{-1}$ and 2.5 m s^{-1}	<ol style="list-style-type: none"> (1) The hydrophobic PS membrane experienced a sharp flux decline in contact with surfactant solution, because of the interaction between the membrane material and the hydrophobic part of the surfactant molecules, leading to adsorption, probably within the membrane pores. Concentration polarization is unlikely in this work since no significant flux reduction was observed for CA membrane. The hydrophilic membrane showed weaker interactions with non-ionic surfactants in this study. (2) The flux of the surfactant solution was a linear function of pressure. (3) As the surfactant concentration approaches the CMC, the most hydrophobic surfactant causes the greatest decline in flux. The surfactant with intermediate hydrophobicity shows an intermediate behavior. 	[152]
	20	CA (CA 600 PP)	Dobanol	$C_xH_{2x+1}O(CH_2CH_2O)_nH$ $n = 5,6,7,8$		0.8 – 1.0 mM				
UF	20	PS (GR 61 PP)	Tritons	Alkylphenol ethoxylates $C_8H_{17}(C_6H_4)O(CH_2CH_2O)_n$ H $n = 8,10,12$	Non-ionic	0.265 mM 0.28 mM 0.37 mM	$C \leq CMC$ ($C/CMC =$ 0.1, 0.33, 0.5, 0.75, 1.0)	$T = 20\text{ }^\circ\text{C}$, $pH = 7$ and $pH = 2$	<ol style="list-style-type: none"> (1) The surfactant adsorption on the membranes depends on the chemical composition and structure of both the surfactant and the membrane used, as both the chemical composition and structure determine the type of interactions controlling this adsorption. The interactions are due to intermolecular and interfacial forces, which develop between the substrate (in this case membrane) and the surfactant. (2) The adsorption of surfactant onto the hydrophobic membranes is larger than hydrophilic membranes. (3) Upon increasing the hydrophilicity of the nonionic surfactant by increasing the ethylene oxide groups (EO), the adsorption decreases. (4) In the early stages of adsorption, surfactant molecules lie flat 	[153]
	20	PVDF- hydrophobic (FS 61 PP)								

									on the membrane surface; as the concentration increases, close packed assembly will result by orienting perpendicular to the surface, with hydrophilic head groups towards the aqueous phase.	
	20	CA (CA 600 PP)	Dobanol-series surfactants	$C_xH_{2x+1}O(CH_2CH_2O)_nH$ n = 5,6,8 x = 9,10,11		0.8 mM 0.9 mM 1.0 mM				
	20	PVDF- modified (ETNA 20 A)								
UF	6 20 500	PS	Triton X-100		Nonionic	0.24 mM	C/CMC = 0.1, 0.4, 1.0, 4.0	$\Delta P = 0.5$ MPa, T = 25 °C, pH = 7 $v = 0.75$ and 1.05 m s^{-1}	<ol style="list-style-type: none"> (1) The flux declines of the hydrophobic membranes were found to be much more significant than that of the hydrophilic ones, since the adsorption of surfactants is more pronounced for hydrophobic than for hydrophilic solids. (2) The influence of the anionic surfactants on the low cut-off PS membranes was highly irregular, as the flux increased markedly at the CMC. The impurities in the solution caused the divergent performance of the membranes. (3) Retention of the ionic surfactants was quite high even at low concentrations. (4) The performance of the hydrophobic membranes was determined by both the material and the MWCO of the membranes. 	[154]
	6 20	PVDF	oleate and SDBS	Potassium oleate and sodium dodecylbenzene- sulphonate	anionic	0.9 mM 1.10 mM				
	8 20	CA	CTAB	Hexadecyltrimethylammonium bromide	cationic	0.92 mM				

Table 1 - 6: c: Membrane filtration of surfactants in literature: nanofiltration

PES : Polyethersulfone, PS : Polysulfone, C: Regenerated cellulose, CA: Cellulose acetate, PA: Aromatic polyamide, PVDF: Poly(vinylidene fluoride)

Membrane		Surfactant						Operating condition	Interesting results	Ref.
	MWCO (Da)	Composition	Composition		Charge	CMC (25 °C)	Conc.			
NF	190	Desal 51HL	Neodol	RO(CH ₂ CH ₂ O) _n H	Nonionic	1150 mg L ⁻¹	20 – 70 mg L ⁻¹	ΔP = 8 bar, T = 20 °C, pH = 6, v = 4.5 m s ⁻¹	(1) Membrane performance decreases with increasing concentration. (2) The flux decline is related to the adsorbed amount of surfactants. (3) The adsorption of surfactants is determined by the hydrophobic and/or electrostatic (in the case of ionic surfactants) interactions with the membrane. Hydrophilic membranes have less surfactant adsorption amount than hydrophobic ones. (4) The nonionic surfactant can undergo chain folding, and penetrate into and be adsorbed in the large pores of the hydrophobic membrane, causing large amount of adsorption. (5) The retentions of ionic surfactants did not change significantly while the retention of nonionic surfactant decreased with increasing concentration.	[112]
	155									
	310	NF 270	SDBS	CH ₃ (CH ₂) ₁₁ C ₆ H ₄ SO ₃ Na	Anionic	2320 mg L ⁻¹				
	1200	NTR 7450 NFPES10	cetrimide	CH ₃ (CH ₂) ₁₅ N(CH ₃) ₃ Br	cationic	1320 mg L ⁻¹				

NF	400	PES (NF PES 10)	LABS	Linear alkyl benzene sulfonate	Anionic	0.64 g L ⁻¹	C < CMC For single surfactant solutions, C = 50, 200, 500 mg L ⁻¹ for LABS, SLES, and NPE, respectively.	ΔP = 12 bar, T = 18 ± 1 °C, v = 3.0 L min ⁻¹	<p>(1) The rejection of surfactants and flux decline took place due to the adsorption of surfactants onto both surface and pore walls, which is depending on MWCO and contact angles of the membranes.</p> <p>(2) A secondary membrane layer formed on the surface of N 30F and XN 45 membrane in addition to the surfactant aggregates; which occurred on the surfaces of all membranes. A large number of small aggregates formed on N 30 F (smooth and negatively charged); while less aggregates with larger sizes formed on NF PES 10. Surfactant aggregates accumulated densely on XN 45 surface, which is neutral and rough.</p> <p>(3) Anionic surfactants are bond to membrane surface through hydrophobic attraction, stronger than electrostatic repulsion on membrane surfaces with negative charge.</p> <p>(4) The most surface fouling occurred on XN 45 membrane for anionic surfactants, since anionic surfactants consisting of long chains are able to fold to a substantial degree, thus could penetrate into the pores of this membrane with a MWCO smaller than the molecular weights of anionics at relatively low rejections.</p>	[164]
	1000	PES (N 30F)		R-C ₆ H ₄ SO ₃ H	Anionic	0.30 g L ⁻¹				
	200	PA (XN 45)	SLES	Sodium dodecylether sulfate R-O-(CH ₂ CH ₂ O) ₂ -SO ₃ Na Nonylphenol ethoxylate NPE (C ₄ H ₉) ₂ CHC ₆ H ₄ (OC ₂ H ₄) ₉ OH	Nonionic	0.06 g L ⁻¹				

Table 1 - 6: d: Membrane filtration of surfactants in literature: reverse osmosis

PES : Polyethersulfone, PS : Polysulfone, C: Regenerated cellulose, CA: Cellulose acetate, PA: Aromatic polyamide, PVDF: Poly(vinylidene fluoride)

Membrane			Surfactant				Operating condition	Interesting results	Ref.	
		Composition	Composition		Charge	CMC (25 °C)	Conc			
RO		CA-10 CA-75 CA-90	FT 248 BAC	Tetraethylammonium-perfluorooctane sulfonate Benzalkonium chloride	Anionic Cationic		0.11 mM	$\Delta P = 10 - 40$ bar, $T = 20 \pm 0.3$ °C, $v = 0.9 \text{ L min}^{-1}$ pH = 3	(1) The flow reduction caused by the anionic surfactant is reversible. (2) A gel layer is formed on the membrane at a very low concentration for BAC; the amount of BAC adsorption on the CA-10 membrane increases from 1.0 to 4.2 g m ⁻² with the applied pressure increasing from 10 to 40 bars. The corresponding values for the CA-75 membrane were 2.0 and 3.5 g m ⁻² , respectively.	[171]
RO	SG1812C-28D	Thin-film PA		- Fluorinated surfactant	Anionic	-	23 - 417 mg L ⁻¹ 470 mg L ⁻¹ 140 mg L ⁻¹	$\Delta P = 20$ bar, $T = 25$ °C, $v = 0.084 \text{ m s}^{-1}$ pH = 6.8, 7.5, 8.2	(1)Pure water permeability was 2L h ⁻¹ m ⁻² bar ⁻¹ . (2)Surfactant retention rates were higher than 99.9%, and flux decline is significant. (3)Mass balance showed that certain quantity of surfactants was adsorbed onto the membrane surface. (4)Flux permeability decreased with increasing the surfactant concentration.	[144]
RO	E-398-3	Modified CA	ABS	Sodium dodecylbenzene sulfonate	anionic	1.40 mM	C < CMC	$\Delta P = 40$ bar, $v = 250 \text{ mL min}^{-1}$	(1)The rejection of ionic surfactants was larger than that of nonionic surfactants, especially at concentrations below CMC. (2)The flux decreased with the increase of molecular weight for	[166]

			TDBNC	Tetradecylbenzylammonium chloride	Cationic	4.20 mM			nonionic surfactants. (1) The CMC affected the transport significantly of nonionic surfactants. (2) Concentration polarization on the membrane surface could be predicted by taking into account the difference between surfactant fluxes below and above CMC.	
			NP-10 NP-16 NP-27	Polyoxyethylene nonylphenyl ether	Nonionic	0.0527 mM 0.068 mM 0.144 mM				
RO	CA	Negatively charged CA	BAC	Benzalkonium chloride	Cationic		0.11 mM	$\Delta P = 5 - 40$ bar, $T = 20 \pm 1$ °C, $v = 0.9 \text{ L min}^{-1}$	(1) The adsorption of surfactants on the membrane surface caused a slight decrease in the flux. (2) At CMC, the surfactant rejection increased, which could be explained by a change in the activity. By adsorption of the surfactants at the pore walls of the membranes, the water transport is reduced, and the fixed charge in the pores increased by adsorption of charged surfactant, leading to a more pronounced Donnan exclusion of the solutes.	[168]
		SPSU	Sulfonated PS(negative)	FT 248	Tetraethylammonium	Anionic				
RO	FT-30	Thin film composite PA	SDS	Sodium dodecyl sulfate	Anionic	8.2 mM	1.0 mM	M NaCl, $\Delta P = 5 - 40$ bar, $\text{pH} = 3 - 9$, $T = 20$ °C, $v = 0.9 \text{ L min}^{-1}$	1. The surfactants were found to readily adsorb to the membrane surface and markedly influence the membrane surface charge. The negatively-charged sulfate functional groups of the surfactant molecules cause the membrane to become more negatively charged. 2. The formation of surfactant hemimicelles on the membrane surfactant resulted in a secondary filtration layer on the membrane surface, which caused decreased flux and increased salt rejection at low pH.	[148]
		CG								

From the table, we can see that although various membrane filtrations have been undertaken, the majority of these works focused on membrane performance. There has been no work studying the adsorption isotherm of surfactants on the membrane surface due to operating conditions, such as continuous pressure as well as the tangential flow along the membrane surface. In addition, the characteristics of the morphology or surface organization of these amphiphilic molecules during membrane filtration seem to have not yet been realized. A fundamental work on this aspect is needed for providing enough information on the filtration process.

1.4 Membrane filtration

The main limitations to the wild spread of membrane processes and its performance optimization are the membrane fouling leading to flux decline, the cleaning and the selectivity. Recently the scientists look for a better understanding of the local mechanisms and modeling has played an important role [101], [173], [174], [175], [176], [177]. The porous media constituting the membrane was a black box few years ago and simple hypothesis and modeling are still used to describe what happens on or inside the membrane: resistance-in-series model, concentration polarization, cake formation, pore blocking or pore constriction [178]. But the local description of the porous media is now more and more studied, because this is the place where everything happens. Membranes are complex structures, organic or mineral, with variable compositions. During the filtration they can generate various interactions (hydrogen bonding, Van der Waal, Lewis, ionic exchange etc), depending on the membrane and the composition of the complex solution to treat. A better understanding of the local interaction could help to propose new strategies to enhance the performances of membrane processes, to reach an efficient separation, limiting the energy cost due to flux decline and limiting cleaning periods.

The membrane characterization and the deepen study of the interaction have been published in recent papers dealing with fouling, life time [179], mapping of fouling etc..The main difficulty is the submicronic size of the structure to analyze; analytical methods are still limited. It is neither possible at the moment to describe experimentally the 3D structure of membranes in different materials, with rare exceptions [180], nor to detail the organization of amphiphilic molecules at the membrane surface. That is why modeling is a complementary tool to reach the local scale. The modeling tools developed at the moment are mostly for

macroscopic scale: process modeling with semi empirical laws [178], [181], [182] or at molecular scale ([183]). No work was published on mesoscopic modeling of fouling using coarse graining, like Dissipative Particle Dynamics (DPD), allowing the simulation of great ensembles of molecules. This would be a useful tool to understand the behavior of organic matter at the membrane interface.

1.5 Simulation of surfactant systems

Although a lot of work, both experimentally and theoretically, is directed at an understanding of the various surfactants systems, the detailed behavior in solution and at interfaces has not yet fully been understood. It is important to note that, the assumed types of surface aggregates (monolayers, bilayers, admicelles, hemimicelles, and hemicylinders) on the solid surfaces are idealized borderline cases. A lot of factors are expected to influence these surface structures. However, most of experimental methods are not capable to determine the layer structure in detail from a dynamic view. This is primarily due to the fact that the surface organization occurs on a very fast time scale (nanosecond to millisecond), and on a very short length scale (nanometer), thus making experimental investigation difficult. Theoretical considerations and computer simulation can essentially support the interpretation of experimental results and provide immediate and comprehensive information on the structure of adsorption layers [184].

There is significant interest in developing theoretical and simulation models of the micellization process as well as surfactant adsorption onto solid surfaces. More details on the molecular dynamics simulation and coarse-grained molecular dynamics methods could be found in several reports [185], [186], [187], [188], [189].

In this work, we applied a mesoscopic simulation method — Dissipative Particles Dynamics (DPD) simulation to investigate the micellization and the adsorption of surfactants onto liquid-solid interfaces. This method is similar to MD studies using coarse grain models except that dissipative and random forces act between particles as well as the usual conservative ones. At present DPD seems to be able to employ more detailed descriptions than experimental results. It has been successfully applied to various surfactant systems, including the micellization of surfactants in solution, adsorption at air-water surfaces, and so on.

1.6 Thesis outline

Surfactants are widely used in industry and in daily life. They are good examples of organic compounds. Due to their specific properties, they can influence the treatment process by adsorbing onto interfaces and forming specific aggregates in the solution.

The present work aims at studying the behaviors of surfactants at the membrane-solution interfaces to deepen the understanding of organic fouling during membrane processes. Experimentally, we will measure the adsorption of surfactants on RO membranes in cross flow filtration conditions and evaluate its impact on the permeate flux J and the retention R , and characterize the surface modification. Then in the simulation part, we build a new method to simulate the surfactant adsorption at the membrane-solution interface from mesoscopic scale. In the first step, we will choose and validate the DPD parameters through CMC calculation; in the second step, the selected parameters will be used to simulate the behavior and organization of surfactant molecules in contact with polymeric membranes. The final objective is to compare the modeling of the behavior of surfactants at the membrane-solution interface to experimental data (as described in Figure 1 - 17) to elucidate the structure of surfactant aggregation at the membrane interface. In the future this method will allow to better understand the impact of microscopic organization on macroscopic measurements and could give key information to improve membrane separation by limiting the fouling.

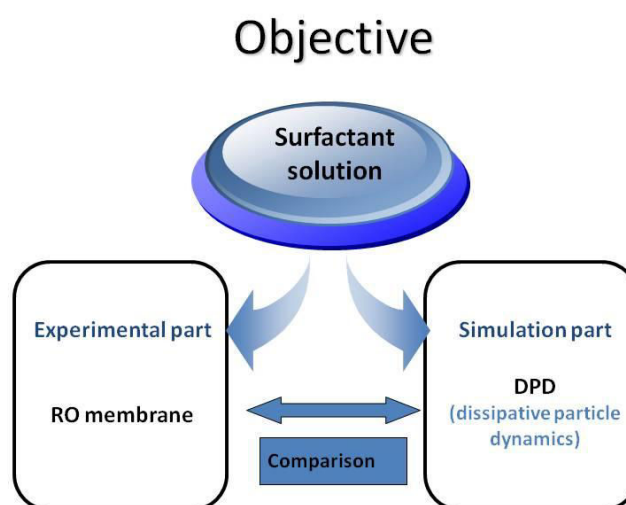


Figure 1 - 17: Thesis objective

Chapter 2

Experimental part:

Fouling of RO membranes by surfactants

2.1 Introduction

The aim of this work is to study the fouling of reverse osmosis membrane by organic matter. Surfactants were selected as model organic matter molecule because, despite their simple chemical structure (compared to proteins for example), they present a strong ability to organize and generate complex aggregates, that could also occur in a complex effluent. Moreover, surfactants are extensively used in household products, detergents, industrial processes and pesticide formulations due to their fundamental properties, such as micellization in solutions and adsorption onto interfaces/surfaces [7]. Surfactants may also persist in wastewater treatment systems at relatively high concentrations as a consequence of their frequent use and relatively high resistance to bio-degradation [127]. To prevent serious health and environmental problems that might result from direct and indirect releases of surfactants, surfactants should be removed from water before release to the environment.

Various research has shown that using a membrane may be an effective technique to remove surfactants from effluents [141], [144], [164] (see chapter 1, section 1.3.6). However, two major phenomena may occur during membrane filtration of surfactants: fouling and concentration polarization, which will limit its productivity. Fouling occurs principally from pore plugging, adsorption and/or cake formation at membrane surface [178], [190]. Especially for nonporous reverse osmosis (RO) membranes, surfactant molecules might accumulate at the membrane surface and gradually deteriorate membrane performances, such as the decrease in permeate flux [6], [64], [160], [191]. Despite adsorption onto the active layer of the membranes, large quantity of surfactants are able to fold and thus penetrate (i.e. partitions) inside the membrane as well as adsorb onto the internal surface area, just as other trace organics [192]. Understanding the behavior and transport of surfactants at RO membranes in filtration mode requires the knowledge of the interactions between surfactants and membranes and the mechanism governing the process.

The behavior of surfactants at the membrane surface is determined by an interplay among several chemical and physical factors, including feed water composition (e.g. surfactant structure, concentration, pH, ionic strength), membrane properties (e.g. roughness, charge, hydrophobicity), and hydrodynamic conditions (e.g. pressure, flux, cross-flow velocity) [175]. The chemical composition and structure of both the surfactant and the membrane determine the type of interactions between them. Interactions due to intermolecular and interfacial forces

developed between the membrane surface and the surfactant, mainly includes electrostatic interactions, hydrogen bonding, and hydrophobic interactions [139].

The association and arrangement of surfactant molecules controlled by these interactions could lead to modification of the membrane surface characteristics and consequently affect the performance of membrane. In the case of nonionic surfactants, a more hydrophobic membrane would form if the hydrophobic tails of surfactants are directed towards the aqueous solution, giving rise to more adsorption and hence to more membrane fouling. For ionic surfactants, not only the hydrophobicity but also the charge of the membrane and of the surfactant is important to explain the adsorbed amount and membrane fouling [112]. Particularly, the characterization of membranes to determine the membrane-foulant interactions involved in a specific system has been studied mainly by contact angle and zeta potential measurements [74], [76], [81], [82], [111], [151], [153], [164], [193], [194], [195], [196], [197], [198].

Membrane filtration of surfactant solutions has been studied mainly in the case of ultrafiltration [9], [100], [141], [145], [146], [152], [153], [154], [155], [156], [157]. Studies on the influence of surfactants upon reverse osmosis are rather limited in the literature [148], [149], [166], [167], [168], [169], [170], [171]. The main results were summed up in chapter 1 section 1.3.6. The fundamental mechanisms controlling the fouling of RO membranes are complex and not well understood, especially for surfactant solutions which show more specific characteristics (i.e. micelle formation) than other organic pollutants [170]. Thus a systematic and thorough study on fouling of RO membranes by surfactant solution is required. The focus of this study is to elucidate how membrane performances (e.g. flux, permeability) and surface characteristics (e.g. hydrophobicity/hydrophilicity) are affected during surfactant filtration. An anionic surfactant, sodium dodecyl sulfate, was selected for the experiments. First, a series of batch experiments were performed to evaluate membrane performances and to determine the adsorption isotherms of surfactants onto the membrane surface. Then the measurement of contact angles was carried out by sessile drop method to compare membrane surface properties before and after the filtration of surfactant solution. Finally a proposed mechanism is developed to relate the adsorption of surfactants, the membrane performances and the modification in membrane properties.

2.2 Materials and methods

2.2.1 Surfactant solutions

An anionic surfactant, sodium dodecyl sulfate (SDS), with purity $\geq 99.0\%$ and solubility of 250 g L^{-1} in water at $20 \text{ }^\circ\text{C}$, was purchased from Sigma-Aldrich and was used as received. The SDS (molar mass = $288.38 \text{ g mol}^{-1}$) is used as a model surfactant due to its commercial availability as well as its important role in commercial detergents. Solutions were prepared using distilled water and homogenized by gentle magnetic agitation for 30 min. The reported value of CMC (critical micelle concentration) in pure water lies in the range of 8.0 to 8.4 mmol L^{-1} at $25 \text{ }^\circ\text{C}$ [199], and the aggregation number at this concentration ranges from 54 to 64 [199].

The CMC of SDS was determined in the laboratory at $25 \text{ }^\circ\text{C}$ by measuring the conductivity values and absorbance of SDS solutions at various concentrations. Both methods revealed a CMC value of 8.2 mmol L^{-1} , which agrees well with literature.

2.2.2 RO membranes

Thin film composite polyamide SG reverse osmosis membranes (GE Water & Process Technologies, USA) were chosen for the tests. Typical thin film composite RO membranes are composed of three layers: a top dense polyamide layer responsible for selectivity, a microporous polysulfone layer, and a non-woven fabric layer as support [142]. Akin et al. provided detailed information on SG membrane [61]. They found that the SG membrane's top active layer was about 100 - 150 nm , lying on a polysulfone support with a thickness of $60 \text{ }\mu\text{m}$. The suggested chemistry of SG membrane is shown in Figure 2 - 1. The membrane has been reported to be negatively charged in contact with solution chemistries typical to wastewater effluents, with an isoelectric point lower than $\text{pH} = 4$ (see Figure 2 - 4) [142].

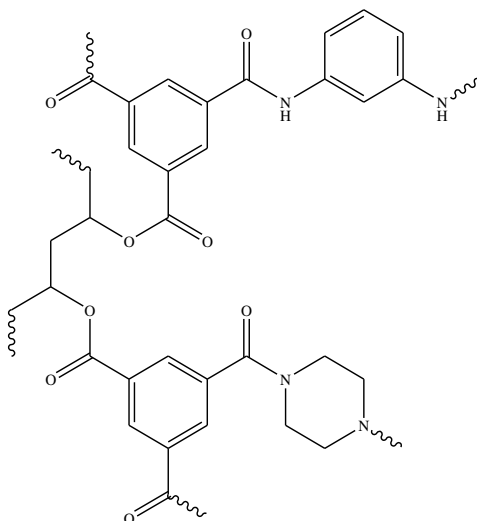


Figure 2 - 1: Suggested chemistry of the top polyamide layer of SG membrane: polyesteramide [61]

The SG membrane element is characterized by high sodium chloride rejection (average NaCl rejection 98.5%, minimum NaCl rejection 97% after 24 hours operation) and a smooth, fouling-resistant membrane surface (see chapter 1, Figure 1 - 11). The operating and Clean-In-Place (CIP) parameters of SG membranes are summarized in Table 2 - 1.

Table 2 - 1: Operating and CIP parameters of SG membranes*

Typical operating flux	8-34 L h ⁻¹
Maximum operating pressure	41.37 bars if T < 35 °C 30.00 bars if T > 35 °C
Maximum temperature	Continuous operation: 50 °C Clean-In-Place (CIP): 50 °C
pH range	Optinuous rejection: 5.5 – 7.0 Continuous operation: 2.0 – 10.0 Clean-In-Place (CIP): 1.0 – 10.5
Maximum pressure drop	Over an element 1.03 bars per housing: 4.14 bars
Chlorine tolerance	500+ ppm hours, Dechlorination recommended

*Resources from GE Water & Process Technologies.

2.2.3 Analytical methods

A reversed phase high performance liquid chromatography (HPLC) method using evaporative light scattering detector (ELSD, Chromachem, Eurosep Instrument) was used for the detection and quantification of SDS. HPLC measurements were performed with an analytical system composed of a Hitachi L – 2130 gradient pump (Eurosep Instruments), a Rheodyne valve with a 40 μL injection loop, an Eclipse Zorbax XDB-C8 analytical column (Agilent Technologies, 4.6 mm diameter, 150 mm length, 5 μm particle size), a column oven at 35 $^{\circ}\text{C}$. The mobile phase with methanol: water 70:30 (v : v) was fixed at a isocratic flow rate of 1.0 mL min^{-1} . The parameters of the ELSD detector were as follows: attenuation was 2; nitrogen pressure was 1.5 bar; nebulization and evaporation temperatures were 50 and 70 $^{\circ}\text{C}$, respectively; data acquisition and processing was done with Azur[®] software.

Simultaneous resolution of the anionic surfactants could be detected with a detection limit of 1.4 mg L^{-1} . The calibration curve was established from 5 mg L^{-1} to 500 mg L^{-1} , and the error was below 5%. Every sample was injected three times and the out of range concentrated samples were diluted with milliQ water (Millipore, Billerica, MA, USA) (conductivity 18.2 $\text{M}\Omega\cdot\text{cm}$ at 25 $^{\circ}\text{C}$, and TOC total organic carbon < 3 ppm). For the samples of permeate solution at very low concentration (< 2 mg L^{-1}), a concentration method was set up. It consisted of an evaporation step to reduce the volume of water and then a step of surfactants redissolution by a 70% methanol recovery solution containing 30 mg L^{-1} of NaCl. Accurate volumes near 50 mL of permeate solutions were evaporated to dry at 100 $^{\circ}\text{C}$ in glass vials. After cooling at room temperature 2.5 mL of recovery solution were added to the vials before vortex agitation for sample homogenization [13].

2.2.4 Filtration set-up and reverse osmosis of surfactant solutions

The proneness of the RO membranes to fouling and the variations of transport properties were investigated in a laboratory set-up of SEPA CF II Membrane Element Cell from Osmonics, which is a stainless steel unit (see Figure 2 - 2). A single piece of precut flat sheet membrane with an effective area of 140 cm^2 (19.1 \times 14.0 cm) was accommodated in the cell body bottom on top of the feed spacer and shim.

The feed stream was pumped by a high pressure pump from the feed vessel to the feed inlet which was located on the cell body bottom. The solution flew tangentially along the

membrane surface and was laminar or turbulent depending on the shim, feed spacer, fluid viscosity, and fluid velocity. The solution permeate flow across the membrane and through the permeate carrier and the permeate outlet. The retentate stream flow along the membrane and through the concentrate flow control valve and then back into the feed vessel.

In order to maintain similar conditions of the feed solution throughout the experiment, the permeate and the retentate were re-circulated to the feed vessel. Two manually controlled valves were placed to the inlet and the outlet of filtration cell to create a constant transmembrane pressure of 30 bars and a constant flow. The superficial velocity was set at 0.5 m s^{-1} , corresponding to an average circulation flow along the membrane of approximately 135 L h^{-1} (the width and height of the flow channel are 9.5 cm and 0.7874 mm, respectively). The liquid temperature within the feed vessel was maintained at 25°C by an external thermocryostat throughout the experiments.

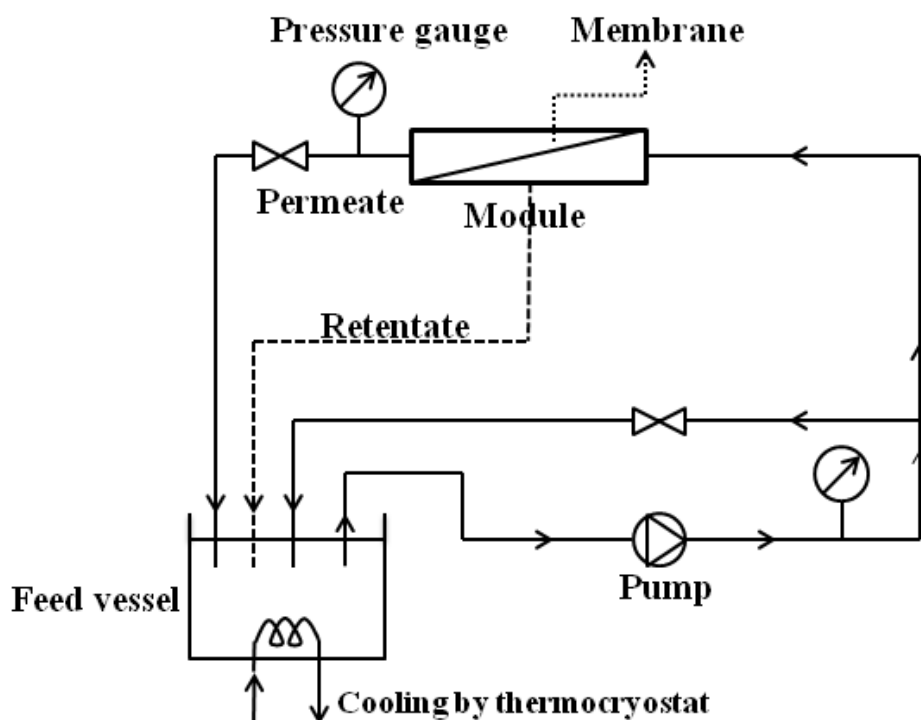


Figure 2 - 2: Schematic representation of the SEPA CF II Membrane Element Cell

Every experimental trial was carried out with a new membrane. Before the filtration of surfactant solutions in each experiment, membranes were washed with distilled water for 20 min, followed by an alkaline solution (NaOH, pH = 10 – 10.5) for 30 min, and then with distilled water again until the pH returned neutral.

A trial is mainly comprised of two stages: measurement of the permeability of pure water, then reverse osmosis of the SDS solution. A beaker of 5 L in volume was filled with 4 L of SDS solutions at various initial concentrations (pH = 6.0 ± 0.1), from 0.1 CMC (i.e. 0.8 mmol L⁻¹), 0.2 CMC, 0.5 CMC, CMC, 2 CMC, 3.75 CMC, 5 CMC, to 10 CMC (i.e. 80.0 mmol L⁻¹). Samples of permeate, retentate and feed solution were taken at 0, 0.5h, 1h, 2h, 3h, 4h, 5h for the analysis of surfactant concentrations. The permeate flux was simultaneously calculated when samples were collected. It has been observed that for most filtrations, the flux kept relatively constant after 4 h.

After the filtration of surfactant solutions, the membranes were removed from the filtration set-up, gently rinsed for 20 s with distilled water and then dried in a ventilated oven at 40 °C, and finally stored in a desiccator for the contact angle measurements.

The surfactant separation is evaluated in terms of surfactant rejection, R , which is determined using the following equation:

$$R = 1 - \frac{C_P}{C_F} \quad (\text{Equation 2 - 1})$$

where C_P is the surfactant concentration of permeates (mol L⁻¹), and C_F the surfactant concentration of feed solution (mol L⁻¹).

The water flow through the membrane is reported in terms of water flux, J_w (L · h⁻¹ · m⁻²) where

$$J_w = \frac{\text{volumetric permeation rate}}{\text{membrane area}} \quad (\text{Equation 2 - 2})$$

Solution permeate flux (J_s) is sometimes normalized relative to pure water flux (J_{w0}) as relative flux $\frac{J_s}{J_{w0}}$ or as flux decline:

$$\text{Flux Decline} = 1 - \frac{J_s}{J_{w0}} \quad (\text{Equation 2 - 3})$$

The permeability (L · h⁻¹ · m⁻² · bar⁻¹) is calculated as follows:

$$\text{Permeability} = \frac{J}{\Delta P} \quad (\text{Equation 2 - 4})$$

where J is the flux of permeate (L · h⁻¹ · m⁻²); ΔP is the transmembrane pressure applied on the membrane surface (here, it is 30 bars for every experiments)

The amount of surfactant retained during the experiment was estimated using a mass balance equation throughout the experiments. The mass loss of surfactant during filtration per membrane surface (q_f in mmol m^{-2}) was calculated by:

$$q_f = \frac{C_0 V_0 - C_t (V_0 + V_{\text{Hold}} - V_{\text{out}}) - m_{\text{out}}}{M_{\text{SDS}} \times A} \quad (\text{Equation 2 - 5})$$

where C_0 (mg L^{-1}) and V_0 (L) are the initial concentration and volume of surfactant solution, respectively; C_t is the retentate concentration (mg L^{-1}) when samples are taken at each time interval; V_{Hold} is the hold-up volume of the system, estimated as 175 mL; V_{out} (L) and m_{out} (g) are the total volume of samples and the total mass of SDS that had been taken out as samples for quantification analysis (including permeate, concentrate and feed solution samples); M_{SDS} ($= 288.38 \text{ g mol}^{-1}$) is the molar mass of SDS molecules and A (m^2) is the surface area of the membrane. It is worth to note that there is a small quantity of surfactant left in the tubing of permeate, but the volume is very small (only 3.27×10^{-3} L), so the mass in this part is negligible.

2.2.5 Adsorption in reverse osmosis set-up without pressure

The behavior of surfactants on the membrane in the pressure-driven RO system might be quite different from that in the circulation system without pressure. To investigate the effect of pressure on the fouling of RO membranes, the same filtration set-up was used to measure the adsorption of surfactants on the SG membrane surface without pressure. Only one test was conducted at initial concentration of 0.1 CMC (0.8 mmol L^{-1}). The pretreatment and the sample collecting were the same as those in the filtration experiments under pressure (see section 2.2.4). Since there was no pressure in the system, the permeate flux of water through membrane was negligible. Thus the permeability, the permeate concentration and the retention of the surfactants were not calculated; only the quantity of surfactant adsorption was analyzed in this experiment.

2.2.6 Static adsorption of surfactants onto SG membranes

In order to characterize the maximum quantity of surfactants which can adsorb onto the whole membrane (active layer and porous support media) without pressure and flow, we have undertaken a series of experiments of static adsorption.

Prior to the adsorption test, membrane samples were cut into pieces with a nominal membrane area of 9.0 cm² from flat sheets. The small membrane pieces were submerged in Milli-Q water for 24 h and then dried at 40 °C for 1 day in a ventilated oven until constant weight was achieved.

Static adsorption experiments were carried out in ten sealed erlenmeyer flasks, which were mechanically shaken at 180 rpm in a water bath at 25 °C. The dried membranes were placed in the flask with 20 mL of the surfactant solution. After the membrane had been in contact with the solution at the studied concentration for the required time (0.5, 1, 2, 3, 4, 5, 6, 8, 12, 24h), the membrane was removed. A sample of the liquid left in the flask was analyzed by HPLC in order to determine the concentration after surfactant adsorption. For each surfactant solution at different initial concentrations (from 0.1 CMC to 10 CMC), the average of three replicates was used for the calculation of adsorption quantity.

The amount of surfactant adsorbed onto the membrane (q_s in mmol m⁻²) was estimated as following:

$$q_s = \frac{(C_{s0} - C_{st}) \times V_{s0}}{M_{SDS} \times A_m} \quad (\text{Equation 2 - 6})$$

where C_{s0} (mg L⁻¹) and V_{s0} (L) are the initial concentration and volume of the surfactant solution in the flask, respectively; C_{st} (mg L⁻¹) is the liquid concentration when the membrane is taken out of the flask; M_{SDS} (= 288.38 g mol⁻¹) is the molar mass of SDS molecules and A_m (m²) is the surface area of membrane samples.

2.2.7 Contact angle measurements

The polar/apolar balance of both the virgin and the fouled membranes can be characterized from contact angle measurements. The contact angle (θ) between a dried surface and a liquid is commonly measured at room temperature by the sessile drop technique. In this work, the method of sessile drop measurement was based on the one developed by Rabilley-baudry et al. [85].

Prior contact angle measurement, the fouled membranes were removed from the module and rinsed gently with distilled water after the filtration of SDS solutions. The virgin membranes samples were pretreated by distilled water and NaOH solution then cleaned by distilled water in the filtration system. So the only difference between virgin and fouled

membrane is the process of SDS filtration. Membranes samples (either fouled membranes or clean membranes) are carefully dried in a ventilated oven at 40 °C for 48 h followed by a minimum of 24 h in a desiccator to avoid water re-adsorption [85]. Notice that 40 °C is lower than the value of maximum temperature (50 °C, provided by the supplier of the membrane) under continuous operation or during CIP process for SG membranes, thus these membranes could be considered as stable during this thermal treatment.

The contact angles of the thin-film RO membranes were measured on TRACKER contact angle instrument (France) in sessile drop mode. The equipment is composed of three main parts: an electronic cabinet and a measurement unit connected with a computer for analysis. This method allows the deposition of a droplet of liquid with a controlled volume (approximately 2.5 µL) on the RO membrane surface stuck on a glass slide. Immediately after the droplet was delivered onto the membrane surface, a static side-view image of the droplet on the membrane surface was captured with a frequency of 80 ms by a video acquisition system equipped with TRACKER.

Image analysis and contact angle computation were performed using Windrop analysis software assuming a circular profile of the droplet. For ensuring the accuracy, each measured contact angle is the average of at least 12 measurements at different locations, and then the average value was regarded as the final contact-angle result. With this well-controlled sample preparation the accuracy on contact angle is $\pm 3^\circ$.

On a theoretical point of view, θ depends on the thermodynamic characteristics of both the surface and the liquid. The relationship between the different parameters is given by the Young–Dupré–van Oss equation as mentioned in section [7], [200]:

$$(1 + \cos \theta) \gamma_{lv} = 2 \left[(\gamma_{sv}^{LW} \times \gamma_{lv}^{LW})^{\frac{1}{2}} + (\gamma_{sv}^A \times \gamma_{lv}^B)^{\frac{1}{2}} + (\gamma_{sv}^B \times \gamma_{lv}^A)^{\frac{1}{2}} \right] \quad (\text{Equation 2 - 7})$$

with:

θ : contact angle with the liquid.

S is the subscript for the dried membrane surface, v or s the subscript for gas or the chosen liquid, respectively.

γ_{lv} and γ_{sv} (in J m^{-2}) are the overall surface tensions of the liquid and the membrane surface, respectively. Each of these overall values can be decomposed in different contributions, namely the apolar (γ_{lv}^{LW}) and polar (γ^A : Lewis acid, γ^B : Lewis base) ones.

Knowing γ_{lv} , γ_{lv}^{LW} , γ_{lv}^A and γ_{lv}^B of three different solvents (that can be found in literature) and the three contact angles measured with this solvent triplet on a given membrane, the values of γ_s , γ_s^{LW} , γ_s^A and γ_s^B can be calculated with accuracy better than 10%. The three solvents used in this study are water, formamide and di-iodomethane. Their characteristics are given in Table 2 - 2.

Table 2 - 2: Surface tensions (mJ m^{-2}) of liquids according to Van Oss [7]

solvent	γ_{lv}	γ_{lv}^{LW}	γ_{lv}^A	γ_{lv}^B
Water	72.8	21.8	25.5	25.5
Formamide	58.0	39.0	2.3	39.6
Di-iodomethane	50.8	50.8	0.0	0.0

2.3 Results

The output data from this series of experiments are mainly: membrane performance, mass loss of surfactants during RO process under pressure, mass loss of surfactants in the RO system without pressure, static adsorption and contact angle measurements. According to these results, fouling mechanisms and structure of fouling are proposed.

First, we examined the effect of SDS concentration on permeate flux and rejection. Then we related the quantity of surfactant adsorption to the flux decline. Finally we measured the change of membrane surface hydrophobicity, in order to determine the effect of surfactant adsorption on the membrane surface and its performance during filtration.

2.3.1 Membrane performance

2.3.1.1 SDS rejection

The effect of the SDS concentration on the surfactant rejection and permeate flux after at least 4 hours' filtration is shown in Table 2 - 3. The surfactant rejection was observed to be higher than 99.9% in nearly all the experiments over a wide range of feed concentrations. The rejection was so large that no significant difference was observed between the solutions below

and above CMC. The high rejection of anionic surfactant was also found in a previous research [144], [166].

There have been two rejection mechanisms in previous studies for organic molecules by RO membranes: electrostatic repulsion and size exclusion [142]. Electrostatic repulsion between the negatively charged SDS molecules and the negatively charged membrane could be correlated with high rejection by SG membrane. Rejection by size exclusion was previously reported for rejection of the natural hormone estrone (molar mass of 270 g mol⁻¹) and perfluorooctane sulfonate (PFOS, molar mass of 500 g mol⁻¹) [142]. This mechanism is reasonable because SDS monomers (molar mass of 288 g mol⁻¹) are relatively large and can hardly pass through the membrane. At concentrations above the CMC, surfactants form micelles in the solution. A SDS micelle is supposed to be composed of 54 – 64 monomers, making it even larger and thus easier to be rejected by the membrane.

Table 2 - 3: Retention and flux decline during RO membrane filtration, P = 30 bar, T=25°C. The CMC of SDS is 8.2 mmol L⁻¹.

Feed Concentration (mmol L ⁻¹)	Name of membrane sheet	Permeate concentration (mmol L ⁻¹)	Retention (%)	Water flux with pure water J ₀ (L·h ⁻¹ ·m ⁻²)	Water flux with SDS solution J _s (L·h ⁻¹ ·m ⁻²)	Flux decline (%)
0.8	A25	4.16 × 10 ⁻⁴	99.95%	84.92	55.48	34.67%
1.6	A24	8.67 × 10 ⁻⁴	99.94%	75.06	53.84	28.27%
4.0	A05	0.80 × 10 ⁻²	99.85%	84.12	60.76	27.77%
4.0	A11	2.39 × 10 ⁻³	99.95%	81.14	60.14	25.89%
8.0	A13	5.30 × 10 ⁻³	99.94%	94.90	70.52	25.69%
16.0	J02	8.28 × 10 ⁻³	99.94%	84.76	63.95	24.55%
16.0	A04	1.20 × 10 ⁻²	99.93%	84.85	67.31	20.66%
30.0	J01	-	- ^a	78.25	57.55	26.45%
40.0	A21	4.30 × 10 ⁻³	99.99%	80.08	60.97	23.87%
40.0	A22	5.13 × 10 ⁻³	99.99%	80.04	63.19	21.05%
80	A14	5.32 × 10 ⁻³	99.99%	84.98	67.86	20.14%
80.0	A15	5.97 × 10 ⁻³	99.99%	88.72	70.08	21.00%

^a the permeate concentration was not analyzed since this is an additional experiment for the adsorption isotherm.

However, a small percentage of SDS was analyzed in the permeate, as shown in Table 2 - 3, indicating that some SDS molecules were able to pass through the RO membrane. One possible explanation might be that SDS molecules could undergo chain folding, by which it can penetrate into the polyamide layer of the RO membrane, and subsequently diffuse through or adsorb in the large pores of the support layer, as proposed from a previous study for PFOS [142]. The penetration and diffusion inside the membrane will be further discussed in the section 2.3.2.

2.3.1.2 Permeate flux

The relative fluxes of the RO membrane processes for SDS solutions at concentrations ranging from 0.8 mM (0.1 CMC) to 80.0 mM (10 CMC) are plotted in Figure 2 - 3. Unexpectedly, the relative flux rises slightly with concentration at lower concentrations (below the CMC). At initial surfactant concentration of 0.8 mmol L⁻¹, the relative flux is 65.33%. The increase in the relative flux from 65.33% to 74.31% when the initial SDS concentration increases from 0.8 mmol L⁻¹ to 8.0 mmol L⁻¹ suggests that the membrane fouling is decreased. The results obtained in this study conflicted with the ones reported in the literature [112], which demonstrated that the relative flux decreased with increasing surfactant concentration. This result was attributed to the fact that the adsorption of surfactants on the fouled membrane surface probably enhanced the hydrophilicity of the RO membrane. The RO membrane became more permeable by reducing the availability of hydrophobic sites occupied by surfactant molecules [9]. While at higher concentrations above the CMC (8.0 mmol L⁻¹), the relative flux does not change significantly and stabilizes at a higher value around 79 %. A reasonable flux was still achievable at the highest SDS concentration of 80.0 mmol L⁻¹.

The flux decline is probably associated with the entrapment of SDS molecules in the polyamide layer and their accumulation on the membrane surfaces. As shown in Figure 2 - 4, the thin-film composite polyamide RO membrane (FT-30) has a slight negative charge at pH \approx 6 [170], [198]. For a polymeric membrane surface, surfactant molecules were adsorbed even when the surface and the surfactant had the same charge [146], [154].

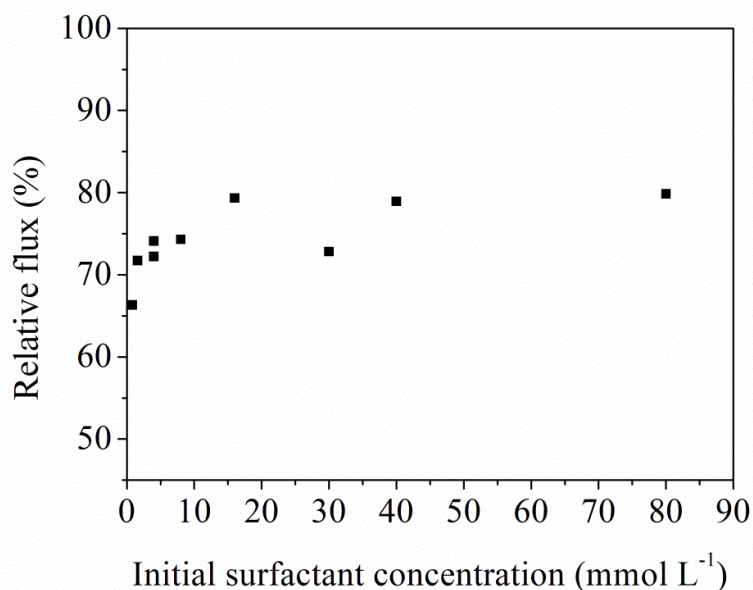


Figure 2 - 3: Influence of the initial surfactant concentration on the relative flux of the RO membrane. $\Delta P = 30$ bar, $T=25^{\circ}\text{C}$. The CMC of SDS is 8.2 mmol L^{-1} .

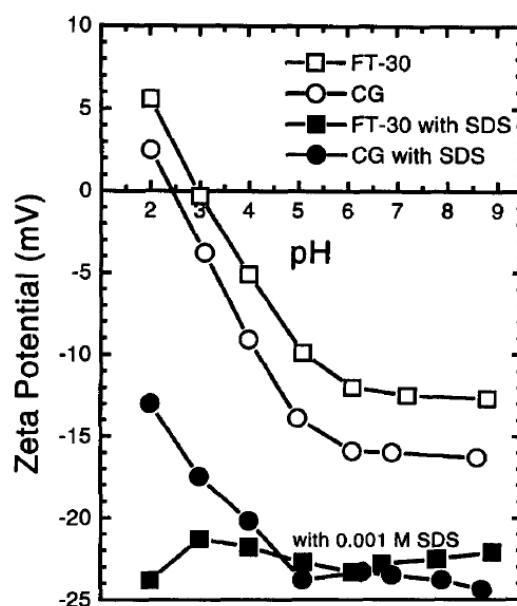


Figure 2 - 4: Zeta potentials ζ of a thin-film composite polyamide (FT-30) and an asymmetric cellulose acetate (CG) RO membrane in the presence and absence of SDS [198].

When the concentration is below the CMC, the increase in the relative flux could probably be explained by the change of hydrophilicity due to surfactant adsorption. According to the literature, at low adsorption density, the adsorbed surfactant monomers lie parallel to the membrane surface, making the membrane surface more hydrophobic and thus less permeable

for water. With concentration increase, the adsorption of surfactant molecules on the membrane surface could cause the formation of more compact structures (hemicylinder, monomolecular layer, or Langmuir-Blodgett film [146], [201]). The surfactant anions adsorb onto the membrane in a mode that the hydrophobic part of the surfactant is adsorbed onto the membrane surface through hydrophobic interaction and the hydrophilic head group orients itself towards the aqueous solution through electrostatic repulsion with membrane surface and hydrophilic interaction with water. This orientation could probably increase the hydrophilicity of the fouled SG membrane. The hydrophilicity increase was verified by contact angle measurements which will be discussed in the section 2.3.3.

Another reason for this phenomenon could be explained by the reduction of concentration polarization by enhanced diffusion of surfactant micelles due to high shear rates. At a concentration below 0.5 CMC (4.0 mmol L^{-1}), there is no micelles in the aqueous solution, so the number of micelles near the membrane surface should be very small, and a compact coverage on membrane by surfactant monomers may occur. Then micelles form as the concentration rises to the CMC. Also the electrostatic repulsion between negatively charged SDS micelles helps to produce a less compact concentration polarization layer. Therefore the relative flux increases with increasing feed concentration below the CMC. But at concentrations higher than the CMC, a compact structure is already formed on the membrane surface and no additional surfactant molecules could be adsorbed onto the saturated membrane due to electrostatic repulsion, so the flux decline is not significantly affected by increasing the surfactant concentration.

As discussed above, during all the filtrations at different surfactant concentrations, the membrane did not experience severe flux decline, with a ratio of 20 – 35 %. The flux decline caused by the surfactant solution seemed to occur in the first several minutes, and then no significant flux reduction was observed thereafter.

If we take a closer look at the permeability during the filtration at concentrations below and above the CMC, a slight difference could be observed. Figure 2 - 5 illustrates the time evolution of permeability for SDS solutions at 0.2 CMC (1.6 mmol L^{-1}) and 5 CMC (40.0 mmol L^{-1}), respectively. It is clear that the flux permeability decreased rapidly at the beginning of the filtration for both concentrations. The reason for the sharp decrease is most likely due to the interaction between polyamide material on the membrane surface and the hydrophobic part of the surfactant molecules, leading to surfactant adsorption on the dense

membrane surface, as discussed above. Another reason for the flux decrease is concentration polarization of the surfactant solutions upon coming into contact with the polyamide membrane.

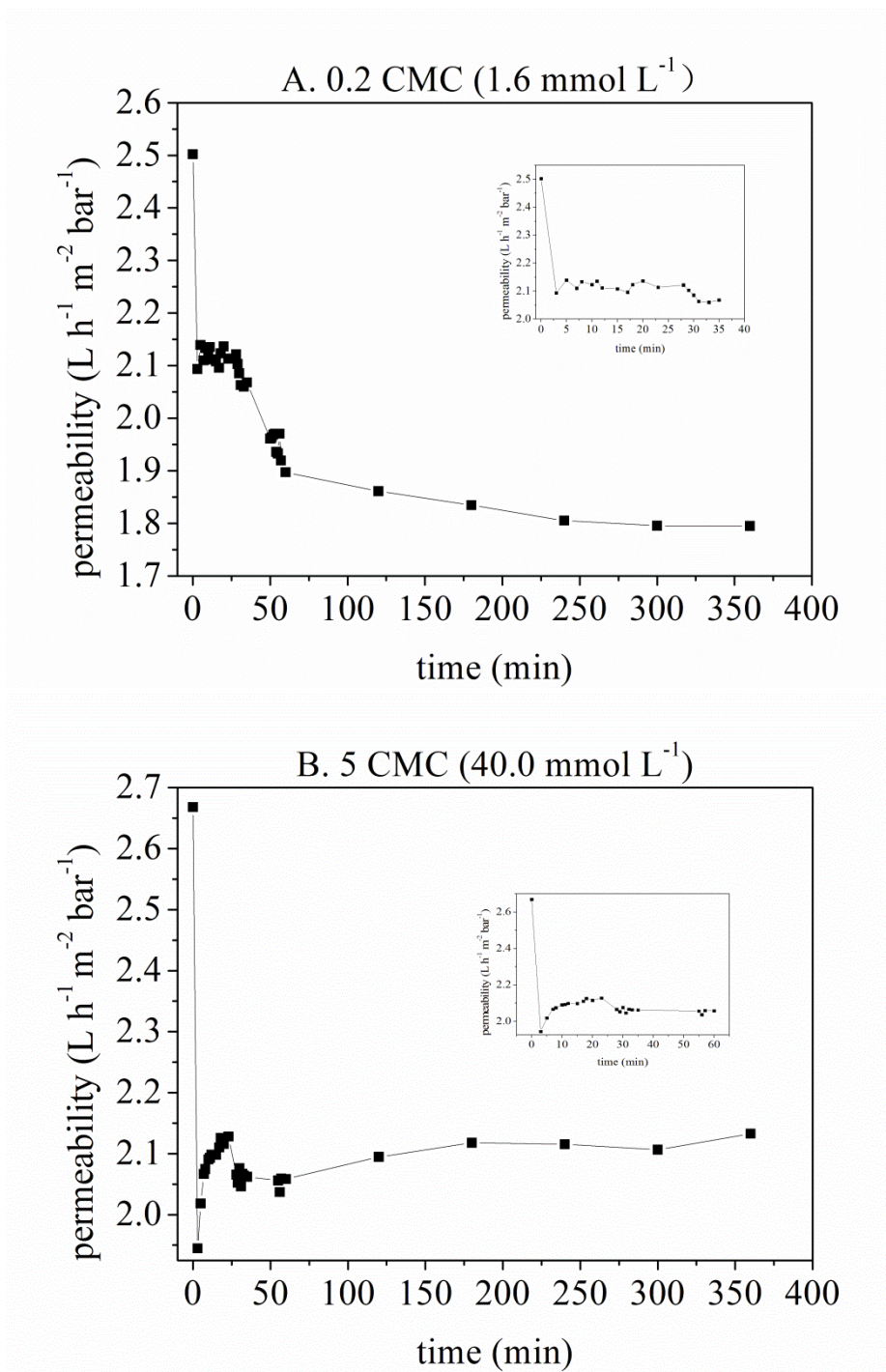


Figure 2 - 5: Time evolution of permeate flux of SDS solutions (J_s) in fouling tests with SG membrane at two different surfactant concentrations: (A) 0.2 CMC; (B) 5 CMC. Experiments were carried out at $\text{pH} = 6.0 \pm 0.1$ under pressure of 30 bar.

For the 0.2 CMC (1.6 mmol L^{-1}) solution as illustrated in Figure 2 - 5 (A), the surfactant solution with foam equilibrated for about 30 min. During this period, the permeability kept roughly constant at $2.1 \text{ L}^{-1} \text{ h}^{-1} \text{ m}^{-2} \text{ bar}^{-1}$. Then it decreased again in the next 30 minutes to below $1.9 \text{ L}^{-1} \text{ h}^{-1} \text{ m}^{-2} \text{ bar}^{-1}$ and slowed down gradually until the end of the filtration at 6h.

Different behaviors were observed for surfactant solutions with concentrations above the CMC. As illustrated in Figure 2 - 5 (B), a sharp decrease in the initial flux of the SG membrane was observed as soon as the membrane came into contact with the surfactant solution at a very high concentration 40.0 mmol L^{-1} , followed, however, by no substantial additional flux decrease but an increase in the first 25 minutes. The change in the permeability was accompanied by the stabilization of foam produced by the surfactant solution under pressure from the pump. Then the flux decreased a little in the next 30 minutes. After that, very little flux variation with time was observed [152]. These phenomena may be representative of the kinetics of the surfactant organization on the membrane surface.

2.3.2 Surfactant adsorption

2.3.2.1 Adsorption during filtration process

The surfactant adsorption on the membranes during the filtration depends on the chemical composition and structure of both the surfactant and the membrane [153]. The interactions responsible for surfactant adsorption onto solid substrates include the contributions of various mechanisms, e.g., polar interactions (electrostatic repulsion between negatively charged membrane surface and surfactant head group, Lewis acid-basic interactions, hydrogen bonding), Lifshitz-Van der Waals forces, hydrophobic interactions between hydrocarbon chains of the surfactant and hydrophobic sites on the membrane, and hydrophobic lateral interactions between surfactant chains. The relative balance of those interactions determines the mode of surfactant adsorption. According to the surfactant structure in this work, electrostatic repulsion and hydrophobic interactions should dominate, so the adsorption of the anionic surfactants may occur in a manner that the hydrophobic group is towards the solid membrane surface and the hydrophilic head group is oriented towards the aqueous phase.

However, in this work, the adsorption in the filtration mode is more complicated than the static adsorption due to the tangential flow and the high pressure applied on the membrane surface, which could affect the adsorption and subsequent fouling.

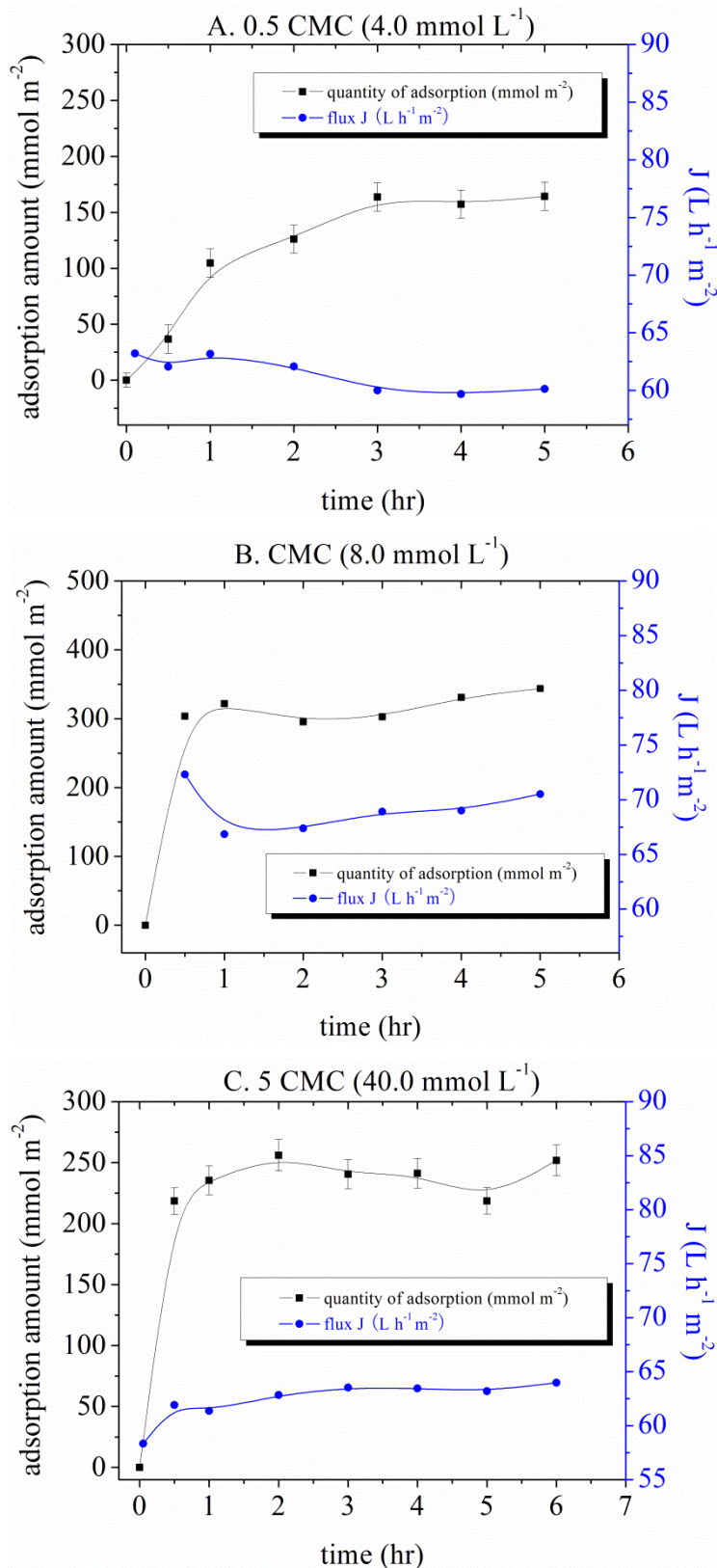


Figure 2 - 6: Flux ($\text{L h}^{-1} \text{m}^{-2}$) and accumulated amount as a function of time during fouling with the RO membrane. The concentrations of SDS are: (A) 4.0 mM; (B) 8.0 mM; and (C) 40.0 mM, respectively. Solution pH = 6.0 ± 0.1 , operating temperature = 25°C , and applied pressure = 30 bar.

The time evolutions of accumulated amount of surfactants on the membrane surface from aqueous solutions with different concentrations (below, equivalent and above CMC) is shown in Figure 2 - 6 and Table 2 - 4, together with the corresponding permeate fluxes for each concentration. In general, the adsorption amount showed a quick increase at the beginning and then reached a plateau regime [139]. The total equilibrium time is approximately 3-4 h and at least 50% adsorption was complete within one hour. The plateau value indicates the maximum amount adsorbed onto the membrane at equilibrium, which can be used to determine the adsorption isotherm.

Table 2 - 4: The time evolution of permeate flux and adsorption amount for different surfactant solutions during RO filtration (corresponding to Figure 2 - 6).

Time (hr)	0.5 CMC		CMC		5 CMC	
	Flux (Lh ⁻¹ m ⁻²)	Adsorption amount (mmol L ⁻¹)	Flux (Lh ⁻¹ m ⁻²)	Adsorption amount (mmol L ⁻¹)	Flux (Lh ⁻¹ m ⁻²)	Adsorption amount (mmol L ⁻¹)
Pure water	81.14		94.90		80.04	
0.00	63.20	0.00	-	0.00	58.34	0.00
0.50	62.06	36.72	72.31	303.64	61.93	218.50
1.00	63.17	104.65	66.85	321.90	61.36	235.46
2.00	62.08	126.13	67.38	295.45	62.84	256.01
3.00	60.00	163.68	68.90	302.58	63.53	240.45
4.00	59.68	157.22	69.00	330.97	63.46	241.12
5.00	60.14	164.30	70.52	343.81	63.19	218.65
6.00	-	-	-	-	63.98	251.87

Adsorption isotherm

Adsorption isotherms are mathematical models that describe the distribution of the adsorbate species between liquid and solid phases, based on a set of assumptions that are related to the heterogeneity/homogeneity of the solid surface, the type of coverage, and the possible interactions between the adsorbate species or between the adsorbate and surface [139]. There are three typical models in literature to investigate the adsorption isotherm: the linear, Langmuir, and Freundlich models (see Chapter 1 Section 1.3.4.2). But due to the specific characteristics of surfactants (i.e. aggregation into micelles), their adsorption behaviors are quite different from that of other organic components. According to the literature, the most acceptable model for surfactant adsorption onto solid surfaces is described as an S shape model.

In general, a typical isotherm can be subdivided into four regions when plotted on a log – log scale [202], as described in Figure 1 - 15 (Chapter 1, section 1.3.4.2). In region I, the adsorption obeys Henry's law and increases linearly with concentration. This region usually occurs at low concentrations, where monomers are adsorbed to the substrate continuously. Region II shows a sudden increase in adsorption due to surface aggregation of the surfactants, caused by lateral interaction between the adsorbed monomers, while III shows a slower rate of adsorption than region II. Region IV is the plateau region above the CMC. In some cases, the region IV may show a maximum [134], [135], [136].

The equilibrium adsorbed amount of surfactants on the polyamide RO membrane in the filtration mode, together with the flux decline, is plotted against the equilibrium surfactant concentration in aqueous solutions (as presented in Figure 2 - 7). The results showed that SDS adsorption on the RO membrane at 30 bar occurred in three steps. First, a rapid increase from 0.8 mmol L^{-1} (0.1 CMC) was observed in adsorption amount to a plateau at around 8.0 mmol L^{-1} (CMC) of SDS concentration in aqueous phase. Then at 40.0 mmol L^{-1} (5 CMC), another increase was observed in the adsorbed amount of SDS to a value close to 530 mmol m^{-2} at 80.0 mmol L^{-1} (10 CMC).

To be comparable to literature, the log-log scale of the isotherm is plotted in Figure 2 - 8. The isotherm obtained in our experiments is similar to the S type isotherm presented in Figure 1 - 15, commonly observed in the adsorption of various surfactants to solid interfaces. Since there is no universal agreement on how the adsorption occurs to the solid surfaces, it has been speculated in our work that at low concentrations, the anionic surfactants interact with the negatively charged polyamide membrane surface mainly due to hydrophobic interaction. As surfactant concentration increased, hydrophobic attraction between surfactant monomers resulted in the formation of surface aggregates (monolayer, hemimicelle, micelle like structure, etc). The first increase in Figure 2 - 8 is explained by the continuous monomer adsorption at low concentrations until saturation of the surface by aggregates. When micelles occurred in the aqueous solution, the surface structure formed by adsorbed surfactants rearranged and achieved a new stable state, corresponding to the plateau region in Figure 2 - 8. The sudden increase of adsorption amount at 80.0 mmol L^{-1} might be related to more penetration of the adsorbed surfactants into internal structure of the membrane and/or a rearrangement of the adsorbed structure

At the same time, membrane fouling shows an opposite trend. At 0.8 mmol L^{-1} , the membrane fouling is most severe, with a flux decline of 35 %. The flux decline subsequently decreased with increasing equilibrium surfactant concentrations from 0.8 mmol L^{-1} to 8.0 mmol L^{-1} . The flux decline between a concentration of 16.0 mmol L^{-1} and 80.0 mmol L^{-1} keeps almost constant at around 20 %. Compared to the adsorption amount, it seems that more adsorption amount resulted in a less fouled membrane. The adsorption of SDS on the membrane reached a plateau at a concentration of the aqueous phase that corresponded to the plateau observed in the curve of permeate flux versus the equilibrium surfactant concentration in solution.

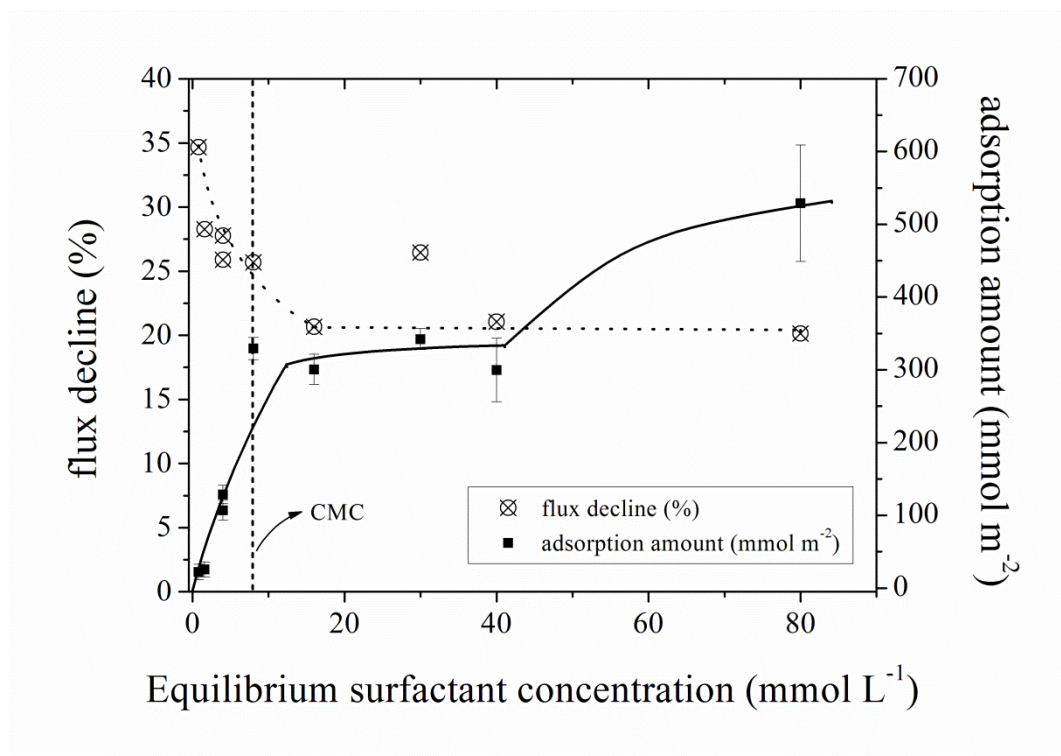


Figure 2 - 7: Flux decline and adsorption amount *versus* equilibrium SDS concentration in the system during RO filtration with a polyamide SG membrane at 30 bar.

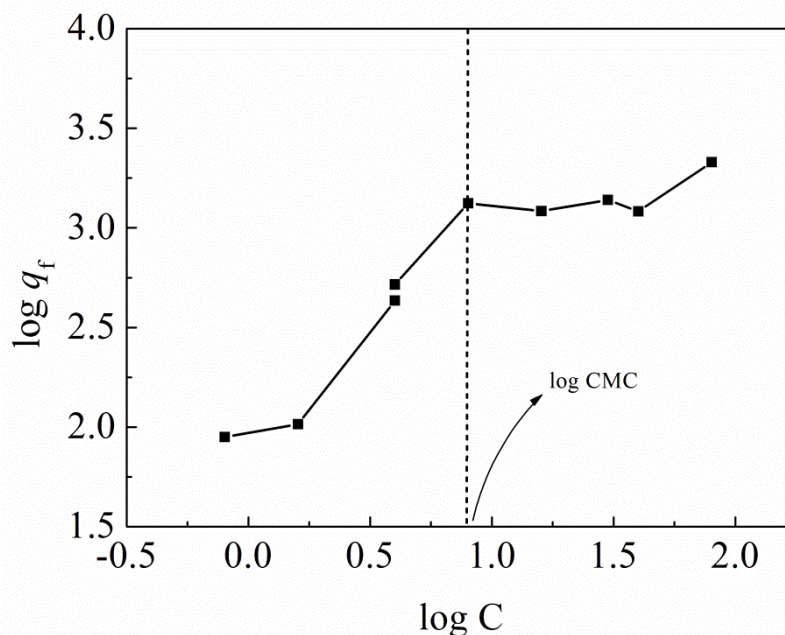


Figure 2 - 8: Equilibrium adsorption isotherm for SDS on RO membrane in filtration mode. C: the equilibrium surfactant concentration in the SDS solution; q_f : the adsorption amount of SDS on the RO membrane in filtration mode.

As indicated in (Equation 2 - 5), the adsorption amount in Figure 2 - 7 is estimated as the mass loss of surfactants in the filtration system based on the mass balance of the solutions' composition, with an assumption that the membrane was the only interface where significant adsorption took place.

The adsorption experimental values can be compared to theoretical values. The theoretical value of the adsorption amount in the case of a close-packed monolayer of SDS molecules can be estimated as follows: the cross sectional area of the SDS molecule at the air-water interface is reported to be 45 \AA^2 , and it will be smaller at liquid-solid interfaces [203], so the value at all interfaces would fall in the range of $10 - 45 \text{ \AA}^2$ (the sectional area of a water molecule is 9.66 \AA^2 at 25°C [204]). If the membrane surface (surface area = 0.014 m^2) is saturated by a close-packed monolayer of the SDS molecules with a cross sectional area between 10 and 45 \AA^2 , we would expect a surface excess of $3.69 - 17 \text{ \mu mol m}^{-2}$, 1300 - 6000 times lower than the lowest value ($22.07 \text{ mmol m}^{-2}$ at initial SDS concentration of 0.8 mmol L^{-1}) we have obtained from the adsorption during filtration. Similarly, large adsorption quantity of ionic surfactants on RO membrane surface in filtration mode has been observed by Hinke et al.[171]. They observed that the amount of anionic surfactant FT 248 adsorbed onto a CA-10

membrane was 1.59 mmol m^{-2} at 10 bar, and it increased to 6.68 mmol m^{-2} at 40 bar. Another group also found huge amount (77 mmol m^{-2}) of SDBS adsorbed on a NF membrane [112].

To explain this difference, the first hypothesis is that the calculated adsorption amount might be greater than the real value because a fraction of surfactants may adsorb not only on the membrane but also on the other parts of the system (becker, tubing, spacer etc.) First of all it is necessary to estimate this fraction.

With regard to the mechanisms at the membrane interface, possible explanations for this unexpected huge adsorption amount calculated from surfactant mass loss could be that: (1) large quantity of surfactants adsorption on the membrane really occurred. The high pressure accelerates the motion of surfactant molecules or even the micelles onto the membrane, forming much more complicated surface structures than hemimicelles, monolayer or multilayer due to concentration polarization, such as semicontinuous islands or high-density solid layer nucleates [205]; (2) according to the solution-diffusion mechanism for polymeric membranes, the surfactant molecules are likely to dissolve in the membrane surface and diffuse through the membrane matrix; (3) the SDS molecules which penetrate the membrane may stay in the internal structure of the support, in the polymer matrix or adsorbed at the pores surface. The penetration might be larger than the adsorption on the membrane, because the pressure is like a physical force, the influence of which could be several orders of magnitude higher than the chemical interactions between the surfactant molecules and the membrane.

To investigate the possibilities of these effects, we examined the results obtained from a series of static adsorption experiments and a test of adsorption in the recirculated filtration system without pressure at 0.8 mmol L^{-1} , because at this concentration, the adsorption amount has already been tremendous compared to literature values.

2.3.2.2 Adsorption in the filtration system

Apart from the RO membrane, there is several plastic tubing in the filtration system, which is also probably favorable to the attachment of surfactant molecules. Estimated interfaces in contact with the surfactant solution in the system are listed in Table 2 - 5, including: (1) the glass feed vessel; (2) the stainless steel pipes; and (3) the plastic (PVC, polyvinyl chloride) tubing for drawing the feed solution into the filtration system, flow back carrier, concentrate and permeate flow carriers, connection parts (e.g. feed to pump, feed inlet to membrane, feed

outlet to concentrate as well as to permeate). Here, the surfactant adsorption on stainless steel was negligible.

Table 2 - 5: System interface areas in contact with the surfactant solution*

	Diameter (m)	Width (m)	Length (m)	Area (m ²)	Static adsorption (mmol)	Adsorption for a monolayer ($A_{SDS} = 45$ \AA^2) (mmol)
Feed vessel (glass)	0.185	-	0.25	0.1722	0.0193	6.3545×10^{-4}
Connection pipe to pump	0.013	-	0.95	0.0388	0.0425	1.4318×10^{-4}
Pump-feed back	0.010	-	0.900	0.0283	0.0310	1.0443×10^{-4}
Feed spacer (with holes)	0.007	0.095	0.146	0.0071	0.0078	2.6200×10^{-5}
Retentate connection	0.013	-	0.150	0.0059	0.0065	2.1772×10^{-5}
Retentate outlet	0.007	-	1.450	0.0296	0.0324	1.0923×10^{-4}
Total				0.2819	0.1394	1.0742×10^{-3}

*Machine dimensions are cited from the manual operation guide for SEPA CF II membrane system.

In order to clarify the amount of SDS adsorption on other system interfaces presented in Table 2 - 5, a small piece of plastic tubing (see Figure 2 - 9) was cut from the filtration set-up system and then submerged into a SDS solution with a concentration of 0.8 mmol L^{-1} for 48 h. The inside and outside diameter of the tubing sample was 1.03 cm and 1.50 cm, respectively. The length of the tubing sample was 1.05 cm. The calculated total tubing surface area was 8.3456 cm^2 . From the decrease in initial SDS concentration after 48 h (from C_{t0} to C_{t48}), we can calculate the amount of adsorption of SDS per surface area of the tubing (q_{tub} in mmol m^{-2}), as expressed in (Equation 2 - 8).

$$q_{tub} = \frac{C_{t0} - C_{t48}}{M_{SDS} \times A_{tub}} \times V_{tub} \quad (\text{Equation 2 - 8})$$

where C_{t0} and C_{t48} (mg L^{-1}) are the SDS concentrations in the initial solution and after 48 h, respectively; V_{tub} (L) is the volume of the SDS solution in this experiment; M_{SDS} ($=288.38 \text{ g mol}^{-1}$) is the molar mass of SDS molecules and A_{tub} (m^2) is the surface area of the tubing sample.

The calculated static adsorption amount of SDS on the tubing sample was observed to be $1.095 \text{ mmol m}^{-2}$ in the SDS solution at initial concentration of 0.8 mmol L^{-1} . The adsorption amount per surface area of the glass vessel was obtained using the same method and the value was observed to be $0.112 \text{ mmol m}^{-2}$, much less than that of the plastic materials. The adsorption on all plastic materials and glass vessel in the system were calculated and presented in Table 2 - 5. It showed that the total adsorption onto these system materials accounted for 0.139 mmol representing about 45.12% of the surfactant mass loss at 0.8 mmol L^{-1} SDS solution (0.31 mmol) (Figure 2 - 7) The results suggested that the areas of these interfaces could not be negligible since they contributed to the large quantity of SDS adsorption. However it is not sufficient to explain the order of magnitude of adsorption on the membrane.

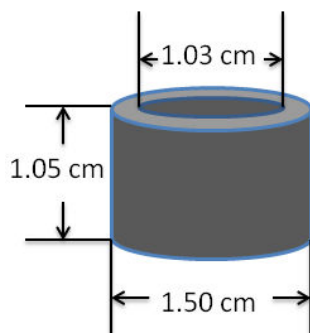


Figure 2 - 9: The plastic tubing cut from the filtration system.

2.3.2.3 Static adsorption

One of the hypothesis was that SDS penetrate into the membrane and adsorb in the whole material which would represent a larger interface. The objective of the next experiment was to estimate the quantity of SDS which can adsorb into the whole membrane (active layer and internal surface of porous support) without pressure.

2.3.2.3.1 Adsorption kinetics

The time-dependent static adsorption of SDS at 0.8 mmol L^{-1} onto the RO membrane is shown in Figure 2 - 10. During 24 h, the amount of SDS adsorbed on the membrane from aqueous solution increased rapidly in the first stage, reaching a value of 0.36 mmol m^{-2} up to 3 hours, and then slowed until a constant adsorption amount of 0.42 mmol m^{-2} was reached,

indicating that the membrane approached equilibrium with the SDS solution. For a low surfactant concentration at 0.8 mmol L^{-1} , the apparent adsorption amount per membrane surface area q_s ($\approx 0.42 \text{ mmol m}^{-2}$) is much lower than that in the filtration mode ($\approx 22.07 \text{ mmol m}^{-2}$).

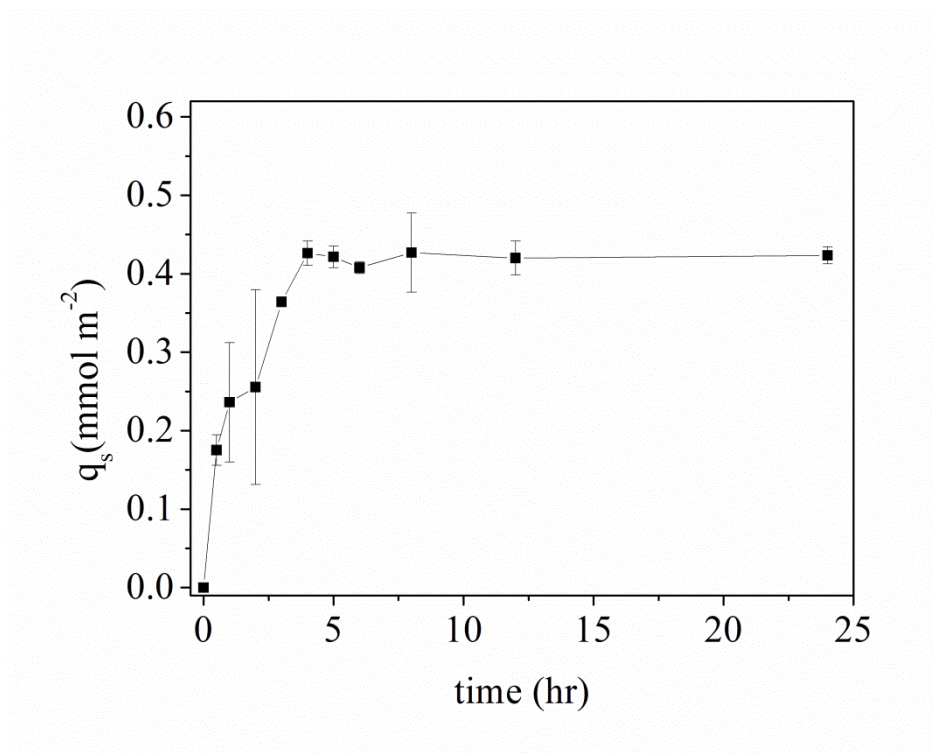


Figure 2 - 10: Kinetics of SDS adsorption on RO membrane. C_0 (initial bulk concentration) = 0.8 mmol L^{-1} ; $\text{pH} = 6.0 \pm 0.1$; adsorption carried out for 24 h; shaking speed = 180 rpm. q_s = adsorption amount per membrane surface area (mmol m^{-2}).

2.3.2.3.2 Adsorption isotherm

The plot of adsorption amount per membrane surface area against surfactant equilibrium concentration in the static adsorption experiments and a plot in log-log scale are given in Figure 2 - 11. The adsorption isotherm showed a sharp increase with concentrations lower than the CMC, then a plateau region above the CMC. The maximum adsorption was reached at approximately 0.71 mmol m^{-2} . The maximum adsorbed amount was approximately 3.25 % of what was observed for SDS in the dynamic filtration mode at the lowest surfactant concentration.

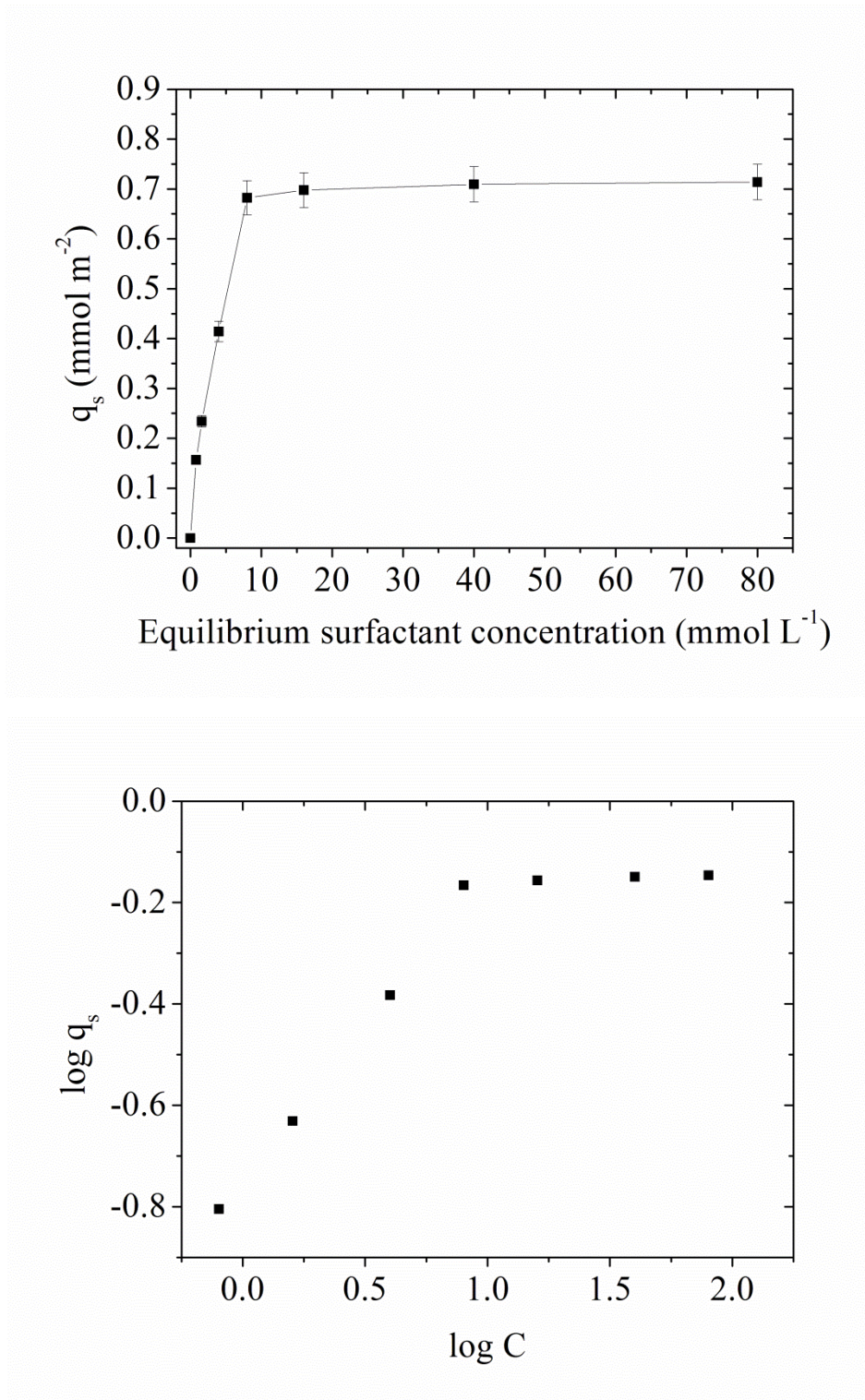


Figure 2 - 11: Adsorption isotherm of static adsorption on RO membrane. pH = 6.0 ± 0.1; adsorption carried out for 24 h; 180 rpm shaking speed. q_{ads} = amount adsorbed per membrane surface area (mmol m⁻²).

The whole available membrane surface in the static experiment was estimated according to the following hypothesis based on MEB analysis presented in Figure 1 - 5 [61]: the PA thin film, considered as layer (1) as presented in Figure 2 - 12, lies on a porous media constituted of two layers. The layer (2) has a thickness (e_2) of 40 μm , a porosity (ε_2) of 0.6 and contains cylindric pores with a diameter (dp_2) of 2 μm . The layer (3) has a thickness (e_3) of 150 μm , a porosity (ε_3) of 0.6 and contains cylindrical pores with a diameter (dp_3) of 10 μm .

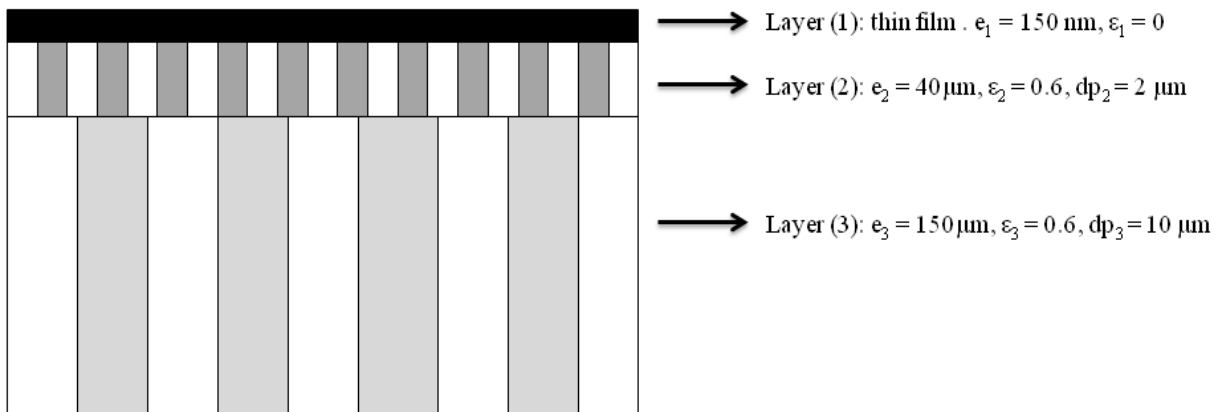


Figure 2 - 12: Hypothesis of RO membrane structure to estimate the whole membrane surface area.

In this system the whole area can be estimated through the following equations:

$$A_{tot} = A_1 + A_2 + A_3 \quad (\text{Equation 2 - 9})$$

where A_1 : the apparent area of the thin film ($9 \times 10^{-4} \text{ m}^2$);

A_2 : the internal area of layer 2;

A_3 : the internal area of layer 3.

$$A_2 = \text{number of pores 2} \times \text{area of each pore 2}$$

$$A_2 = \frac{A_1 \cdot \varepsilon_2}{\pi \cdot dp_2^2 / 4} \times \pi \cdot dp_2 \cdot e_2$$

$$A_2 = 4 \cdot A_1 \cdot \varepsilon_2 \cdot \frac{e_2}{dp_2} \quad (\text{Equation 2 - 10})$$

$$A_3 = 4 \cdot A_1 \cdot \varepsilon_3 \cdot \frac{e_3}{dp_3} \quad (\text{Equation 2 - 11})$$

The numerical application of (Equation 2 - 9 gives

$$A_{tot} = 0,0765 m^2$$

According to this calculation, the whole membrane area is 85 times larger than the apparent area.

The maximum surface concentration of the surfactant taking into account the whole area, in the static adsorption test, is equal to $8.35 \mu\text{mol m}^{-2}$. This result corresponds to the range of surface concentration in the case of a monolayer.

We can conclude from this experiment that if the surfactant manages to penetrate the PA thin film and adsorbs at the internal surface of the porous support, considering that the pressure on the permeate side is negligible, it may form a thin film like in static experiment and this would represent a maximum apparent adsorption of 0.71 mmol m^{-2} , 3.25% of the global adsorption.

This experiment took place without pressure and we can suppose that neither penetration in the polymer matrix nor complicated structures were present.

2.3.2.4 Circulation of surfactant solution in the system without pressure

In this experiment, the role of pressure is focused. The adsorption in the same hydrodynamic conditions as filtration but without pressure is measured and compared to experiments under 30 bar.

The mass loss of SDS per membrane surface area in the circulated filtration system without pressure was observed to be 1.67 mmol m^{-2} for a SDS solution at initial concentration of 0.8 mmol L^{-1} . Excluding the adsorption on the system materials (e.g. glass and plastic materials), which took up nearly 45% of the total mass loss, the adsorption on the membrane was 0.92 mmol m^{-2} .

To summarize different adsorption processes, the estimated adsorption amount (in mmol m^{-2}) on the membrane surface in dynamic and static adsorption experiments are listed in Table 2 - 6.

Comparing the results of dynamic adsorption without pressure to that in the dynamic mode under high pressure, the adsorption amount was much lower. The adsorption amount in the system (excluding the adsorption on the system materials) during RO filtration process was

12.11 mmol m⁻², 29 times higher than that in the static adsorption, and 13 times higher than that in the dynamic system without pressure.

Table 2 - 6: The mass loss and adsorption of SDS per membrane surface area in different systems (mmol m⁻²). q_{tot} is the mass loss of SDS per membrane surface area in the filtration system; q_{sys} , and a_{mem} are the adsorption amount on the system materials and on the membrane, respectively.

Dynamic adsorption (mmol m ⁻²)			Dynamic adsorption (mmol m ⁻²)			Static adsorption (mmol m ⁻²)	Theoretical adsorption amount for a monolayer on the external surface of the thin film (mmol m ⁻²)	Reference
C = 0.8 mmol L ⁻¹ ΔP = 30 bar			C = 0.8 mmol L ⁻¹ ΔP = 0 bar			C = 0.8 mmol L ⁻¹		
q_{tot}	q_{sys}	q_{mem}	q_{tot}	q_{sys}	q_{mem}	q_{mem}	q_{mono}	[203], [204]
22.07	9.96	12.11	1.67	0.75	0.92	0.42	3.69×10^{-3}	

The adsorption in dynamic system is 2 times higher than in the static adsorption. The tangential flow could probably accelerate the motion and diffusion of molecules to the adjacent of membrane surface, thus resulted in enhanced attachment of surfactants onto the membrane. Note that the influence of roughness on adsorption was not deepened in this work.

From the comparison above, it is obvious that the most important factor to influence the adsorption during RO filtration is the pressure, which acts as an external physical force and pushes the surfactant molecules to attach to the membrane surface. In this case, some of the surfactant molecules may even be forced to penetrate the membrane. According to the static adsorption tests, the simple adsorption of surfactants at the surface of internal pores after penetration could not explain the huge amount of global mass loss.

The two last hypothesis of solubilization of SDS in the polymer matrix and the organization of the surfactants in more complicated surface structures (semi-continuous islands or high density solid layers nucleates) could not be experimentally verified in this work because of a lack of precise observation method to study this microscopic organisation.

Nevertheless, the macroscopic impact of surfactant adsorption on the hydrophobicity of the membrane was studied by contact angles measurements.

2.3.3 Contact angle measurements

After the adsorption experiments, the hydrophobicity of the membrane surfaces was determined by contact angle measurements. Surfactants adsorption on solid substrates can modify the surface hydrophobicity, depending on the orientation of adsorbed surfactant molecules [206]. In this part, the permeate flux and the amount of surfactant adsorption onto the membrane are made in relation with contact angle measurements.

The static contact angles of the RO membrane surface fouled by SDS solutions at 0.8, 1.6, 4.0, 8.0, 16.0, 40, 80 m mol L⁻¹ are shown in Table 2 - 7, together with the results of the clean membrane, as measured with ultrapure water, formamide and di-iodomethane. All the contact angles given are obtained 80 ms after 2.5 µL of the liquid drop was in contact with the membrane surface. The reason for using the contact angle at a precise shot time is that the liquid drop on the membrane surface exhibited a dynamic course in the case of high surfactant concentration [207].

Table 2 - 7: Contact angles with water, formamide and di-iodomethane for virgin SG membrane and membranes after filtering SDS solutions.

membrane	C (n CMC)	contact angles					
		θ_{water}	S (standard deviation)	$\theta_{\text{formamide}}$	S	$\theta_{\text{di-iodomethane}}$	S
A01	0	79.44	2.12	51.45	1.92	38.13	1.34
A25	0.1	88.53	3.51	67.74	3.79	46.09	5.32
A24	0.2	80.83	1.36	51.59	2.86	40.91	1.36
A05	0.5	72.65	3.18	47.84	2.64	39.32	1.59
A11	0.5	72.33	1.58	42.31	0.59	39.23	1.37
A13	1	71.16	2.35	39.98	0.86	39.64	1.14
A04	2	73.99	1.58	43.16	1.97	37.14	1.34
A21	5	70.22	2.39	49.01	3.57	51.18	5.12
A22	5	68.95	2.13	40.49	2.65	53.27	7.23
A14	10	41.64	2.62	52.10	4.26	60.44	3.41
A15	10	70.16	4.69	43.24	1.91	42.71	0.93

Table 2 - 8: Surface tensions (mJ m^{-2}) of SG membranes in various forms: clean membrane, membranes after filtration with SDS solutions at different concentrations (inferred from contact angles listed in Table 2 - 7, calculation based on (Equation 2 - 7)).

membrane	concentration (n CMC)	$\gamma_s(\text{LW})$	$\gamma_s(\text{A})$	$\gamma_s(\text{B})$	$\gamma_s(\text{AB})$	γ_s
A01	0	39.32	0.69	3.80	3.20	42.52
A25	0.1	36.43	0.01	3.63	0.35	36.78
A24	0.2	39.15	0.72	2.97	2.92	42.07
A05	0.5	40.10	0.54	6.46	3.55	43.65
A11	0.5	40.00	1.37	5.66	5.56	45.56
A13	1	39.67	1.76	5.66	6.32	45.99
A04	2	41.06	1.16	5.20	4.90	45.96
A21	5	33.62	1.25	10.05	7.08	40.70
A22	5	32.43	3.27	7.42	9.85	42.28
A14	10	28.32	0.17	52.68	6.05	34.37
A15	10	38.22	1.36	7.69	6.46	44.68

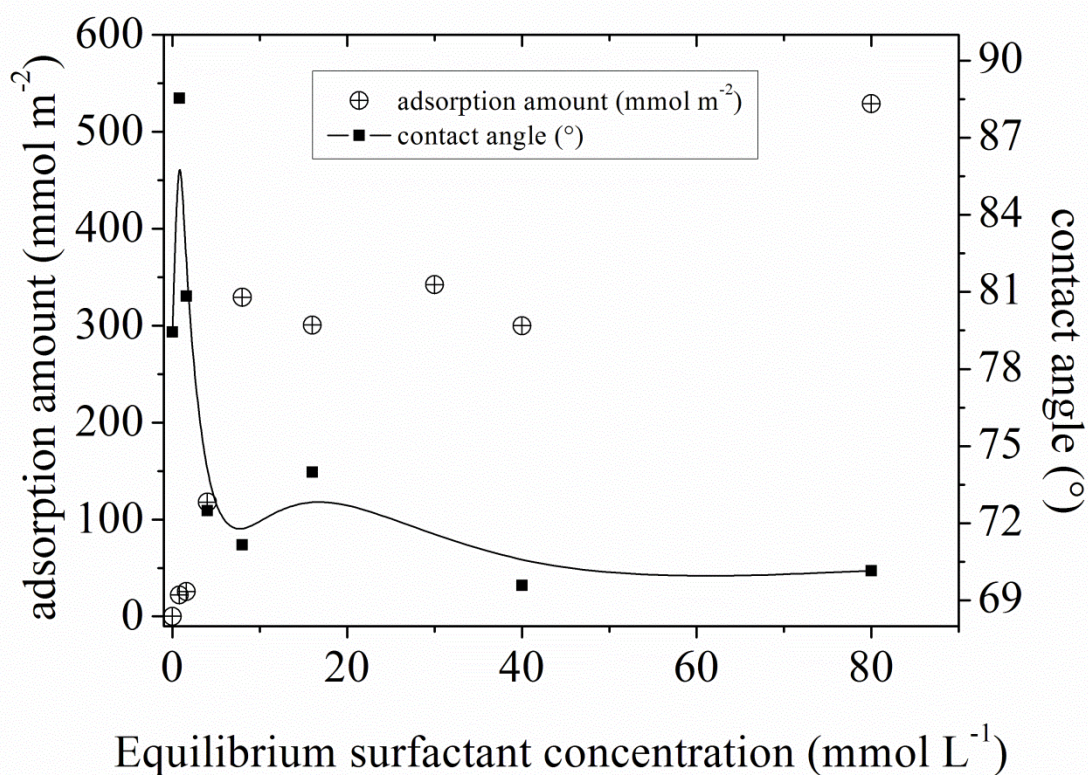


Figure 2 - 13: Adsorption isotherm and contact angle with water for RO membrane.

The contact angle measurement results in Table 2 - 7 and Figure 2 - 13 indicated that the virgin membrane had a high hydrophobicity, with a contact angle of 79.44° with ultrapure water. The result was higher than the literature value of 69.3° for the same membrane [61]. This may be due to different operating conditions, such as temperature, humidity, etc. After filtration of a 0.8 mmol L^{-1} SDS solution, the membrane had a contact angle of 88.53° with water, indicating that the membrane surface became more hydrophobic after the contact of the SDS solution. Since there are no micelles in these solutions under the CMC, surfactant monomers would probably lay parallel onto the membrane surface, occupying the hydrophobic site on the membrane surface with their hydrocarbon chain through hydrophobic interactions. This made the membrane more hydrophobic. Contact angle with water decreased from 88.5 to 72° with increasing surfactant concentration above 1.6 mmol L^{-1} , showing an increase in the hydrophilicity for the SG membranes, which corresponded to a decrease in the flux decline (see Figure 2 - 7) with the SDS concentration in solution. The difference in hydrophobicity was slight when the concentration of SDS in the solution is higher than the CMC, since the contact angles in this region kept constant to a value of around 72° , corresponding to the small change in the permeate flux. It could be concluded that a higher SDS concentration gives a bigger increase in the hydrophilicity of SG membrane until the membrane surface is saturated with a certain structure formed by the surfactants at concentration above the CMC. On the other hand, for concentrations higher than the CMC, monomers and micelles coexist in equilibrium in the surfactant solution [128], [155]. With concentration increase, more and more micelles are formed in the bulk solution. These micelles tend to deposit close to the membrane surface under high pressure, with their hydrophilic heads towards water. The constant flux and increase of adsorption from CMC to 10 CMC indicated that there might be a complicated structure, the top layer of which kept stable but the under layer structure increased with concentration.

The electron-donor surface tension parameter (γ^B) is a fairly good semiquantitative indicator of the degree of hydrophilicity of a surface. A strong increase in γ^B , result in an increase in hydrophilicity of the surface. From Figure 2 - 14, it is clear that an increase in γ^B occurred with increasing the surfactant concentration from 1.6 mmol L^{-1} in solution. The increase in the charge of negatively charged RO membrane surface, by the adsorption of surfactant anions as electron-donors, through the head on top of the surface, significantly increases their electron-donicity parameter (γ^B), and thus renders them more hydrophilic.

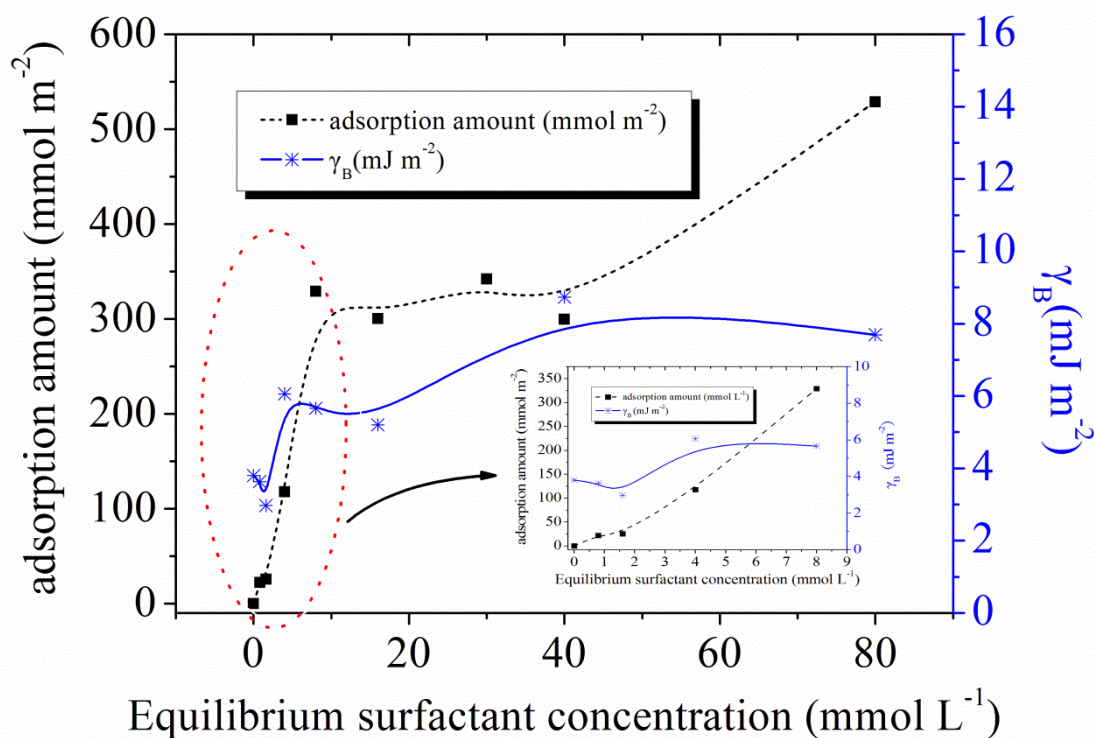


Figure 2 - 14: Adsorption isotherm and electro-donor parameter of the surface tension for RO membrane. The inset shows a zoomed-in version of the region from 0 to 8.0 mmol L⁻¹.

These phenomena are consistent with published observations with zeta potential measurements. A previous work has revealed that the zeta potentials of the membranes in the presence of surfactant were much more negative than the case with no SDS [198]. The reason was that surfactant molecules were readily adsorbed on the membrane surface and their negatively-charged functional groups dominated the membrane surface charge.

The adsorption of anionic surfactant on negatively charged membrane can be explained by the microscopic heterogeneity of the surface. Inherent local variations in the chemical nature of the polymer at the membrane surface can produce non-uniform distribution of surface charge and local variations in the hydrophobicity of the membranes. Theoretical analyses show that surface chemical heterogeneities can have a profound effect on the attachment rate of colloids onto stationary surfaces. Surface chemical heterogeneities may provide favorable sites for attachment onto what is otherwise an unfavorable surface for colloid attachment. The rate of colloid attachment to these favorable sites may be several orders of magnitude higher than that to the unfavorable sites [170]. For example, in polyamide thin film (see Figure 2 - 1), aromatic cycles may generate hydrophobic interactions; on the contrary to amide or carboxylic sites which may enhance hydrophilic interaction.

2.3.4 Mechanism of surfactant adsorption onto membrane surface

The main mechanisms taken into account in this study are described as the equilibrium among three main phases in Figure 2 - 15: the micellization in the aqueous phase, the adsorption of surfactants at the membrane-solution interface, and the eventual penetration of surfactant in the solid polymer matrix. According to the previous section, due to the huge mass loss of surfactants in the system and the influence of pressure, a simple model of monolayer is not sufficient to explain the quantity of surfactants retained by the membrane. Two main hypothesis were proposed: the construction of a more complicated structure at the surface, and the solubilization of surfactants into the membrane polymer. Unfortunately, no experimental methods were available to investigate the repartition between the superficial deposition of surfactants and the penetration into the membrane material.

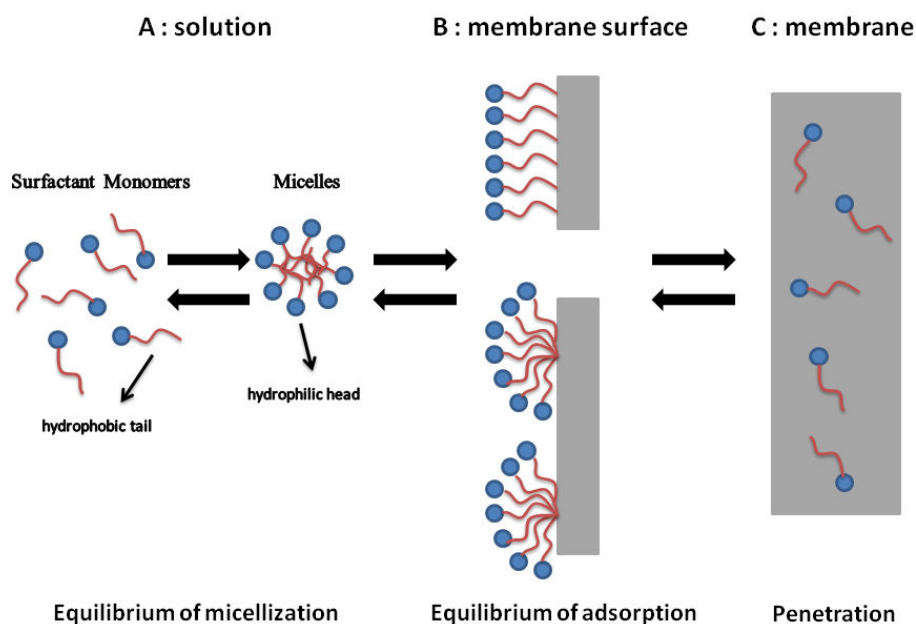


Figure 2 - 15: Equilibrium among different phases in the filtration system. A. Aqueous phase of SDS solution; B. Interface of SDS solution and RO membrane; C. Solid phase of RO membrane.

Nevertheless the results obtained on membrane retention rate, permeate flux, surfactant adsorption and the change of membrane hydrophilicity provided enough information to draw some hypothesis. In our work, it is possible that a secondary membrane formation occurred on the RO membrane surface due to concentration polarization, as proposed in previous work

[146], [151], [171]. The high pressure applied in the filtration system might cause this surface structure more thicker and denser than a monolayer. The orientation of surfactants on the top layer of the secondary membrane determined the hydrophobicity and charge of the fouled RO membrane surface, and thus dominated the rejection of the surfactants and the permeate flux. The behaviours of surfactants on the RO membrane surface and possible mechanism of surfactant adsorption as well as penetration could be drawn as follows.

- (1) When the concentration of surfactants is lower than the CMC, there are surfactant monomers, pre-micelles and possibly micelles near the RO membrane surface due to concentration polarization. The few micelles are easier to be swept away by the flux flow than small aggregates and monomers, because the lateral migration of particles and surface shear are the functions of particle diameters [151]. As a result, monomers and smaller aggregates form a compact structure, as illustrated in Figure 2 - 16 (a), which decreases the permeate flux, as aforementioned in section 3.1.2. When the concentration is very low (i.e. 0.1 CMC), the top layer of the secondary membrane formed by surfactant might be more hydrophobic than the virgin RO membrane, which could be supported by contact angle measurements in section 2.3.3. It is worth noting that in this case, a small quantity of surfactants are able to pass through the dense secondary membrane and penetrate into the RO membrane.
- (2) It should be noted that experiments were carried out separately and that the surfactant concentration in the feed did not rise progressively. The structures of the concentration polarization and the deposit didn't evolve progressively from a low concentration to a higher concentration. A new structure might be built for each surfactant concentration. When the surfactant concentration is between 0.2 and 1 CMC, the compact structure might also be formed by surfactant monomers, as illustrated in Figure 2 - 16 (a). But the secondary membrane is probably more hydrophilic with their hydrophilic heads directing towards the aqueous solution due to hydrophobic interactions between surfactant tails and the membrane, as well as the electrostatic repulsion between the negatively charged heads and the adsorbed secondary membrane. This hypothesis is consistent with what has been discussed in section 3.1.2 and section 3.3, that the permeate flux increased slightly and the contact angle of water became smaller when the surfactant concentration increased from 0.2 to approximately 1 CMC. The mass loss of the surfactant increased when the concentration increased in this region ($C \leq$

CMC), might result in an increase to the area, thickness and/or density of the secondary membrane.

- (3) When the surfactant concentration reaches the CMC, micelles occur in the aqueous solution. In this case, the organization of surfactants at the RO membrane surface is assumed to be quite different from that in the cases of lower concentrations. Because of the concentration polarization caused by retained micelles, surfactant adsorption most likely results in a thick but loose secondary membrane structure on top of the RO membrane surface (as shown in Figure 2 - 16 (b), allowing water molecules to pass through. So the permeate flux (section 2.3.1.2) increased slightly, as illustrated in Figure 2 - 3 and Figure 2 - 7, compared to that of surfactant solutions under the CMC. But the rejection of surfactants (section 2.3.1.1) remained high due to the negative charge of the micelles which could retained the negative surfactant anions.
- (4) Further increasing the surfactant concentration above the CMC (from 1 CMC to 5 CMC), the quantity of surfactant mass loss remained roughly constant. It seemed that the amount of adsorption on the RO membrane surface and penetration in the membrane kept unchanged due to the relatively stable structure of the porous secondary membrane. The top layer of the secondary membrane formed by surfactant micelles was supposed to be a layer of surfactant molecules with the hydrophilic heads towards the aqueous phase. Though there was a sudden increase in the mass loss at 10 CMC, which could be explained by an increase in the penetration into the RO membrane and/or in the thickness of the secondary membrane, the top layer structure was still considered to be unchanged. So the contact angles of membranes fouled by surfactant solutions above CMC kept almost constant. The relative permeate flux remained stable and higher than that of surfactant solutions below CMC.

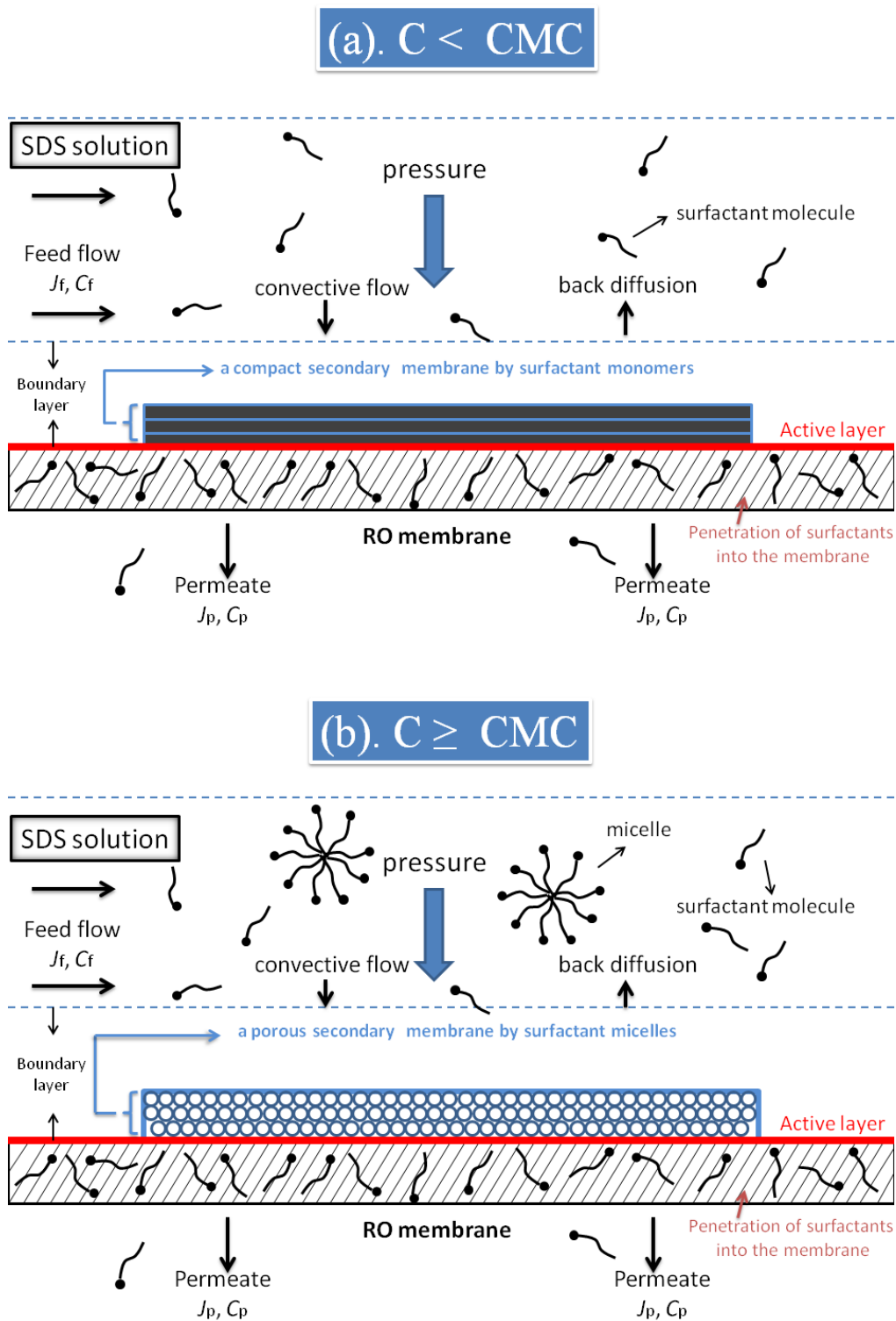


Figure 2 - 16: Possible mechanism of surfactant adsorption onto RO membrane and penetration into the membrane. (a). Formation of a compact secondary membrane by surfactant monomers below the CMC; (b). Formation of a porous secondary membrane by surfactant micelles above the CMC.

2.4 Conclusions

In the present study, the effect of surfactants on RO membrane fouling was systematically investigated. A thin film polyamide RO membrane was used for the treatment of SDS from aqueous solutions. The membrane performance, including both separation and transport properties, were firstly analysed. From these results, the orientation of surfactants on the membrane surface was assumed. Then the adsorption amount of surfactants was related to the membrane performance and the organisation of surfactants on the membrane surface. With the results from contact angle measurements, the behaviours of surfactants on the RO membrane and the fouling mechanism were proposed. Main results are as follows:

- The results obtained for the membrane separation properties suggest that reverse osmosis is very efficient for the removal of surfactants: more than 99.5% of the surfactants were rejected by the membrane over the whole concentration range (below, equivalent and above the CMC) in this work.
- However, the membrane fouling during filtration through RO membranes caused by surfactant adsorption affected the membrane performance and its surface characteristics. The relative fluxes of surfactant solutions were reduced compared to that of pure water, indicating a certain degree of membrane fouling. Unexpectedly, The relative flux did not decrease with surfactant concentration in the solution, but there was even an increase when the initial SDS concentration was below the CMC (8.0 mmol L^{-1}). The unexpected phenomenon could be explained by the interactions between the surfactant and the membrane, which in turn affected the membrane hydrophobicity and thus the transport of solute or water molecules.
- The contact angle measurements confirmed the modification of membrane surface characteristics in terms of contact angle (an index of hydrophobicity) and surface charge due to surfactant adsorption at different concentrations, hence potentially affecting transport mechanisms of surfactants compared to virgin membranes.
- The results of the adsorption experiments were investigated to relate the flux decline to the amount of surfactant adsorption. In addition to the adsorption during RO filtration experiments, both dynamic and static adsorption experiments without pressure were conducted. The huge amount of surfactant adsorption during RO filtration was explained by the adsorption of surfactants on the system materials (e.g. glass beacker and plastic tubing), the penetration into the internal structure and most

importantly, the formation of complicated surfactant deposits (e.g. a secondary membrane) at the membrane surface due to concentration polarization. The orientation of surfactants on the top layer of the secondary membrane determined the hydrophobicity and charge of the fouled RO membrane surface, and thus dominated the rejection of the surfactants and the permeate flux. When the surfactant solution contained no micelles under the CMC, surfactant molecules were supposed to form a dense secondary membrane. While the micelles were formed, the secondary membrane was supposed to be no longer dense but loose.

The fouling due to surfactant adsorption has been investigated in macroscopic scale in this experimental part. However, the behaviors of surfactant at the solution/membrane interface were just proposed as assumptions in this work. It should be noted that the interaction between surfactants and polymeric membranes play an important role in the behavior of surfactants on the membrane, which will in turn affect the transport and separation properties, as well as the surface characteristics of the membranes. The surfactant organization on the membrane controlled by surfactant-membrane interactions should be studied in detail from a microscopic view. This issue will be addressed in the next part of this thesis by means of DPD simulations of surfactant solutions. Indeed, DPD simulations could offer the possibility to connect macroscopic properties to a microscopic description of physical-chemical phenomena.

Chapter 3

Simulation part:

Mesoscopic simulations

of surfactant micellization and adsorption

by Dissipative Particle Dynamics

In this chapter, we are going to answer the questions that are still incompletely characterized or understood in the previous experimental chapter: what are the interactions between the surfactants and the polymeric membrane? What are the behaviors of surfactants in the aqueous solutions, and especially, how are the surfactants organized at the interface of an aqueous solution and a solid membrane made of polymers? And how do they influence the properties of the membrane processes?

To solve the above-listed problems, the methods of computer simulations are used. Numerical simulation is the use of a model to develop more detailed analysis that provides insight into the behavior of any real world elements. DPD simulations use the same concept but require a mesoscopic model that is different from the atomistic and macroscopic models. This method has been increasingly employed to supplement both real experiments and theoretical approaches. It has become possible to consider increasingly complex systems including surfactants and polymers, as well as systems of aggregates in solutions.

In a first step, the simulations of surfactant micellization in aqueous solution were performed to provide an appropriate model for surfactants to be correspondingly related to experimental results. Then the validated model was extended to complex systems containing both surfactants and a polymeric membrane. The obtained results from simulations, though the molecular structures of the studied compounds (surfactants and polyamide membrane) had been simplified, were compared to experimental results from chapter 2.

3.1 Introduction

As mentioned in chapter 1, the amphiphilic molecules of surfactants, containing both a hydrophilic head and a hydrophobic tail, are well known for their tendency to adsorb at surface/interface, where they can lower the surface/interfacial tension and modify the surface/interface properties [208]. Another fundamental characteristic feature of surfactants is that they can spontaneously self-assemble into a variety of aggregate structures in solution, such as micelles, bilayers, vesicle, and lamellae, when the concentration surpasses the critical micelle concentration (CMC) [128]. Thanks to these special properties, surfactants play an important role as cleaning, wetting, dispersing, emulsifying and foaming agents in many practical applications and industrial products [128], [209].

Due to their various applications, surfactants are also one of the most discharged organic materials in wastewaters that are to be treated by membrane processes. However, the adsorption of surfactants might be a huge obstacle for membrane filtration since surfactant molecules will accumulate on the membrane surface and cause fouling to the membrane. This will adversely affect both the quantity (permeate flux) and quality (solute concentration) of the product water, resulting in loss of performance of the membrane processes [44], [166]. In order to better understand the mechanism of membrane fouling by surfactants, we firstly need to develop a model able to account for the microscopic interactions involved in micellization in aqueous solution, which is expected to be accurate enough to reproduce quantitatively structural and thermodynamic properties of the surfactant self-assembly. Then it will be expanded to a system including a membrane in contact with the surfactant solution.

The self-assembly processes of amphiphilic molecules in solution have been actively studied during the past decades. Although reports on the experimental and theoretical studies are abundant in literature, in which values of the CMC and average aggregation number for a wide range of surfactants can be readily found [130], [210], [211], [212], [213], [214], [215], [216], [217], [218], [219], [220], [221], they can hardly provide any details into the complex interactions between surfactants and between surfactant and solvent. Thus development of a detailed understanding of the process of surfactant micellization as well as the physicochemical properties of the micellar system is still a target of active research.

Computer simulations, a promising tool in the study of structure – performance relationship of chemical products, has recently received much attention and can be employed here to correlate the thermodynamic properties and the microstructure of surfactant system [188], [222]. Major advances have been made at several levels of computer simulation for surfactant solutions. It has been proved that molecular dynamics (MD) simulation could be applied to yield information on the free energy of micelle formation [223], the structure of a single micelle [224], [225], [226], [227], [228], the relaxation of a molecular chain [229], and so on. However, the time and length scales of these simulation methods limit their application in simulating larger-scale behaviors. A recent report on the micellization of sodium alkyl sulfates (sodium hexyl, heptyl, octyl and nonyl sulfates) during very long time periods (up to 400 nanoseconds) using MD simulations provided insights into equilibrium properties such as CMC with respect to temperature and alkyl chain length [230]. Even though the powerful computational technique was very promising, their models underpredicted the experimental

CMCs and thus a refinement is needed to be able to reproduce experimental properties of surfactant self-assembly.

Recently, coarse-grained molecular dynamics (CG-MD) methods have been applied to extend the feasible size and length scales of atomistic simulations and have been more and more frequently used to investigate the meso-structures of micelles, including those formed by much complex surfactant [231], [232], [233]. Maiti *et al.* [231] studied the self-assembly of surfactant oligomers in an aqueous medium by CG-MD simulations, and observed that the spherical, cylindrical, and wormlike micelles would form as a function of surfactant concentration. A CG model was applied to probe morphological and thermodynamic properties of ionic surfactants at concentrations much higher than their CMCs [233]. The GPU-accelerated procedure made it possible to generate a simulation long enough (up to millisecond) to estimate the CMC of sodium hexyl sulfate, though the CMC values of sodium nonyl sulfate and sodium dodecyl sulfate were underestimated using the same simulation procedure.

As an alternative method, dissipative particle dynamics (DPD), a new mesoscopic simulation [11], [12], [234], [235], has made it possible to investigate the mesostructure of surfactant systems up to the microsecond range. DPD is similar to molecular dynamics studies using coarse grain models except that dissipative and random forces act between particles as well as the usual conservative ones. While intended to mimic the influences of neglected degrees of freedom, the dissipative and random forces also collectively serve as a thermostat. The simulation strategy is to regard a cluster of atoms or molecules as a single, coarse-grained particle whose motion is governed by Newton's equations of motion. The beads within the DPD models typically correspond to more atoms than in coarse-grained models. The representation of larger collections of atoms, with considerable internal flexibility, by a single bead leads to very soft conservative interaction potentials between beads which permit very large time-steps to be applied. All of the forces employed in typical DPD simulations conserve momentum and hydrodynamic interactions are correctly represented [222]. Groot and Madden [236] first applied DPD method to examine the microphase separation behavior of block copolymers and much research has been devoted to the exploration of the application of DPD simulation method ever since.

However, to the best of our knowledge, DPD studies of micellization have been rather sparse in the literature. The first attempt to employ the repulsive soft potential to study the

micelle formation of surfactants was unsuccessful, resulting much lower CMCs for the nonionic surfactants than experimental values [237]. The authors demonstrated that the CMC was very much dependent on a hard-core solvent. Wu *et al.* [238] used DPD method to investigate the self-assembly and the morphology of surfactant oligomers in an aqueous medium, and the calculated CMC of sodium dodecyl sulfate (SDS) turned out to be in qualitative agreement with available experimental results. However, the repulsive interaction parameters in their work were adjusted by Groot [239] for a simple two-bead surfactant to form spherical micelles. The model was only a qualitative model for surfactant, thus more specific parameters for a particular real system should be precisely defined. Duan *et al.* [240] simulated a model surfactant solution-air system by adjusting mesoscopic parameters, from which they found that the interaction between water and tail (a_{WT}) affected the CMC most significantly. They related the CMCs obtained from DPD simulations to several sodium alkyl sulfonates with different tail lengths, but the strategy of varying the interaction parameter a_{WT} with increasing the tail length is not strictly correct. In fact, the scaling of the coarse graining would change if the tail bead contains more carbon atoms [241]. Thus it was hard to make a quantitative comparison between the behaviors of the simulated systems and the experiments. Recently, a well established model for diblock copolymer micellization was developed by Li *et al.* [242]. The proposed approach could be applied to study the equilibrium properties (CMC and average aggregation number) of nonionic surfactant solutions. Lin *et al.* [243] used a surfactant model corresponding closely to realistic surfactant like molecules to calculate their CMCs. The use of DPD simulation method seemed a good option for investigating the general properties of surfactant system, but the main problem to model a realistic surfactant correctly by DPD method is a lack of more systematic work to reproduce both thermodynamic and structural properties using verified interaction parameters as well as structure constrains. In fact, if one transforms the simulation results calculated in the work of Lin *et al.* [243] in DPD units to real physical units, the CMC values (0.0023 to 0.015 mol L⁻¹) are not within the range of experimental values for C₂₄H₄₉(OC₃H₆)₂OH (less than 10⁻⁴ mol L⁻¹) [7].

The first success in predicting micellar properties of particular nonionic surfactants by DPD method was achieved recently. To avoid the mismatch properties caused by the approximation of Flory-Huggins model for DPD parameterization, Vishnyakov *et al.* [244] made efforts in developing a new approach to rigorously parameterize the repulsive interaction and rigidity parameters, by fitting to the infinite dilution activity coefficients of binary solutions formed

by reference compounds that represent coarse-grained fragments of surfactant molecules. The obtained CMCs and aggregation numbers for the three particular surfactants were found consistent with experimental results, which in turn proved the capability of DPD method to quantitatively model the micellization of realistic nonionic surfactant system.

Systematic DPD studies published so far have not been successfully and correctly applied to the micellization of a specific reference ionic surfactant to predict their micellization properties, such as the CMC, micelle size, and so forth. A predictive understanding of micellization process and the determination of micelle size are still problems remained to be solved. In this chapter, we investigate the ability to predict accurate micellar properties of typical ionic surfactant models by DPD simulations. In the first part, the theory of DPD simulations is presented. Then in the following part, a parametric study is developed which will in turn contribute to the general understanding of common features of ionic surfactants. Then DPD simulation was applied to model the process of micelle formation and analyze the equilibrium properties (*e.g.*, CMC and the average aggregation number) as functions of different factors (*e.g.*, surfactant total concentration and hydrophobic chain length). The best set of parameters is selected and then the significance of these results as well as the limit of the model is discussed. The relationship between simulated results to current theories of micelle formation is considered. Finally, first results of simulation of a membrane-surfactant system are presented and perspectives are drawn.

3.2 Theory

Dissipative Particle Dynamics

The dissipative particle dynamics simulation method describes a fluid system by dividing it up into small interacting fluid packages which are represented by DPD beads. We consider a set of interacting beads with mass (m), position (\mathbf{r}_i) and velocity (\mathbf{v}_i) of a bead i . All bead masses are set equal to unity. The time evolution of the position \mathbf{r}_i and velocity \mathbf{v}_i of every bead is governed by Newton's second law of motion:

$$\frac{\partial \mathbf{r}_i}{\partial t} = \mathbf{v}_i \quad (\text{Equation 3 - 1})$$

$$\mathbf{f}_i = m \frac{\partial \mathbf{v}_i}{\partial t} = m \frac{\partial^2 \mathbf{r}_i}{\partial t^2} \quad (\text{Equation 3 - 2})$$

The equations of motion are solved using the modified Velocity-Verlet algorithm presented by Groot and Warren [11].

$$\begin{cases} \mathbf{r}_i(t + \Delta t) = \mathbf{r}_i(t) + \mathbf{v}_i(t) \Delta t + \frac{1}{2} \mathbf{f}_i(t) \Delta t^2 / m \\ \mathbf{w}_i = \mathbf{v}_i(t) + \lambda_i \mathbf{f}_i(t) \Delta t / m \\ \mathbf{f}_i(t + \Delta t) = \mathbf{f}_i(\mathbf{r}(t + \Delta t), \mathbf{w}) \\ \mathbf{v}_i(t + \Delta t) = \mathbf{v}_i(t) + \frac{1}{2} [\mathbf{f}_i(t) + \mathbf{f}_i(t + \Delta t)] \Delta t / m \end{cases} \quad (\text{Equation 3 - 3})$$

The time interval Δt is the time step with which the equations of motion are solved. It has to be chosen as a compromise between fast simulation and satisfying the equilibrium condition.

The total force has three components between each pair of beads, corresponding to conservative, dissipative and random force. The total force \mathbf{F}_i on bead i can be written as:

$$\mathbf{F}_i = \sum_{i \neq j} (\mathbf{F}_{ij}^C + \mathbf{F}_{ij}^D + \mathbf{F}_{ij}^R) \quad (\text{Equation 3 - 4})$$

All forces are short-range within a certain cutoff radius r_c , consequently only local interactions are considered. The radius r_c is usually set to unity so that lengths are measured relative to the interaction range.

The conservative force \mathbf{F}_{ij}^C directly repels the particles from each other. This force is a soft-repulsive interaction given by: (when $r_{ij} < r_c$)

$$\mathbf{F}_{ij}^C = a_{ij} (1 - r_{ij}/r_c) \mathbf{e}_{ij} \quad (\text{Equation 3 - 5})$$

Here $\mathbf{r}_{ij} = \mathbf{r}_i - \mathbf{r}_j$ is the distance vector between beads i and j , $r_{ij} = |\mathbf{r}_{ij}|$, \mathbf{e}_{ij} is the unit vector \mathbf{r}_{ij}/r_{ij} , and a_{ij} is the repulsion parameter between beads i and j .

Groot and Warren [11] have developed a link between the repulsive parameter a_{ij} and χ -parameters in Flory–Huggins type models. To reproduce the compressibility of water at room temperature, the repulsion parameter between the identical DPD beads a_{ii} in has to be chosen according to:

$$a_{ii} = \frac{(16N_m - 1)}{0.2} \times \frac{k_B T}{\rho} \quad (\text{Equation 3 - 6})$$

where N_m is the number of molecules in a bead, which represents the level of coarse-graining. The temperature factor $k_B T$ is used as the energy unit, where k_B is Boltzmann's constant and T temperature. ρ is the density of the system (see Appendix). The repulsion parameter between different types of beads is obtained from the following equation [245]:

$$a_{ij} = a_{ii} + \frac{1}{0.231} \chi_{ij} \quad (\rho = 3) \quad (\text{Equation 3 - 7})$$

The dissipative force \mathbf{F}_{ij}^D could be expressed as:

$$\mathbf{F}_{ij}^D = -\gamma_{ij} \omega^D(r_{ij}) (\mathbf{v}_{ij} \cdot \mathbf{e}_{ij}) \mathbf{e}_{ij} \quad (\text{Equation 3 - 8})$$

where $\gamma_{ij} = \gamma_{ji} > 0$, is the friction coefficient; $\omega^D(r_{ij})$ is a weight function and \mathbf{v}_{ij} (equal to $\mathbf{v}_i - \mathbf{v}_j$) is the velocity difference between beads i and j .

The random force \mathbf{F}_{ij}^R acts between pairs of beads and provides an energy input into the system and build a thermostat together with the dissipative force [11]. The random force \mathbf{F}_{ij}^R is given by:

$$\mathbf{F}_{ij}^R = \sigma_{ij} \omega^R(r_{ij}) \zeta_{ij} \frac{1}{\sqrt{\Delta t}} \mathbf{e}_{ij} \quad (\text{Equation 3 - 9})$$

Here $\sigma_{ij} = \sigma_{ji} > 0$, which defines the fluctuation amplitude. The noise term $\zeta_{ij} = \zeta_{ji}$ is a random number drawn from a Gaussian distribution with zero mean and unit variance.

According to Espanol and Warren [12], the system relaxes to the canonical ensemble if the random and dissipative forces are balanced according the fluctuation-dissipation theorem. This implies the following relations between the weight function $\omega^D(r_{ij})$ and $\omega^R(r_{ij})$, and between σ_{ij} and γ_{ij} :

$$\omega^R(r) = \sqrt{\omega^D(r)} = 1 - r/r_c \quad (\text{Equation 3 - 10})$$

$$\sigma_{ij} = \sqrt{2 \gamma_{ij} k_B T} \quad (\text{Equation 3 - 11})$$

In addition, intramolecular interactions including bond stretching and angle bending are accounted for using harmonic potentials. The beads in a molecule are connected together by a harmonic spring force \mathbf{F}_i^S due to bonded neighbors. This force is described in the equation below:

$$\mathbf{F}_i^S = \sum_j k_r (r_{ij} - r_0) \mathbf{e}_{ij} \quad (\text{Equation 3 - 12})$$

where k_r is the bond spring constant and r_0 is the equilibrium distance between two consecutive beads.

To control the flexibility of the bonded bead pairs, we add a harmonic bond-bending potential with bending constant k_θ and equilibrium angle θ_0 , given by [246]:

$$\mathbf{F}_i^B = \sum_j k_\theta (\theta_{ij} - \theta_0) \quad (\text{Equation 3 - 13})$$

3.3 Methodology

3.3.1 DPD Models for surfactants and water

The target anionic model surfactants are sodium hexyl sulfate (SHS, $C_6H_{13}OSO_3Na$) and sodium nonyl sulfate (SNS, $C_9H_{19}OSO_3Na$). Sodium dodecyl sulfate (SDS, $C_{12}H_{25}OSO_3Na$) was also supposed to be taken into account, but it took much longer time for the simulation, and the results are still in progress. So for the moment, we will investigate the properties of the two shorter chains in the same series of sodium alkyl sulfates. The molecular structures of the two sodium alkyl sulfates are shown in Figure 3 - 1. The experimental values for the CMC and aggregation numbers of the two surfactants are listed in Table 3 - 1.

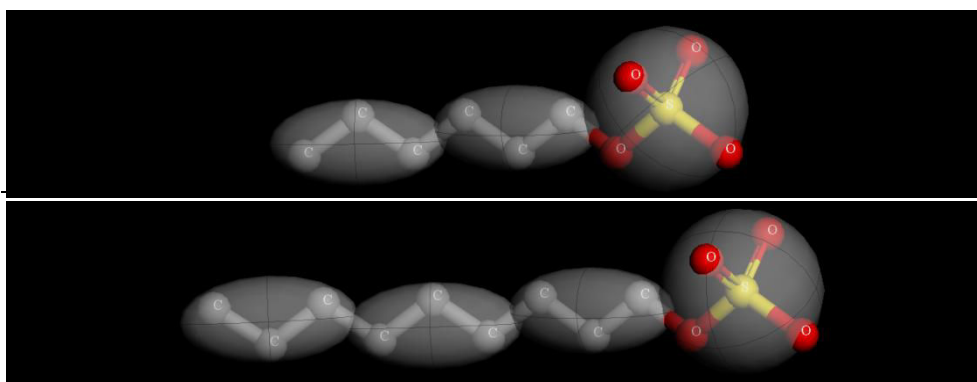


Figure 3 - 1: Molecular structures of (a) sodium hexyl sulfate (SHS, $C_6H_{13}OSO_3Na$) and (b) sodium nonyl sulfate (SNS, $C_9H_{19}OSO_3Na$) modeled in this study. The sodium atoms are not shown in this figure.

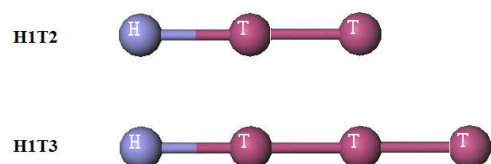


Figure 3 - 2: Coarse-grained models used in the simulations with their nomenclature. H1T2 and H1T3 correspond to SHS and SNS, respectively.

Each surfactant molecule is coarse-grained to a linear bead-spring chain H_1T_x , $x = 2$ and 3 for SHS and SNS, respectively (see Figure 3 - 2). Bead H represents the anionic hydrophilic head ($-SO_4^-$) and bead T represents central ($-CH_2CH_2CH_2-$) and terminal ($-CH_2CH_2CH_3$) propyl groups in the hydrophobic tail; x denotes the number of hydrophobic beads in the tails; bead W contains three water molecules ($N_m = 3$). The choice in this work is consistent with previous studies which demonstrated that roughly the volume of one CH_2 group in the T-bead corresponds to the volume of one water molecule in the W-bead [247], [248], [249]. All beads in our simulations are assumed to have the same mass m_0 and diameter r_c , which will be used as units of mass and length.

Table 3 - 1: Experimental values of CMC and aggregation numbers for SHS and SNS at 25 °C

Surfactant	CMC (mol L ⁻¹)	Reference	Aggregation number	Reference
C ₆ H ₁₃ NaSO ₄	0.42	[250]	17	[128], [251]
	0.517	[252]		
C ₉ H ₁₉ NaSO ₄	6.0×10^{-2}	[250], [253]	35 to 44	[254]
	6.46×10^{-2}	[254], [255]		

3.3.2 Detailed DPD simulation procedure

Simulations were realized using the molecular simulation package NEWTON [256] running on the local calculation center — Mesocentre of Ecole Centrale Paris. Some of initial DPD simulations were carried out in the NVT ensemble (constant particle number, volume, and temperature) using Mesocite software (Materials Studio 5.5, Accelrys Inc.).

In this work, all input and output values were reported in DPD units (or reduced units). Table 3 - 2 summarizes several scales in DPD and their corresponding physical units, thus it is possible for us to extract a large amount of information from the simulation results by these conversions.

Table 3 - 2: Time, mass, length and energy scales of the system

	Length scale	Mass scale	Energy scale	Time scale
	(r_c)	(m)	($k_B T$)	(t)
DPD Units	1	1	1	1
Physical units	6.46Å	54 amu	2.48 kJ/mol	3.02 ps*

*the time scale is 80 ps by matching the diffusion constant for pure water.

See Appendix for more information.

Table 3 - 3: Bead–bead repulsion parameter set I used in the simulation systems of Groot [257]

a_{ij}	H	T	W
H	86.7		
T	104	78	
W	75.8	104	78

In DPD simulations, we have to choose the repulsion parameters and intramolecular interactions such that the simulations yield the experimentally obtained values, such as the CMC and aggregation number for surfactants studied in this work. At the beginning of this work, the conservative bead-bead interaction parameters were chosen from Groot’s work [257] as listed in Table 3 - 3, which were calculated from Flory-Huggins χ -parameter. Then on the basis of the comparison with experimental values, we define the parameter sets to perform the simulation. The parameter set listed in Table 3 - 4 for our simulations is developed from Table 3 - 3.

Table 3 - 4: Bead–bead repulsion parameter set II used in our simulation systems

a_{ij}	H	T	W
H	86.7		
T	84 – 124	78	
W	65 – 75.8	92 – 104	78

For the harmonic spring force parameters describing bead-bead bonding in surfactants, Groot and Rabone [257] have used a bond spring constant $k_f = 4$ and the equilibrium distance between two consecutive beads $r_0 = 0$ for a nonionic surfactant $C_{12}E_6$. But Kranenburg *et al.* [249] and Rekvig *et al.* [258] used another parameter set: $k_f = 100$ and $r_0 = 0.7$. In this work, both parameter sets were used and the influence of them on the surfactant properties was investigated. The angle bending parameters were also taken into account. Two parameter sets were investigated: (1) no angle bending, as described in Groot and Rabone's work [257]; (2) bending constant $k_\theta = 6$ and equilibrium angle $\theta_0 = 180^\circ$, based on the work of Kranenburg *et al.* [249].

Other parameters are chosen as follows: the friction coefficient $\gamma = 4.5$, bead density of the system $\rho = 3.0$ (real density of the system 1.0 g cm^{-3}) and step size for the integration of the Newton equations $\Delta t = 0.04$.

All simulations were performed under periodic boundary conditions in a cubic box. The volume of the simulation box was $20 r_c \times 20 r_c \times 20 r_c$, for H1T2 system, containing 24,000 beads, and $30 r_c \times 30 r_c \times 30 r_c$, containing 81,000 beads for H1T3 system. This rather large box size was selected to accommodate a large number of surfactants molecules and hence micelles at equilibrium.

Table 3 - 5: Composition details for each H1T2 system ($20 r_c \times 20 r_c \times 20 r_c$) simulated in this work

number of molecules		real concentration (mol L ⁻¹)
H1T2	H ₂ O	
130	23610	0.1
260	23220	0.2
390	22830	0.3
520	22440	0.4
650	22050	0.5
780	21660	0.6
910	21270	0.7
1040	20880	0.8

As shown in Table 3 - 1, the experimental CMC values of SHS and SNS are approximately 0.42 mol L^{-1} and 0.06 mol L^{-1} , respectively. So simulation systems were constructed at different initial concentrations, from 0.1 to 0.8 mol L^{-1} for HIT2 and from 0.01 to 0.1 mmol L^{-1} for HIT3, respectively. The details of each individual simulation system for HIT2 and HIT3 are listed in Table 3 - 5 and Table 3 - 6, respectively. The initial positions of water and surfactant molecules were randomly distributed.

During the simulation process, firstly the geometry of each system structure was optimized, using the steepest descent algorithm in Mesocite, in which the bead coordinates were adjusted until minimal or convergence criteria had been met. In general, therefore, the optimized structure corresponded to a minimum in the potential energy surface. Then the DPD simulations started and the process of micelle formation was monitored. The trajectories were collected every 100 time steps for data analysis.

Table 3 - 6: Composition details for each HIT3 system ($30 r_c \times 30 r_c \times 30 r_c$) simulated in this work

number of molecules		real concentration (mol L^{-1})
HIT3	H ₂ O	
44	80824	0.01
132	80472	0.03
176	80296	0.04
220	80120	0.05
264	79944	0.06
308	79768	0.07
440	79240	0.10

3.3.3 Analysis details

3.3.3.1 Micelle formation

The most direct approach to investigate the morphology of the micellar aggregates and the spatial organization of different parts of individual surfactants is to look at the snapshots of the system. In all simulation runs, we observed that the originally randomly dispersed surfactant molecules self-assembled into small aggregates very quickly. Figure 3 - 3 shows

typical instantaneous snapshots of HIT2 aggregation along the course of micelle formation at relatively low concentration (0.3 mol L^{-1}), and Figure 3 - 4 for a higher concentration (0.8 mol

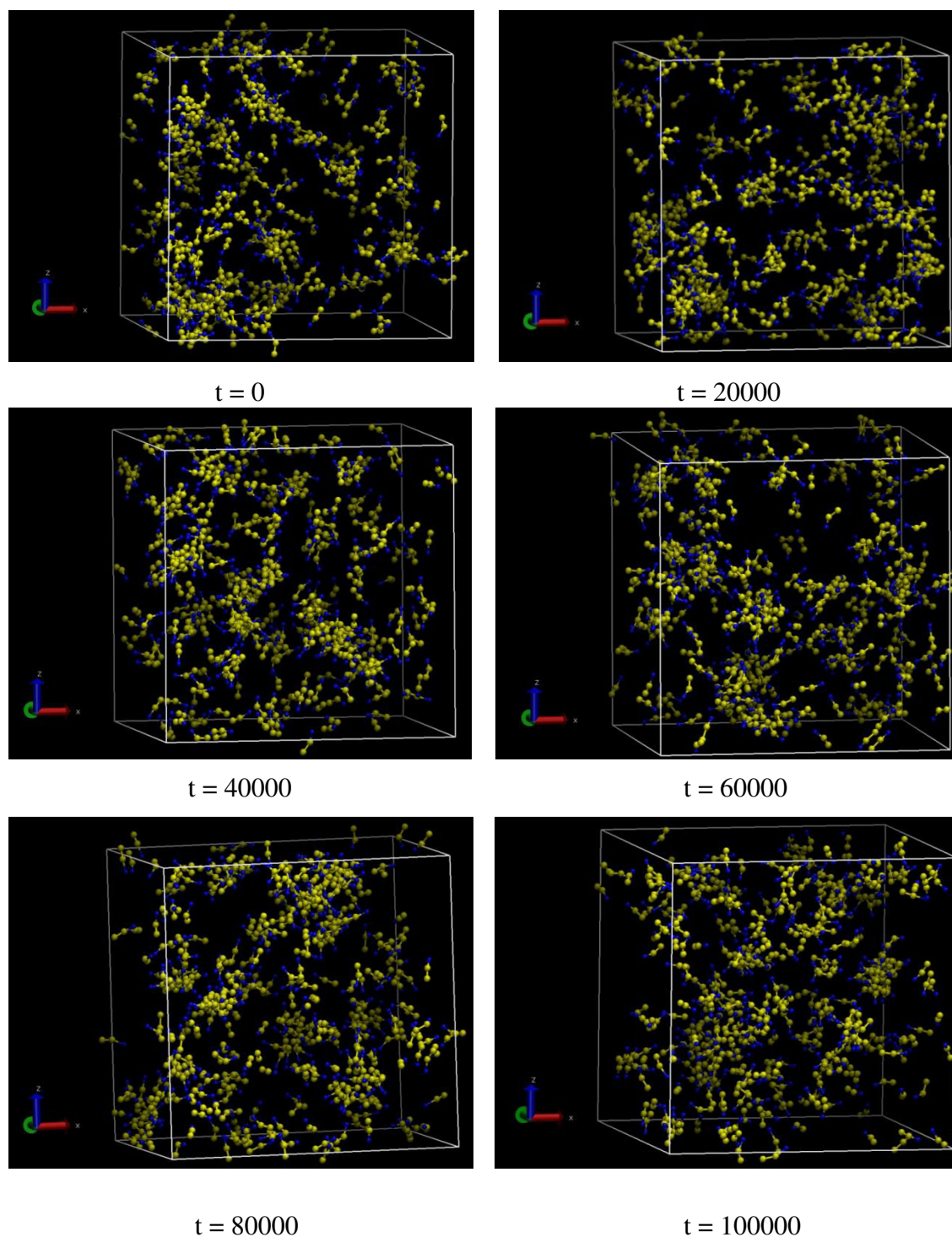


Figure 3 - 3: Snapshots for the simulation box containing HIT2 molecules obtained in the course of micelle formation. The hydrophobic tail bead is shown by yellow balls, the hydrophilic head bead is shown by blue balls, and water beads are not shown, rendered by VMD ($a_{HT} = 104$, $a_{HW} = 65$, $a_{WT} = 98$, $C_{HIT2} = 0.3 \text{ mol L}^{-1}$).

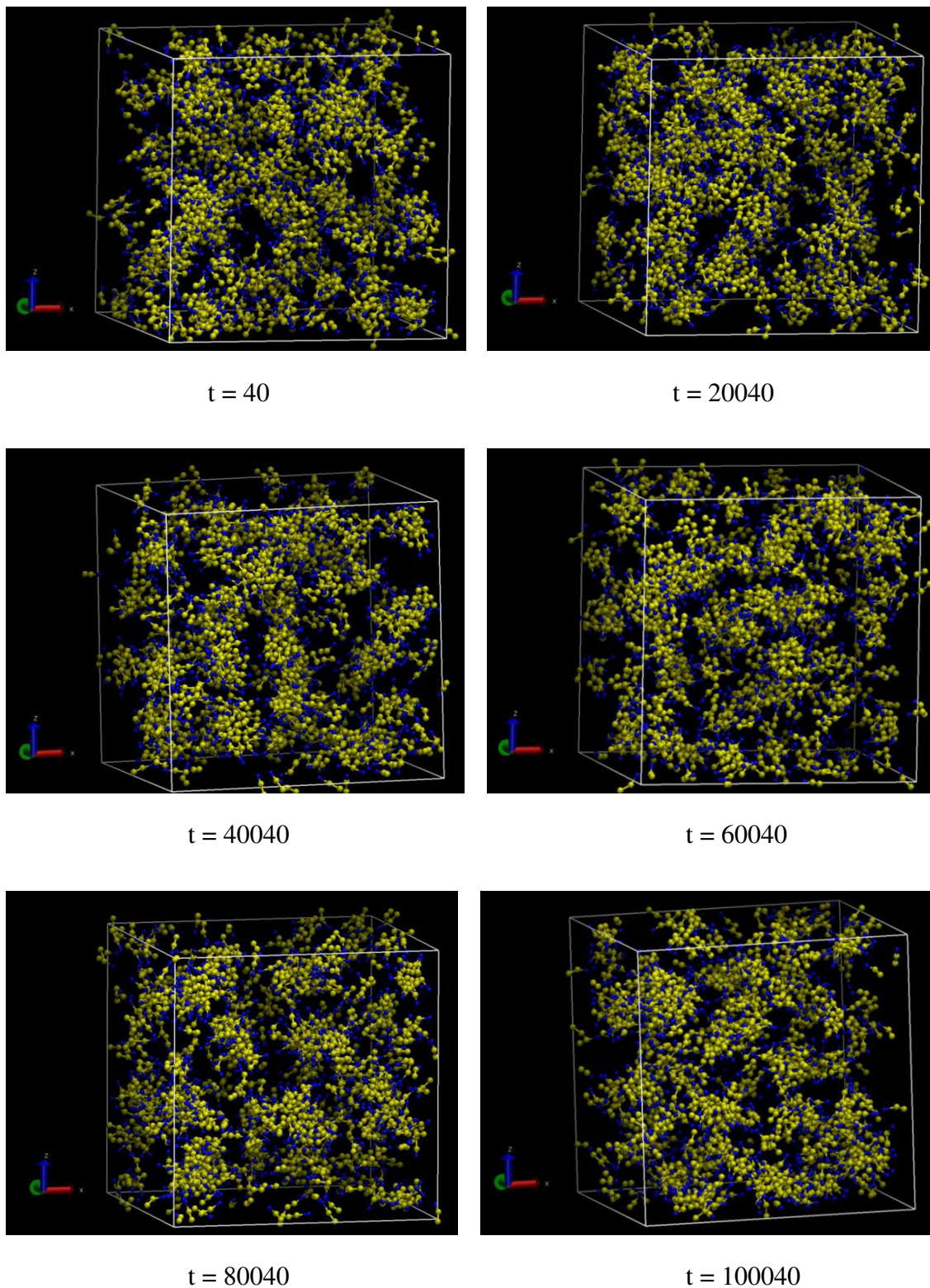


Figure 3 - 4: Snapshots for the simulation box containing H1T2 molecules obtained in the course of micelle formation. The hydrophobic tail bead is shown by yellow balls, the hydrophilic head bead is shown by blue balls, and water beads are not shown, rendered by VMD ($a_{HT} = 104$, $a_{HW} = 65$, $a_{WT} = 98$, $C_{H1T2} = 0.8 \text{ mol L}^{-1}$).

L^{-1}). For systems at low concentrations, there is no micelle but a few small aggregates, along with some surfactant molecules not attached to any aggregate (Figure 3 - 3). When the concentration of the surfactant is large enough ($C > \text{CMC}$), spherical micelles accumulate individual monomers until a critical size is reached (Figure 3 - 4). Due to the periodic boundary conditions, aggregates often appear dissected by the boundaries.

3.3.3.2 Cluster definition

We adopt a cluster-based definition based on a general distance criterion to determine micellar aggregates in the simulation, which has been proposed in both atomistic [225], [259] and coarse-grained [233], [260] studies on surfactant self-assembly [225], [261]. With this criterion, two surfactant molecules are defined to belong to the same cluster if the distance between their centers of mass, R_{cm} , is smaller than a cutoff threshold R_{agg} . The value of R_{agg} was selected from the radial distribution functions (RDFs) of the centers of mass of surfactant molecules.

Figure 3 - 5 shows radial distribution function (see Appendix) of centers of mass of the HIT2 molecules *versus* reduced distance r at 0.8 mol L^{-1} . It is clear that the first peak in the RDF is steep at a distance of about 0.78, which implies a high density of surfactant molecules in isolated aggregates. The surfactant center of mass (CM) – center of mass (CM) pair-correlation function $g(r)_{\text{CM-CM}}$ shows a distinct shoulder between the two peaks at a distance of approximately 1.25, which could be used as the cutoff threshold R_{agg} as mentioned above to distinguish different clusters in our simulation. While the exact position of the minimum in the RDFs varies slightly for systems at different concentrations, a common value of 1.25 was selected for simplicity. In fact, cutoff values between 1.2 and 1.5 shows less than 10% differences to the CMC and average aggregation number. However, cutoff values larger than 2.0 will lead to incorrect results with larger cluster sizes. The selection of this cutoff value will be discussed in section 3.3.3.4.

The same criterion could be applied to the radial distribution function between intermolecular surfactant heads, $g(r)_{\text{H-H}}$, as shown in Figure 3 - 6. Compared to $g(r)_{\text{CM-CM}}$, where a non-zero zone appeared at very short distances ($r \approx 0$) because of the overlap of surfactant centers of mass, a more structured $g(r)_{\text{H-H}}$ could be observed with a more distinct first peak at around $r = 0.95$. The cutoff threshold R_{agg} , selected as the minimum between the

first two peaks in the RDF, falls at the distance of approximately $r = 1.2$. So it is confirmed that a value of 1.25 for R_{agg} is reasonable.

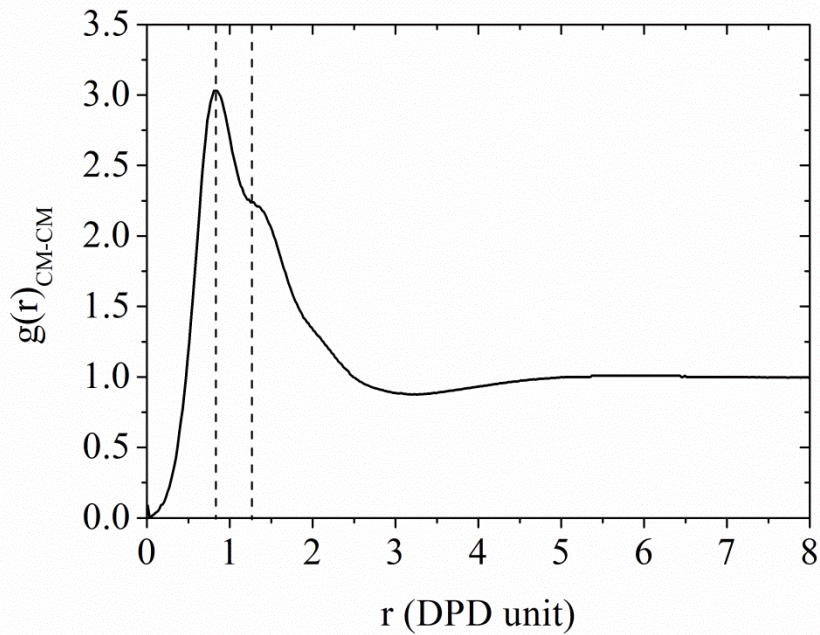


Figure 3 - 5: Radial distribution functions of surfactant centers of mass, $g(r)_{\text{CM-CM}}$ for H1T2 system. ($a_{\text{HT}} = 104$, $a_{\text{HW}} = 65$, $a_{\text{WT}} = 98$, $C_{\text{H1T2}} = 0.8 \text{ mol L}^{-1}$, $t = 100000$).

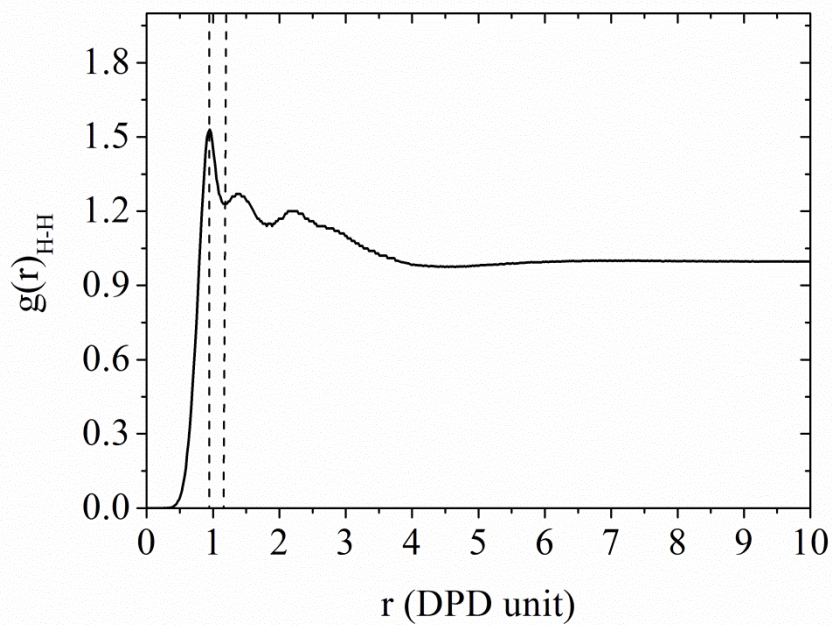


Figure 3 - 6: Radial distribution functions of intermolecular surfactant heads, $g(r)_{\text{H-H}}$ for H1T2 system. ($a_{\text{HT}} = 104$, $a_{\text{HW}} = 65$, $a_{\text{WT}} = 98$, $C_{\text{H1T2}} = 0.8 \text{ mol L}^{-1}$, $t = 100000$).

In this way the cluster size/aggregation number of each aggregate, which can be used to illustrate the cluster size distribution and evaluate the mean micelle aggregation number, can be clearly determined. With all the aggregates identified, the weight-average aggregation number (N_w) was calculated as [225]:

$$N_w = \frac{\sum_i n_i N_i^2}{\sum_i n_i N_i} \quad (\text{Equation 3 - 14})$$

where n_i is the number of aggregates (including monomers) with the same weight containing N_i surfactant molecules.

3.3.3.3 Equilibrium

The process of surfactant self-assembly into micelles started from a homogeneously dispersed monomer solution. We obtained the configurations for each system with different concentrations after the initial random configuration was equilibrated. The equilibrium of the surfactant system was checked for by observing the bonding energy, chemical potential, and temperature of the system. It is shown in Figure 3 - 7 that for a H1T2 system at 0.1 mol L⁻¹, the bonding energy, chemical potential and temperature have equilibrated less than 50 DPD time units and kept constant thereafter. Other H1T2 systems at different concentrations also showed quick equilibration.

For a longer chain such as H1T3, it will take very long time to achieve equilibrium. To decide how long the simulation should run exactly, the time dependency of weight-average aggregation number (N_w) distributions were checked.

Figure 3 - 8 shows the weight-average aggregation number N_w as a function of time during the micellization process of a H1T3 solution with a total concentration $C_{\text{H1T3}} = 0.07$ mol L⁻¹ for a typical simulation run. As is seen in Figure 3 - 8, the overall convergence analysis of aggregation number along with the whole simulation process suggests that the self-assembly of ionic surfactant occurs on three distinct stages (I, II, III): the growth of the weight-average aggregation number experiences a first increase in the beginning (I) and gradual saturation (II) until reaching their respective equilibrium plateau level later on which is regarded as a slow relaxation process(III), as described in a previous article [220].

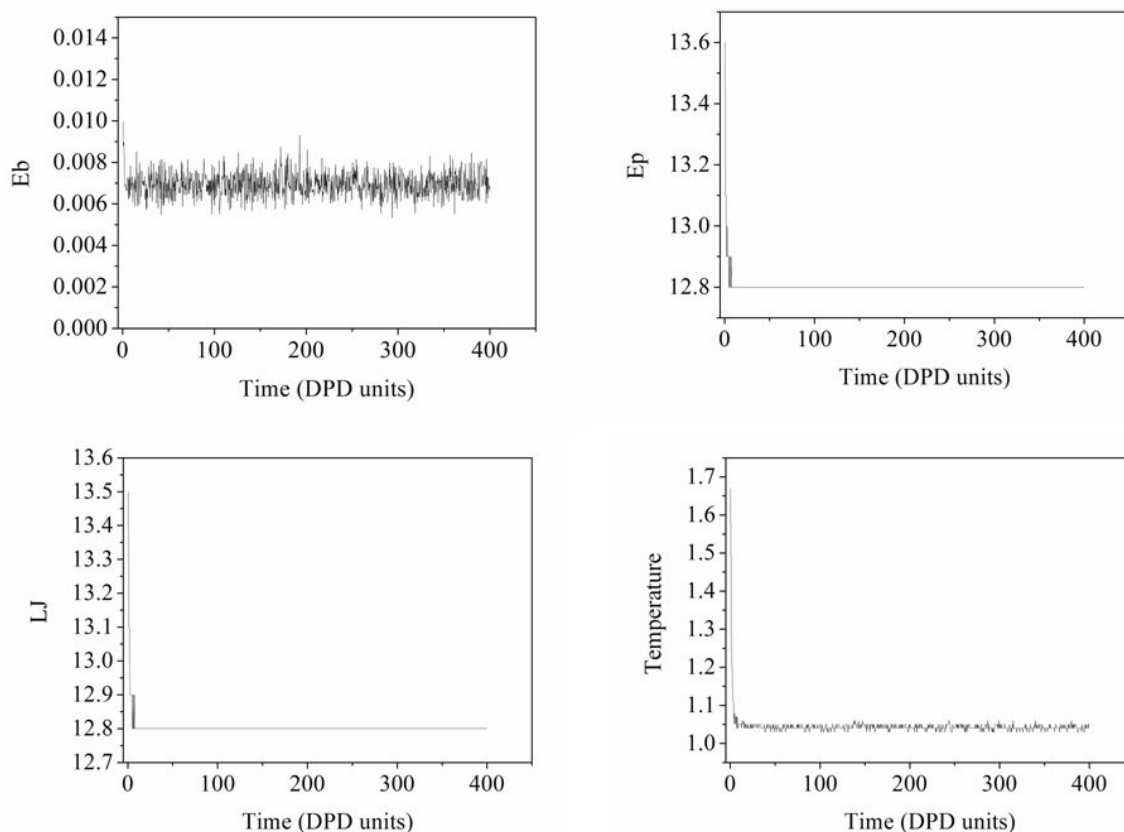


Figure 3 - 7: Time evolution of bonding energy (E_b), chemical potentials (E_p), Lennard-Jones potential (LJ) and temperature (T) in the HIT2 system. ($a_{HT} = 104$, $a_{HW} = 65$, $a_{WT} = 98$, $C_{HIT2} = 0.1 \text{ mol L}^{-1}$).

During the first stage I (from $t = 0$ to $t \approx 3000$), the weight-average aggregation number continuously increases to about 15 by the end of this stage after most monomers are consumed. It can be predicted that during the first stage only rather small aggregates are formed in the solution.

At the beginning of the second stage of micellization II, the weight-average aggregation numbers experiences strong fluctuations but later, it comes to its equilibrium level (≈ 20), implying that the average size of aggregates have reached the thermodynamically preferred values. N_w keeps relatively stable after $t = 8000$ (stage III), which could be considered as an indication that the system has achieved equilibrium.

It is important to note that micellization is a continuous and slow process, and our purpose in dividing the overall process into different stages is merely to distinguish the most representative pathways of micelle growth. It can be explained by standard aggregation

theory[225] and previous work[242] that micelle formation is driven by the fusion/fission mechanism. Micelle fusion/fission together with the exchanges among monomers and small aggregates all contribute to the slow process of weight-average aggregation number growth/adjustment.

As well as the weight-average aggregation number of the surfactant, the energy and temperature of the system also keep constant at the end of the simulation for HIT3 systems.

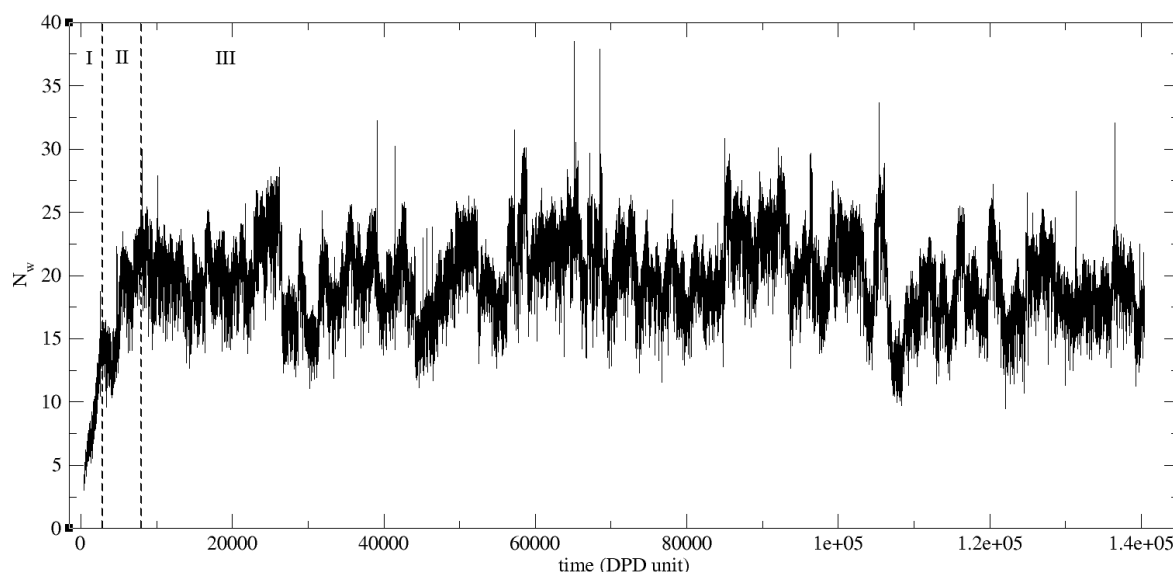
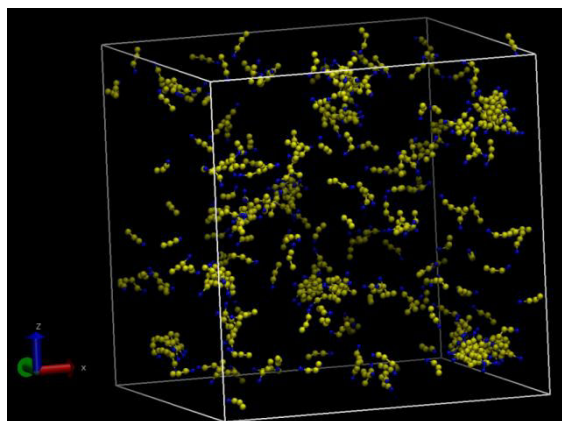
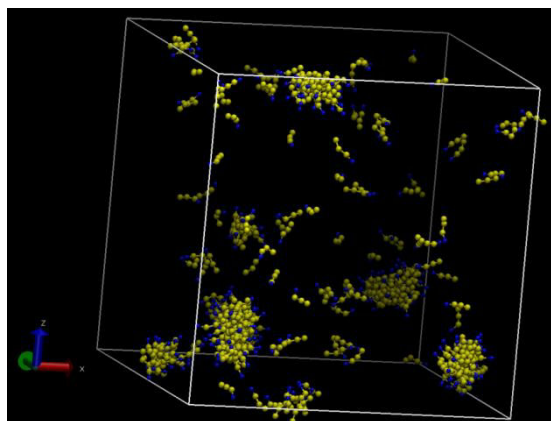


Figure 3 - 8: Weight-average aggregation number N_w as a function of time during the process of micelle formation in a concentrated HIT3 solution ($a_{HT} = 104$, $a_{HW} = 65$, $a_{WT} = 96$, $C_{HIT2} = 0.07 \text{ mol L}^{-1}$). Vertical dashed lines indicate the approximate boundaries between different stages of micellization process.

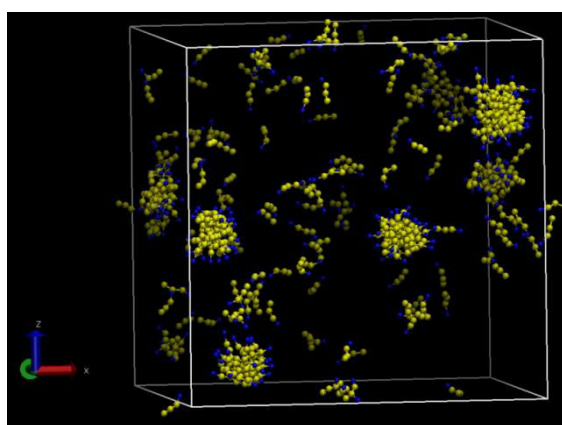
The equilibrium simulation time can be estimated from the evolution of N_w when it reaches the plateau level. For HIT2 system, every simulation ran by 2.0×10^6 time steps ($t = 80000$) to allow the micelles to relax toward their equilibrium structure. The simulations were conducted for an additional 0.5×10^6 time steps ($t = 20000$) to characterize the equilibrium properties of the solution. The equilibration time of HIT3 systems is much longer than that of HIT2 systems due to the slower evolution of longer hydrocarbon chain. Snapshots of the simulation box containing HIT3 molecules at 0.07 mol L^{-1} during the micellization course are shown in Figure 3 - 9. Simulation procedures for HIT3 were run for 3.5×10^6 time steps ($t = 140000$) and the data of the last 0.5×10^6 time steps ($t = 20000$) were collected for analysis.



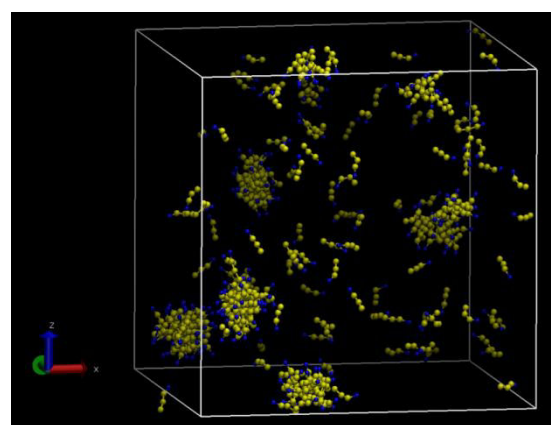
t = 40



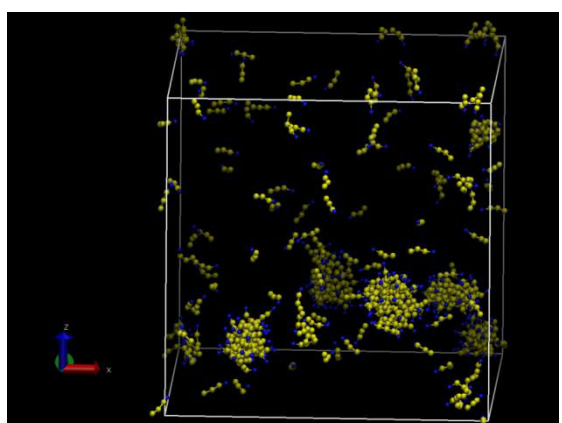
t = 10040



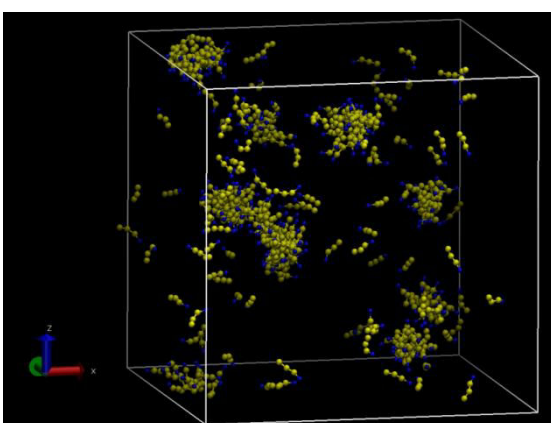
t = 40040



t = 60040



t = 100040



t = 140040

Figure 3 - 9: Snapshots for the simulation box containing H1T3 molecules obtained in the course of micelle formation. The hydrophobic tail bead is shown by yellow balls, the hydrophilic head bead is shown by blue balls, and water beads are not shown, rendered by VMD ($a_{HT} = 104$, $a_{HW} = 65$, $a_{WT} = 96$, $C_{H1T2} = 0.07 \text{ mol L}^{-1}$).

For comparison, the equilibrium time for H1T2 and H1T3 systems together with the total simulation time are listed in Table 3 - 7.

Table 3 - 7: Equilibrium time and total simulation time for H1T2 and H1T3 systems (in DPD units)

	System size	Total beads	Equilibrium time	Total simulation time
H1T2	$20 r_c \times 20 r_c \times 20 r_c$	24000	<10000 time steps	2.5×10^6 time steps
H1T3	$30 r_c \times 30 r_c \times 30 r_c$	81000	200000 time steps	3.5×10^6 time steps

3.3.3.4 Cluster size distribution

We calculated for each system the cluster size distribution (or aggregation number distribution) based on the occurrence probability of a given aggregate (cluster size = N) collected after the equilibrium state was achieved in the simulation. The distribution functions are normalized such that the integral over all aggregation numbers is unity. The maximum of the distribution corresponds to the most probable micelle aggregation number under the specific conditions. The average micelle aggregation number for each surfactant system could be obtained by calculating the average cluster size of micellar aggregates at the peak region in the aggregation number distribution at equilibrium.

Before calculating the average micelle aggregation number, we will use the cluster size distribution to verify the cutoff value R_{agg} we have chosen in section 3.3.3.2. In Figure 3 - 10, we plot the cluster size distribution for H1T2 and H1T3 systems with different cutoff values from 1.0 to 2.0. The cluster size distribution does not change much when the cutoff varies from 1.2 to 1.5 for both surfactants, and the observed difference in the average aggregation number $\langle N_w \rangle$ (including all aggregates and monomers) is less than 10%. For H1T2 system, a value of R_{agg} higher than 1.5 leads to a larger average micellar aggregation number because it increases the probability of two separate aggregates being considered as a single one, and some free dispersed monomers would probably be considered to belong to the aggregates nearby. As illustrated in Figure 3 - 10 a, the probability to find a small aggregates with $R_{agg} = 2.0$ is smaller than that with $R_{agg} \leq 1.5$, but the occurrence probability of large aggregates ($N > 40$) is higher. The selection of R_{agg} between 1.2 and 2.0 does not influence the cluster size distribution of H1T3 system, and the curve with $R_{agg} = 2.0$ exhibits the same tendency with that of $R_{agg} = 1.5$ in Figure 3 - 10 b. So the general cutoff distance of 1.25 for both H1T2 and

H1T3 systems is selected and it could provide reliable estimation of CMC and aggregation number. This cutoff also leads to visual agreement with the distribution of free surfactants and micelles in the system (Figure 3 - 4 and Figure 3 - 9).

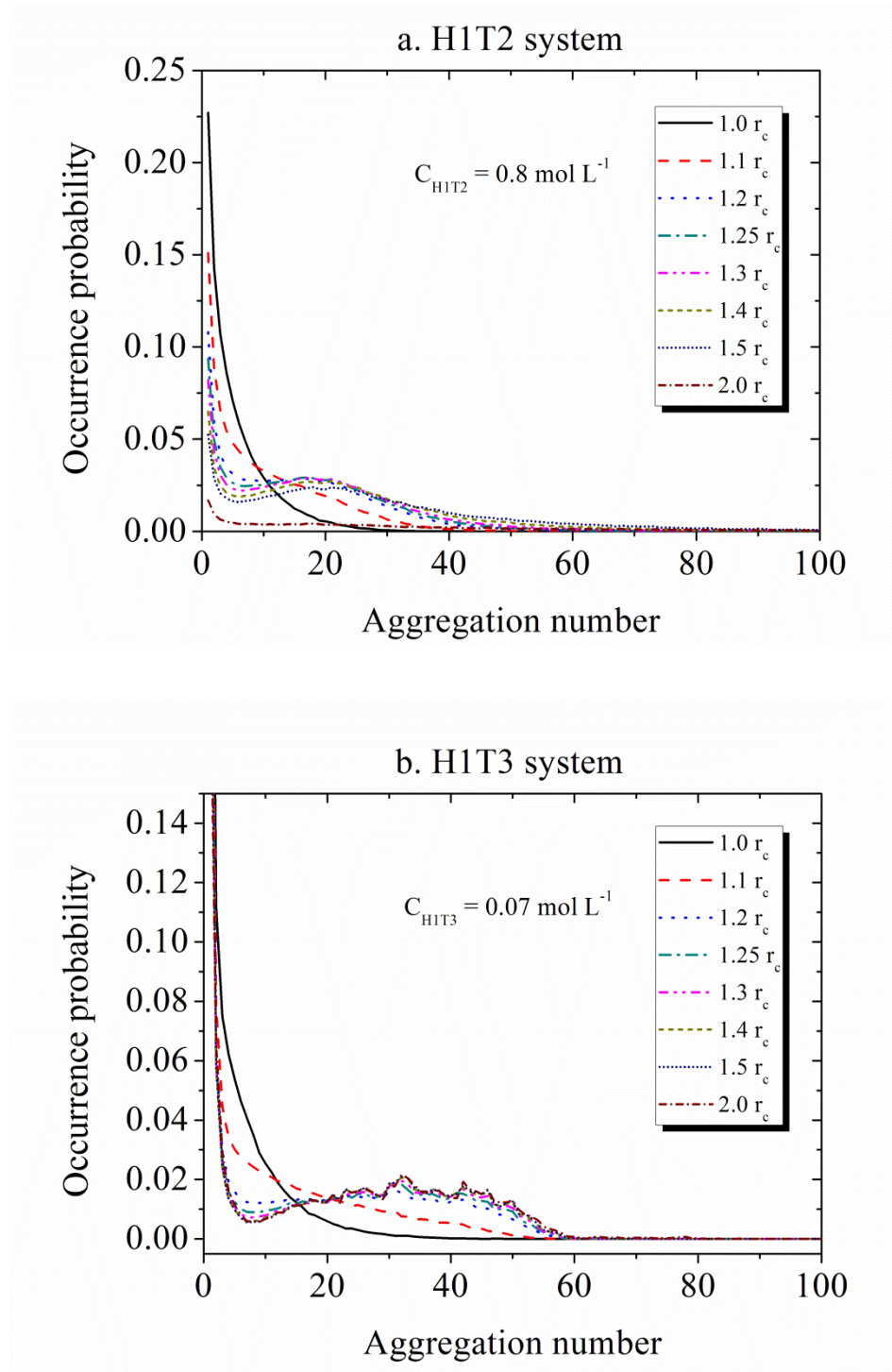


Figure 3 - 10: Cluster size distribution of surfactant solutions with different cutoff values to distinguish the clusters. a. H1T2 system, $C_{H1T2} = 0.8 \text{ mol L}^{-1}$ ($a_{HT} = 104$, $a_{HW} = 65$, $a_{WT} = 98$); b. H1T3 system, $C_{H1T3} = 0.07 \text{ mol L}^{-1}$ ($a_{HT} = 104$, $a_{HW} = 65$, $a_{WT} = 96$).

To investigate the influence of surfactant concentration on the micellization properties, we have performed an analysis of the cluster size distribution of the HIT2 system as a function of overall surfactant concentration, and the results are shown in Figure 3 - 11.

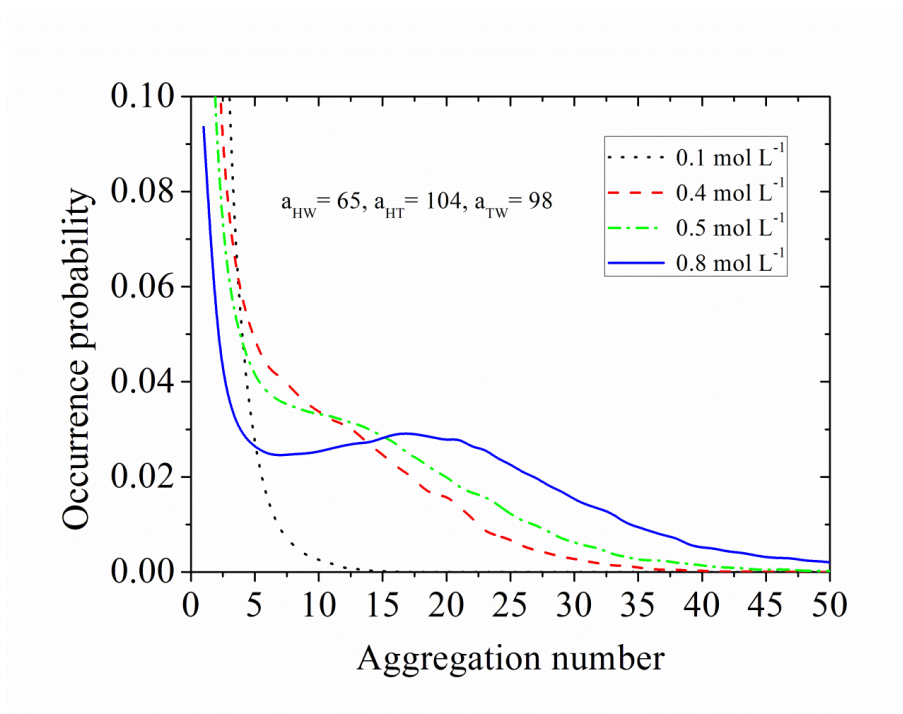


Figure 3 - 11: Cluster size distribution for HIT2 systems with different concentrations at equilibrium ($a_{HT} = 104$, $a_{HW} = 65$, $a_{TW} = 98$).

As can be seen in Figure 3 - 11, there is only one pronounced peak for small cluster size at 0.1 mol L^{-1} because at very low concentrations, the majority of the surfactant molecules in the solution exist in the form of monomers or small aggregates. At total surfactant concentration of 0.4 mol L^{-1} , despite the peak for monomers and small aggregates, a second broad peak emerges in the region between $N = 6$ and $N = 25$, which means pre-micelle aggregates are formed. There is also a slight possibility to find micelles with aggregation number larger than 25. It should be mentioned that the aggregation number of SHS in experimental measurements is 17 at 0.648 mol L^{-1} in literature [117], [128], [251], which falls within the peak region observed in our simulations. For concentrations higher than 0.5 mol L^{-1} , the distribution exhibits two distinct regions, one for small aggregates including monomers ($N \leq 6$) and the other for micellar aggregates ($N \geq 6$), indicating equilibrium between free surfactants and micelles. The peak for micelles occurs in the same region as that for the solution at concentration of 0.4 mol L^{-1} and becomes higher. Though the two peaks are not well

separated due to a relatively small aggregation number for SHS with a short hydrocarbon chain, the appearance of the second peak is a sign for the formation of micelles. We can roughly estimate that the CMC of H1T2, where micelles begin to appear, falls in the concentration region between 0.4 and 0.5 mol L⁻¹, which is in agreement with experimental values between 0.42 and 0.517 mol L⁻¹ for SHS [250], [252].

It can also be observed from Figure 3 - 11 that, the average micelle aggregation number becomes an increasing function of total surfactant concentration, *i.e.*, the mean micelle aggregation number shifts from 17 to 22 while the total surfactant concentration increased from 0.5 mol L⁻¹ to 0.8 mol L⁻¹, the tendency being in agreement with other simulation observations [230], [262] and experimental results [117], [199], [250].

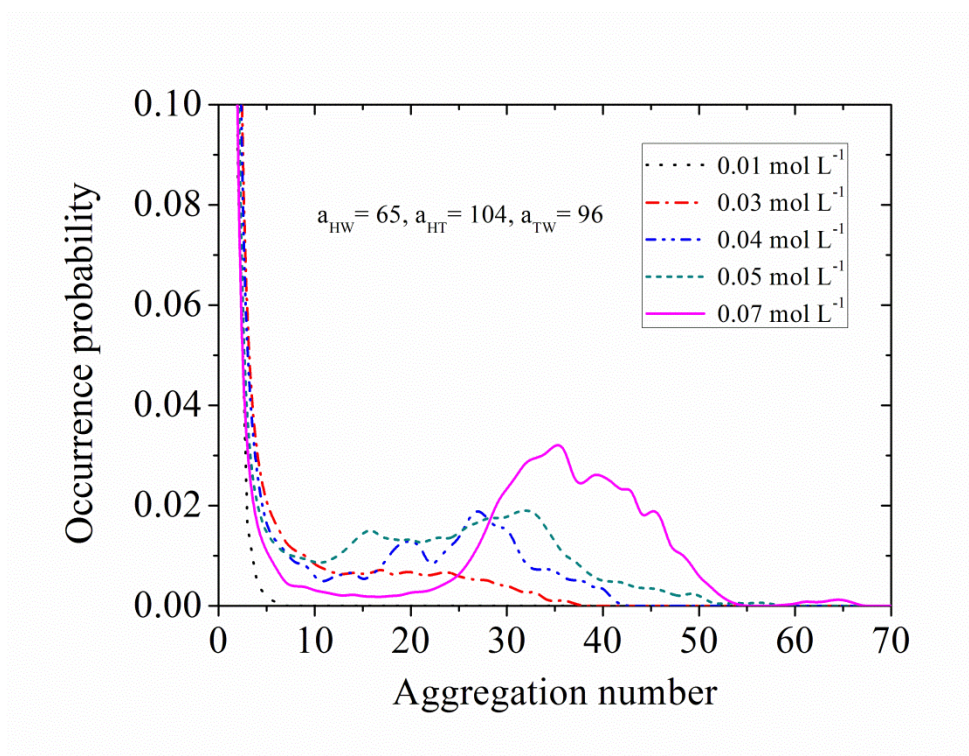


Figure 3 - 12: Cluster size distribution for H1T3 solutions with different concentrations in equilibrium ($a_{HT} = 104$, $a_{HW} = 65$, $a_{WT} = 96$).

Although there is much polydispersity in the cluster size distribution of H1T3 (see Figure 3 - 12) due to slow dynamics for the longer chain compared to H1T2, the cluster size distribution shows similar trends: two peaks are observed for concentrations higher than 0.04 mol L⁻¹, one at a low aggregation number corresponding to free surfactants (including monomers and pre-micelle aggregates) and another at a higher aggregation number

corresponding to the micelles. The CMC of H1T3 could be roughly estimated at between 0.03 and 0.04 mol L⁻¹, since the micelles begin to appear in this concentration region. As shown in Figure 3 - 12, the average micelle aggregation number of H1T3 is somewhat sensitive to the overall concentration as we have observed in the system of H1T2: it shows a similar increase from $N = 25 \pm 1$ to 36 ± 2 as the concentration rises from 0.04 mol L⁻¹ to 0.07 mol L⁻¹. The values of aggregation number are in reasonable agreement with experimental data ($N = 33$ at 0.0402 mol L⁻¹ for SNS) [117], [233].

3.3.3.5 Critical micelle concentration

The CMC, the concentration of surfactant above which micelles are formed spontaneously, is the single most useful quantity for characterizing surfactants, since at that point many important properties of surfactant solution, *e.g.*, surface/interfacial tension, conductivity, osmotic pressure and so on, usually change sharply due to the occurrence of micelles [210]. However, in the literature, the definition of CMC is somewhat arbitrary and may depend on the criteria applied [242], [263], [264].

In the present work, the CMC is obtained from the plot of free surfactant concentration *versus* total surfactant concentration [242]. Based on simple thermodynamics arguments, the equilibrium that the surfactant solution achieves at or above the CMC, represents equilibrium among monomers, small aggregates and micelles. In this study, the free surfactants was defined as the surfactants that exist as monomers and small aggregates up to the cluster size at the minimum between the two peaks of the cluster size distribution (see Figure 3 - 11 and Figure 3 - 12) [225]. The rest of the surfactants are counted as micelles. For the H1T2 system as illustrated in Figure 3 - 13, the concentration of free surfactants increases rapidly when the total surfactant concentration increases from 0.1 mol L⁻¹ to around 0.4 mol L⁻¹. Then it levels off and reaches a plateau upon further increase of the total concentration. The break in the curve (approximately 0.42 mol L⁻¹) is interpreted as evidence of the formation of surfactant micelles at that point from the unassociated state, hence corresponding to the CMC. Nevertheless, the free surfactant concentration at the plateau level is lower than the CMC value because of the contribution of probable occurrence of micelles, which could be confirmed by the fact that the cluster size distributions are not very well separated in Figure 3 - 11.

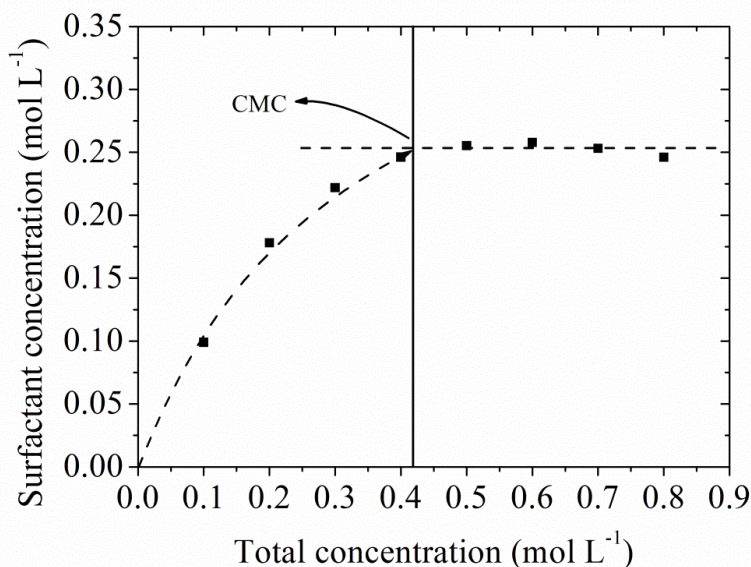


Figure 3 - 13: The concentration of free surfactants versus the total concentration of H1T2. The vertical line corresponds to the estimated CMC $\approx 0.42 \text{ mol L}^{-1}$ ($a_{HT} = 104$, $a_{HW} = 65$, $a_{WT} = 98$).

In the later part of this work, the CMC will be identified with a point at which a break in the slope of the free surfactant concentration *versus* total surfactant concentration occurs. Similar definitions of free surfactant concentration have provided a reasonable approximation to the CMC [242], [259].

3.4 Results and discussion

In this part, we will compare the results obtained using the parameter set in Table 3 - 3 from Groot's work [257] to experimental data, and then develop a method to choose an appropriate parameter set for the simulations of our target components. The quantities to compare are the CMC and average micelle aggregation number of the two surfactants. After the validation of the parameter set, a series of simple tests for adding a membrane to the surfactant system were performed to investigate the adsorption of surfactants on the membrane.

3.4.1 Parameter set I

A successful DPD simulation of a mesoscopic system depends on the appropriate selection of conservative bead-bead interaction parameters. Since Groot and Warren [11] established an

important link between conservative interaction parameters and the Flory-Huggins χ parameter for polymer solutions in 1997, a great amount of work has been focused on the approximation of conservative interaction parameters from the χ parameter [265], [266], [267], [268].

At the beginning of the study, we selected the initial conservative parameters in Table 3 - 3, which was appropriate for a phospholipid system. Considering the difference between the head group of the sodium sulfates in our study and that of the phospholipid, we just applied this parameter set for test.

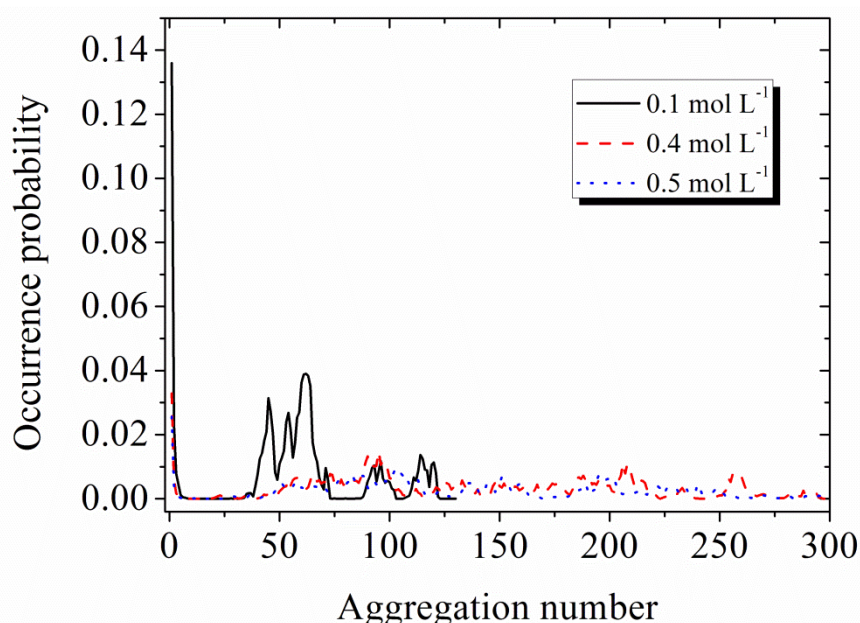


Figure 3 - 14: Cluster size distribution for HIT2 system with different concentrations in equilibrium, using Groot's parameters ($a_{HT} = 104$, $a_{HW} = 75.8$, $a_{WT} = 104$).

The cluster size distributions of three HIT2 systems at different concentrations are plotted in Figure 3 - 14. Even at very low concentration of 0.1 mol L^{-1} , the curve exhibits a proper micelle peak with a maximum around aggregation number $N = 62$. The predicted average aggregation number was three times larger than the literature value 17 [117], [128], [233], [251]. The corresponding snapshot at this concentration is illustrated in Figure 3 - 15. It is clear that a large micelle was formed at the end of simulation in this condition. At higher concentrations, the probability of finding large micelles became higher and the average aggregation number increased to nearly 98 at 0.4 mol L^{-1} and even 119 at 0.5 mol L^{-1} (Table 3

- 8). The estimated CMC for these strongly micellizing systems with larger aggregation numbers, was much lower than experimental value of 0.42 mol L^{-1} .

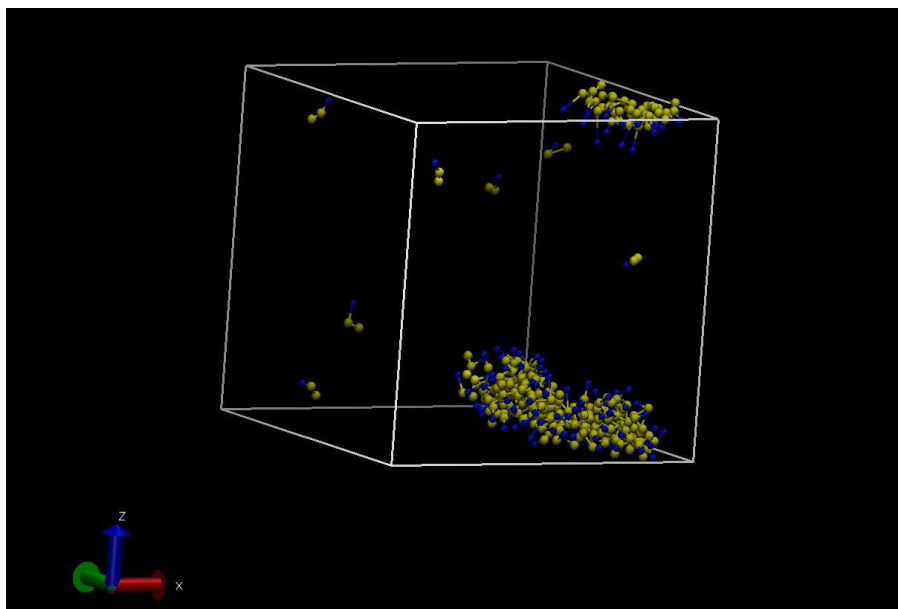


Figure 3 - 15: Snapshot of HIT2 system at equilibrium, using Groot's parameters ($a_{HT} = 104$, $a_{HW} = 75.8$, $a_{WT} = 104$, $C_{HIT2} = 0.1 \text{ mol L}^{-1}$).

Table 3 - 8: Values of the aggregation numbers for sodium hexyl sulfate calculated from DPD simulation at different concentrations, using Groot's parameter set I ($a_{HT} = 104$, $a_{HW} = 75.8$, $a_{WT} = 104$)

Concentration (mol L^{-1})	0.1	0.4	0.5	0.648 (Experimental data) [233]
Aggregation number by DPD	62	98	119	17

Similar disagreement of the CMC for HIT3 from this simulation and experimental data was also observed (Table 3 - 9). From the above validation, we deduce that the parameter set of Groot is not suitable for our target components.

Table 3 - 9: Experimental and simulation data of CMCs (mol L^{-1}) for H1T2 and H1T3 at 25 °C

Molecular formula	Mesostructure in DPD	CMC calculated by DPD parameter set I	CMC by experiment	Reference
$\text{C}_6\text{H}_{13}\text{NaSO}_4$	H1T2	< 0.1	0.42	[250]
			0.517	[252]
$\text{C}_9\text{H}_{19}\text{NaSO}_4$	H1T3	< 1.0×10^{-2}	6.0×10^{-2}	[250], [253]
			6.46×10^{-2}	[254]

3.4.2 Effect of DPD parameters on micellar properties

As the CMC definition is based on the aggregation number distribution in this study, a reliable average aggregation number consistent with literature values is the precondition to produce realistic results for CMC values. In order to modify the model with parameter set I to improve the agreement with experimental values for a real ionic surfactant solution, the influence of repulsive interaction parameters a_{ij} on the CMC and average aggregation number was investigated.

To find appropriate interaction parameters for anionic alkyl sulfates, we adjusted the χ parameters cited in literature. The χ parameters for each pair of bead-bead interactions and the corresponding a_{ij} calculated from Equation 3 – 7 are listed in Table 3 - 10. For the sake of simplicity, we assumed that the repulsion parameter between water-water beads (a_{WW}) and between tail-tail beads (a_{TT}) were the same as in Groot's work [257]. Considering the partial charges on the head beads of the anionic surfactant molecules, electrostatic interactions were implicitly taken into account by increasing the repulsion between the head groups, thus $a_{\text{HH}} = 86.7 > a_{\text{TT}} = a_{\text{WW}} = 78$. It should be noted that here we ignored the counterions in the system, but the effect of the head groups is supposed to more significant when the chain is short.

For all other repulsive parameters, the range investigated has been chosen in agreement with typical values in the literature. The pertinent χ parameter between hydrocarbon (per carbon atom) and water $\chi_{\text{carbon-water}}$ is reported to be between 1.6 and 2.0, determined by matching the solubility data of oil in water and vice versa [257], [269]. In the present study, repulsion parameter between tail and water beads a_{WT} , varied from 92 to 104, was derived

from $\chi_{TW} = 3.0$ to 6.0 ($\chi_{carbon-water} = 1.0$ to 2.0), corresponding to three water molecules or carbon atoms in the T bead. The sulfate head group of the surfactant molecule, H, is miscible with water, thus the χ parameter describing the interaction between head bead and water is varied from -3 to -0.5 . Only sparse experimental data is available to estimate the interaction between sulfate head and hydrocarbon tail groups. To study the influence of this parameter, we varied a_{HT} from 84 to 124 , corresponding to a reasonable value of χ_{HT} between 1.5 and 10.5 .

Table 3 - 10: Derivation of parameter set II used in our simulation systems

<i>Bead-bead</i>	χ	a
H - H	2	86.7
H - T	1.5 to 10.5	84 to 124
H - W	-3 to -0.5	65 to 75.8
T - T	0	78
T - W	3 to 6	92 to 104
W - W	0	78

In the parameterization procedure, we kept the value for water-tail repulsion parameter (a_{TW}) to be 104 , the same with that used in Groot's work, because the structure in the tails are the same for phospholipid and the surfactants in our work. Since the head group chemistry of sodium alkyl sulfates is different from that of the phospholipid, we adjusted the interactions a_{HW} and a_{HT} first. We varied a_{HW} from 75.8 to 65 (χ_{HW} from -0.5 to -3), and for each a_{HW} set, we varied a_{HT} from 84 to 124 . Though $\langle N_w \rangle$ (including all aggregates and monomers) is not the same as the average aggregation number for micelles, it is valuable to investigate the effects of each repulsive interaction parameter.

The dependence of average aggregation number $\langle N_w \rangle$ on the two interaction parameters for H1T2 at 0.5 mol L^{-1} is shown in Figure 3 - 16. It can be seen that the average aggregation number $\langle N_w \rangle$ increases with a_{HW} when a_{HT} is fixed. With a value of $a_{HT} = 124$, $\langle N_w \rangle$ increases from 26 to 41 as a_{HW} increases from 65 to 75.8 . The increasing tendency in $\langle N_w \rangle$ with increasing a_{HW} is observed to be more rapid for smaller a_{HT} systems. With a value of $a_{HT} = 84$, $\langle N_w \rangle$ increases from 73 to 636 as a_{HW} increases from 65 to 75.8 . The variation of a_{HW} can be used to present the hydrophilicity of the head group if the surfactants have the same

hydrophobic tail. A weaker repulsion between head groups and water indicates a more hydrophilic head group, which is more soluble in water. In the simulation, if the surfactant model has a smaller a_{HW} , surfactant molecules tend to stay in water and are more difficult to migrate from the bulk to self-assemble into micelles. Therefore, a smaller a_{HW} corresponds to a smaller aggregation number, and a larger CMC.

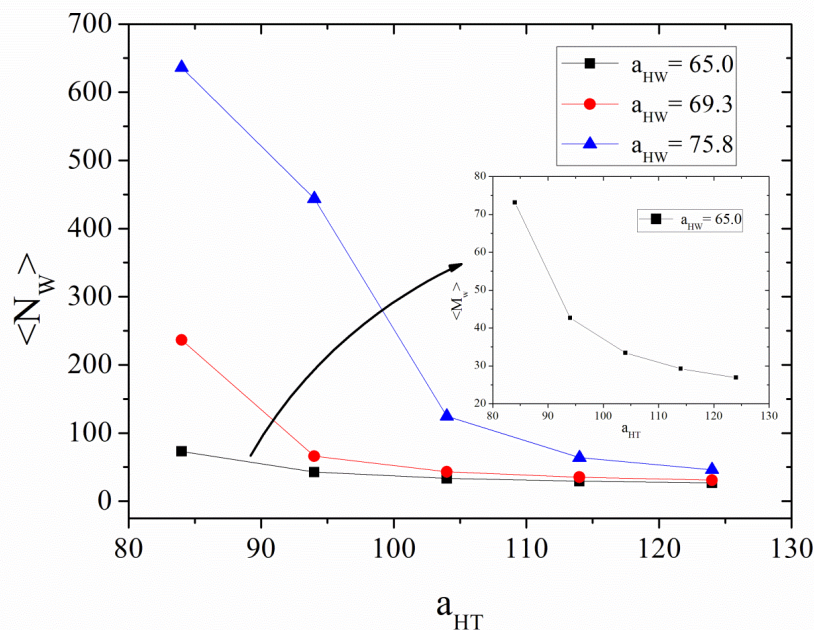


Figure 3 - 16: Average aggregation number versus head-tail interaction parameter (a_{HT}) and head-water interaction parameter (a_{HW}). $a_{WT} = 104$ and $C_{HIT2} = 0.5 \text{ mol L}^{-1}$. The inset shows the plot of $a_{HW} = 65$ at small scales.

The effect of a_{HT} on the micellization properties of surfactants has rarely been investigated in the literature. Previous work used values $a_{HT} = a_{WT}$, considering the head group interacts with tail groups as water bead does [257]. However, we studied on different values for a_{HT} here. Since the repulsive interactions between head and tail beads can be intermolecular and intramolecular, the intramolecular effect depends also on bond spring force. In Figure 3 - 16, the bond spring constant between the connected beads $k = 100$ is huge and limits the intra H-T repulsion forces. In this case, a_{HT} might play a more important role in the interactions between intermolecular head and tail beads. The structure of the molecules would be affected and thus the distance between surfactant molecules. As illustrated in Figure 3 - 16, the average

aggregation number decreases with a_{HT} . A huge $\langle N_w \rangle$ is observed to be 636 when $a_{HT} = 84$, while it decreases to 41 when $a_{HT} = 124$. A larger a_{HT} means a stronger repulsion between intermolecular head-tail beads, thus it is difficult for surfactant molecules to get close to each other and form micelles. Therefore, the average aggregation number decreases with the increase of a_{HT} . The large N_w value 636 at the point of $a_{HT} = 84$ and $a_{HW} = 75.8$ corresponds to the total number of surfactants in the system. It seems that the system totally demixes and that no micellization occurs at all. Also, on the left of the curve of $a_{HW} = 75.8$ in Figure 3 - 16, a_{HT} is smaller than a_{HH} . Therefore, surfactants can "pack" together if a_{HW} repulsion is too high.

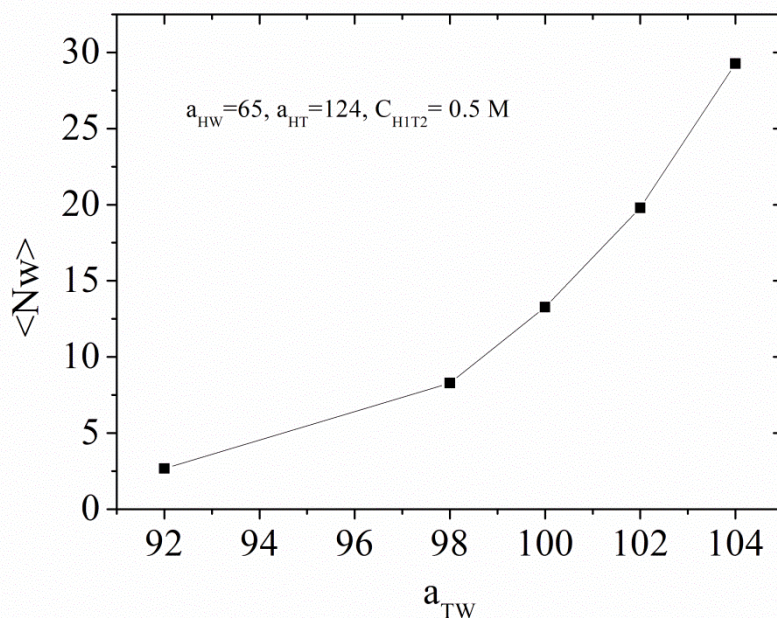


Figure 3 - 17: Average aggregation number of HIT2 versus tail-water interaction parameter a_{TW} ($a_{HW} = 65$, $a_{HT} = 124$, $C_{HIT2} = 0.5 \text{ mol L}^{-1}$).

Because the aggregation number for SHS is reported to be small, we selected the parameters $a_{HW} = 65$ and $a_{HT} = 124$ which give a relatively small $\langle N_w \rangle$ as shown in Figure 3 - 16, and then changed the repulsion parameter between tail and water beads a_{TW} . The influence of a_{TW} on $\langle N_w \rangle$ is illustrated in Figure 3 - 17. Similar to a_{HW} , the variation of a_{TW} is used to describe the hydrophobicity of the surfactant molecules. A larger a_{TW} means stronger repulsion between tail group and water, thus poorer solubility in water. Therefore, surfactant molecules with larger a_{TW} are able to migrate from the liquid phase more easily, and form larger micelles or form micelles at lower concentrations, indicating a lower CMC. As shown in Figure 3 - 17,

the surfactant with $a_{TW} = 92$, which corresponds to a lowest repulsion between tail group and water in this series of simulations, has a smallest average aggregation number of only 2.5. $\langle N_w \rangle$ increases to 30 when a_{TW} increases to 104.

From the above discussion, we can conclude that, in general, the CMC in aqueous media decreases as the hydrophobic character of the surfactant increases. Increasing the interaction parameter a_{HW} or a_{TW} makes it easier for surfactant molecules to migrate from water and to form micelles, leading to a bigger aggregation number and correspondingly a smaller CMC. The parameter a_{HT} would affect the interaction between intermolecular head and tail beads in the way that a higher value of a_{HT} with stronger repulsion will cause a smaller aggregation number and a higher CMC.

3.4.3 Effect of intramolecular interactions

The bonding constant k_r and r_0 control the stiffness of the surfactant molecules. The harmonic spring force plays an important role in the micellization of surfactants. It is expected that with a larger spring constant k_r , the surfactant molecules are more rigid. Thus the distance between centers of mass is larger. If k_r is small, large intramolecular repulsive interactions will act between the bonded surfactant beads and intermolecular repulsive interaction will dominate the aggregation of surfactants. As observed in Figure 3 - 16, increasing the repulsive interaction between surfactant head and tail beads will decrease the aggregation number of the micelles and increase the CMC.

To investigate the influence of the intramolecular interactions on the micellization properties, we plotted the cluster size distribution at different surfactant concentrations with different bonding parameters in Figure 3 - 18. The two bonding parameter sets are: (1) $k_r = 4$, $r_0 = 0$; (2) $k_r = 100$, $r_0 = 0.7$ as mentioned in section 3.3.2. Repulsion parameter set I was chosen with the bending constant $k_\theta = 6$, $\theta = \pi$.

As can be seen, with the same angle bending in the surfactant molecules, the surfactants tend to form larger aggregates when k_r is smaller. It is reasonable because, when k_r is small, the intramolecular harmonic forces between connected beads in the surfactant molecule are weak. The average distance between head and tail beads was shorter when $k_r = 4$ than $k_r = 100$. So surfactant molecules are more easily to get close to each other. The same shorter distance with a smaller k_r could be observed in the RDF of surfactant center of mass $g(r)_{CM-CM}$ as

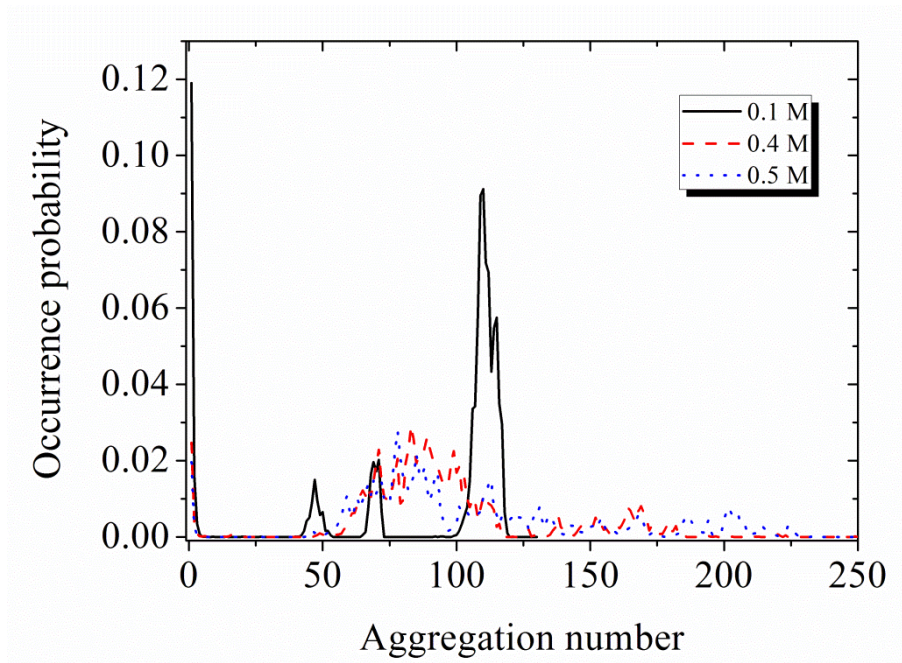
illustrated in Figure 3 - 19. So the average aggregation number $\langle Nw \rangle$ at 0.1 mol L^{-1} is much larger when $k_r = 4$ than $k_r = 100$. But the average aggregation number $\langle Nw \rangle$ shows no obvious difference when the concentration is higher than 0.4 mol L^{-1} , with both the spring constant $k_r = 4$ or $k_r = 100$ as listed in Table 3 - 11.

For another parameter set III, the same trend that a smaller k_r led to larger average aggregation number was observed for all the three concentrations investigated in this study as illustrated in Figure 3 - 20 and Table 3 - 12.

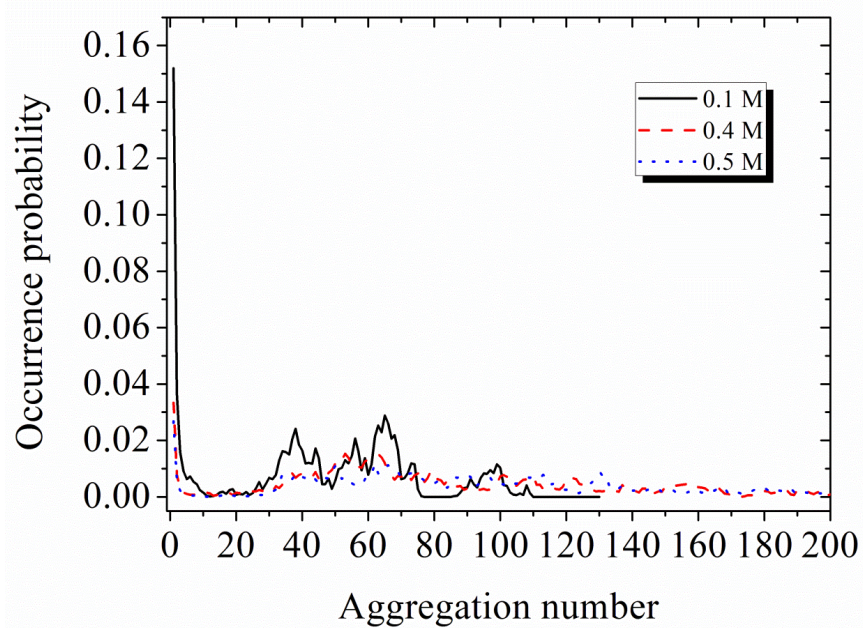
The effect of angle bending is also investigated. As can be seen in Table 3 - 11, with angle bending, the average aggregation number is larger at low concentrations (0.1 mol L^{-1}) when the spring constant k_r is 4, compared to the value when there is no angle bending. However, the average aggregation number is smaller at high concentrations with angle bending. It is indicated that when there is no angle bending in the surfactant molecules, the surfactants self-assemble into larger micelles at higher concentrations. In addition, when there is no angle bending in the surfactant molecules, the radial distribution function for surfactant centers of mass $g(r)_{\text{CM-CM}}$ is not well structured, showing only one peak. The $g(r)_{\text{CM-CM}}$ for surfactant molecules with angle bending shows structured curves with several peaks after the first peak at 0.78. So in the following simulations, we added the angle bending to properly describe the rigidity of the surfactant molecules.

Table 3 - 11: Aggregation numbers for H1T2 with different intramolecular interaction sets ($a_{\text{HT}} = 104$, $a_{\text{HW}} = 75.8$, $a_{\text{WT}} = 104$)

Concentration (mol L ⁻¹)	$k_r = 4$	$k_r = 4$	$k_r = 100$	Literature value
	$r_0 = 0$ No angle bending	$r_0 = 0$ $k_\theta = 6$ $\theta = \pi$	$r_0 = 0.7$ $k_\theta = 6$ $\theta = \pi$	
0.1	56	88	44	-
0.4	157	95	98	-
0.5	198	111	123	17
Estimated CMC (mol L ⁻¹)	$\ll 0.1$	< 0.1	< 0.1	0.42



A



B

Figure 3 - 18: Cluster size distribution for H1T2 system with different intramolecular interactions at equilibrium, using Groot's parameter set in Table 3 - 3 ($k_\theta = 6$, $\theta = \pi$). A. $k_r = 4$, $r_0 = 0$; B. $k_r = 100$, $r_0 = 0.7$.

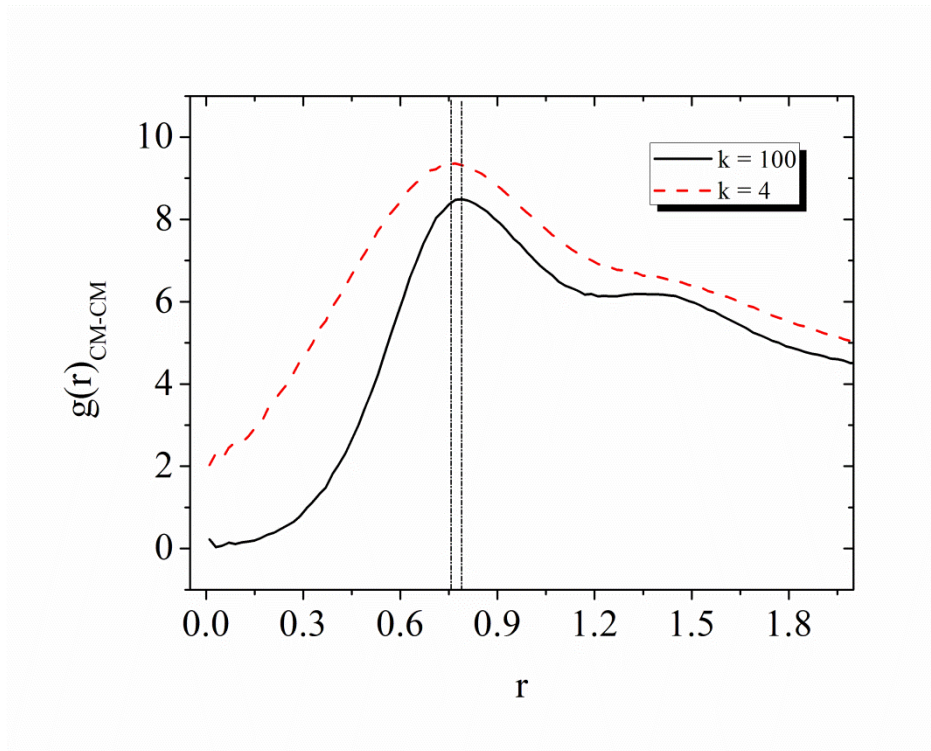


Figure 3 - 19: $g(r)_{\text{CM-CM}}$ of HIT2 systems with different bonding parameter sets

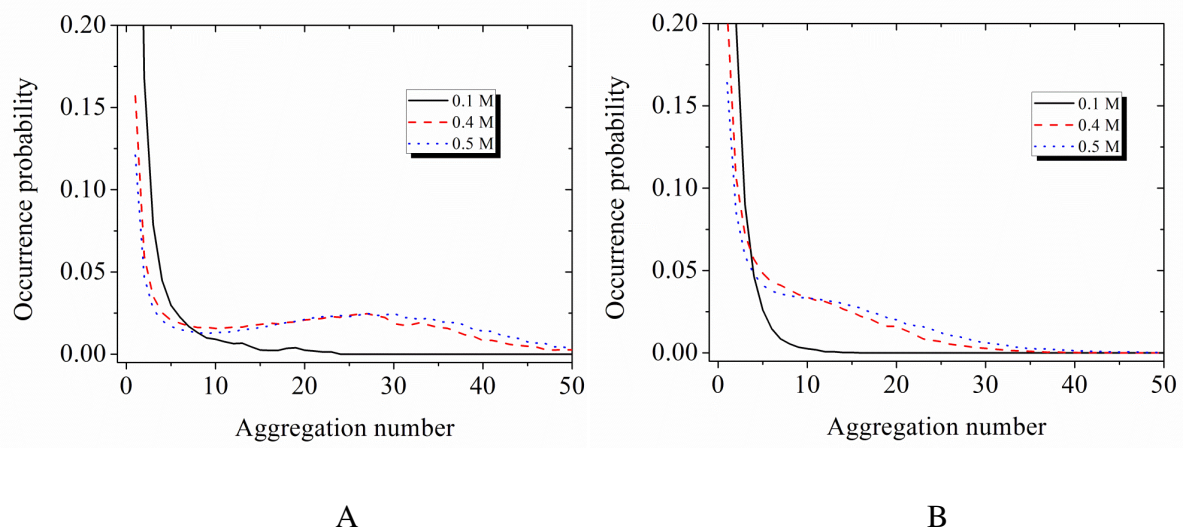


Figure 3 - 20: Cluster size distribution for HIT2 system with different intramolecular interactions at equilibrium, using parameter set III ($k_0 = 6$, $\theta = \pi$). A. $k_r = 4$, $r_0 = 0$; B. $k_r = 100$, $r_0 = 0.7$.

Table 3 - 12: Average aggregation numbers $\langle N_w \rangle$ for H1T2 with different intramolecular interaction sets ($a_{HT} = 104$, $a_{HW} = 65$, $a_{WT} = 98$)

	$k_r = 4$	$k_r = 100$	
Concentration (mol L ⁻¹)	$r_0 = 0$	$r_0 = 0.7$	Literature value
	$k_\theta = 6$	$k_\theta = 6$	
	$\theta = \pi$	$\theta = \pi$	
0.1	2.7	1.9	-
0.4	18	8.3	-
0.5	21	10.5	17
Estimated CMC (mol L ⁻¹)	$\ll 0.1$	< 0.1	0.42

From the above discussion, it can be demonstrated that there is a balance between intramolecular and intermolecular interactions, which controls the local structure and micellization properties of the surfactants in the solution. Adjustment can be done using both N_{agg} and CMC and parameters act differently on these two distinct properties. Intermolecular interactions (conservative forces) influences the CMC more pronounced on the CMC, but the intramolecular interactions (bonding, bending and repulsive interactions) can modify the aggregation number from a subtle way. An increase in the repulsive parameter a_{HT} will increase the CMC, especially with a large k_r value, because surfactant molecules are difficult to get close to each other with strong repulsion between them, micelles cannot form unless the concentration reaches a high value. The trivial effect of bonding and bending constants on the aggregation number is explained that, increasing k_r will reduce the average distance between bonded beads in surfactant molecules, in this case, the repulsive interaction dominates the micellization with other surfactant molecules.

3.4.4 CMC of surfactants

The CMC of H1T2 is appropriately predicted after adjustment of DPD parameters. The selected parameter set of the optimization of the CMC and aggregation number is listed in Table 3 - 13. In these conditions, the parameter set III with bonding and bending parameters as follows: $k_r = 100$, $r_0 = 0.7$, $k_\theta = 6$, $\theta = \pi$ is the best fit set to provide a CMC value (0.42 mol L^{-1}) similar to experimental values for SHS, reported from ultrasonic relaxation (0.42 mol L^{-1}) [250], electrical conductivity experiments (0.517 mol L^{-1}) [252] and an atomistic simulation (0.46 mol L^{-1}) [230]. The calculated average aggregation number for H1T2 micelles is 17, in good agreement with the experimental value of 17 [117], [128], [251].

Table 3 - 13: Bead–bead repulsion parameter set III used in for the optimization of H1T2 systems

a_{ij}	H	T	W
H	86.7		
T	104	78	
W	65	98	78

In order to evaluate the transferability of the interaction parameters, the same parameter set (Table 3 - 13) is applied to H1T3 system. Similarly, we determined the value of CMC for H1T3 by plotting the curves of the free surfactant concentration *versus* the total surfactant concentration. Unexpectedly, the calculated average aggregation number of H1T3 micelles (about 48 at 0.04 mol L^{-1}) is larger than experimental value of SNS ($N = 33$) [117], [128], [251], and micelles occur at lower concentrations (lower than 0.04 mol L^{-1}) than the experimental CMC values (0.06 to $0.0646 \text{ mol L}^{-1}$) [250], [253], [254], [255]. The cluster size distributions of three H1T3 systems at different concentrations (0.04 , 0.06 and 0.07 mol L^{-1}) are illustrated in

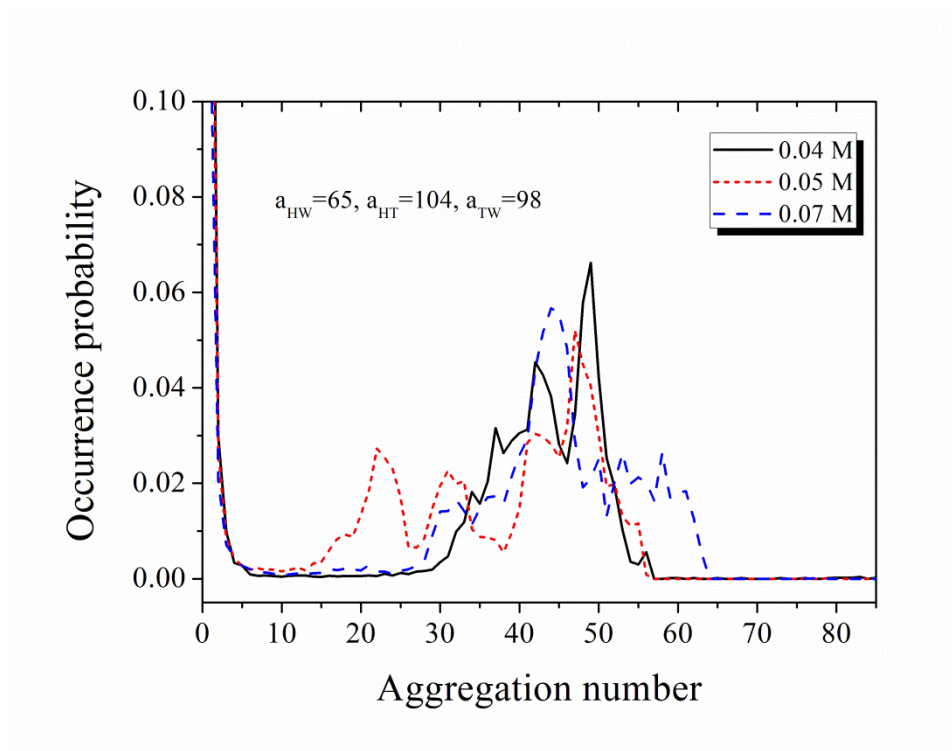


Figure 3 - 21: Cluster size distributions for HIT2 systems with different concentrations at equilibrium, using parameter set III ($a_{HT} = 104$, $a_{HW} = 65$, $a_{TW} = 98$).

Table 3 - 14: Bead–bead repulsion parameter set IV used in for the optimization of HIT3 systems

a_{ij}	H	T	W
H	86.7		
T	104	78	
W	65	96	78

To obtain a smaller aggregation number and a larger CMC, we decreased a_{TW} to 96 (parameter set IV in Table 3 -14), in anticipation of a better agreement with experimental values. The results turned out to be acceptable. The calculated average aggregation number for HIT3 is between 25 and 36 at concentrations between 0.04 and 0.07 mol L⁻¹, in reasonable agreement with experimental value of 33 [117], [128], [251].

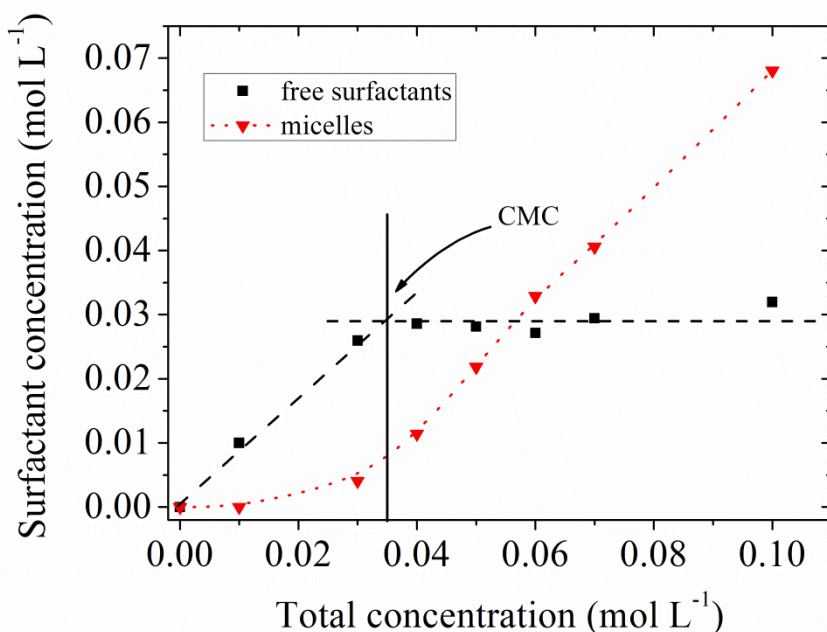


Figure 3 - 22: The concentration of free surfactants and micelles versus the total concentration of H1T3. The vertical line corresponds to the estimated CMC $\approx 0.035 \text{ mol L}^{-1}$ ($a_{\text{HT}} = 104$, $a_{\text{HW}} = 65$, $a_{\text{WT}} = 96$).

The calculated CMC with $a_{\text{TW}} = 96$, is identified at the turning point in the curve of the free surfactant concentration against total surfactant concentration, as indicated in Figure 3 - 22, to be 0.035 mol L^{-1} . Another curve of the concentration of surfactants in micelles is also plotted against the total surfactant concentration in Figure 3 - 22. This curve keeps parallel to the horizontal axis at low total surfactant concentrations and then experiences a sudden increase. The break occurs almost at the same concentration where the curve of free H1T3 concentration with cluster size $N \leq 11$ reaches a plateau. The break in both curves could be regarded as a sign of the appearance of micelles. The estimated CMC at 0.035 mol L^{-1} is somewhat underpredicted for H1T3, compared to CMC values obtained by experiments from ultrasonic relaxation studies (0.06 mol L^{-1}) [250], UV-VIS measurements (0.06 mol L^{-1}) [253] and electrical conductivity measurement ($0.0646 \text{ mol L}^{-1}$) [254], [255].

The parameter set IV was also applied to H1T2 systems to verify if it is fit for both surfactant systems. The results of CMC values and aggregation numbers for H1T2 and H1T3 systems obtained from different parameter sets are listed in Table 3 - 15. Compared to experimental data, it is indicated that parameter set III provides better agreement for the

simulations of H1T2 systems with the experiments, but for H1T3 systems, the parameter set IV seems much better. The difference of the two parameter sets might be due to the coarse-graining of the tail beads. Simulations on longer chains with the same head group (H1T4) are under testing for verifying the parameter sets.

Table 3 - 15: CMC values and aggregation numbers for H1T2 and H1T3 systems with different a_{ij} parameter sets

Parameter set	H1T2		H1T3	
	III	IV	III	IV
CMC (mol L ⁻¹)	0.42	0.61	<< 0.04	0.035
Aggregation number	17 (at 0.5 mol L ⁻¹)	12 (at 0.7 mol L ⁻¹)	48 (at 0.04 mol L ⁻¹)	25 to 36 (at 0.04 to 0.07 mol L ⁻¹)

The numerical discrepancy can be attributed to a few possible reasons. The aggregation number of H1T3 is not large enough, so it is difficult to separate the small aggregates and micelles completely. The definition of free surfactants is difficult in some simulations, especially when the peaks of free surfactants and of micelles in the cluster size distribution are not clearly separated, as shown in Figure 3 - 12.

Even though each a_{ij} parameter is selected from reasonable range of experimental values, the parameterization for the model is still somewhat arbitrary. More specific care should be taken into the detailed chemical structure and solubility when selecting the repulsive parameters from optimal values. Another reason could be a lack of counterions that are taken here into account implicitly. In section 3.4.2, we have simplified the model by increasing the H-H beads repulsion to include the electrostatic interactions between head groups. The change in counterion entropy contributions caused by counterion condensation effects due to micelle formation will affect the free surfactants as the total surfactant concentration becomes higher, and electrostatic effects play an important role for the free surfactant behavior. Thus, association between micelles and counterions also could be taken into account for the refinement of this model.

3.4.5 Adsorption of surfactants on the membrane

To prove our model further and investigate the adsorption of anionic surfactants on polymeric membranes, we applied the parameter set III (see Table 3 - 16) to H1T2 and H1T3 system with a simplified membrane for DPD simulation, using the software Material Studio 5.5. The reason why we did not choose SDS as in Chapter 2 as our target surfactant was that the simulation for this long chain H1T4 took considerably more time (more than 30 days) than H1T2/H1T3 and it required an enormous simulation system (about 810000 beads in the simulation box) for allowing enough surfactant molecules around its CMC (around 8.0 mmol L⁻¹). From the micellization of H1T2 and H1T3 in the precedent section, it can be deduced that there are close relations between surfactants in this series in the micellar properties, and hopefully, the adsorption mechanism of surfactants with shorter chains onto membranes could provide information and guidance for the investigation of SDS adsorption onto polymeric membranes as in chapter 2.

In the present work, the simulation box ranged in size of $20r_c \times 20r_c \times 20 r_c$ (for H1T2 systems, but $30r_c \times 30r_c \times 30 r_c$ for H1T3 systems) in which periodic boundary conditions were implemented in all dimensions. Since the RO membrane in our experimental part is dense and smooth, it was simplified as a smooth hydrophobic solid plane at $z = 0$ in the cubic DPD simulation box, as seen in Figure 3 - 23. Due to periodic boundary conditions, the upper surface of box at $z = 20$ for H1T2 system ($z = 30$ for H1T3 system) is also represented as the membrane. It should be noted that more rigorous constructions of the polymeric membrane with more precise structures as proposed in Figure 2 - 1 is expected, including both polar and apolar beads. This might be realized by the simulation package NEWTON in a future work.

In order to test the model's ability to predict adsorption properties, we developed a general DPD parameter set for the surfactants and membrane as an extension to our previously validated model. The negatively charged SG membrane, acting as a hydrophobic solid wall, showed repulsive interaction with the head beads of the anionic surfactants through electrostatic interactions, while it showed attractive interaction with the tail beads through hydrophobic interactions. The parameter set for the simulation of adsorption of surfactants H1T2 and H1T3 onto the membrane is listed in Table 3 - 16. Parameters for H, T, and W beads are the same with those in Table 3 -13 for H1T2 systems. The interactions concerning the membrane were set as follows (M represents the membrane): $a_{HM} = 104$ to represent the

repulsive interaction between the negatively charged head beads and the membrane surface, $a_{WM} = 78$ considering that the membrane did not interact with water beads. Intramolecular bonding and bending parameters were chosen as: $k_r = 100$, $r_0 = 0.7$, $k_\theta = 6$, $\theta = \pi$. In contrast to a_{HM} , a_{TM} strongly affects the adsorption and aggregation morphologies of surfactants on solid surfaces, and correspondingly, in this work, we varied the values of a_{TM} to study its influences on surfactant adsorption. The time step is set as $\Delta t = 0.05$. Other simulation parameters are the same as in section 3.3.2.

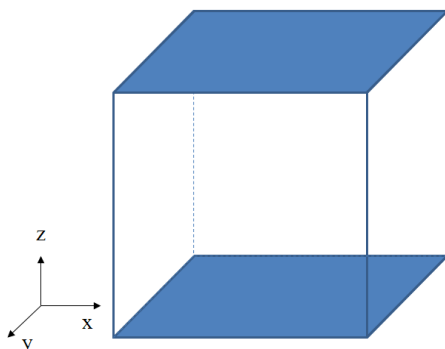


Figure 3 - 23: Simulation box for the adsorption of surfactants on the membrane. The membrane is represented as a simplified plane at $z = 0$. Due to periodic boundary conditions, the plane at the top of this box is also considered as the membrane.

Table 3 - 16: Bead-bead repulsion parameter set used in the simulation of surfactant adsorption

a_{ij}	H	T	W	M
H	86.7			104
T	104	78		65 to 78
W	65	98	78	78

3.4.5.1 The effect of a_{TM}

Simulations were performed for 1000000 time steps ($t = 50000$) for both H1T2 and H1T3 systems. This was the longest simulation time that Material Studio permitted. From configurations of different systems, we can consider that all systems have achieved equilibrium at $t = 50000$. Although the trajectory is impossible to obtain from the commercial software at the moment, discussions based on morphologic snapshots along with the simulation courses were accessed for investigating the organization of the surfactant molecules in the solution and on the membrane-solution interface. Firstly we will study the

effect of the interaction between surfactant tail beads and the membrane a_{MT} on the adsorption process.

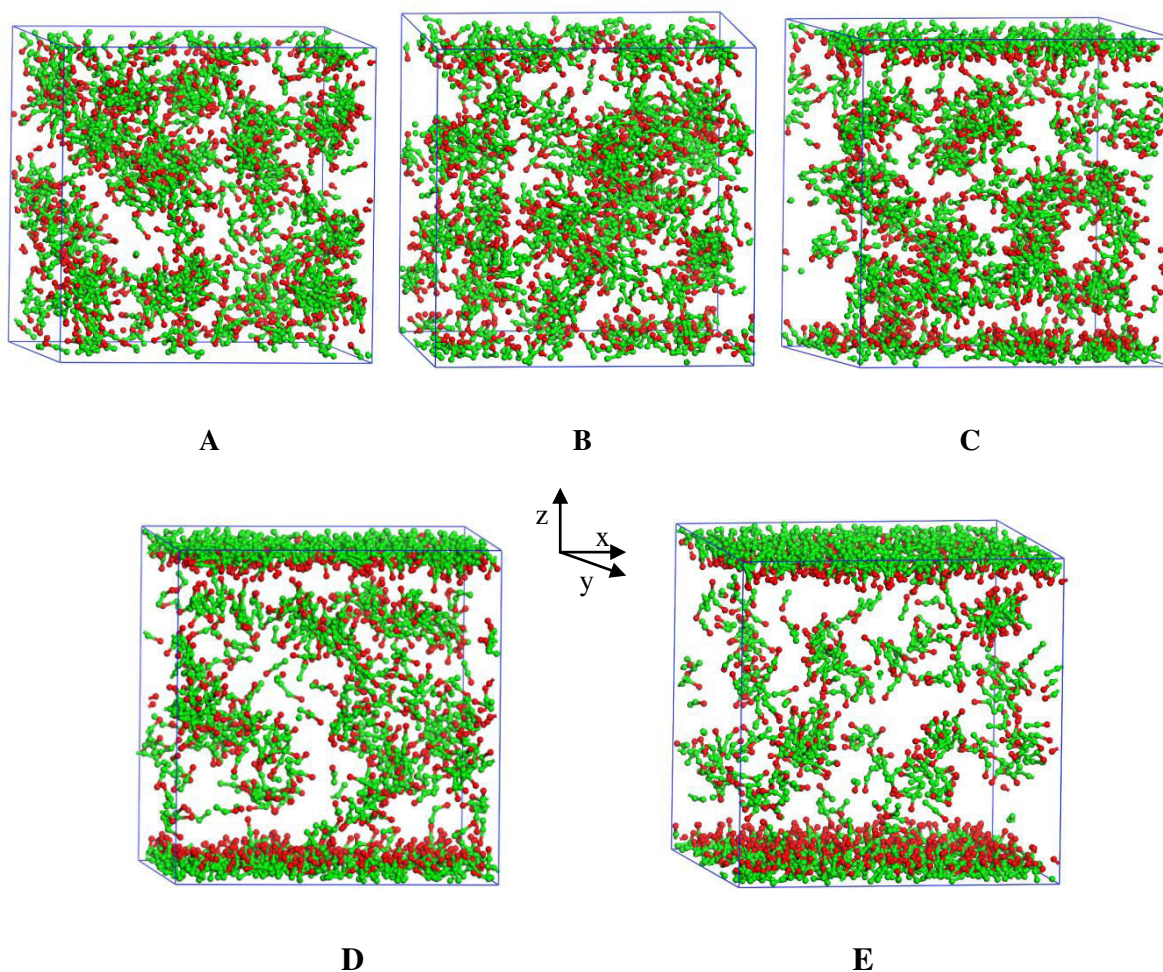


Figure 3 - 24: Final snapshots of H1T2 adsorption structures at the membrane surfaces with different parameter a_{MT} , starting from random configurations. A. $a_{MT} = 78$; B. $a_{MT} = 75.8$; C. $a_{MT} = 73.7$; D. $a_{MT} = 69.3$; E. $a_{MT} = 65$. Box size : $20 r_c \times 20 r_c \times 20 r_c$, The total concentration of H1T2 $C_{H1T2} = 0.8 \text{ mol L}^{-1}$, $t = 50000$. Head groups are shown in red beads, tail groups are shown in green, water beads are not shown for clarity. The membrane is presented at the bottom and top of the box.

Figure 3 - 24 shows snapshots (with water removed for clarity) of the adsorption H1T2 structures at a total concentration of 0.8 mol L^{-1} with different a_{MT} , when simulations terminated at $t = 50000$. It can be seen that, at this concentration, micelles were already formed in the aqueous solutions no matter how tail bead – membrane interactions a_{MT} varied. When $a_{MT} = 78$, there was no repulsion or attraction between surfactant tail beads and the membrane, so most surfactants existed in the solution as micelles and only a few surfactant molecules adsorbed onto the membrane. As a_{MT} gradually decreased from 78 to 65, the

attraction between surfactant tail groups and the membrane surface due to hydrophobic interactions increased, thus the amount of surfactant adsorption increased significantly. As can be seen, when $a_{MT} = 75.8$, several surface aggregates adsorbed on the membrane and with $a_{MT} = 69.3$, a monolayer of H1T2 was visible in the system. This structure became denser when a_{MT} decreased to 65, indicating a strong adsorption of surfactants on the membrane.

It is also interesting to note that the arrangement of surfactants on the membrane were in the same mode for these systems as illustrated in Figure 3 - 24: the surfactant tail groups were adsorbed on the membrane and the head groups directing towards the aqueous solution. This is because there is strong electrostatic repulsion between head groups and the membrane surface. In these cases, $a_{MT} < a_{MH}$, so the surfactant tail groups are more favorable to adsorb on the surface. It also illustrated the assumption of Chapter 2 that the orientation of the adsorbed surfactants modifies the hydrophilicity of the membrane surface.

3.4.5.2 The effect of surfactant concentration

In this part, we chose $a_{MT} = 65$ to investigate the effect of surfactant total concentration on the adsorption because this value exhibited most adsorption in Figure 3 - 24. H1T2 systems with total concentrations ranging from 0.1 to 0.7 mol L⁻¹ with randomize surfactant positions were generated. The snapshots of these systems at $t = 50000$ were illustrated in Figure 3 - 25. As can be seen, H1T2 molecules adsorbed onto membranes easily even at low concentrations. At C_{H1T2} lower than 0.7 mol L⁻¹, most surfactants in the system adsorbed onto the membrane and there were few isolated molecules in the solution. As the total concentration of surfactant increases, the amount of surfactant adsorption became larger and the adsorbed structure turned from surface aggregates to monolayer. Simultaneously, the amount of surfactants in solution also increased and at 0.7 mol L⁻¹, micelles or premicelles began to appear.

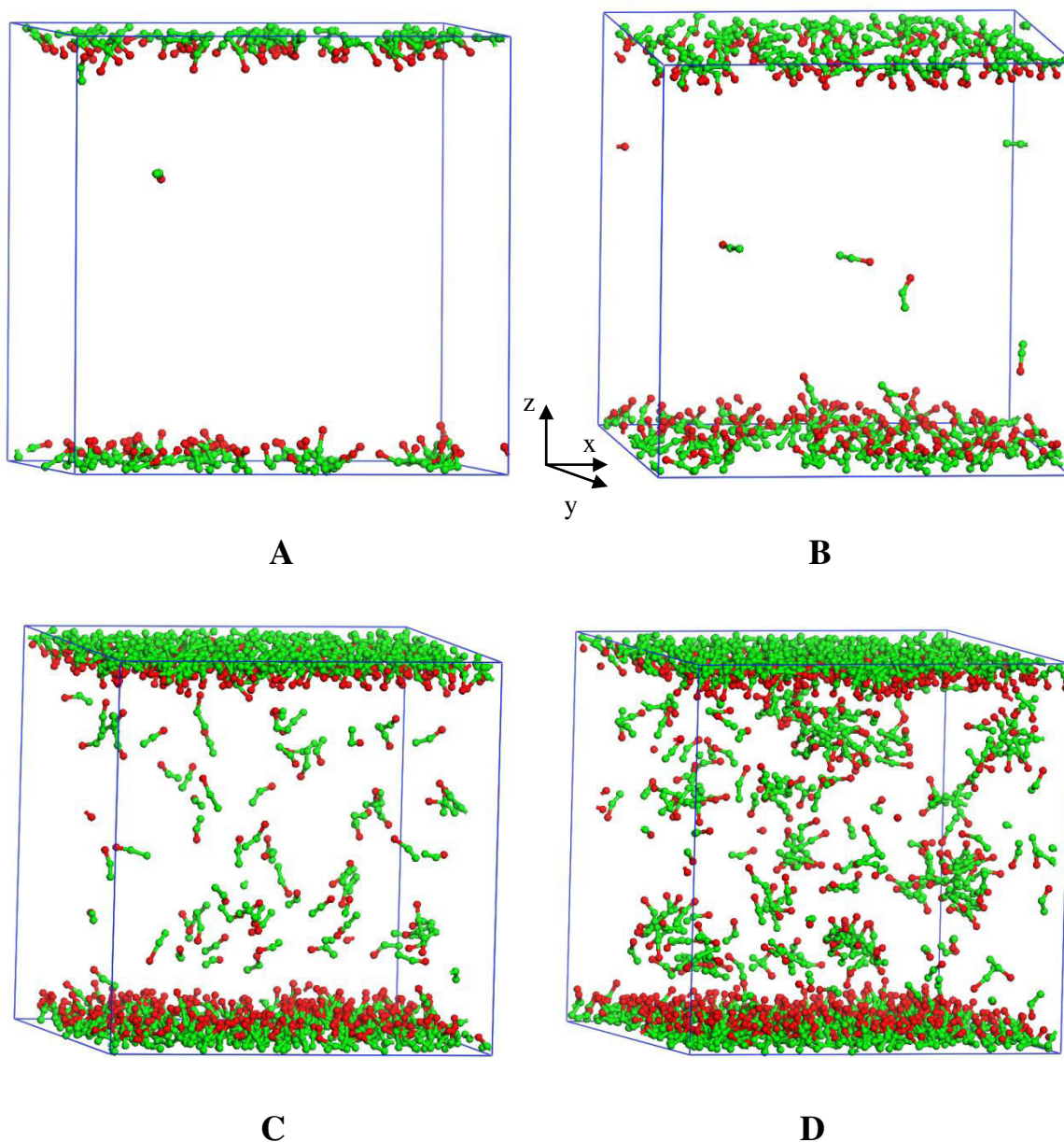


Figure 3 - 25: Final snapshots of HIT2 adsorption structures at the membrane surfaces at different total concentrations, starting from random configurations. A. $C_{\text{HIT2}} = 0.1 \text{ mol L}^{-1}$; B. $C_{\text{HIT2}} = 0.2 \text{ mol L}^{-1}$; C. $C_{\text{HIT2}} = 0.5 \text{ mol L}^{-1}$; D. $C_{\text{HIT2}} = 0.7 \text{ mol L}^{-1}$; Box size : $20 r_c \times 20 r_c \times 20 r_c$, $a_{\text{MT}} = 65$, $t = 50000$. The color scheme for the snapshots is the same as Figure 3 - 24.

It should be noted that in the present study, Material Studio did not provide trajectory analysis, so it was difficult to precisely distinguish surfactants in the aqueous solution and those adsorbed onto the membrane, which caused difficulties to the estimation of surfactant concentration in different phases. To conquer this problem, we need to further explore the package NEWTON which may allow the construction of a membrane as in this work, or a coarse-grained polymeric membrane composed of both polar and apolar beads, and most

importantly, provide the trajectory information for the estimation of distribution of surfactant molecules in different phases.

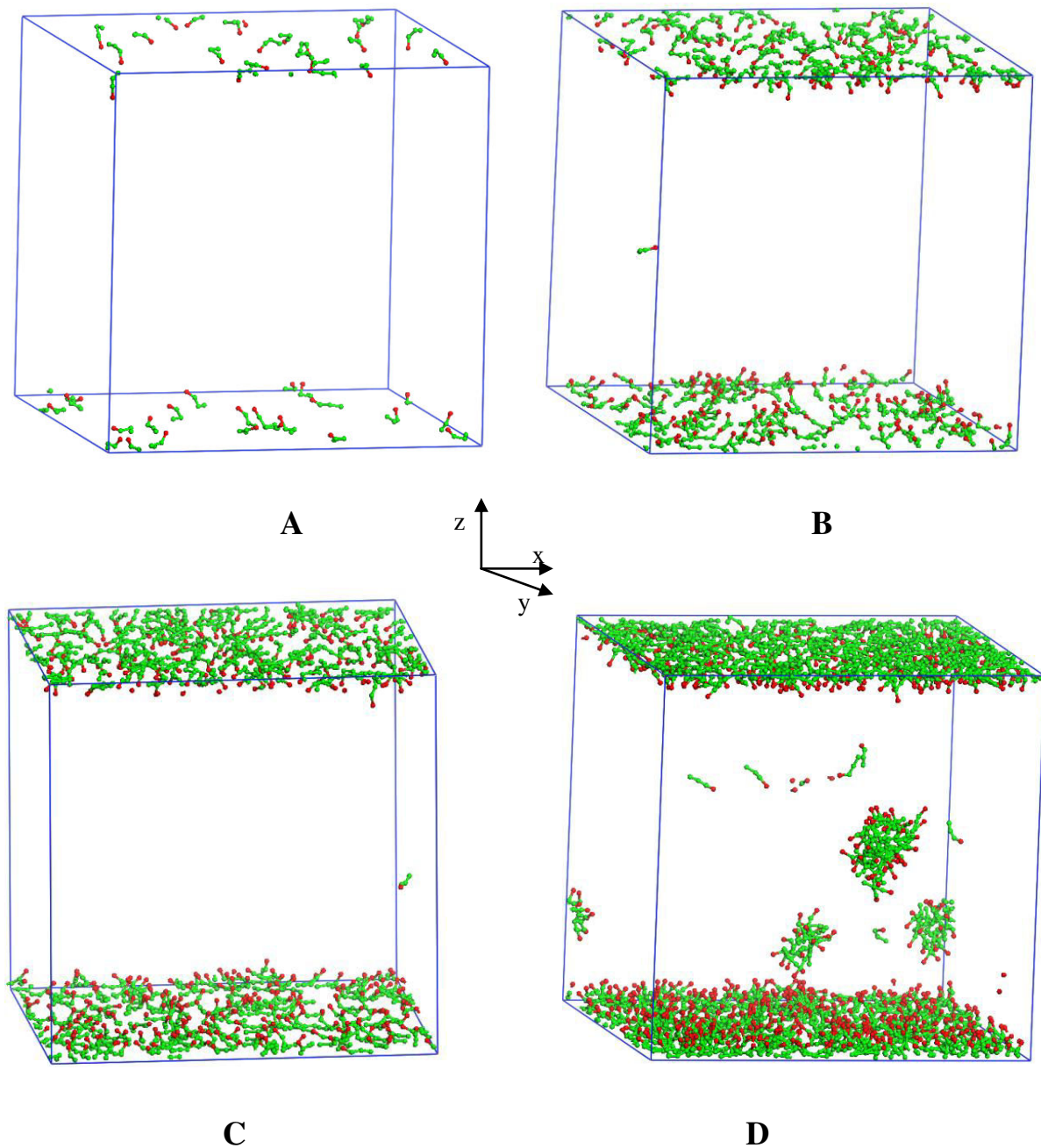


Figure 3 - 26: Final snapshots of H1T3 adsorption structures at the membrane surfaces at different total concentrations, starting from random configurations. A. $C_{\text{H1T3}} = 0.01 \text{ mol L}^{-1}$; B. $C_{\text{H1T3}} = 0.06 \text{ mol L}^{-1}$; C. $C_{\text{H1T3}} = 0.1 \text{ mol L}^{-1}$; D. $C_{\text{H1T3}} = 0.2 \text{ mol L}^{-1}$; Box size : $30 r_c \times 30 r_c \times 30 r_c$, $a_{\text{MT}} = 65$, $t = 50000$. The color scheme for the snapshots is the same as Figure 3 - 24.

Even though the amount of surfactant adsorption could not be calculated from the morphologies in the present study, it can be deduced that if there are enough surfactant

molecules in the aqueous solution, both micellization and adsorption may occur. For HIT2 systems, micellization will not occur until the concentration in aqueous solution surpasses its CMC (around 0.42 mol L^{-1} , as we have calculated in section 3.4.4). In Figure 3 - 24, where the micellization of surfactants in the solution and adsorption onto the membrane surface coexist, the surfactant concentration in the aqueous solution must be higher than its CMC. But in Figure 3 - 25, most surfactants were adsorbed on the membrane surface at lower total concentrations, so the concentration in aqueous solution is lower than the CMC.

For the longer chain HIT3, similar phenomenon was observed as illustrated in Figure 3 - 26. The adsorption of HIT3 molecules on the membrane increased as the total surfactant concentration was increased from 0.01 to 0.2 mol L^{-1} . The structure of the adsorbed surfactants transitioned from monomers at low concentrations ($\leq 0.01 \text{ mol L}^{-1}$), to surface aggregates at an intermediate concentration (around 0.06 mol L^{-1}), and to a monolayer at high concentrations ($\geq 0.1 \text{ mol L}^{-1}$). At the same time, the number of surfactants in aqueous solution increased and at 0.2 mol L^{-1} , micelles were observed. It was interesting to note that the surfactant molecules lay parallel on the membrane with their hydrophobic chain at low concentrations, with their head groups towards the aqueous solution. This is also in good agreement with our assumption in Chapter 2.

3.4.5.3 Kinetic competition between micellization and adsorption

From Figure 3 - 25 and Figure 3 - 26, we found that from a certain concentration, both micellization and adsorption may occur in the system. The competition between the two processes depends upon the surfactant concentration as well as interactions between tail beads and membrane. Figure 3 - 27 shows snapshots captured at different simulation time of an HIT3 solution with a total concentration of 0.1 mol L^{-1} . The first panel shows the initial random configuration. Figure 3 - 27 B shows a snapshot after 1650 DPD time unit, where micellization was already taking place and several surfactant molecules adsorbed onto the membrane surface with their hydrophobic part parallel to the surface and their hydrophilic part facing the solution. As simulation went on, more surfactants were adsorbed onto the membrane, and the micelles in the solution became decomposed because the hydrophobic interaction between tail bead and the membrane was more favorable than interactions between tail-tail beads. At the end of the simulation, almost all surfactants adsorbed and accumulated at the membrane surface and formed a dense monolayer.

The strong adsorption is explained by the relatively strong attraction between tail beads and the membrane because in this system, the parameter $a_{MT} = 65$. This could be applied to explain the huge amount of surfactant adsorption on the membrane in Chapter 2. However, estimation of the adsorption amount cannot be realized in the present simulation. Nevertheless, in Chapter 2, we have proposed a secondary membrane on the RO membrane, but it was not observed in the two surfactant systems with shorter chains during DPD simulations of surfactant adsorption. So the hypothesis and the simulations need further verification. Both model improvement and experimental characterization methods require further investigation in the future.

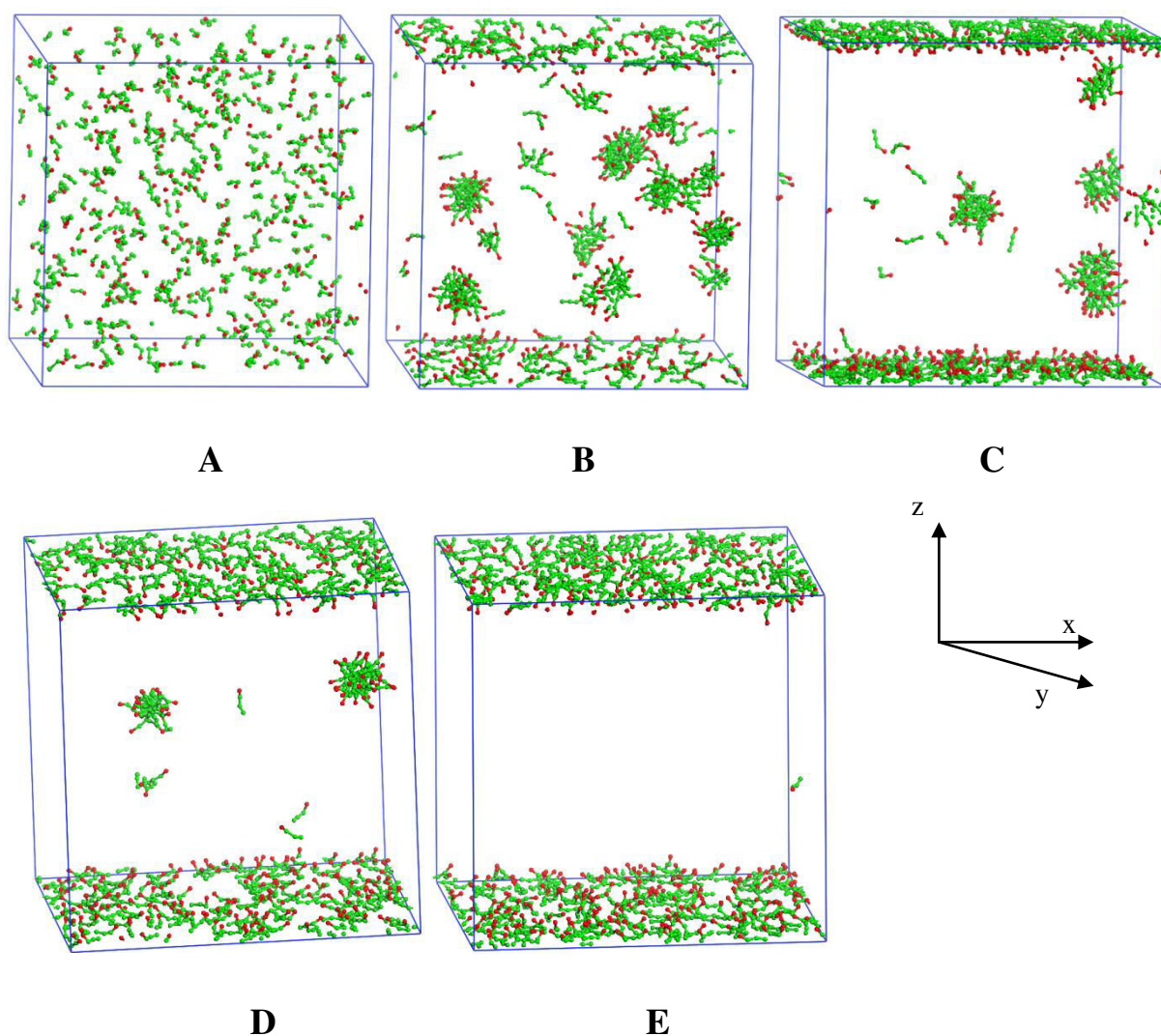


Figure 3 - 27: Time evolution of HIT3 adsorption onto the membrane from an initial random distribution. A. $t = 0$; B. $t = 1650$; C. $t = 8000$; D. $t = 20250$; E. $t = 50000$. The total surfactant concentration $C_{HIT3} = 0.1 \text{ mol L}^{-1}$. Box size : $30 r_c \times 30 r_c \times 30 r_c$, $a_{MT} = 65$. The color scheme for the snapshots is the same as Figure 3 - 24.

3.5 Conclusion

Dissipative particle dynamics (DPD) simulations were applied to study the self-assembly processes and the aggregation properties of mesoscopic models for sodium hexyl sulfate and sodium nonyl sulfate in aqueous solution. The model surfactants are composed of tail beads and a single head group connected by a harmonic spring force. The course of surfactant micellization started from a randomly dispersed state to a well-equilibrated solution. In agreement with previous work, this method is proved to be a very efficient technique to study the equilibrium properties of surfactant systems.

The present work is based on Groot's model, with some refinements in the repulsive interaction parameters and surfactant structure (bonding and bending). To obtain a best agreement with experimental values of the critical micelle concentration and micelle size, the parameters were optimized and the best fit of parameter set for H1T2 was chosen and then an extrapolation for H1T3 was verified. The adjustment of interaction between water and head/tail beads, and interaction between head and tail beads results in obvious change in micellization properties. An increase in hydrophobicity of the surfactant molecule, e.g., increasing the repulsion parameter between water and head/tail beads (a_{HW} or a_{TW}), will decrease the CMC of the amphiphilic molecule and the aggregation number will accordingly increase. From the parameterization procedure, we found that the adjustment can be done using both N_{agg} and CMC of the surfactant, because they are a result of the balance between intramolecular and intermolecular interactions.

Parameter values for SHS and SNS are obtained by optimizing goodness of fit on the CMC and average aggregation number compared with literature values. The CMC values of the two anionic surfactants are computed by the transition point where the free surfactant concentration stabilizes while the micelle concentration increases sharply with increasing the total surfactant concentration. We find that for the purely repulsive and soft DPD potential, the predicted CMCs are reasonably close to, or at least in the same magnitude as experimental values reported in literature. While promising, the results suggest more rigorous parameterization with further refinements for quantitative agreement of predicted micellization behaviors. It would be noted that our model does not include explicit counterions and electrostatics, which might influence the micellization significantly,

especially for surfactants with short hydrophobic tails. Further investigation of the effect of counterions on the surfactant behavior should be taken into account.

Compared with experimental and theoretical results, our model, despite its simplicity and some discrepancies, turns out to be reliable to yield empirically verifiable properties for these surfactant solutions. Extrapolation of the model to other series of surfactants would also be needed to verify the usefulness of DPD method.

This approach was also valuable for the study on the mechanism of membrane fouling involved with surfactant solutions. DPD method based on coarse-grained model is used in this work to simulate the adsorption of surfactants on a hydrophobic membrane surface. Although the solid plane is a simple description of the polymeric membrane surface, and the coarse-grained model simplifies the atomic structure of the amphiphilic surfactants, it is capable to capture, at least qualitatively, much of their underlying physics at long time scales. The capability of DPD simulations to generate the experimental trend demonstrated that our model catches the main characteristics of surfactant adsorption. However, due to the limitation of available methods, simulations on surfactant adsorption were undertaken by commercial software. The trajectory of surfactant molecules, the concentration of surfactants on the membrane and in the solution, the interactions between different part of the surfactant and the membrane, need to be investigated by more efficient simulation packages. So that the experimental obtained data, such as the amount of surfactant adsorption onto the membrane, the permeate flux and the membrane surface characteristics, could be related to simulation data. And the questions that cannot be explained from experiments, such as how it influence the separate and transport properties of membranes by surfactant adsorption, could be solved from microscopic way. Three main parameters were not taken into account in DPD simulations presented here: charged particles, pressure and tangential flow, which play an important role in the surfactant behavior during the filtration. But recent works give positive perspectives on the introduction of these parameters [270], [271], [272].

General conclusions and perspectives

General conclusions and perspectives

During the past years, membrane process, as a promising technology, has been greatly improved with significantly enhanced performance and commercial markets have been spreading rapidly throughout the world. Among all types of membrane technologies available today, reverse osmosis (RO) is gaining worldwide acceptance in both water treatment and desalination applications.

Though the improvement of RO membranes has been tremendous in the past few years, their performance and economics are still far from perfect. Membrane life time and permeate fluxes are significantly affected by the phenomena of concentration polarization and fouling. During the pressure-driven membrane processes, dissolved organic matters continuously accumulate onto the membrane or block the membrane pores, leading to a decrease in solvent permeability and enhancing the difficulty for the transport of solutes. The reasons for fouling are reported as consisting of chemical fouling, biological fouling and scale formation. Organic fouling is caused by the adsorption of organic materials from the feed water such as humic substances, proteins, polysaccharides, surfactants etc. onto or into the membrane. The chemical fouling depends on hydrophobic interaction and electrostatic interaction between organic materials in the feed water and the membrane surface.

The objective of this study was to develop a mechanistic understanding of the phenomenon of membrane fouling by organic components during high-pressure driven membrane processes, based upon an integrated framework of solute properties, membrane characteristics, solute-membrane interactions and operational conditions. This work was organized in three parts.

In the first chapter, the background theories were reviewed, focusing on the membrane processes, the target composition that are to be treated with, and the available technologies or methods in literature to investigate the phenomena that might occur during the membrane processes. Different methods for investigating the physical-chemical characteristics of the membranes were also analyzed. From this part, the knowledge on the properties of surfactants was deepened and then a succinct state-of-art on the simulation methods was proposed. At the end of this first part it was chosen to study the adsorption of anionic surfactants on reverse osmosis membrane, both experimentally and with a mesoscopic simulation method: the Dissipative Particle Dynamics (DPD) simulation.

General conclusions and perspectives

In the second chapter the fouling of reverse osmosis membrane by surfactants was experimentally studied. The objective of this chapter was to elucidate how membrane performances (e.g. selectivity, permeate flux) and surface characteristics (e.g. hydrophobicity / hydrophilicity) would be affected during surfactant filtration when adsorption occurred. In addition to membrane separation and transport properties, the adsorption isotherms of the anionic surfactant SDS at different concentrations during RO processes were analyzed. As far as we know, there has been no such study on the surfactant adsorption under filtration mode. The results obtained from contact angle measurements were used to compare membrane surface properties before and after the filtration of surfactant solution. With these experimental observations, a proposed mechanism of surfactant adsorption was developed to relate the adsorption of surfactants, the membrane performances and the modification in membrane properties. From the results we can conclude that RO is very efficient for the removal of surfactants because more than 99.5% of the surfactants were rejected by the membrane over the whole concentration range (below, equivalent to and above the CMC). However, the membrane fouling during filtration caused by surfactant adsorption affected the membrane performance and its surface characteristics. The relative fluxes of surfactant solutions were reduced compared to that of pure water, indicating a certain degree of membrane fouling. Surprisingly, the relative flux did not decrease with surfactant concentration in the solution as has been reported in literature for various organic matters, but there was even an increase when the initial SDS concentration increased to above the CMC (8.0 mmol L^{-1}). The unexpected phenomenon could be explained by the interactions between the surfactant and the membrane surface, which affected the membrane hydrophobicity and in turn influenced significantly the transport of solute or water molecules. The increase in the permeate flux indicated that the adsorption structure of surfactant molecules or surface aggregates became more and more hydrophilic. The contact angle measurements confirmed this hypothesis that due to surfactant adsorption, membrane surface was modified, the modification was in agreement with the change in membrane performance.

In addition to the adsorption during RO filtration experiments, both dynamic and static adsorption experiments without pressure were conducted. The huge amount of surfactant adsorption during RO filtration was explained by the adsorption of surfactants on the system materials (e.g. glass beacker and plastic tubing), the penetration into the internal structure and most importantly, the formation of complicated surfactant deposits (e.g. a secondary membrane) at the membrane surface. The orientation of surfactants on the top layer of the

General conclusions and perspectives

secondary membrane determined the hydrophobicity and charge of the fouled RO membrane surface, and thus dominated the rejection of the surfactants and the permeate flux. When the surfactant solution contained no micelles under the CMC, surfactant molecules were supposed to form a dense secondary membrane. While the micelles were formed, the secondary membrane was supposed to be no longer dense but loose. So permeate flux was enhanced with increasing the surfactant concentration.

The fouling due to surfactant adsorption has been investigated in macroscopic scale in this experimental part. However, the behaviors of surfactant at the solution/membrane interface were just proposed as assumptions in this work. It should be noted that the interaction between surfactants and polymeric membranes play an important role in the behavior of surfactants on the membrane, which will in turn affect the transport and separation properties, as well as the surface characteristics of the membranes. The surfactant organization on the membrane controlled by surfactant-membrane interactions should be studied in detail from a microscopic view. This issue was addressed in the third part by means of DPD simulations of surfactant solutions.

In the third chapter, before investigating the surfactant adsorption onto membrane, DPD simulations were firstly applied to study the self-assembly processes and the aggregation properties of SHS and SNS in aqueous solution, in order to develop a parameter set fit for the models. These surfactants are in the same series with SDS but with shorter hydrophobic chains. The similarity of micellization and adsorption properties of these sodium alkyl sulfates might facilitate our simulation, and provide information for longer chains such as SDS which required huge simulation box and long time.

The model surfactants were composed of head and tail beads representing different solubility in water. Since there has been no appropriate parameter set in the literature for the specific compound in our study, the present work has undertaken a parameterization based on Groot's model, with some refinements in the intermolecular and intramolecular interaction parameters. To obtain a best agreement with experimental values of the critical micelle concentration and micelle size, the parameters were optimized and the best fit of parameter set for SHS was chosen and then an extrapolation for SNS was verified. The adjustment of interaction between water and head/tail beads, and between head and tail beads results in obvious change in micellization properties. It was observed that increasing the interaction parameter between water and surfactant head beads a_{HW} or the interaction parameter between

General conclusions and perspectives

water and surfactant tail beads a_{TW} would significantly decrease the CMC. Because the two parameters determined the hydrophobicity of the surfactant molecules, an enhancement of the surfactant hydrophobicity made those amphiphilic molecules harder to dissolve in the aqueous solution, the tendency to form micelles was correspondingly enhanced. In addition, intramolecular interactions also play an important role in the micellization, but from a more complicated way. The balance between intermolecular and intramolecular forces dominated the CMC, aggregation number and other aggregation properties. It should be noted that our model did not include explicit counterions and electrostatics, which might influence the micellization significantly, especially for surfactants with short hydrophobic tails. Further investigation of the effect of counterions on the surfactant behavior should be taken into account. And the study on intramolecular interactions should be further investigated.

This approach was also valuable for the study on the mechanism of membrane fouling involved with surfactant solutions from a mesoscopic scale. The validated coarse-grained models in the section of micellization were used to simulate the adsorption of surfactants on a hydrophobic membrane surface. Although the chosen solid plane was a simple description of the polymeric membrane surface, and the coarse-grained model simplified the atomic structure of the amphiphilic surfactants, it was demonstrated that our model catches the main characteristics of surfactant adsorption. However, due to the limitation of available methods, simulations on surfactant adsorption were undertaken by commercial software. The trajectory of surfactant molecules, the concentration of surfactants on the membrane and in the solution, the interactions between different part of the surfactant and the membrane, need to be investigated by more efficient simulation packages. Three main parameters were not taken into account in DPD simulations presented here: charged particles, pressure and tangential flow, which play an important role in the surfactant behavior during the filtration. Promisingly, a lot of recent work gives positive perspectives on the introduction of these parameters, which might provide guidance for our investigations.

To conclude, the objective of this work was to develop new methods to better understand the fouling of filtration membranes by organic matters. Through the example of RO fouling by surfactants it was demonstrated that the combination of adsorption experiments and DPD simulations permit to better understand the microscopic behavior of foulant that influence the macroscopic performances of filtration process. These methods could be applied to new systems membrane/compounds. Further experiments and new improvements to the simulation

General conclusions and perspectives

tool could be undertaken to offer larger perspectives: a new experimental filtration system limiting dead volume and external pipes interfaces could be developed to obtain more precise adsorption values. The quantification of adsorption could also be realized with spectroscopic methods, using fluorescent molecules for example. The membrane charge measurement (streaming potential) at different instants of filtration could help to understand the behavior of surfactants and confirm their organization. As presented above, the improvement of simulation package NEWTON by introducing charged particles, solid polymer, tangential flow and pressure would be really useful; but it represents an important work since DPD is a young coarse grain simulation method, and the increase of phenomenon to take into account will require more powerful calculation tools.

Appendix

1. Interaction parameters

If the thermodynamic state of an arbitrary liquid is to be described correctly by the present soft sphere model, the fluctuations in the liquid should be described correctly. These are determined by the compressibility of the system, hence, analogously to the Weeks-Chandler-Anderson perturbation theory of liquids, we ought to choose our model such that[11]

$$\kappa^{-1} = \frac{1}{n k_B T \kappa_T} = \frac{1}{k_B T} \left(\frac{\partial p}{\partial n} \right)_T \quad (1)$$

has the correct value. The parameter n appearing in Eq. (1) is the number density of molecules, and κ_T is the usual isothermal compressibility.

In fact, the bead density in the simulation is not the same with the density of water molecules in real liquid water. The following relation should hold[257]:

$$\frac{1}{k_B T} \left(\frac{\partial p}{\partial \rho} \right)_{simulation} = \frac{1}{k_B T} \left(\frac{\partial p}{\partial n} \right)_{experiment} \quad (2)$$

Where ρ is the bead density in the simulation, and n is the density of, e.g., water molecules in liquid water. However, this relation only holds if one DPD bead corresponds to one water molecule. In general, the system should satisfy

$$\frac{1}{k_B T} \left(\frac{\partial p}{\partial \rho} \right)_{simulation} = \frac{1}{k_B T} \left(\frac{\partial n}{\partial \rho} \right) \left(\frac{\partial p}{\partial n} \right)_{experiment} = \frac{N_m}{k_B T} \left(\frac{\partial p}{\partial n} \right)_{experiment} \quad (3)$$

Where N_m is the number of water molecules per DPD bead. In this work, N_m is chosen at $N_m = 3$.

According to Groot et al.[11], a good approximation for the pressure that holds for sufficiently high density ($\rho > 2$) is:

$$p = \rho k_B T + \alpha a \rho^2 \quad (\alpha = 0.101 \pm 0.001) \quad (4)$$

This implies that the dimensionless compressibility, as introduced in Eq. (1) and Eq.(3), is given by

$$\kappa^{-1} = \frac{1}{N_m k_B T} \left(\frac{\partial p}{\partial \rho} \right)_{simulation} = \frac{1}{N_m} \left(1 + \frac{2\alpha a \rho}{k_B T} \right) \approx \frac{1}{N_m} \left(1 + \frac{0.2 a \rho}{k_B T} \right) \quad (5)$$

Combining this with the numerical value of compressibility of water at room temperature (300 K), $\kappa^{-1} = 15.9835$, the repulsion parameter in Eq. (5) is determined at

$$a_{ii} = \frac{(16N_m - 1)}{0.2} \times \frac{k_B T}{\rho} \quad (6)$$

where a_{ii} is the repulsion parameter between particles of the same type.

The other parameters are calculated from Flory- Huggins χ -parameters. For the case where three water molecules are represented by one DPD bead, the interaction parameter is found as $\chi_{hydrocarbon-water} \approx 6.0$, and appears to be relatively independent of temperature. Because this parameter scales linearly with the bead volume, the value $6.0/N_m = 2.0$ should be compared to values cited in the literature for the χ -parameter per carbon atom [257].

2. The time scale of the present simulation

The mean square displacement of atoms in a simulation can be easily computed by its definition:

$$MSD = \langle |r(t) - r(0)|^2 \rangle \quad (7)$$

where $\langle \dots \rangle$ denotes here averaging over all the atoms (or all the atoms in a given subclass).

The MSD contains information on the atomic diffusivity. If the system is solid, MSD saturates to a finite value, while if the system is liquid, MSD grows linearly with time. In this case it is useful to characterize the system behavior in terms of the slope, which is the *diffusion constant* D :

$$D_w = \lim_{t \rightarrow \infty} \frac{1}{6t} \langle |r(t) - r(0)|^2 \rangle \quad (8)$$

The 6 in the above formula must be replaced with 4 in two-dimensional systems.

In our simulation, because the simulated bead density is $\rho R_c^3 = 3$, a cube of R_c^3 contains three beads and therefore corresponds to a volume of 270 \AA^3 . Thus, we find the physical size of the interaction radius,

$$r_c = \sqrt[3]{270} \text{ \AA} = 6.4633 \text{ \AA} \quad (9)$$

The time scale listed in Table 1 is calculated from the following equation:

$$\tau' = \sqrt{\frac{m r_c^2}{k_B T}} = 3.01 \text{ ps} \quad (10)$$

where m is the mass of a water bead, R_c is the length scale of the interaction radius, k_B is Boltzmann's constant and T temperature.

Because the noise and friction are included in the simulation method, the hydrodynamic regime is simulated already with few particles and time steps. The consequence of this strategy, however, is that we have lost track of our physical unit of time. The real physical unit of time in this work is calculated from the long-time diffusion constant of water, using the same method as mentioned in Groot and Rabone' work [257].

In fact, the self-diffusion constant of a water bead is not the same as that of water in real system, because the bead is composed of three water molecules. The mean square displacement of the water beads, R_w^2 , is thus the ensemble average of the three molecules, described as follows:

$$MSD_{DPD} = R_w^2 = \langle \mathbf{R}_w \cdot \mathbf{R}_w \rangle = (\langle \mathbf{R}_1 \cdot \mathbf{R}_1 \rangle + \langle \mathbf{R}_2 \cdot \mathbf{R}_2 \rangle + \langle \mathbf{R}_3 \cdot \mathbf{R}_3 \rangle) / 3 = R^2 / 3 \quad (11)$$

Where \mathbf{R}_w is the movement vector of the center of mass of the water beads containing three water molecules; $\mathbf{R}_1, \mathbf{R}_2, \mathbf{R}_3$ are the movement vectors for the three water molecules in the bead; R^2 is the mean square displacement of a water molecule.

Because the mean square displacement of the water beads is one-third of the water molecules, the diffusion constant of the beads is one-third of that of water. As the method used in the work of Groot and Rabone [257], the diffusion constant of the water beads was obtained by averaging the mean square displacement over three runs of 100,000 time steps each, and determining the slope of $R_w^2(t)$ against time. We obtained the MSD of water beads as follows:

$$MSD_{DPD} = R_w^2 = 3.90 \times 10^{-15} t_{DPD} \text{ cm}^2 \quad (12)$$

where t_{DPD} is the DPD time unit, and the real physical time t should be calculated using the time scale τ in the simulation, thus $t = t_{DPD} \times \tau$. At the noise and repulsion parameters used here, according to Eq. 2 and Eq.6, the water molecule diffusion constant,

$$D_w = \frac{1}{6t} R^2 = \frac{1}{6(\tau * t_{DPD})} * (3R_w^2) = \frac{1}{\tau} * (1.95 \times 10^{-15}) \text{ cm}^2 \text{ s}^{-1} \quad (13)$$

Equating this to the experimental diffusion constant of water, $D_w = (2.43 \pm 0.01) \times 10^{-5} \text{ cm}^2 \text{ s}^{-1}$, leads, together with Eq. 4, to the time scale τ

$$\tau = \frac{1.95}{D_w} \times 10^{-15} \text{ s} = 80.24 \text{ ps} \quad (14)$$

3. Radial distribution function

The radial distribution function (also sometimes referred to as the pair correlation function) gives a measure of the probability that, given the presence of an atom at the origin of an arbitrary reference frame, there will be an atom with its center located in a spherical shell of infinitesimal thickness at a distance, r , from the reference atom. This concept also embraces the idea that the atom at the origin and the atom at distance r may be of different chemical types, say α and β . The resulting function is then commonly given the symbol $g_{\alpha\beta}(r)$ and is defined by Hansen and McDonald [273]:

$$x_\alpha x_\beta \rho g_{\alpha\beta}(r) = \frac{1}{N} \langle \sum_{i=1}^{N_\alpha} \sum_{j=1}^{N_\beta} \delta(r - r_i - r_j) \rangle \quad (14)$$

where x_i is the mole fraction of chemical type i , N_i is the number of atoms of chemical type i , N is the total number of atoms, and ρ is the overall number density. The prime indicates that terms where $i = j$ are excluded when the chemical types are the same.

It should be noted that for simulations that employ periodic boundary conditions the value of ρ is easily deduced from the cell volume and content. For simulations that do not employ periodic boundary conditions (for example gas phase systems) the value of ρ is more arbitrary, depending on the reference volume being used. To compare simulations with and without periodic boundary conditions, the $g(r)$ obtained must be multiplied by the cell volume, in \AA^3 . A useful check is that, in the limit of larger r , the $g(r)$ tends to unity.

The pair correlation function has found applications in structural investigations of both solid and liquid packing (local structure), in studying specific interactions such as hydrogen bonding, in statistical mechanical theories of liquids and mixtures, and in a practical sense for correcting the results of computer simulations for artifacts which arise due to the inevitable need to study physically small systems when performing atomistic computer simulations.

References

- [1] N. N. Li, A. G. Fane, W. S. W. Ho, and T. Matsuura, *Advanced Membrane Technology and Applications*. Hoboken, NJ, USA: John Wiley & Sons, Inc., 2008.
- [2] E. Drioli and L. Giorno, *Membrane Operations: Innovative Separations and Transformations*. Weinheim, Germany: Wiley-VCH Verlag GmbH & Co. KGaA, 2009.
- [3] C. de Moraes Coutinho, M. C. Chiu, R. C. Basso, A. P. B. Ribeiro, L. A. G. Gonçalves, and L. A. Viotto, “State of art of the application of membrane technology to vegetable oils: A review,” *Food Research International*, vol. 42, no. 5–6, pp. 536–550, Jun. 2009.
- [4] L. Malaeb and G. M. Ayoub, “Reverse osmosis technology for water treatment: State of the art review,” *Desalination*, vol. 267, no. 1, pp. 1–8, Feb. 2011.
- [5] K. P. Lee, T. C. Arnot, and D. Mattia, “A review of reverse osmosis membrane materials for desalination—Development to date and future potential,” *Journal of Membrane Science*, vol. 370, no. 1–2, pp. 1–22, Mar. 2011.
- [6] M. F. A. Goosen and S. S. Sablani, “FOULING OF REVERSE OSMOSIS AND ULTRAFILTRATION MEMBRANES : A CRITICAL REVIEW,” *Separation Science and Technology*, vol. 39, no. 10, pp. 2261–2298, 2004.
- [7] M. J. Rosen, *Surfactants and Interfacial Phenomena, 3rd Edition*. John Wiley & Sons, 2004, p. 464.
- [8] R. Renner, “European bans on surfactant trigger transatlantic debate,” *Environmental science technology*, vol. 31, no. 7, p. 316A–320A, 1997.
- [9] I. Xiarchos, D. Doulia, V. Gekas, and G. Trägårdh, “Polymeric Ultrafiltration Membranes and Surfactants,” *Separation & Purification Reviews*, vol. 32, no. 2, pp. 215–278, Jan. 2003.
- [10] D. F. Evans and H. Wennerström, *The Colloidal Domain: Where Physics, Chemistry, Biology, and Technology Meet, 2nd Edition*. John Wiley & Sons, 1999.
- [11] R. D. Groot and P. B. Warren, “Dissipative particle dynamics: Bridging the gap between atomistic and mesoscopic simulation,” *The Journal of Chemical Physics*, vol. 107, no. 11, p. 4423, 1997.
- [12] P. Español and P. Warren, “Statistical Mechanics of Dissipative Particle Dynamics,” *Europhysics Letters (EPL)*, vol. 30, no. 4, pp. 191–196, May 1995.
- [13] C. Baudequin, “Conception d’une unité mobile pour le post-traitement d’eau utilisée pendant des opérations d’extinction d’incendie,” Ecole Centrale Paris, 2011.
- [14] M. Mulder, “Basic principles of membrane technology,” *Journal of Membrane Science*, vol. 72, no. 3, p. 564, 1996.

- [15] A. E. C. Morão, “Transport mechanisms governing the nanofiltration of multi-component solutions – application to the isolation of clavulanic acid,” Universidade Técnica de Lisboa, 2008.
- [16] E. Drioli and E. Fontananova, “Membrane technology and sustainable growth,” vol. 82, no. December, pp. 1557–1562, 2004.
- [17] DACH Hanane, “Comparison of nanofiltration (NF) and reverse osmosis (RO) for the treatment of brackish water feeds,” University of Angers, 2008.
- [18] F. Macedonio, E. Drioli, a. a. Gusev, a. Bardow, R. Semiat, and M. Kurihara, “Efficient technologies for worldwide clean water supply,” *Chemical Engineering and Processing: Process Intensification*, vol. 51, pp. 2–17, Jan. 2012.
- [19] J. Remigy and S. Desclaux, “Filtration membranaire (OI, NF, UF) Présentation des membranes et modules,” *Technique de l’Ingénieur*, vol. 10, no. 3, pp. 1–20, 2007.
- [20] B. Keskinler, E. Yildiz, E. Erhan, M. Dogru, Y. K. Bayhan, and G. Akay, “Crossflow microfiltration of low concentration-nonliving yeast suspensions,” *Journal of Membrane Science*, vol. 233, no. 1–2, pp. 59–69, 2004.
- [21] J. Mueller, Y. Cen, and R. H. Davis, “Crossflow microfiltration of oily water,” *Journal of Membrane Science*, vol. 129, no. 2, pp. 221–235, 1997.
- [22] B. Maiorella, G. Dorin, A. Carion, and D. Harano, “Crossflow microfiltration of animal cells,” *Biotechnology and Bioengineering*, vol. 37, no. 2, pp. 121–126, 1991.
- [23] G. Samuelsson, I. H. Huisman, G. Trägårdh, and M. Paulsson, “Predicting limiting flux of skim milk in crossflow microfiltration,” *Journal of Membrane Science*, vol. 129, no. 2, pp. 277–281, 1997.
- [24] J. H. Hanemaaijer, “Microfiltration in whey processing,” *Desalination*, vol. 53, no. 1–3, pp. 143–155, 1985.
- [25] D. C. P. Campos, A. S. Santos, D. B. Wolkoff, V. M. Matta, L. M. C. Cabral, and S. Couri, “Cashew apple juice stabilization by microfiltration,” *Desalination*, vol. 148, no. 1–3, pp. 61–65, 2002.
- [26] T. A. Doneva, C. S. Vassilieff, and E. D. Krusteva, “Cross-flow microfiltration of latex suspensions: test of different models,” *Colloids and Surfaces A Physicochemical and Engineering Aspects*, vol. 138, no. 2–3, pp. 245–254, 1998.
- [27] B. Zhu, D. A. Clifford, and S. Chellam, “Comparison of electrocoagulation and chemical coagulation pretreatment for enhanced virus removal using microfiltration membranes,” *Water Research*, vol. 39, no. 13, pp. 3098–3108, 2005.
- [28] D. M. Kanani, X. Sun, and R. Ghosh, “Membrane Fouling during Microfiltration of Protein Solutions,” Massey University New Zealand, 2008.

- [29] D. B. Frewin, J. R. Jonsson, K. G. Davis, A. M. Beilby, D. N. Haylock, R. W. Beal, and W. J. Russell, "Effect of microfiltration on the histamine levels in stored human blood.," *Vox Sanguinis*, vol. 52, no. 3, pp. 191–194, 1987.
- [30] C. H. Xing, X. H. Wen, Y. Qian, D. Sun, P. S. Klose, and X. Q. Zhang, "Fouling and cleaning of microfiltration membrane in municipal wastewater reclamation.," *Water Science and Technology*, vol. 47, no. 1, pp. 263–270, 2003.
- [31] M. H. Al-Malack, G. K. Anderson, and A. Almasi, "Treatment of anoxic pond effluent using crossflow microfiltration," *Water Research*, vol. 32, no. 12, pp. 3738–3746, 1998.
- [32] B. Han, T. Runnells, J. Zimbron, and R. Wickramasinghe, "Arsenic removal from drinking water by flocculation and microfiltration," *Desalination*, vol. 145, no. 1–3, pp. 293–298, 2002.
- [33] W. H. Howard and R. Lambert, "Ultrafiltration in the Ontario Dairy Industry," *Canadian Journal of Agricultural Economics*, vol. 41, no. 2, pp. 177–195, 1993.
- [34] K. L. Jones and C. R. O'Melia, "Ultrafiltration of protein and humic substances: effect of solution chemistry on fouling and flux decline," *Journal of Membrane Science*, vol. 193, no. 2, pp. 163–173, 2001.
- [35] A. Hinkova, Z. Bubnik, V. Pour, S. Henke, and P. Kadlec, "Application of cross-flow ultrafiltration on inorganic membranes in purification of food materials," *Czech Journal of Food Sciences*, vol. 23, no. 3, pp. 103–110, 2005.
- [36] S. Vidya and D. Mohan, "Application Studies of Cellulose Acetate and Polymethylmethacrylate Blend Ultrafiltration Membranes," *Separation Science and Technology*, vol. 45, no. 6, pp. 740–750, 2010.
- [37] R. S. Tutunjian, "Ultrafiltration processes in biotechnology.," *Annals Of The New York Academy Of Sciences*, vol. 413, pp. 238–253, 1983.
- [38] R. Ghosh and Z. F. Cui, "Purification of lysozyme using ultrafiltration.," *Biotechnology and Bioengineering*, vol. 68, no. 2, pp. 191–203, 2000.
- [39] R. Magin and H.-C. Chan, "Rapid separation of liposomes using ultrafiltration," *Biotechnology Techniques*, vol. 1, no. 3, pp. 185–188, 1987.
- [40] D. Bhattacharyya, J. L. Bewley, and R. B. Grieves, "Ultrafiltration of Laundry Waste Constituents," *Journal Water Pollution Control Federation*, vol. 46, no. 10, pp. 2372–2386, 1974.
- [41] E. R. Christensen and K. W. Plaumann, "Waste Reuse: Ultrafiltration of Industrial and Municipal Wastewaters," *Journal Water Pollution Control Federation*, vol. 53, no. 7, pp. 1206–1212, 1981.
- [42] A. D. Revchuk and I. H. M. Suffet, "Ultrafiltration separation of aquatic natural organic matter: chemical probes for quality assurance.," *Water Research*, vol. 43, no. 15, pp. 3685–3692, 2009.

- [43] W. J. Koros, Y. H. Ma, and T. Shimidzu, "Terminology for membranes and membrane processes (IUPAC Recommendations 1996)," *Pure and Applied Chemistry*, vol. 68, no. 7, pp. 1479–1489, 1996.
- [44] L. F. Greenlee, D. F. Lawler, B. D. Freeman, B. Marrot, and P. Moulin, "Reverse osmosis desalination: water sources, technology, and today's challenges.," *Water Research*, vol. 43, no. 9, pp. 2317–2348, May 2009.
- [45] M. R. Teixeira and M. J. Rosa, "Microcystins removal by nanofiltration membranes," *Separation and Purification Technology*, vol. 46, no. 3, pp. 192–201, 2005.
- [46] K.-H. Choo, D.-J. Kwon, K.-W. Lee, and S.-J. Choi, "Selective removal of cobalt species using nanofiltration membranes.," *Environmental science technology*, vol. 36, no. 6, pp. 1330–1336, 2002.
- [47] C. P. Leo, W. K. Chai, A. W. Mohammad, Y. Qi, A. F. A. Hoedley, and S. P. Chai, "Phosphorus removal using nanofiltration membranes," *Water Science Technology*, vol. 64, no. 1, p. 199, 2011.
- [48] C. Causserand, P. Aimar, J. P. Cravedi, and E. Singlande, "Dichloroaniline retention by nanofiltration membranes.," *Water Research*, vol. 39, no. 8, pp. 1594–1600, 2005.
- [49] L. D. Nghiem, A. I. Schäfer, and M. Elimelech, "Pharmaceutical Retention Mechanisms by Nanofiltration Membranes," *Environmental science technology*, vol. 39, no. 19, pp. 7698–7705, 2005.
- [50] A. V Volkov, G. A. Korneeva, and G. F. Tereshchenko, "Organic solvent nanofiltration: prospects and application," *Russian Chemical Reviews*, vol. 77, no. 11, pp. 983–993, 2010.
- [51] J. O'Grady, A. Losikoff, J. Poiley, D. Fickett, and C. Oliver, "Virus removal studies using nanofiltration membranes.," *Developments in Biological Standardization*, vol. 88, pp. 319–326, 1996.
- [52] I. Koyuncu, O. A. Arikan, M. R. Wiesner, and C. Rice, "Removal of hormones and antibiotics by nanofiltration membranes," *Journal of Membrane Science*, vol. 309, no. 1–2, pp. 94–101, 2008.
- [53] J.-H. Choi, K. Fukushi, and K. Yamamoto, "A study on the removal of organic acids from wastewaters using nanofiltration membranes," *Separation and Purification Technology*, vol. 59, no. 1, pp. 17–25, 2008.
- [54] A. K. Goulas, A. S. Grandison, and R. A. Rastall, "Fractionation of oligosaccharides by nanofiltration," *Journal of the Science of Food and Agriculture*, vol. 83, no. 7, pp. 675–680, 2003.
- [55] J. Ecker, T. Raab, and M. Harasek, "Nanofiltration as key technology for the separation of LA and AA," *Journal of Membrane Science*, vol. 389, no. 0, pp. 389–398, 2012.

- [56] I. Vincze and G. Vatai, "Application of nanofiltration for coffee extract concentration," *Desalination*, vol. 162, pp. 287–294, 2004.
- [57] a. Bódalo-Santoyo, J. L. Gómez-Carrasco, E. Gómez-Gómez, F. Máximo-Martín, and a. M. Hidalgo-Montesinos, "Application of reverse osmosis to reduce pollutants present in industrial wastewater," *Desalination*, vol. 155, no. 2, pp. 101–108, Jun. 2003.
- [58] M. E. Williams, "A Brief Review of Reverse Osmosis Membrane Technology," pp. 1–29, 2003.
- [59] R. J. Petersen, "Composite reverse osmosis and nanofiltration membranes," *Journal of Membrane Science*, vol. 83, no. 1, pp. 81–150, Aug. 1993.
- [60] S. LEOB and S. SOURIRAJAN, "Sea water demineralization by means of an osmotic membrane," *Advances in Chemistry*, vol. 38, no. 117, pp. 117–132, 1962.
- [61] O. Akin and F. Temelli, "Probing the hydrophobicity of commercial reverse osmosis membranes produced by interfacial polymerization using contact angle , XPS , FTIR , FE-SEM and AFM," *Desalination*, vol. 278, no. 1–3, pp. 387–396, 2011.
- [62] L. Song and M. Elimelech, "Theory of Concentration Polarization in Crossflow Filtration," *Journal of the Chemical Society Faraday Transactions*, vol. 91, no. 19, pp. 3389–3398, 1995.
- [63] V. Chen, a. . Fane, S. Madaeni, and I. . Wenten, "Particle deposition during membrane filtration of colloids: transition between concentration polarization and cake formation," *Journal of Membrane Science*, vol. 125, no. 1, pp. 109–122, Mar. 1997.
- [64] S. S. Sablani, M. F. A. Goosena, and M. Wilf, "Concentration polarization in ultrafiltration and reverse osmosis : a critical review," *Desalination*, vol. 141, pp. 269–289, 2001.
- [65] S. Kim and E. Hoek, "Modeling concentration polarization in reverse osmosis processes," *Desalination*, vol. 186, no. 1–3, pp. 111–128, Dec. 2005.
- [66] K. Mizoguchi, K. Fukui, H. Yanagishita, T. Nakane, and T. Nakata, "Ultrafiltration behavior of a new type of non-ionic surfactant around the CMC," *Journal of Membrane Science*, vol. 208, no. 1–2, pp. 285–288, Oct. 2002.
- [67] B. Van der Bruggen, M. Mänttari, and M. Nyström, "Drawbacks of applying nanofiltration and how to avoid them: A review," *Separation and Purification Technology*, vol. 63, no. 2, pp. 251–263, Oct. 2008.
- [68] D. G. Cahill, V. Freger, and S.-Y. Kwak, "Microscopy and Microanalysis of Reverse-Osmosis and Nanofiltration Membranes," *Materials Research Society Bulletin*, vol. 33, no. January, pp. 27–32, 2008.
- [69] V. Silva, "TESIS DOCTORAL : THEORETICAL FOUNDATIONS AND MODELLING IN."

- [70] M. Liu, Z. Chen, S. Yu, D. Wu, and C. Gao, "Thin-film composite polyamide reverse osmosis membranes with improved acid stability and chlorine resistance by coating N-isopropylacrylamide-co-acrylamide copolymers," *Desalination*, vol. 270, no. 1–3, pp. 248–257, Apr. 2011.
- [71] S. Y. Kwak, S. G. Jung, and S. H. Kim, "Structure-motion-performance relationship of flux-enhanced reverse osmosis (RO) membranes composed of aromatic polyamide thin films.," *Environmental science & technology*, vol. 35, no. 21, pp. 4334–4340, Nov. 2001.
- [72] D. a. Woods, J. Petkov, and C. D. Bain, "Surfactant adsorption by total internal reflection Raman spectroscopy. Part III: Adsorption onto cellulose," *Colloids and Surfaces A: Physicochemical and Engineering Aspects*, vol. 391, no. 1–3, pp. 10–18, Nov. 2011.
- [73] D. Flosch, G. Clarottlb, K. E. Geckeler, F. Schueb, and W. Gopel, "Characterization of plasma-treated poly (hydroxybutyrate) membrane surfaces by ESCA and contact angle measurements," *Journal of Membrane Science*, vol. 73, pp. 163–172, 1992.
- [74] M. Oldani and G. Schock, "Characterization of ultrafiltration membranes by infrared spectroscopy, ESCA, and contact angle measurements," *Journal of Membrane Science*, vol. 43, pp. 243–258, 1989.
- [75] G. R. Guillen, Y. Pan, M. Li, and E. M. V. Hoek, "Preparation and Characterization of Membranes Formed by Nonsolvent Induced Phase Separation: A Review," *Industrial & Engineering Chemistry Research*, vol. 50, no. 7, pp. 3798–3817, Apr. 2011.
- [76] Q. Li, X. Pan, Z. Qu, X. Zhao, Y. Jin, H. Dai, B. Yang, and X. Wang, "Understanding the dependence of contact angles of commercially RO membranes on external conditions and surface features," *Desalination*, vol. 309, pp. 38–45, Jan. 2013.
- [77] C. Jarusutthirak and G. Amy, "Role of soluble microbial products (SMP) in membrane fouling and flux decline.," *Environmental science & technology*, vol. 40, no. 3, pp. 969–974, Mar. 2006.
- [78] J. Cho, G. Amy, J. Pellegrino, and Y. Yoon, "Characterization of clean and natural organic matter (NOM) fouled NF and UF membranes, and foulants characterization," *Desalination*, vol. 118, no. 1–3, pp. 101–108, Sep. 1998.
- [79] C. Tang, Y. Kwon, and J. Leckie, "Probing the nano- and micro-scales of reverse osmosis membranes—A comprehensive characterization of physiochemical properties of uncoated and coated membranes by XPS, TEM, ATR-FTIR, and streaming potential measurements," *Journal of Membrane Science*, vol. 287, no. 1, pp. 146–156, 2007.
- [80] E. M. Vrijenhoek, S. Hong, and M. Elimelech, "Influence of membrane surface properties on initial rate of colloidal fouling of reverse osmosis and nanofiltration membranes," *Journal of Membrane Science*, vol. 188, no. 1, pp. 115–128, Jun. 2001.

- [81] Y. Baek, J. Kang, P. Theato, and J. Yoon, “Measuring hydrophilicity of RO membranes by contact angles via sessile drop and captive bubble method: A comparative study,” *Desalination*, vol. 303, pp. 23–28, Oct. 2012.
- [82] L. Gourley, M. Britten, S. F. Gauthier, and Y. Pouliot, “Characterization of adsorptive fouling on ultrafiltration membranes by peptides mixtures using contact angle measurements,” *Journal of Membrane Science*, vol. 97, no. 94, pp. 283–289, Dec. 1994.
- [83] A. Subramani, X. Huang, and E. M. V Hoek, “Direct observation of bacterial deposition onto clean and organic-fouled polyamide membranes.,” *Journal of colloid and interface science*, vol. 336, no. 1, pp. 13–20, Aug. 2009.
- [84] M. Rabiller-Baudry, L. Bégoïn, D. Delaunay, L. Paugam, and B. Chaufer, “A dual approach of membrane cleaning based on physico-chemistry and hydrodynamics,” *Chemical Engineering and Processing*, vol. 47, no. 3, pp. 267–275, Mar. 2008.
- [85] N. Wemsy Diagne, M. Rabiller-Baudry, and L. Paugam, “On the actual cleanability of polyethersulfone membrane fouled by proteins at critical or limiting flux,” *Journal of Membrane Science*, vol. 425–426, pp. 40–47, Jan. 2013.
- [86] P. Xu, J. E. Drewes, T.-U. Kim, C. Bellona, and G. Amy, “Effect of membrane fouling on transport of organic contaminants in NF/RO membrane applications,” *Journal of Membrane Science*, vol. 279, no. 1–2, pp. 165–175, Aug. 2006.
- [87] C. Y. Tang, Y.-N. Kwon, and J. O. Leckie, “Characterization of humic acid fouled reverse osmosis and nanofiltration membranes by transmission electron microscopy and streaming potential measurements.,” *Environmental science & technology*, vol. 41, no. 3, pp. 942–949, Mar. 2007.
- [88] C. Tang, Y. Kwon, and J. Leckie, “Probing the nano- and micro-scales of reverse osmosis membranes—A comprehensive characterization of physiochemical properties of uncoated and coated membranes by XPS, TEM, ATR-FTIR, and streaming potential measurements,” *Journal of Membrane Science*, vol. 287, no. 1, pp. 146–156, 2007.
- [89] M. Elimelech, W. H. Chen, and J. J. Waypa, “Measuring Zeta Potential of reverse osmosis membrane by a streaming potential analyzer,” *Desalination*, vol. 95, pp. 269–286, 1994.
- [90] V. Freger and S. Bason, “Characterization of ion transport in thin films using electrochemical impedance spectroscopyI. Principles and theory,” *Journal of Membrane Science*, vol. 302, no. 1–2, pp. 1–9, 2007.
- [91] S. Bason, Y. Oren, and V. Freger, “Characterization of ion transport in thin films using electrochemical impedance spectroscopyII: Examination of the polyamide layer of RO membranes,” *Journal of Membrane Science*, vol. 302, no. 1–2, pp. 10–19, 2007.
- [92] C. Charcosset and J. Bernengo, “Comparison of microporous membrane morphologies using confocal scanning laser microscopy,” *Journal of Membrane Science*, vol. 168, no. 1–2, pp. 53–62, 2000.

- [93] M. Ferrando, A. Rrzek, M. Zator, F. Lopez, and C. Guell, "An approach to membrane fouling characterization by confocal scanning laser microscopy," *Journal of Membrane Science*, vol. 250, no. 1–2, pp. 283–293, 2005.
- [94] C. Charcosset, "Characterization of microporous membrane morphology using confocal scanning laser microscopy," *Chemical Engineering Science*, vol. 55, no. 22, pp. 5351–5358, 2000.
- [95] M. Zator, M. Ferrando, F. Lopez, and C. Guell, "Membrane fouling characterization by confocal microscopy during filtration of BSA/dextran mixtures," *Journal of Membrane Science*, vol. 301, no. 1–2, pp. 57–66, 2007.
- [96] K.-J. Hwang and P.-Y. Sz, "Membrane fouling mechanism and concentration effect in cross-flow microfiltration of BSA/dextran mixtures," *Chemical Engineering Journal*, vol. 166, no. 2, pp. 669–677, 2011.
- [97] M. Hashino, K. Hiram, T. Ishigami, Y. Ohmukai, T. Maruyama, N. Kubota, and H. Matsuyama, "Effect of kinds of membrane materials on membrane fouling with BSA," *Journal of Membrane Science*, vol. 384, no. 1–2, pp. 157–165, Nov. 2011.
- [98] F. A. Pacheco, I. Pinnau, M. Reinhard, and J. O. Leckie, "Characterization of isolated polyamide thin films of RO and NF membranes using novel TEM techniques," *Journal of Membrane Science*, vol. 358, no. 1–2, pp. 51–59, 2010.
- [99] H.-J. Butt, B. Cappella, and M. Kappl, "Force measurements with the atomic force microscope: Technique, interpretation and applications," *Surface Science Reports*, vol. 59, no. 1–6, pp. 1–152, Oct. 2005.
- [100] I. Xiarchos and D. Doulia, "Interaction behavior in ultrafiltration of nonionic surfactant micelles by adsorption," *Journal of Colloid and Interface Science*, vol. 299, no. 1, pp. 102–111, Jul. 2006.
- [101] D. Delaunay, M. Rabiller-Baudry, J. M. Gozávez-Zafrilla, B. Balannec, M. Frappart, and L. Paugam, "Mapping of protein fouling by FTIR-ATR as experimental tool to study membrane fouling and fluid velocity profile in various geometries and validation by CFD simulation," *Chemical Engineering and Processing*, vol. 47, no. 7, pp. 1106–1117, Jul. 2008.
- [102] K. C. Khulbe and T. Matsuura, "Characterization of synthetic membranes by Raman spectroscopy, electron spin resonance, and atomic force microscopy; a review," *Polymer*, vol. 41, no. 5, pp. 1917–1935, 2000.
- [103] K. Chon, S. J. Kim, J. Moon, and J. Cho, "Combined coagulation-disk filtration process as a pretreatment of ultrafiltration and reverse osmosis membrane for wastewater reclamation: an autopsy study of a pilot plant," *Water research*, vol. 46, no. 6, pp. 1803–1816, Apr. 2012.
- [104] B. Kaeselev, P. Kingshott, and G. Jonsson, "Influence of the surface structure on the filtration performance of UV-modified {PES} membranes," *Desalination*, vol. 146, no. 1–3, pp. 265–271, 2002.

- [105] A. M. Belu, D. J. Graham, and D. G. Castner, "Time-of-flight secondary ion mass spectrometry: techniques and applications for the characterization of biomaterial surfaces.," *Biomaterials*, vol. 24, no. 21, pp. 3635–3653, 2003.
- [106] C. J. van Oss, *Interfacial Forces in Aqueous Media, Second Edition*. Taylor & Francis, 2006.
- [107] V. Freger and S. Bason, "Characterization of ion transport in thin films using electrochemical impedance spectroscopyI. Principles and theory," *Journal of Membrane Science*, vol. 302, no. 1–2, pp. 1–9, 2007.
- [108] S. Bason, Y. Oren, and V. Freger, "Characterization of ion transport in thin films using electrochemical impedance spectroscopyII: Examination of the polyamide layer of RO membranes," *Journal of Membrane Science*, vol. 302, no. 1–2, pp. 10–19, 2007.
- [109] J. Benavente, X. Zhang, and R. Garcia Valls, "Modification of polysulfone membranes with polyethylene glycol and lignosulfate: electrical characterization by impedance spectroscopy measurements.," *Journal of Colloid and Interface Science*, vol. 285, no. 1, pp. 273–280, 2005.
- [110] N. Ochoa, M. Masuelli, and J. Marchese, "Effect of hydrophilicity on fouling of an emulsified oil wastewater with PVDF/PMMA membranes," *Journal of Membrane Science*, vol. 226, no. 1–2, pp. 203–211, Dec. 2003.
- [111] C. Bellona, J. E. Drewes, P. Xu, and G. Amy, "Factors affecting the rejection of organic solutes during NF/RO treatment--a literature review.," *Water research*, vol. 38, no. 12, pp. 2795–2809, Jul. 2004.
- [112] K. Boussu, C. Kindts, C. Vandecasteele, and B. Van der Bruggen, "Surfactant fouling of nanofiltration membranes: measurements and mechanisms.," *ChemPhysChem*, vol. 8, no. 12, pp. 1836–1845, Aug. 2007.
- [113] G. K. Pearce, "Introduction to membranes: Fouling control," *Filtration Separation*, vol. 44, no. 6, pp. 30–32, 2007.
- [114] M. Mulder, *Basic Principles of Membrane Technology. Second Edition*. Boston: Kluwer, 1996.
- [115] V. Freger, J. Gilron, and S. Belfer, "TFC polyamide membranes modified by grafting of hydrophilic polymers: an FT-IR/AFM/TEM study," *Journal of Membrane Science*, vol. 209, no. 1, pp. 283–292, 2002.
- [116] E. Campus and S. Ampangan, "Development of a highly hydrophilic nanofiltration membrane for desalination and water treatment," vol. 168, pp. 215–221, 2004.
- [117] D. F. Evans and H. Wennerström, *The colloidal domain: where physics, chemistry, and biology meet*. Wiley-VCH New York, 1999.

- [118] C. Charcosset and J. Bernengo, "Comparison of microporous membrane morphologies using confocal scanning laser microscopy," *Journal of Membrane Science*, vol. 168, no. 1–2, pp. 53–62, 2000.
- [119] M. Ferrando, A. Rrzek, M. Zator, F. Lopez, and C. Guell, "An approach to membrane fouling characterization by confocal scanning laser microscopy," *Journal of Membrane Science*, vol. 250, no. 1–2, pp. 283–293, 2005.
- [120] C. Charcosset, "Characterization of microporous membrane morphology using confocal scanning laser microscopy," *Chemical Engineering Science*, vol. 55, no. 22, pp. 5351–5358, 2000.
- [121] M. Zator, M. Ferrando, F. Lopez, and C. Guell, "Membrane fouling characterization by confocal microscopy during filtration of BSA/dextran mixtures," *Journal of Membrane Science*, vol. 301, no. 1–2, pp. 57–66, 2007.
- [122] K.-J. Hwang and P.-Y. Sz, "Membrane fouling mechanism and concentration effect in cross-flow microfiltration of BSA/dextran mixtures," *Chemical Engineering Journal*, vol. 166, no. 2, pp. 669–677, 2011.
- [123] J. S. Louie, I. Pinnau, I. Ciobanu, K. P. Ishida, A. Ng, and M. Reinhard, "Effects of polyether–polyamide block copolymer coating on performance and fouling of reverse osmosis membranes," *Journal of Membrane Science*, vol. 280, no. 1–2, pp. 762–770, Sep. 2006.
- [124] B. Chistyakov, "6. Theory and practical application aspects of surfactants," *Studies in Interface Science*, vol. 13, pp. 511–618, 2001.
- [125] A. Singh, J. D. Van Hamme, and O. P. Ward, "Surfactants in microbiology and biotechnology: Part 2. Application aspects.," *Biotechnology Advances*, vol. 25, no. 1, pp. 99–121, 2007.
- [126] T. Cosgrove, *Colloid Science: Principles, Methods and Applications, 2nd Edition*. John Wiley & Sons, 2010, p. 394.
- [127] M. J. Scott and M. N. Jones, "The biodegradation of surfactants in the environment," *Biochimica et Biophysica Acta*, vol. 1508, no. 1–2, pp. 235–251, Nov. 2000.
- [128] K. Holmberg, B. Jönsson, B. Kronberg, and B. Lindman, *Surfactants and Polymers in Aqueous Solution. 2nd Edition*. John Wiley & Sons Ltd, England, 2002.
- [129] K. R. Krovvidi, A. Muscat, P. Stroeve, and E. Ruckenstein, "Transport of monomer surfactant molecules and hindered diffusion of micelles through porous membranes," *Journal of Colloid and Interface Science*, vol. 100, no. 2, pp. 497–505, Aug. 1984.
- [130] R. Nagarajan, "Theory of Surfactant Self -Assembly: A Predictive Molecular Thermodynamic Approach," *Langmuir*, vol. 7, no. 3, pp. 2934–2969, 1991.

- [131] R. Zhang and P. Somasundaran, "Advances in adsorption of surfactants and their mixtures at solid/solution interfaces," *Advances in Colloid and Interface Science*, vol. 123–126, pp. 213–229, Nov. 2006.
- [132] G. G. Warr, "Surfactant adsorbed layer structure at solid/solution interfaces: impact and implications of AFM imaging studies," *Current Opinion in Colloid & Interface Science*, vol. 5, no. 1–2, pp. 88–94, Mar. 2000.
- [133] R. Atkin, V. S. J. Craig, E. J. Wanless, and S. Biggs, "Mechanism of cationic surfactant adsorption at the solid-aqueous interface," *Advances in colloid and interface science*, vol. 103, no. 3, pp. 219–304, May 2003.
- [134] R. a Johnson and R. Nagarajan, "Modeling self-assembly of surfactants at solid/liquid interfaces. I. Hydrophobic surfaces," *Colloids and Surfaces A: Physicochemical and Engineering Aspects*, vol. 167, no. 1–2, pp. 31–46, Jun. 2000.
- [135] F. Tiberg, J. Brinck, and L. Grant, "Adsorption and surface-induced self-assembly of surfactants at the solid-aqueous interface," *Current Opinion in Colloid & Interface Science*, vol. 4, no. 6, pp. 411–419, Dec. 2000.
- [136] S. Nielsen, G. Srinivas, C. Lopez, and M. Klein, "Modeling Surfactant Adsorption on Hydrophobic Surfaces," *Physical Review Letters*, vol. 94, no. 22, pp. 10–13, Jun. 2005.
- [137] R. F. Tabor, J. Eastoe, and P. J. Dowding, "A two-step model for surfactant adsorption at solid surfaces.," *Journal of Colloid and Interface Science*, vol. 346, no. 2, pp. 424–428, Jun. 2010.
- [138] P. Somasundaran and D. W. Fuerstenau, "Mechanisms of Alkyl Sulfonate Adsorption at the Alumina-Water Interface," *Journal of Physical Chemistry*, vol. 70, no. 1, pp. 90–96, 1966.
- [139] S. Paria and K. C. Khilar, "A review on experimental studies of surfactant adsorption at the hydrophilic solid-water interface," *Advances in Colloid and Interface Science*, vol. 110, no. 3, pp. 75–95, Aug. 2004.
- [140] M. Ahmed and M. Corresponding, "Equilibrium Adsorption Isotherms of Anionic , Nonionic Surfactants and Their Mixtures to Shale and Sandstone," *Adsorption Journal Of The International Adsorption Society*, vol. 3, no. 2, pp. 158–167.
- [141] K. Majewska-Nowak, I. Kowalska, and M. Kabsch-Korbutowicz, "Ultrafiltration of SDS solutions using polymeric membranes," *Desalination*, vol. 184, no. 1–3, pp. 415–422, Nov. 2005.
- [142] C. Y. Tang, Q. S. Fu, A. P. Robertson, C. S. Criddle, and J. O. Leckie, "Use of reverse osmosis membranes to remove perfluorooctane sulfonate (PFOS) from semiconductor wastewater.," *Environmental Science & Technology*, vol. 40, no. 23, pp. 7343–7349, Dec. 2006.
- [143] C. Y. Tang, Q. S. Fu, C. S. Criddle, and J. O. Leckie, "Effect of flux (transmembrane pressure) and membrane properties on fouling and rejection of reverse osmosis and

- nanofiltration membranes treating perfluorooctane sulfonate containing wastewater.,” *Environmental science & technology*, vol. 41, no. 6, pp. 2008–14, Mar. 2007.
- [144] C. Baudequin, E. Couallier, M. Rakib, I. Deguerry, R. Severac, and M. Pabon, “Purification of firefighting water containing a fluorinated surfactant by reverse osmosis coupled to electrocoagulation–filtration,” *Separation and Purification Technology*, vol. 76, no. 3, pp. 275–282, Jan. 2011.
- [145] M. Mietton-Peuchot, O. Ranisio, and C. Peuchot, “Study of Behaviour of Membranes in the Presence of Anionic or Nonionic Surfactants,” *Membranes & Surfactants*, vol. 34, no. 10, pp. 883–886, 1997.
- [146] Z. Tu, L. Ding, M. Frappart, and M. Y. Jaffrin, “Studies on treatment of sodium dodecyl benzene sulfonate solution by high shear ultrafiltration system,” *Desalination*, vol. 240, no. 1–3, pp. 251–256, May 2009.
- [147] M. Chapman Wilbert, J. Pellegrino, and A. Zydney, “Bench-scale testing of surfactant-modified reverse osmosis/nanofiltration membranes,” *Desalination*, vol. 115, no. 1, pp. 15–32, Mar. 1998.
- [148] “Effect of humic substances and anionic surfactants on the surface charge and performance of reverse osmosis membranes,” *Desalination*, vol. 118, no. 1–3, pp. 167–174, 1998.
- [149] Y. Zhou, S. Yu, C. Gao, and X. Feng, “Surface modification of thin film composite polyamide membranes by electrostatic self deposition of polycations for improved fouling resistance,” *Separation and Purification Technology*, vol. 66, no. 2, pp. 287–294, Apr. 2009.
- [150] W. S. Ang, A. Tiraferri, K. L. Chen, and M. Elimelech, “Fouling and cleaning of RO membranes fouled by mixtures of organic foulants simulating wastewater effluent,” *Journal of Membrane Science*, vol. 376, no. 1–2, pp. 196–206, Jul. 2011.
- [151] C. A. Basar, A. Karagunduz, A. Cakici, and B. Keskinler, “Removal of surfactants by powdered activated carbon and microfiltration,” *Water Research*, vol. 38, no. 8, pp. 2117–2124, Apr. 2004.
- [152] D. Doulia, V. Gekas, and G. Tragardh, “Interaction behaviour in ultrafiltration of nonionic surfactants . Part 1 . Flux behaviour,” *Journal of Membrane Science*, vol. 69, pp. 251–258, 1992.
- [153] D. Doulia, G. Tragardh, and V. Gekas, “Interaction behaviour in ultrafiltration of nonionic surfactants Part II . Static adsorption below CMC,” *Journal of Membrane Science*, vol. 123, no. 1, pp. 133–142, 1997.
- [154] A. Jonsson and B. Jonsson, “The influence of nonionic and ionic surfactants on hydrophobic and hydrophilic ultrafiltration membranes,” *Journal of Membrane Science*, vol. 56, pp. 49–76, 1991.

- [155] E. Fernández, J. M. Benito, C. Pazos, and J. Coca, “Ceramic membrane ultrafiltration of anionic and nonionic surfactant solutions,” *Journal of Membrane Science*, vol. 246, no. 1, pp. 1–6, Jan. 2005.
- [156] B. Van der Bruggen, G. Cornelis, C. Vandecasteele, and I. Devreese, “Fouling of nanofiltration and ultrafiltration membranes applied for wastewater regeneration in the textile industry,” *Desalination*, vol. 175, no. 1, pp. 111–119, May 2005.
- [157] I. Kowalska, K. Majewska-nowak, and M. Kabsch-korbutowicz, “Influence of temperature on anionic surface active agent removal from a water solution by ultrafiltration,” vol. 198, no. 9, pp. 132–139, 2006.
- [158] I. Kowalska, “Surfactant removal from water solutions by means of ultrafiltration and ion-exchange,” *Desalination*, vol. 221, pp. 351–357, 2008.
- [159] J.-S. Yang, K. Baek, and J.-W. Yang, “Crossflow ultrafiltration of surfactant solutions,” *Desalination*, vol. 184, no. 1–3, pp. 385–394, Nov. 2005.
- [160] H. Byhlin and A. Jönsson, “Influence of adsorption and concentration polarisation on membrane performance during ultrafiltration of a non-ionic surfactant,” *Desalination*, vol. 151, no. 4, pp. 21–31, 2003.
- [161] Y.-Y. Fang, G.-M. Zeng, J.-H. Huang, J.-X. Liu, X.-M. Xu, K. Xu, and Y.-H. Qu, “Micellar-enhanced ultrafiltration of cadmium ions with anionic–nonionic surfactants,” *Journal of Membrane Science*, vol. 320, no. 1–2, pp. 514–519, Jul. 2008.
- [162] M. Aoudia, N. Allal, A. Djennet, and L. Toumi, “Dynamic micellar enhanced ultrafiltration: use of anionic (SDS)–nonionic(NPE) system to remove Cr³⁺ at low surfactant concentration,” *Journal of Membrane Science*, vol. 217, no. 1–2, pp. 181–192, Jun. 2003.
- [163] F. Ferella, M. Prisciandaro, I. De Michelis, and F. Veglio’, “Removal of heavy metals by surfactant-enhanced ultrafiltration from wastewaters,” *Desalination*, vol. 207, no. 1–3, pp. 125–133, Mar. 2007.
- [164] Y. Kaya, C. Aydiner, H. Barlas, and B. Keskinler, “Nanofiltration of single and mixture solutions containing anionics and nonionic surfactants below their critical micelle concentrations (CMCs),” *Journal of Membrane Science*, vol. 282, no. 1–2, pp. 401–412, Oct. 2006.
- [165] B. Wendler, B. Goers, and G. Wozny, “Nanofiltration of solutions containing surfactants - prediction of flux decline and modelling of mass transfer,” *Desalination*, vol. 147, no. 1–3, pp. 217–221, 2002.
- [166] C. KAMIZAWA and S. ISHIZAKA, “Study on reverse osmosis. The permeation behavior of surfactant solution through cellulose acetate membranes,” *Bulletin of the Chemical Society of Japan*, vol. 45, pp. 2967–2969, 1972.
- [167] G. Kang and Y. Cao, “Development of antifouling reverse osmosis membranes for water treatment: A review.,” *Water research*, vol. 46, no. 3, pp. 584–600, Mar. 2012.

- [168] E. Staude, E. Hinke, and F. Malejka, "Interactions in reverse osmosis of electrolyte/charged surfactant solutions through porous membranes," *Colloids and Surfaces*, vol. 42, no. 2, pp. 365–374, 1989.
- [169] T. Srisukphun, C. Chiemchaisri, T. Urase, and K. Yamamoto, "Foulant interaction and RO productivity in textile wastewater reclamation plant," *Desalination*, vol. 250, no. 2, pp. 845–849, Jan. 2010.
- [170] M. Elimelech, X. Zhu, A. E. Childress, and S. Hong, "Role of membrane surface morphology in colloidal fouling of cellulose acetate and composite aromatic polyamide reverse osmosis membranes," *Journal of Membrane Science*, vol. 127, pp. 101–109, 1997.
- [171] E. Hinke, D. Laslop, and E. Staude, "The influence of charged surfactants upon reverse osmosis," *Progress in Colloid & Polymer Science*, vol. 99, pp. 94–99, 1988.
- [172] a. Bakx, a. M. D. E. Timmerman, and G. Frens, "Shear stimulated adsorption of surfactants from micellar solutions," *Colloids and Surfaces A: Physicochemical and Engineering Aspects*, vol. 183–185, pp. 149–157, Jul. 2001.
- [173] P. Bacchin, P. Aimar, and R. Field, "Critical and sustainable fluxes: Theory, experiments and applications," *Journal of Membrane Science*, vol. 281, no. 1–2, pp. 42–69, Sep. 2006.
- [174] B. Espinasse, P. Bacchin, and P. Aimar, "Filtration method characterizing the reversibility of colloidal fouling layers at a membrane surface: analysis through critical flux and osmotic pressure.," *Journal of colloid and interface science*, vol. 320, no. 2, pp. 483–490, Apr. 2008.
- [175] C. Y. Tang, T. H. Chong, and A. G. Fane, "Colloidal interactions and fouling of NF and RO membranes: a review.," *Advances in Colloid and Interface Science*, vol. 164, no. 1–2, pp. 126–143, May 2011.
- [176] P. Aimar and P. Bacchin, "Slow colloidal aggregation and membrane fouling," *Journal of Membrane Science*, vol. 360, no. 1–2, pp. 70–76, Sep. 2010.
- [177] X. Zhu and M. Elimelech, "Colloidal Fouling of Reverse Osmosis Membranes: Measurements and Fouling Mechanisms," *Environmental Science & Technology*, vol. 31, no. 12, pp. 3654–3662, Dec. 1997.
- [178] J. HERMIA, "Constant Pressure Blocking Filtration Law Application to Powder-Law Non-Newtonian Fluid," *Trans. Inst. Chem. Eng.*, vol. 60, pp. 183–187, 1982.
- [179] A. Simon, W. E. Price, and L. D. Nghiem, "Implications of chemical cleaning on the performance of NF / RO membranes: the retention of pharmaceutically active compounds (PhACs)," in *6th IWA Specialist Conference on Membrane Technology for Water and Wastewater Treatment Aachen Germany*, 2011.
- [180] J. Vicente, Y. Wyart, and P. Moulin, "From 2D to 3D Characterization of Ceramic Membranes," *Procedia Engineering*, vol. 44, pp. 517–520, Jan. 2012.

- [181] N. Ghaffour, “Modeling of fouling phenomena in cross-flow ultrafiltration of suspensions containing suspended solids and oil droplets,” *Desalination*, vol. 167, no. 8, pp. 281–291, 2004.
- [182] K. Katsoufidou, S. Yiantsios, and a Karabelas, “A study of ultrafiltration membrane fouling by humic acids and flux recovery by backwashing: Experiments and modeling,” *Journal of Membrane Science*, vol. 266, no. 1–2, pp. 40–50, Dec. 2005.
- [183] Z. Cui, “Protein separation using ultrafiltration — an example of multi-scale complex systems,” *China Particuology*, vol. 3, no. 6, pp. 343–348, 2005.
- [184] F. Zheng, X. Zhang, and W. Wang, “Comment on Monte Carlo simulation of surfactant adsorption on hydrophilic surfaces.,” *Langmuir: the ACS journal of surfaces and colloids*, vol. 25, no. 13, pp. 7766–7, Jul. 2009.
- [185] S. Karaborni and B. Smit, “Computer simulations of surfactant structures,” *Current Opinion in Colloid & Interface Science*, vol. 1, no. 3, pp. 411–415, Jun. 1996.
- [186] G. Srinivas, S. O. Nielsen, P. B. Moore, and M. L. Klein, “Molecular dynamics simulations of surfactant self-organization at a solid-liquid interface.,” *Journal of the American Chemical Society*, vol. 128, no. 3, pp. 848–853, Jan. 2006.
- [187] S. Bandyopadhyay, M. Tarek, and M. L. Klein, “Computer simulation studies of amphiphilic interfaces,” *Current Opinion in Colloid & Interface Science*, vol. 3, no. 3, pp. 242–246, Jun. 1998.
- [188] E. N. Brodskaya, “Computer simulations of micellar systems,” *Colloid Journal*, vol. 74, no. 2, pp. 154–171, Mar. 2012.
- [189] X. Zhang, B. Chen, and Z. Wang, “Computer simulation of adsorption kinetics of surfactants on solid surfaces.,” *Journal of Colloid and Interface Science*, vol. 313, no. 2, pp. 414–422, Sep. 2007.
- [190] W. Guo, H.-H. Ngo, and J. Li, “A mini-review on membrane fouling,” *Bioresource technology*, vol. 122, pp. 27–34, Oct. 2012.
- [191] T. Srisukphun, C. Chiemchaisri, T. Urase, and K. Yamamoto, “Experimentation and modeling of foulant interaction and reverse osmosis membrane fouling during textile wastewater reclamation,” *Separation and Purification Technology*, vol. 68, no. 1, pp. 37–49, Jun. 2009.
- [192] A. J. C. Semião and A. I. Schäfer, “Removal of adsorbing estrogenic micropollutants by nanofiltration membranes. Part A—Experimental evidence,” *Journal of Membrane Science*, vol. 431, pp. 244–256, Mar. 2013.
- [193] M. C. Kaplan, a. Jégou, B. Chaufer, M. Rabiller-Baudry, and M. C. Michalsky, “Adsorption of lysozyme on membrane material and cleaning with non-ionic surfactant characterized through contact angle measurements,” *Desalination*, vol. 146, no. 1–3, pp. 149–154, Sep. 2002.

- [194] N. Subhi, A. R. D. Verliefde, V. Chen, and P. Le-Clech, "Assessment of physicochemical interactions in hollow fibre ultrafiltration membrane by contact angle analysis," *Journal of Membrane Science*, vol. 403–404, pp. 32–40, Jun. 2012.
- [195] V. Geka, M. Perssona, M. Wahlgrenb, and B. Sivik, "Contact angles of ultrafiltration membranes and their possible correlation to membrane performance," *Journal of Membrane Science*, vol. 72, pp. 293–302, 1992.
- [196] A. R. D. Verliefde, E. R. Cornelissen, S. G. J. Heijman, E. M. V Hoek, G. L. Amy, B. Van der Bruggen, and J. C. Van Dijk, "Influence of solute-membrane affinity on rejection of uncharged organic solutes by nanofiltration membranes.," *Environmental science & technology*, vol. 43, no. 7, pp. 2400–2406, Apr. 2009.
- [197] B. Wendler, B. Goers, and G. Wozny, "Nanofiltration of solutions containing surfactants—prediction of flux decline and modelling of mass transfer," *Desalination*, vol. 147, no. 1–3, pp. 217–221, Sep. 2002.
- [198] A. E. Chddress and S. S. Deshmukh, "Effect of humic substances and anionic surfactants on the surface charge and performance of reverse osmosis membranes," vol. 118, pp. 167–174, 1998.
- [199] M. Benrraou, B. L. Bales, and R. Zana, "Effect of the Nature of the Counterion on the Properties of Anionic Surfactants. 1. Cmc, Ionization Degree at the Cmc and Aggregation Number of Micelles of Sodium, Cesium, Tetramethylammonium, Tetraethylammonium, Tetrapropylammonium, and Tetrabutylammoniu," *Journal of Physical Chemistry B*, vol. 107, no. 48, pp. 13432–13440, 2003.
- [200] C. J. Van Oss, "Development and applications of the interfacial tension between water and organic or biological surfaces.," *Colloids and surfaces B Biointerfaces*, vol. 54, no. 1, pp. 2–9, 2007.
- [201] J. A. Zasadzinski, R. Viswanathan, L. Madsen, J. Garnaes, and D. K. Schwartz, "Langmuir-Blodegett film.pdf," *Science*, vol. 263, no. 3, pp. 1726–1733, 1994.
- [202] S. Paria and K. C. Khilar, "A review on experimental studies of surfactant adsorption at the hydrophilic solid-water interface.," *Advances in Colloid and Interface Science*, vol. 110, no. 3, pp. 75–95, Aug. 2004.
- [203] H. B. de Aguiar, M. L. Strader, A. G. F. de Beer, and S. Roke, "Surface structure of sodium dodecyl sulfate surfactant and oil at the oil-in-water droplet liquid/liquid interface: a manifestation of a nonequilibrium surface state.," *The journal of physical chemistry. B*, vol. 115, no. 12, pp. 2970–2978, Mar. 2011.
- [204] B. Kronberg, "Thermodynamics of adsorption of nonionic surfactants on latexes," *Journal of Colloid and Interface Science*, vol. 96, no. 1, pp. 55–68, Nov. 1983.
- [205] R. Xing and S. E. Rankin, "Three-stage multilayer formation kinetics during adsorption of an anionic fluorinated surfactant onto germanium. 1. Concentration effect.," *The journal of physical chemistry. B*, vol. 110, no. 1, pp. 295–304, Jan. 2006.

- [206] H. Nakahara, O. Shibata, and Y. Moroi, "Examination of surface adsorption of cetyltrimethylammonium bromide and sodium dodecyl sulfate," *The Journal of Physical Chemistry B*, vol. 115, no. 29, pp. 9077–9086, Jul. 2011.
- [207] M. Cao, X. Song, J. Wang, and Y. Wang, "Adsorption of hexyl- α,ω -bis(dodecyldimethylammonium bromide) gemini surfactant on silica and its effect on wettability," *Journal of colloid and interface science*, vol. 300, no. 2, pp. 519–525, Aug. 2006.
- [208] Q. Song, A. Couzis, P. Somasundaran, and C. Maldarelli, "A transport model for the adsorption of surfactant from micelle solutions onto a clean air/water interface in the limit of rapid aggregate disassembly relative to diffusion and supporting dynamic tension experiments," *Colloids and Surfaces A: Physicochemical and Engineering Aspects*, vol. 282–283, pp. 162–182, Jul. 2006.
- [209] L. L. Schramm, E. N. Stasiuk, and D. G. Marangoni, "2. Surfactants and their applications," *Annual Reports Progress in Chemistry Section C*, vol. 99, pp. 3–48, 2003.
- [210] Z. Wang, G. Li, X. Zhang, R. Wang, and A. Lou, "A quantitative structure-property relationship study for the prediction of critical micelle concentration of nonionic surfactants," *Colloids and Surfaces A: Physicochemical and Engineering Aspects*, vol. 197, no. 1–3, pp. 37–45, Feb. 2002.
- [211] K. Ogino, T. Kakihara, and M. Abe, "Estimation of the critical micelle concentrations and the aggregation numbers of sodium alkyl sulfates by capillary-type isotachopheresis," *Colloid & Polymer Science*, vol. 265, no. 7, pp. 604–612, Jul. 1987.
- [212] W. Li, M. Zhang, J. Zhang, and Y. Han, "Self-assembly of cetyl trimethylammonium bromide in ethanol-water mixtures," *Frontiers of Chemistry in China*, vol. 1, no. 4, pp. 438–442, Dec. 2006.
- [213] S.-Y. Kim, A. Z. Panagiotopoulos, and M. A. Floriano, "Ternary oil—water—amphiphile systems: self-assembly and phase equilibria," *Molecular Physics*, vol. 100, no. 14, pp. 2213–2220, Jul. 2002.
- [214] P. Huibers, V. Lobanov, A. Katritzky, D. Shah, and M. Karelson, "Prediction of Critical Micelle Concentration Using a Quantitative Structure-Property Relationship Approach," *Journal of Colloid and Interface Science*, vol. 187, no. 1, pp. 113–120, Mar. 1997.
- [215] J. Coret, a. Shiloach, P. Berger, and D. Blankshtein, "Critical micelle concentrations of ternary surfactant mixtures: Theoretical prediction with user-friendly computer programs and experimental design analysis," *Journal of Surfactants and Detergents*, vol. 2, no. 1, pp. 51–58, Jan. 1999.
- [216] T. Gilányi, "Fluctuating micelles: a theory of surfactant aggregation 2. Ionic surfactants," *Colloids and Surfaces A: Physicochemical and Engineering Aspects*, vol. 104, no. 1, pp. 119–126, Nov. 1995.

- [217] A. Bhattacharya, "Self-assembly of ionic surfactants and formation of mesostructures," *Journal of Physics: Condensed Matter*, vol. 13, no. 7, pp. 1413–1428, Jan. 2001.
- [218] T. Gilányi, "Fluctuating micelles: a theory of surfactant aggregation part 1. Nonionic surfactants," *Colloids and Surfaces A: Physicochemical and Engineering Aspects*, vol. 104, no. 1, pp. 111–118, Nov. 1995.
- [219] H. B. Klevens, "Structure and aggregation in dilute solution of surface active agents," *Journal of the American Oil Chemists Society*, vol. 30, no. 2, pp. 74–80, 1953.
- [220] a. Patist, S. G. Oh, R. Leung, and D. O. Shah, "Kinetics of micellization: its significance to technological processes," *Colloids and Surfaces A: Physicochemical and Engineering Aspects*, vol. 176, no. 1, pp. 3–16, Jan. 2001.
- [221] T. Tahara, I. Satake, and R. Matuura, "The Micellar Properties of Disodium Monoalkyl Phosphates in Aqueous Solutions.pdf," *Bulletin of the Chemical Society of Japan*, vol. 42, no. 5, pp. 1201–1205, 1969.
- [222] J. C. Shelley and M. Y. Shelley, "Computer simulation of surfactant solutions," *Current Opinion in Colloid & Interface Science*, vol. 5, no. 1–2, pp. 101–110, Mar. 2000.
- [223] N. Yoshii and S. Okazaki, "Free energy of water permeation into hydrophobic core of sodium dodecyl sulfate micelle by molecular dynamics calculation.," *The Journal of Chemical Physics*, vol. 126, no. 9, p. 096101, Mar. 2007.
- [224] C. D. Bruce, M. L. Berkowitz, L. Perera, and M. D. E. Forbes, "Molecular Dynamics Simulation of Sodium Dodecyl Sulfate Micelle in Water: Micellar Structural Characteristics and Counterion Distribution," *The Journal of Physical Chemistry B*, vol. 106, no. 15, pp. 3788–3793, Apr. 2002.
- [225] S. J. Marrink, D. P. Tieleman, and a. E. Mark, "Molecular Dynamics Simulation of the Kinetics of Spontaneous Micelle Formation," *The Journal of Physical Chemistry B*, vol. 104, no. 51, pp. 12165–12173, Dec. 2000.
- [226] E. Ryjkina, H. Kuhn, H. Rehage, M. Felix, and J. Peggau, "Molecular Dynamic Computer Simulations of Phase Behavior of Non-Ionic Surfactants," *Angewandte Chemie International Edition*, vol. 41, no. 6, pp. 983–986, 2002.
- [227] J. Shelley, K. Watanabe, and M. L. Klein, "Simulation of a sodium dodecylsulfate micelle in aqueous solution," *International Journal of Quantum Chemistry*, vol. 38, no. S17, pp. 103–117, Mar. 1990.
- [228] A. D. MacKerell, "Molecular Dynamics Simulation Analysis of a Sodium Dodecyl Sulfate Micelle in Aqueous Solution: Decreased Fluidity of the Micelle Hydrocarbon Interior," *The Journal of Physical Chemistry*, vol. 99, no. 7, pp. 1846–1855, Feb. 1995.
- [229] D. P. Tieleman, D. van der Spoel, and H. J. C. Berendsen, "Molecular Dynamics Simulations of Dodecylphosphocholine Micelles at Three Different Aggregate

- Sizes: Micellar Structure and Chain Relaxation,” *The Journal of Physical Chemistry B*, vol. 104, no. 27, pp. 6380–6388, Jul. 2000.
- [230] S. A. Sanders, M. Sammalkorpi, and A. Z. Panagiotopoulos, “Atomistic simulations of micellization of sodium hexyl, heptyl, octyl, and nonyl sulfates.,” *The Journal of Physical Chemistry B*, vol. 116, no. 8, pp. 2430 – 2437, Mar. 2012.
- [231] P. K. Maiti, Y. Lansac, M. a. Glaser, N. a. Clark, and Y. Rouault, “Self-Assembly in Surfactant Oligomers: A Coarse-Grained Description through Molecular Dynamics Simulations,” *Langmuir*, vol. 18, no. 5. pp. 1908–1918, Mar-2002.
- [232] S. V Burov, N. P. Obrezkov, A. A. Vanin, and E. M. Piotrovskaya, “Molecular Dynamic Simulation of Micellar Solutions : A Coarse-Grain Model,” *Colloid Journal*, vol. 70, no. 1, pp. 1–5, 2008.
- [233] D. N. LeBard, B. G. Levine, P. Mertmann, S. a. Barr, A. Jusufi, S. Sanders, M. L. Klein, and A. Z. Panagiotopoulos, “Self-assembly of coarse-grained ionic surfactants accelerated by graphics processing units,” *Soft Matter*, vol. 8, no. 8, pp. 2385–2397, 2012.
- [234] P. J. Hoogerbrugge and J. M. V. a Koelman, “Simulating Microscopic Hydrodynamic Phenomena with Dissipative Particle Dynamics,” *Europhysics Letters (EPL)*, vol. 19, no. 3, pp. 155–160, Jun. 1992.
- [235] P. B. Warren, “Dissipative particle dynamics,” *Current Opinion in Colloid & Interface Science*, vol. 3, no. 6, pp. 620–624, Dec. 1998.
- [236] R. D. Groot and T. J. Madden, “Dynamic simulation of diblock copolymer microphase separation,” *The Journal of Chemical Physics*, vol. 108, no. 20, p. 8713, 1998.
- [237] R. Pool and P. G. Bolhuis, “Can purely repulsive soft potentials predict micelle formation correctly?,” *Physical Chemistry Chemical Physics*, vol. 8, no. 8, pp. 941–948, Feb. 2006.
- [238] H. Wu, J. Xu, X. He, Y. Zhao, and H. Wen, “Mesoscopic simulation of self-assembly in surfactant oligomers by dissipative particle dynamics,” *Colloids and Surfaces A: Physicochemical and Engineering Aspects*, vol. 290, no. 1–3, pp. 239–246, Nov. 2006.
- [239] R. D. Groot, “Mesoscopic Simulation of Polymer–Surfactant Aggregation,” *Langmuir*, vol. 16, no. 19, pp. 7493–7502, Sep. 2000.
- [240] B. Duan, X. Zhang, B. Qiao, B. Kong, and X. Yang, “Description of ionic surfactant/water system by adjusting mesoscopic parameters.,” *The Journal of Physical Chemistry B*, vol. 113, no. 26, pp. 8854–8859, Jul. 2009.
- [241] R. M. Fuchsli, H. Fellermann, A. Eriksson, and H.-J. Ziock, “Coarse graining and scaling in dissipative particle dynamics.,” *The Journal of Chemical Physics*, vol. 130, no. 21, p. 214102, Jun. 2009.

- [242] Z. Li and E. E. Dormidontova, “Kinetics of Diblock Copolymer Micellization by Dissipative Particle Dynamics,” *Macromolecules*, vol. 43, no. 7, pp. 3521–3531, Apr. 2010.
- [243] C.-M. Lin, G.-P. Chang, H.-K. Tsao, and Y.-J. Sheng, “Solubilization mechanism of vesicles by surfactants: effect of hydrophobicity,” *The Journal of Chemical Physics*, vol. 135, no. 4, p. 045102, Jul. 2011.
- [244] A. Vishnyakov, M.-T. Lee, and A. V. Neimark, “Prediction of the Critical Micelle Concentration of Nonionic Surfactants by Dissipative Particle Dynamics Simulations,” *The Journal of Physical Chemistry Letters*, vol. 4, no. 5, pp. 797–802, Mar. 2013.
- [245] A. Maiti and S. McGrother, “Bead-bead interaction parameters in dissipative particle dynamics: relation to bead-size, solubility parameter, and surface tension,” *The Journal of Chemical Physics*, vol. 120, no. 3, pp. 1594–1601, Jan. 2004.
- [246] M. Kranenburg, J. Nicolas, and B. Smit, “Comparison of mesoscopic phospholipid – water models,” no. Md, 2004.
- [247] R.D. Groot and K. L. Rabone, “Mesoscopic simulation of cell membrane damage, morphology change and rupture by nonionic surfactants,” *Biophysical Journal*, vol. 81, no. 2, pp. 725–736, Aug. 2001.
- [248] M. Kranenburg, M. Vlaar, and B. Smit, “Simulating induced interdigitation in membranes,” *Biophysical journal*, vol. 87, no. 3, pp. 1596–605, Sep. 2004.
- [249] M. Kranenburg, J. Nicolas, and B. Smit, “Comparison of mesoscopic phospholipid – water models,” *Physical Chemistry Chemical Physics*, vol. 6, pp. 4142 – 4151, 2004.
- [250] J. Rassing, P. J. Sams, and E. Wyn-Jones, “Kinetics of micellization from ultrasonic relaxation studies,” *Journal of the Chemical Society, Faraday Transactions 2: Molecular and Chemical Physics*, vol. 70, pp. 1247–1258, 1974.
- [251] J. M. Ruso, D. Attwood, P. Taboada, V. Mosquera, and F. Sarmiento, “Light Scattering and NMR Studies on the Self-Aggregation of Sodium n -Hexyl Sulfate in Aqueous Electrolyte Solution,” *Langmuir*, vol. 16, no. 4, pp. 1620–1625, 2000.
- [252] M. J. Suárez, J. L. López-Fontán, F. Sarmiento, and V. Mosquera, “Thermodynamic Study of the Aggregation Behavior of Sodium n -Hexyl Sulfate in Aqueous Solution,” *Langmuir*, vol. 15, no. 16, pp. 5265–5270, 1999.
- [253] Q.-X. Guo, X.-Q. Zhu, T. Ren, and Y.-C. Liu, “A study of vitamin A as a probe in critical micelle concentration determinations of surfactants,” *Journal of Inclusion Phenomena and Molecular Recognition in Chemistry*, vol. 17, no. 1, pp. 37–44, 1994.
- [254] R. Ranganathan, M. Peric, and B. L. Bales, “Time-Resolved Fluorescence Quenching Measurements of the Aggregation Numbers of Normal Sodium Alkyl Sulfate Micelles Well above the Critical Micelle Concentrations,” *Journal of Physical Chemistry B*, vol. 102, no. 43, pp. 8436–8439, 1998.

- [255] P. Mukerjee and K. J. Mysels, "Critical micelle concentrations of aqueous surfactant systems," *Journal of Electroanalytical Chemistry*, vol. 41, no. 1, pp. 143–144, 1971.
- [256] T. V.-O. Nguyen, C. Houriez, and B. Rousseau, "Viscosity of the 1-ethyl-3-methylimidazolium bis(trifluoromethylsulfonyl)imide ionic liquid from equilibrium and nonequilibrium molecular dynamics.," *Physical chemistry chemical physics: PCCP*, vol. 12, no. 4, pp. 930–6, Jan. 2010.
- [257] R. D. Groot and K. L. Rabone, "Mesoscopic simulation of cell membrane damage, morphology change and rupture by nonionic surfactants.," *Biophysical Journal*, vol. 81, no. 2, pp. 725–736, Aug. 2001.
- [258] L. Rekvig, M. Kranenburg, J. Vreede, B. Hafskjold, and B. Smit, "Investigation of Surfactant Efficiency Using Dissipative Particle Dynamics," *Langmuir*, vol. 19, no. 20, pp. 8195–8205, Sep. 2003.
- [259] M. A. Floriano and E. Caponetti, "Micellization in Model Surfactant Systems," *Langmuir*, vol. 15, no. 9, pp. 3143–3151, 1999.
- [260] B. G. Levine, D. N. LeBard, R. DeVane, W. Shinoda, A. Kohlmeyer, and M. L. Klein, "Micellization Studied by GPU-Accelerated Coarse-Grained Molecular Dynamics," *Journal of Chemical Theory and Computation*, vol. 7, no. 12, pp. 4135–4145, Dec. 2011.
- [261] B. Smit, P. a. J. Hilbers, K. Esselink, L. a. M. Rupert, N. M. Van Os, and a. G. Schlijper, "Structure of a water/oil interface in the presence of micelles: a computer simulation study," *The Journal of Physical Chemistry*, vol. 95, no. 16, pp. 6361–6368, Aug. 1991.
- [262] D. W. Cheong and A. Z. Panagiotopoulos, "Monte carlo simulations of micellization in model ionic surfactants: application to sodium dodecyl sulfate," *Langmuir*, vol. 22, no. 9, pp. 4076–4083, Apr. 2006.
- [263] N. Arai, K. Yasuoka, and Y. Masubuchi, "Spontaneous self-assembly process for threadlike micelles.," *The Journal of Chemical Physics*, vol. 126, no. 24, p. 244905, Jun. 2007.
- [264] A. D. Mackie, A. Z. Panagiotopoulos, and I. Szleifer, "Aggregation Behavior of a Lattice Model for Amphiphiles," *Langmuir*, vol. 13, no. 19, pp. 5022–5031, Sep. 1997.
- [265] K. Pajula, M. Taskinen, V.-P. Lehto, J. Ketolainen, and O. Korhonen, "Predicting the formation and stability of amorphous small molecule binary mixtures from computationally determined Flory-Huggins interaction parameter and phase diagram.," *Molecular Pharmaceutics*, vol. 7, no. 3, pp. 795–804, Jun. 2010.
- [266] F. Zeng, Y. Sun, Y. Zhou, and Q. Li, "Molecular simulations of the miscibility in binary mixtures of PVDF and POSS compounds," *Modelling and Simulation in Materials Science and Engineering*, vol. 17, no. 7, p. 075002, Oct. 2009.

- [267] R. L. C. Akkermans, “Mesoscale model parameters from molecular cluster calculations.,” *The Journal of Chemical Physics*, vol. 128, no. 24, p. 244904, Jun. 2008.
- [268] Y. Zhang, S. K. Mallapragada, and B. Narasimhan, “Dissolution of Styrene – Butadiene Block Copolymers in Biodiesel,” *Journal of Applied Polymer Science*, vol. 118, no. 3, pp. 1859–1866, 2010.
- [269] F. a. M. Leermakers and J. M. H. M. Scheutjens, “Statistical thermodynamics of association colloids. I. Lipid bilayer membranes,” *The Journal of Chemical Physics*, vol. 89, no. 5, pp. 3264–3274, 1988.
- [270] R. D. Groot, “Electrostatic interactions in dissipative particle dynamics—simulation of polyelectrolytes and anionic surfactants,” *The Journal of Chemical Physics*, vol. 118, no. 24, pp. 11265 – 11277, 2003.
- [271] F. Goujon, A. Ghoufi, P. Malfreyt, and D. J. Tildesley, “Frictional forces in polyelectrolyte brushes: effects of sliding velocity, solvent quality and salt,” *Soft Matter*, vol. 8, no. 17, pp. 4635–4644, 2012.
- [272] A. Milchev, D. I. Dimitrov, and K. Binder, “Polymer brushes with nanoinclusions under shear: A molecular dynamics investigation,” *Biomicrofluidics*, vol. 4, no. 3, p. 32202, 2010.
- [273] J. P. Hansen and I. R. McDonald, *Theory of Simple Liquids*. Elsevier Science, 2006.

List of figures

Figure 1 - 1: Membrane flow configurations. Left: Crossflow filtration; Right: Dead-end filtration.....	11
Figure 1 - 2: Cut-offs of different liquid filtration techniques [18]	12
Figure 1 - 3: Osmosis and reverse osmosis system.....	15
Figure 1 - 4: Schematic of (a) RO Membrane Process and (b) RO Process Streams	16
Figure 1 - 5: Cross-section images of a RO membrane: the left image for the whole cross-section (× 850 magnification), the right image for top cross-section (× 75,000 magnification) [61].	19
Figure 1 - 6: The polymerization reactions of most commonly used aromatic PA membranes [61]	20
Figure 1 - 7: Membrane configurations: tubular, spiral-wound, and hollow fiber	22
Figure 1 - 8: Concentration polarization phenomenon	24
Figure 1 - 9: Fouling and cleaning of RO membrane	27
Figure 1 - 10: Schematic of a liquid drop showing the quantities in Young's equation ...	33
Figure 1 - 11: Atomic force microscopy images of RO membranes (a) AK (roughness 54.2 nm) and (b) SG (roughness 15.3 nm) [61].....	37
Figure 1 - 12: Annual production of surfactants in Western Europe from 2000 to 2011 (CESIO Statistics 2011, Dec 2012)	39
Figure 1 - 13: Amphiphilic structure of surfactants. The head corresponds to the hydrophilic part of the surfactant molecule, which is polar; while the tail represents the hydrophobic group of the surfactant molecule, which is apolar.....	40
Figure 1 - 14: Surfactant monomers and micelle formation in water	43
Figure 1 - 15: Schematic presentation of typical four-region adsorption isotherm [139]	50
Figure 1 - 16: Adsorption of surfactants on hydrophobic surface. a: surfactant monomers; b: surfactant micelles; c: isolated adsorbed surfactant monomers; d: surface aggregates[13]	50
Figure 1 - 17: Thesis objectiv	64

Figure 2 - 1: Suggested chemistry of the top polyamide layer of SG membrane: polyesteramide [61]	70
Figure 2 - 2: Schematic representation of the SEPA CF II Membrane Element Cell.....	72
Figure 2 - 3: Influence of the initial surfactant concentration on the relative flux of the RO membrane. $\Delta P = 30$ bar, $T=25^\circ\text{C}$. The CMC of SDS is 8.2 mmol L^{-1}	80
Figure 2 - 4: Zeta potentials ζ of a thin-film composite polyamide (FT-30) and an asymmetric cellulose acetate (CG) RO membrane in the presence and absence of SDS [198].	80
Figure 2 - 5: Time evolution of permeate flux of SDS solutions (J_s) in fouling tests with SG membrane at two different surfactant concentrations: (A) 0.2 CMC; (B) 5 CMC. Experiments were carried out at $\text{pH} = 6.0 \pm 0.1$ under pressure of 30 bar.	82
Figure 2 - 6: Flux ($\text{L h}^{-1} \text{ m}^{-2}$) and accumulated amount as a function of time during fouling with the RO membrane. The concentrations of SDS are: (A) 4.0 mM; (B) 8.0 mM; and (C) 40.0 mM, respectively. Solution $\text{pH} = 6.0 \pm 0.1$, operating temperature = 25°C , and applied pressure = 30 bar.	84
Figure 2 - 7: Flux decline and adsorption amount <i>versus</i> equilibrium SDS concentration in the system during RO filtration with a polyamide SG membrane at 30 bar.	87
Figure 2 - 8: Equilibrium adsorption isotherm for SDS on RO membrane in filtration mode. C : the equilibrium surfactant concentration in the SDS solution; q_f : the adsorption amount of SDS on the RO membrane in filtration mode.	88
Figure 2 - 9: The plastic tubing cut from the filtration system.	91
Figure 2 - 10: Kinetics of SDS adsorption on RO membrane. C_0 (initial bulk concentration) = 0.8 mmol L^{-1} ; $\text{pH} = 6.0 \pm 0.1$; adsorption carried out for 24 h; shaking speed = 180 rpm. q_s = adsorption amount per membrane surface area (mmol m^{-2}).....	92
Figure 2 - 11: Adsorption isotherm of static adsorption on RO membrane. $\text{pH} = 6.0 \pm 0.1$; adsorption carried out for 24 h; 180 rpm shaking speed. q_{ads} = amount adsorbed per membrane surface area (mmol m^{-2}).....	93
Figure 2 - 12: Hypothesis of RO membrane structure to estimate the whole membrane surface area.	94
Figure 2 - 13: Adsorption isotherm and contact angle with water for RO membrane.....	98
Figure 2 - 14: Adsorption isotherm and electro-donor parameter of the surface tension for RO membrane. The inset shows a zoomed-in version of the region from 0 to 8.0 mmol L^{-1}	100

Figure 2 - 15: Equilibrium among different phases in the filtration system. A. Aqueous phase of SDS solution; B. Interface of SDS solution and RO membrane; C. Solid phase of RO membrane.	101
Figure 2 - 16: Possible mechanism of surfactant adsorption onto RO membrane and penetration into the membrane. (a). Formation of a compact secondary membrane by surfactant monomers below the CMC; (b). Formation of a porous secondary membrane by surfactant micelles above the CMC.	104
Figure 3 - 1: Molecular structures of (a) sodium hexyl sulfate (SHS, $C_6H_{13}OSO_3Na$) and (b) sodium nonyl sulfate (SNS, $C_9H_{19}OSO_3Na$) modeled in this study. The sodium atoms are not shown in this figure.	117
Figure 3 - 2: Coarse-grained models used in the simulations with their nomenclature. H1T2 and H1T3 correspond to SHS and SNS, respectively.	117
Figure 3 - 3: Snapshots for the simulation box containing H1T2 molecules obtained in the course of micelle formation. The hydrophobic tail bead is shown by yellow balls, the hydrophilic head bead is shown by blue balls, and water beads are not shown, rendered by VMD ($a_{HT} = 104$, $a_{HW} = 65$, $a_{WT} = 98$, $C_{H1T2} = 0.3 \text{ mol L}^{-1}$).	122
Figure 3 - 4: Snapshots for the simulation box containing H1T2 molecules obtained in the course of micelle formation. The hydrophobic tail bead is shown by yellow balls, the hydrophilic head bead is shown by blue balls, and water beads are not shown, rendered by VMD ($a_{HT} = 104$, $a_{HW} = 65$, $a_{WT} = 98$, $C_{H1T2} = 0.8 \text{ mol L}^{-1}$).	123
Figure 3 - 5: Radial distribution functions of surfactant centers of mass, $g(r)_{CM-CM}$ for H1T2 system. ($a_{HT} = 104$, $a_{HW} = 65$, $a_{WT} = 98$, $C_{H1T2} = 0.8 \text{ mol L}^{-1}$, $t = 100000$). .	125
Figure 3 - 6: Radial distribution functions of intermolecular surfactant heads, $g(r)_{H-H}$ for H1T2 system. ($a_{HT} = 104$, $a_{HW} = 65$, $a_{WT} = 98$, $C_{H1T2} = 0.8 \text{ mol L}^{-1}$, $t = 100000$). .	125
Figure 3 - 7: Time evolution of bonding energy (Eb), chemical potentials (Ep), Lennard-Jones potential (LJ) and temperature (T) in the H1T2 system. ($a_{HT} = 104$, $a_{HW} = 65$, $a_{WT} = 98$, $C_{H1T2} = 0.1 \text{ mol L}^{-1}$).	127
Figure 3 - 8: Weight-average aggregation number N_w as a function of time during the process of micelle formation in a concentrated H1T3 solution ($a_{HT} = 104$, $a_{HW} = 65$, $a_{WT} = 96$, $C_{H1T2} = 0.07 \text{ mol L}^{-1}$). Vertical dashed lines indicate the approximate boundaries between different stages of micellization process.	128
Figure 3 - 9: Snapshots for the simulation box containing H1T3 molecules obtained in the course of micelle formation. The hydrophobic tail bead is shown by yellow balls, the hydrophilic head bead is shown by blue balls, and water beads are not shown, rendered by VMD ($a_{HT} = 104$, $a_{HW} = 65$, $a_{WT} = 96$, $C_{H1T2} = 0.07 \text{ mol L}^{-1}$).	129

Figure 3 - 10: Cluster size distribution of surfactant solutions with different cutoff values to distinguish the clusters. a. H1T2 system, $C_{\text{H1T2}} = 0.8 \text{ mol L}^{-1}$ ($a_{\text{HT}} = 104$, $a_{\text{HW}} = 65$, $a_{\text{WT}} = 98$); b. H1T3 system, $C_{\text{H1T3}} = 0.07 \text{ mol L}^{-1}$ ($a_{\text{HT}} = 104$, $a_{\text{HW}} = 65$, $a_{\text{WT}} = 96$).	131
Figure 3 - 11: Cluster size distribution for H1T2 systems with different concentrations at equilibrium ($a_{\text{HT}} = 104$, $a_{\text{HW}} = 65$, $a_{\text{WT}} = 98$).	132
Figure 3 - 12: Cluster size distribution for H1T3 solutions with different concentrations in equilibrium ($a_{\text{HT}} = 104$, $a_{\text{HW}} = 65$, $a_{\text{WT}} = 96$).	133
Figure 3 - 13: The concentration of free surfactants versus the total concentration of H1T2. The vertical line corresponds to the estimated CMC $\approx 0.42 \text{ mol L}^{-1}$ ($a_{\text{HT}} = 104$, $a_{\text{HW}} = 65$, $a_{\text{WT}} = 98$).	135
Figure 3 - 14: Cluster size distribution for H1T2 system with different concentrations in equilibrium, using Groot's parameters ($a_{\text{HT}} = 104$, $a_{\text{HW}} = 75.8$, $a_{\text{WT}} = 104$).	136
Figure 3 - 15: Snapshot of H1T2 system at equilibrium, using Groot's parameters ($a_{\text{HT}} = 104$, $a_{\text{HW}} = 75.8$, $a_{\text{WT}} = 104$, $C_{\text{H1T2}} = 0.1 \text{ mol L}^{-1}$).	137
Figure 3 - 16: Average aggregation number versus head-tail interaction parameter (a_{HT}) and head-water interaction parameter (a_{HW}). $a_{\text{WT}} = 104$ and $C_{\text{H1T2}} = 0.5 \text{ mol L}^{-1}$. The inset shows the plot of $a_{\text{HW}} = 65$ at small scales.	140
Figure 3 - 17: Average aggregation number of H1T2 versus tail-water interaction parameter a_{WT} ($a_{\text{HW}} = 65$, $a_{\text{HT}} = 124$, $C_{\text{H1T2}} = 0.5 \text{ mol L}^{-1}$).	141
Figure 3 - 18: Cluster size distribution for H1T2 system with different intramolecular interactions at equilibrium, using Groot's parameter set in Table 3 - 3 ($k_{\theta} = 6$, $\theta = \pi$). A. $k_r = 4$, $r_0 = 0$; B. $k_r = 100$, $r_0 = 0.7$	144
Figure 3 - 19: $g(r)_{\text{CM-CM}}$ of H1T2 systems with different bonding parameter sets	145
Figure 3 - 20: Cluster size distribution for H1T2 system with different intramolecular interactions at equilibrium, using parameter set III ($k_{\theta} = 6$, $\theta = \pi$). A. $k_r = 4$, $r_0 = 0$; B. $k_r = 100$, $r_0 = 0.7$	145
Figure 3 - 21: Cluster size distributions for H1T2 systems with different concentrations at equilibrium, using parameter set III ($a_{\text{HT}} = 104$, $a_{\text{HW}} = 65$, $a_{\text{WT}} = 98$).	148
Figure 3 - 22: The concentration of free surfactants and micelles versus the total concentration of H1T3. The vertical line corresponds to the estimated CMC $\approx 0.035 \text{ mol L}^{-1}$ ($a_{\text{HT}} = 104$, $a_{\text{HW}} = 65$, $a_{\text{WT}} = 96$).	149
Figure 3 - 23: Simulation box for the adsorption of surfactants on the membrane. The membrane is represented as a simplified plane at $z = 0$. Due to periodic boundary conditions, the plane at the top of this box is also considered as the membrane. ...	152

Figure 3 - 24: Final snapshots of H1T2 adsorption structures at the membrane surfaces with different parameter a_{MT} , starting from random configurations. A. $a_{MT} = 78$; B. $a_{MT} = 75.8$; C. $a_{MT} = 73.7$; D. $a_{MT} = 69.3$; E. $a_{MT} = 65$. Box size : $20 r_c \times 20 r_c \times 20 r_c$, The total concentration of H1T2 $C_{H1T2} = 0.8 \text{ mol L}^{-1}$, $t = 50000$. Head groups are shown in red beads, tail groups are shown in green, water beads are not shown for clarity. The membrane is presented at the bottom and top of the box..... 153

Figure 3 - 25: Final snapshots of H1T2 adsorption structures at the membrane surfaces at different total concentrations, starting from random configurations. A. $C_{H1T2} = 0.1 \text{ mol L}^{-1}$; B. $C_{H1T2} = 0.2 \text{ mol L}^{-1}$; C. $C_{H1T2} = 0.5 \text{ mol L}^{-1}$; D. $C_{H1T2} = 0.7 \text{ mol L}^{-1}$; Box size : $20 r_c \times 20 r_c \times 20 r_c$, $a_{MT} = 65$, $t = 50000$. The color scheme for the snapshots is the same as Figure 3 - 24..... 155

Figure 3 - 26: Final snapshots of H1T3 adsorption structures at the membrane surfaces at different total concentrations, starting from random configurations. A. $C_{H1T3} = 0.01 \text{ mol L}^{-1}$; B. $C_{H1T3} = 0.06 \text{ mol L}^{-1}$; C. $C_{H1T3} = 0.1 \text{ mol L}^{-1}$; D. $C_{H1T3} = 0.2 \text{ mol L}^{-1}$; Box size : $30 r_c \times 30 r_c \times 30 r_c$, $a_{MT} = 65$, $t = 50000$. The color scheme for the snapshots is the same as Figure 3 - 24..... 156

Figure 3 - 27: Time evolution of H1T3 adsorption onto the membrane from an initial random distribution. A. $t = 0$; B. $t = 1650$; C. $t = 8000$; D. $t = 20250$; E. $t = 50000$. The total surfactant concentration $C_{H1T3} = 0.1 \text{ mol L}^{-1}$. Box size : $30 r_c \times 30 r_c \times 30 r_c$, $a_{MT} = 65$. The color scheme for the snapshots is the same as Figure 3 - 24. 158

List of tables

Table 1 - 1: Size of Materials Retained, Driving Force, and Type of Membrane [1].....	12
Table 1 - 2: Summary for main RO membrane materials [1]	18
Table 1 - 3: Characterization methods for clean membranes [69].....	28
Table 1 - 4: Common hydrophobic groups used in commercially available surfactants [7]	41
Table 1 - 5: Common hydrophilic groups found in commercially available surfactants [7]	42
Table 1 - 6 a: Membrane filtration of surfactants in literature: microfiltration	54
Table 2 - 1: Operating and CIP parameters of SG membranes*.....	70
Table 2 - 2: Surface tensions (mJ m^{-2}) of liquids according to Van Oss [7].....	77
Table 2 - 3: Retention and flux decline during RO membrane filtration, $P = 30$ bar, $T=25^\circ\text{C}$. The CMC of SDS is 8.2 mmol L^{-1}	78
Table 2 - 4: The time evolution of permeate flux and adsorption amount for different surfactant solutions during RO filtration (corresponding to Figure 2 - 6).....	85
Table 2 - 5: System interface areas in contact with the surfactant solution*	90
Table 2 - 6: The mass loss and adsorption of SDS per membrane surface area in different systems (mmol m^{-2}). q_{tot} is the mass loss of SDS per membrane surface area in the filtration system; q_{sys} , and a_{mem} are the adsorption amount on the system materials and on the membrane, respectively.	96
Table 2 - 7: Contact angles with water, formamide and di-iodomethane for virgin SG membrane and membranes after filtering SDS solutions.	97
Table 2 - 8: Surface tensions (mJ m^{-2}) of SG membranes in various forms: clean membrane, membranes after filtration with SDS solutions at different concentrations (inferred from contact angles listed in Table 2 - 7, calculation based on (Equation 2 - 7)).	98
Table 3 - 1: Experimental values of CMC and aggregation numbers for SHS and SNS at 25°C	118

Table 3 - 2: Time, mass, length and energy scales of the system	119
Table 3 - 3: Bead–bead repulsion parameter set I used in the simulation systems of Groot [257].....	119
Table 3 - 4: Bead–bead repulsion parameter set II used in our simulation systems	119
Table 3 - 5: Composition details for each H1T2 system ($20 r_c \times 20 r_c \times 20 r_c$) simulated in this work	120
Table 3 - 6: Composition details for each H1T3 system ($30 r_c \times 30 r_c \times 30 r_c$) simulated in this work	121
Table 3 - 7: Equilibrium time and total simulation time for H1T2 and H1T3 systems (in DPD units)	130
Table 3 - 8: Values of the aggregation numbers for sodium hexyl sulfate calculated from DPD simulation at different concentrations, using Groot's parameter set I ($a_{HT} = 104$, $a_{HW} = 75.8$, $a_{WT} = 104$)	137
Table 3 - 9: Experimental and simulation data of CMCs (mol L^{-1}) for H1T2 and H1T3 at $25\text{ }^\circ\text{C}$	138
Table 3 - 10: Derivation of parameter set II used in our simulation systems	139
Table 3 - 11: Aggregation numbers for H1T2 with different intramolecular interaction sets ($a_{HT} = 104$, $a_{HW} = 75.8$, $a_{WT} = 104$)	143
Table 3 - 12: Average aggregation numbers $\langle N_w \rangle$ for H1T2 with different intramolecular interaction sets ($a_{HT} = 104$, $a_{HW} = 65$, $a_{WT} = 98$).....	146
Table 3 - 13: Bead–bead repulsion parameter set III used in for the optimization of H1T2 systems.....	147
Table 3 - 14: Bead–bead repulsion parameter set IV used in for the optimization of H1T3 systems.....	148
Table 3 - 15: CMC values and aggregation numbers for H1T2 and H1T3 systems with different a_{ij} parameter sets	150
Table 3 - 16: Bead–bead repulsion parameter set used in the simulation of surfactant adsorption	152

RESUME

Les procédés membranaires pour le traitement de l'eau: étude et modélisation des interactions entre membranes et composés organiques

L'objectif de cette thèse est de mettre en évidence le comportement à l'échelle microscopique des composés organiques au cours des procédés de traitement de mélanges complexes, en particulier les procédés membranaires. Pour cela des outils expérimentaux et de modélisation ont été mis au point.

Les méthodes de caractérisation expérimentale des mélanges complexes et de l'état de surface des solides utilisés sont entre autres la construction d'isothermes d'adsorption et la mesure des tensions interfaciales par la méthode de la goutte posée. Le cas étudié ici est celui de la filtration de solutions modèles de tensioactifs par osmose inverse. Nous avons montré que le comportement des composés organiques (tensioactifs) influence la performance du procédé membranaire et les propriétés de membranes.

L'outil de simulation du comportement des composés en phase liquide et à l'interface liquide-solide permettant une description à une échelle plus fine que celle atteignable expérimentalement est la DPD (Dissipative Particle Dynamics). Une première étape a permis de simuler l'agrégation des tensioactifs en solution et de retrouver les valeurs expérimentales des concentrations micellaires critiques et nombres d'agrégation de tensioactifs anioniques. L'étude de l'adsorption des tensioactifs sur une membrane d'osmose inverse a été initiée, avec pour objectif de mettre en évidence l'organisation des composés à l'échelle locale. L'apport des outils développés a été démontré et leur utilisation pourra être approfondie dans des travaux ultérieurs.

Mots clés : procédés membranaires, osmose inverse, tensioactif, adsorption, micellisation, Dissipative Particle Dynamics

ABSTRACT

Membrane processes for water and wastewater treatment: study and modeling of interactions between membrane and organic matter

The aim of this work is a better understanding of the microscopic behavior of organic matters during the wastewater treatment of complex mixtures, especially during the membrane processes. Both experimental and simulation methods were developed in this work.

Experimentally, adsorption isotherms were built to study the adsorption of organic matters on the membrane surface during the filtration. The sessile drop measurement allowed investigating the surface properties (interfacial tensions) of the membrane. After the filtration of surfactants by reverse osmosis (RO), we found that the surfactants played an important role in the performance and the surface properties of the RO membrane.

The DPD (Dissipative Particle Dynamics) simulation method was used to model the behavior of anionic surfactants in solution and at the solid/liquid interface from a more detailed aspect than experiments. Firstly, the micellization of three anionic surfactants in aqueous solution was simulated and the model was validated by comparing the equilibrium properties (the critical micelle concentration and aggregation number) of micelle solutions obtained from simulation to the experimental values in literature. Then the model was extended to simulate the adsorption of surfactants on the RO membrane. The construction of a system with a membrane was initiated, and the study on the organizations of surfactants at the membrane surface opens a door to further active research.

Key words : membrane process, reverse osmosis, surfactant, adsorption, micellization, dissipative particle dynamics